Conference Proceedings

2013 Tokyo Japan

ICEAS | The 2nd International Conference on Engineering and Applied Science

LSBE | International Conference on Life Science & Biological Engineering

ACCMES | Asian Conference on Civil, Material and Environmental Sciences

ICEECS | International Conference on Electrical Engineering and Computer Sciences

Proceedings of *International Conference on Life Science & Biological Engineering*
ISBN 978-986-89298-1-4

Proceedings of Asian Conference on Civil, Material and Environmental Sciences
ISBN 978-986-89298-0-7

Proceedings of International Conference on Engineering and Applied Science
ISBN 978-986-87417-1-3

Proceedings of International Conference on Electrical Engineering and Computer Science
ISBN 978-986-88450-3-9

General Information for Conference Participants

Information and Registration

The Registration and Information Desk will be situated in the **Toshi Center Hotel** on the **sixth floor**, and will be open at the following times:
Saturday, March 16 (08:30-18:00)
Sunday, March 17 (08:30-18:00)

Parallel Sessions

Parallel Sessions will run on March 16 and 17 . Sessions are usually 90 minutes in length.

Presentations and Equipment

All presentation rooms are equipped with a screen, an LCD projector, and a laptop computer installed with PowerPoint software. You will be able to insert your USB flash drive into the computer and double click on your presentation to open it in PowerPoint. We recommend that you bring two copies of your presentation in case of one fails. You may also link your own laptop computer to the projector cable, however if you use your own Mac please ensure you have the requisite connector.

A Polite Request to All Participants

Participants are requested to arrive in a timely fashion for all addresses, whether to their own, or to those of other presenters. Presenters are reminded that the time slots should be divided fairly and equally between the number of presentations, and that they should not overrun. The session chair is asked to assume this timekeeping role.

Poster Sessions & Poster Requirements

Materials Provided by the Conference Organizer:

1. X-frame display & Base Fabric Canvases (60cm×160cm)
2. Adhesive Tapes or Clamps

Materials Prepared by the Presenters:

Home-made Poster(s)

Requirement for the Posters:

1. Material: not limited, can be posted on the canvases
2. Size: smaller than 60cm*160cm

Contents

LSBE International Committee Board

Ahmad Zuhairi Abdullah	Universiti Sains Malaysia
Fadzilah Adibah Abdul Majid	Universiti Teknologi Malaysia
Mohd Farid bin Atan	University of Sarawak Malaysia
Sue-Joan, Chang	National Cheng Kung University
Yen-Chung, Chang	National Tsing Hua University
Yun-Peng, Chao	Feng Chia University
Pei-Jen, Chen	National Taiwan University
H.M. El-Shora	Mansoura University
I Ming Hsing	The Chinese University of Hong Kong
Shang-Da, Huang	National Tsing Hua University
Bing Joe Hwang	National Taiwan University of Science and Technology
Kondabagil K	Indian Institute of Technology Bombay
Sungjee Kim	Sungkyunkwan University
Li-Fen, Lei	National Taiwan University
Yunsheng, Lou	Nanjing University of Information Science and Technology
Mihir Kumar Purkait	Indian Institute of Technology Guwahati
Chung-Sung, Tan	National Tsing Hua University
Tewin Tencomnao	Chulalongkorn University
S.K. Tripathi	Indian Institute of Technology Poorkee
Henry N.C. Wong	The Chinese University of Hong Kong
Yusri b. Yusup	Universiti Sains Malaysia
Hasan Akhtar Zaidi	Guru Gobind Singh Indraprastha University

LSBE Session Chair

Mohd Effendy Abd Wahid	Universiti Malaysia Terengganu
Chong Kim Wong	The Chinese University of Hong Kong
Anne C Beuter	Bordeaux Polytechnic Institute
Praneet Ngamsnae	Ubon Ratchathani University
Enas Talib Abdul-Karim	Al-Nahrain University
Dujreutai Pongkao Kashima	Chulalongkorn University
A. M. Abd El-Aty	Cairo University

ACCMES International Committee Board

Manoj S Soni	The Birla Institute of Technology & Science
Mohd Razman Salim	Universiti Teknologi Malaysia
Monica Sharma	Malaviya National Institute of Technology Jaipur
Nasser Khalili	University of New South Wales
Nilanchal Patel	Birla Institute of Technology Mesra
Nilanjana Das	University of Calcutta
Norhayati Ahmad	Universiti Teknologi Malaysia
P. Sivaprakash	Karpagam Institute of Technology
Pramod Kumar Jain	Indian Institute of Technology Roorkee
Prem Raj P	National Institute of Technology Calicut
Renu Pawels	Cochin University of Science & Technology
S. Chandrakaran	National Institute of Technology Karnataka
Saxena Ashok K	Indian Institute of Technology
Sharad Chandra Srivastava	B.I.T Mesra , Ranchi
Siti Mariyam Shamsuddin	Universiti Teknologi Malaysia
Sri Bandyopadhyay	University of New South Wales
Tuty Asma Abu Bakar	Universiti Teknologi Malaysia
V K Tewari	Indian Institute of Technology Kharagpur
Wiboonluk Pungrasmi	Chulalongkorn University
William K. Mohanty	Indian Institute of Technology

ACCMES Session Chair

Mohammed Enamul Haque	Texas A&M University
Mehmet Sahin	Turksat A.S.
Gianluca Ranzi	The University of Sydney
Fouad Ahmed Gharaybeh	Jordan University of Science and Technology
Luísa Valente Cruz-Lopes	Polytechnic Institute of Viseu
C Y Jim	University of Hong Kong
Masoud Ibrahim Mohamed	Northern Border University

ICEAS International Committee Board

Khalid M. Mosalam	University of California, Berkeley
Chueerat Jaruskulchai	Kasetsart University
M. Cheralathan	SRM University
J N Bandyopadhyay	Indian Institute of Technology Kharagpur
S. Dhar	University of Calcutta
Poongothai Shankar	Annamalai University
Amit Agrawal	Indian Institute of Technology Bombay
Cheng Li	The Hong Kong Polytechnic University
T.M. Indra Mahlia	University of Malaya
Kunal Ghosh	Indian Institute of Technology Kanpur
Narayanan Kulathuramaiyer	University of Sarawak Malaysia
Arup K. Sarma	Indian Institute of Technology Guwahati
Suresh K Bhargava	School of Applied Sciences
Rapeepan Pitakaso	Ubonratchthani University
Jie Liu	Carleton University
Carlos Alejandro Figueroa	Plasmar Tecnologia
Dong-Ho Ha	Konkuk University
Poul Vaeggemose	VIA University College Denmark
Maha M. O. Khayyat	Umm Al-Qura University
Kant Kanyarusoke	Cape Peninsula University of Technology
Paramita Bhattacharjee	Jadavpur University
Nathalia Devina Widjaja	Binus International University
C. M. Khalique	North-West University,South Africa

ICEAS Advisory Committee & Program Committee

Advisory Committee

Banerji P	Indian Institute of Technology Kharagpur
P.K. Ghosh	Indian Institute of Technology Poorkee
E George Dharma Prakash Raj	Bharathidasan University
R.P.Bhatnagar	Birla Institute of Technology
V. Vijayagopal	Annamalai University
Amit Awekar	Indian Institute of Technology Guwahati
Gustavo Carneiro	University of Adelaide
Pui-In Mak	University of Macau
E,Rathakrishnan	Indian Institute of Technology Kanpur
Bassim H. Hameed	University of Science Malaysia
Sudhirkumar Barai	Indian Institute of Technology Kharagpur
S. N. Sarkar	Calcutta University

Program Committee

Samit Bhattacharya	Indian Institute of Technology Kanpur
A. P. Shashikala	Birla Institute of Technology
RM. Senthamarai	Annamalai University
Arnab Bhattacharya	Indian Institute of Technology Kanpur
Zbigniew Michalewicz	University of Adelaide
B. Bhattacharya	Indian Institute of Technology Kharagpur
Amin Heidarpour	Monash University
Faizal Mustapha	Universiti Putra Malaysia

ICEAS Session Chair

Ansgar Kern	Technische Hochschule Mittelhessen
Cho-Pei Jiang	National Formosa University
Enrique Arce Medina	Instituto Politécnico Nacional
H.S. Wang	National Taipei University of Technology
Aniruddha Ghosh	Govt. college of Engg. & Textile Technology
Yi-Ning Tu	Fu Jen Catholic University
Hamdi Bashir	Curtin University
Parkpoom Sriromreun	Srinakharinwirot University
Shafreeza Sobri	Universiti Putra Malaysia
Tran Duc Tang	Le Quy Don Technical University
Siriwan Srisorrachatr	Srinakharinwirot University
S. K. Ghoshal	ME & MME
Rakkreat Wikiniyadhanee	Chulalongkorn University
Elena V. Batrakova	University of North Carolina
Sreerama Kumar Ramdas	King Abdulaziz University
Patcharin Worathanakul	King Mongkut's University of Technology
Alice Maldonado Lacorte	First Asia Institute of Technology and Humanities
Shih-Hsuan Yang	National Taipei University of Technology
Ching-Chi Hsu	National Taiwan University of Science and Technology
San-Yih Lin	National Cheng Kung University
Liang-Chuan Wu	National Chung Hsing University

ICEECS International Committee Board

Suryanarayana Doolla	Indian Institute of Technology Bombay
Subhansu Bandyopadhyay	University of Calcutta
Mridula Gupta	University of Delhi South Campus
Debnath Pal	Indian Institute of Science
Jayaraj. S	Anna University
Alok Barua	IIT Kharagpur
Thipparaju Rama Rao	SRM University
A. Rathinam	SRM University
R. Jegatheesan	SRM University
G. Vijaya Kumari	Jawaharlal Nehru Technological University
S.Viswanadha Raju	Jawaharlal Nehru Technological University
Ashok S	Indian Institute of Information Technology Design and Manufacturing Kancheepuram
P C Subramaniam	Indian Institute of Information Technology Design and Manufacturing Kancheepuram
N Kumarappan	Annamalai University
K.Poulose Jacob	Cochin University of science and technology
Mounir Hamdi	Hong Kong University of Science and Technology
Chaodit Aswakul	Chulalongkorn University
Abdallah, Zahraa	Monash University
Alyani Ismail	Universiti Putra Malaysia
Lau Sei Ping	Universiti Malaysia Sarawak
Lekshmi. M	Visvesvaraya Technological University
Bahadur R P	IIT Kharagpur
P.G.Krishna Mohan	Jawaharlal Nehru Technological University
Jasrul Nizam Ghazali	MARA University of Technology
B. Kannan	Cochin University of science and technology
P. Sanjeevikumar	VIT University

ICEECS Session Chair

Ansgar Kern	Technische Hochschule Mittelhessen
Shu-Ming Hsieh	Hwa Hsia Institute of Technology
Chalie Charoenlarpnopparut	Thammasat Unviersity
Shih-Hsuan Yang	National Taipei University of Technology
Peerawut Suwanjan	King Mongkut's Institute of Technology Ladkrabag

Friday, March 15, 2013

10:30-12:00	**Committee Meeting (Committee Only)**

Saturday, March 16, 2013

Time	Information
08:30-17:30	**Registration (6F, Toshi Center Hotel)**
09:00-10:30	Oral Session Room 603, Life Science I
	Oral Session Room 604, Civil Engineering I
	Oral Session Room 605, Electrical Engineering I
	Poster Session Room 607, Poster Session
	Oral Session Room 608, Business I
	Oral Session Room 609, Management I
10:30-10:45	**Tea Break**
10:45-12:15	Oral Session Room 603, Life Science II
	Oral Session Room 604, Civil Engineering II
	Oral Session Room 605, Biomedical Engineering I
	Poster Session Room 607, Poster Session
	Oral Session Room 608, Welcome Speech/ Keynote Speech/ Politics
	Oral Session Room 609, Communication / Culture
12:15-13:15	**Lunch Time**
13:15-14:45	Oral Session Room 603, Biological Engineering I
	Oral Session Room 604, Environmental Sciences I
	Oral Session Room 605, Chemical Engineering I
	Poster Session Room 607, Poster Session
	Oral Session Room 608, Management II
	Oral Session Room 609, Psychology / Education
14:45-15:00	**Tea Break**
15:00-16:30	Oral Session Room 603, Computer and Information Sciences I
	Oral Session Room 604, Civil Engineering III

	Oral Session Room 605, Mechanical Engineering I
	Poster Session Room 607, Poster Session
	Oral Session Room 608, Economics I
	Oral Session Room 609, Society
16:30-16:45	**Break**
16:45-18:15	Oral Session Room 603, Computer and Information Sciences II
	Oral Session Room 604, Civil Engineering IV
	Oral Session Room 605, Mechanical Engineering II
	Poster Session Room 607, Poster Session
	Oral Session Room 608, Material Science and Engineering I
	Oral Session Room 609, Environmental Sciences II

Sunday, March 17, 2013

Time	Information
08:30-17:30	**Registration (6F, Toshi Center Hotel)**
09:00-10:30	Oral Session Room 603, Life Science III
	Oral Session Room 604, Mechanical Engineering III
	Oral Session Room 605, Environmental Sciences III
	Poster Session Room 607, Poster Session
	Oral Session Room 608, Business II
	Oral Session Room 609, Civil Engineering V
10:30-10:45	**Tea Break**
10:45-12:15	Oral Session Room 603, Life Science IV
	Oral Session Room 604, Mechanical Engineering IV
	Oral Session Room 605, Wireless communication / Multimedia
	Poster Session Room 607, Poster Session
	Oral Session Room 608, Economics II
	Oral Session Room 609, Geosciences and Petroleum Engineering
12:15-13:15	**Lunch Time**
13:15-14:45	Oral Session Room 603, Fundamental & Applied Science
	Oral Session Room 604, Electrical Engineering II
	Oral Session Room 605, Chemical Engineering II
	Poster Session Room 607, Poster Session
	Oral Session Room 608, Management III
	Oral Session Room 609, Civil Engineering VI
14:45-15:00	**Tea Break**
15:00-16:30	Oral Session Room 603, Biological Engineering II
	Oral Session Room 604, Computer and Information Sciences III
	Oral Session Room 605, Material Science and Engineering II
	Poster Session Room 607, Poster Session
	Oral Session Room 608, Finance
	Oral Session Room 609, Computer and Information Sciences IV
16:30-16:45	**Break**
16:45-18:15	Oral Session Room 603, Biomedical Engineering II
	Oral Session Room 604, Computer and Information Sciences V
	Oral Session Room 605, Electronics Engineering

Toshi Center Hotel

Access to the Toshi Center Hotel

- 4 minute-walk from Exit No.1 of Kojimachi station, Yurakucho Subway Line.
- 4 minute-walk from Exit No.4 or 5 of Nagatacho Station, Yurakucho/Hanzomon Subway Lines.
- 3 minute-walk from Exit No.9 of Nagatacho Station,Nanboku Subway Line.
- 8 minute-walk from Exit D of Akasaka Mitsuke Station,Marunouchi / Ginza Subway Lines.
- 14 minute-walk from Kojimachi exit of Yotsuya Station, JR Chuo Line.
- By bus, Hirakawacho 2-chome Toshi Center-mae.
  (Shinbashi - Ichigaya - Kotakibashi Shako route)
- By car, five minutes from kasumigaseki exit, Shuto Expressway.

Program - Oral Sessions

Life Science I

2013/03/16 Saturday 09:00-10:30 Room 603

Session Chair: ***Mohd Effendy Abd Wahid***

LSBE 053

Response of serum IgG upon intranasal inoculation of Exopolysaccharides-adjuvanted vaccine of Pasteurella multocida B:2 in Winstar rats

Mohd Effendy Abd Wahid | *Universiti Malaysia Terengganu*

M.A.K. Sharzehan | *Universiti Malaysia Terengganu*

LSBE 054

Investigation of exposure radiation dose for periapical inter-oral dental X-Ray Examination

Edrees M. Tahir Nury | *University of Salahaddin-Hawler*

Bayan Saber Ibrahim | *Hawler Medical University*

Hewa Y. Abdullah | *University of Salahaddin-Hawler*

LSBE 055

Investigation of Protein-Protein Interaction and its Possible Role in the Formation of Amyloid Fibrils

Sheeren I. Hajee | *Hawler Medical University*

Edrees M. T.Harki | *Salahadden-Hawler University*

LSBE 074

Reproductive success of Eurytemora affinis is unaffected during a diatom-dominated spring bloom

Roswati Md Amin | *Universiti Malaysia Terengganu*

Ulf Båmstedt | *Umeå University*

Carsten Paul | *Friedrich Schiller University Jena*

Larysa Samchyshyna | *Research Centre of Ecomonitoring and Biodiversity of Megalopolis NASU, Ukraine*

Elin Lindehoff | *Umeå University*

Georg Pohnert | *Friedrich Schiller University Jena*

LSBE 386

The study on influence to Cortisol concentration of dwellers for the indoor life space in the disaster prevention tents with causing environmental factors

Kazuo Fukushima | *Kyusyu University*
Takayuki NISHIMURA | *Kyusyu University*
Yosuke Nisato | *Kyusyu University*
Midori MOTO Ⅰ | *Kyusyu University*
Shigeki WATANUKI | *Kyusyu University*

LSBE 307

Changes of peripheral benzodiazepine receptor gene expression in major depressive disorder and methamphetamine dependence

Siriluk Weerasakul | *Naresuan University*
Namtip Tubtimtong | *Naresuan University*
Paritat Watiktinkorn | *Synphaet Hospital*
Samur Thanoi | *Naresuan University*
Sutisa Nudmamud-Thanoi | *Naresuan University*

LSBE 262

Leaf Anatomy and Pollen Studies of Zingiberaceae in Lambusango Wildlife Reserve, Buton Island, Indonesia

Gufrin Amlin | *University of Technologi MARA*
Rita Ningsih | *University of Haluoleo*
Mohd Nazip Suratman | *University of Teknologi MARA*
Nurun Nadhirah Md Isa | *University of Teknologi MARA*
Axel Dalberg Poulsen | *University of Oslo*
Indrawati Indrawati | *University of Haluoleo*

LSBE053
Response of serum IgG upon intranasal inoculation of Exopolysaccharides-adjuvanted vaccine of *Pasteurella multocida* B:2 in Winstar rats

*Effendy, A.W.M.[1]
[1]Institute of Marine Biotechnology, Universiti Malaysia Terengganu

M.A.K. Sharzehan[2]
[2]Department of Biological Science, Faculty of Science and Technology, Universiti Malaysia Terengganu

*Corresponding author: 1

Abstract

1. Objective

The study was conducted to determine the efficacy of exopolysaccharides (EPS)-adjuvanted intranasal vaccine of formalin-killed of *Pasteurella multocida* B:2 in white rats.

2. Materials and Methods

Twelve clinically healthy Winstar rats were divided equally into four groups. Group 1 was intranasally inoculated with EPS-adjuvanted formalin killed *Pasteurella multocida* B:2 at 1.41×10^7 CFU/mL while Group 2 with *P multocida* B:2 in sterile PBS with the same bacterial load. Group 3 was intra-nasally administered with EPS extracts while Group 4 remain as control untreated group. All treated groups were given booster vaccination intra-nasally at two weeks internal. Two weeks after the booster vaccination, all animals were challenged with intra-peritoneal injection of live *Pasteurella multocida* B:2 at 10^8 CFU/mL. Serum was collected from all animals every week to determine the level of IgG. Seven days after the challenge, all animals were euthanized and bacterial isolation was done from heart, lungs, liver and kidney upon post-mortem examination.

3. Results

Based on statistical analysis using ANOVA and T-test, significant level ($p<0.05$) of IgG was observed in the EPS-adjuvanted vaccine group when compared with other groups (Figure 1). The lesions were less severe in EPS-adjuvanted vaccine group compared to others. *Pasteurella multocida* B:2 were successfully re-isolated from all organs of animals in Group 3 and Group 4 that died at day-4 post-challenge.

4. Conclusion

Therefore, EPS-adjuvanted vaccine is effective to be used as potential adjuvant for intranasal vaccination against *Pasteurella multocida* B:2 infection.

5. Acknowledgements

The author wish to acknowledge the Institute of Marine Biotechnology, Universiti Malaysia Terengganu for providing the facilities to run the experiment.

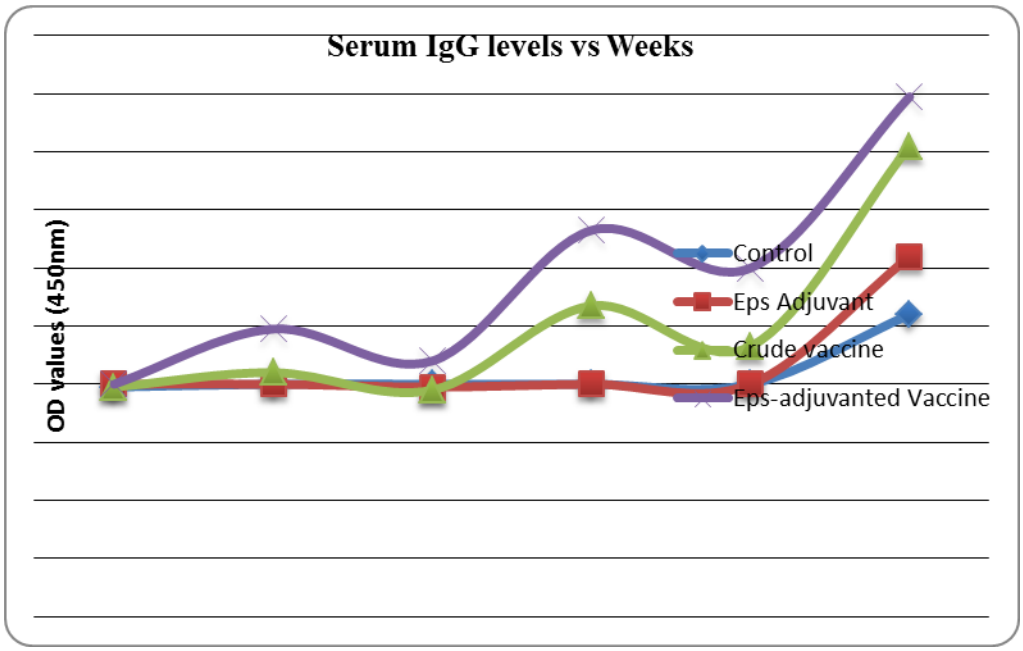

Figure 1: The development of serum IgG antibody response in Winstar white rats for each week.

LSBE054
Investigation of exposure radiation dose for periapical intra-oral dental X-Ray Examination

Edrees M. T.Harki
Physics Department, College of Education,Salahadden-HawlerUniversity ,Krg, Iraq
Email :edreesharki1@yahoo.com

Bayan Saber Ibrahim
Department of Basic sciences-College of Dentistry/Hawler Medical University, Krg,
Email : bayan@yahoo.com

HewaYaseen Abdullah
Physics Department, College of Education,Salahadden-Hawler University ,Krg, Iraq
Email :kuhewa@yahoo.com

The corresponding author:HewaYaseen Abdullah

Abstract

The aim of this study is to estimate the radiation dose for children and to compare this estimate with the radiation dose experienced by adults arising from peripical intra-oral diagnostic exposure In addition, a comparison will be made between the maxillary and mandibular molers.In this study, ESD was measured using LiFthermoluminescent dosimeters (TLD-100) on the skin (either mandibular or maxillary arcs) of all patients. Monte Carlo simulation was performed to estimate an effective dose (ED) by using PCXMC Dose Calculation software. A wide distribution of doses has been obtained. A higher value mean±SD of ESD is recorded for maxillary molar (3.678±1.868) mGy for the (31-60 year) age group and the lowest value is recorded for mandibular molar (2.090±1.061) mGy for (1-15 year) age group. As well, a higher mean value of ED is recorded for mandibular molar, (4.998) µSv for the (1-15 year) group, but the lowest value (2.673) µSv is recorded for mandibular molar for the (16-31year) group.The ESD for maxillary molar is more than the ESD for mandibular molar for all age groups. In general, a wide distribution of doses has been obtained which are in good agreement with others, especially with EU.

Keyword: radiation dose,periapical inter-oral, entrance surface dose, effective

1. Introduction

Medical diagnostic X-rays represent the largest doses of man-made radiation. Dental radiology accounts for about 25% of all world-wide examinations,and intra-oral dental radiology represent almost 90% of the total explorations performed in dentistry[1]. When patients undergo X-ray examinations, millions of photons pass

through their bodies. The ionization by these photonscan do damage to any part of the cells molecular structure but damage to the DNA in the chromosomes is of particular importance. Most DNA damage is repaired immediately, but on rare occasions a portion of a chromosome may be permanently altered (a mutation). This may lead ultimately to the formation of a tumor[2].

In recent years concern has been raised over the hazards of exposure to small doses of ionizing radiation[3,4]. Although radiation doses in dental radiography are low, the probability of a fatal cancer being induced in an individual patient from a single X-ray examinationis dependent on the age of the patient and the type of examination[5].The risk for pediatric patients that undergo X-ray examinations is higher than that of adults because their cells, tissues and organs have higher radio sensitivity. Exposure during childhood may result in a two- to three-fold increase in lifetime risk for certain detrimental cancers compared with adults [6]. The European Commission (EC) [7] states that 'radiation exposure in the first 10 years of life is estimated to have a risk about 4 times greater than exposures incurred at 30–40 years of age for some detrimental effects'. It is important that the radiation dose to children arising from diagnostic medical exposure is minimized.

To assess the probability of health impairment from low doses of ionizing radiation, the International Commission on Radiation Protection (ICRP) proposed a theoretical quantity in 1975. This quantity was initially known as effective dose equivalent and became known as effective dose(ED) in 1990. This quantity gauges the health risk (fatal and nonfatal cancers, taking into account the latency period as well as severe hereditary disorders) of a "standard" patient who is not uniformly exposed to ionizing radiation and transposes it into a situation in which this patient would be uniformly exposed to a radiation field. Effective Dose(ED), which is the same unit as an equivalent dose, is obtained by summing individual organ equivalent doses (HT) multiplied by the corresponding tissue weighting factors.

$$ED = \sum_T W_T H_T \text{ with } \sum_T W_T = 1$$

Where WT is dimensionless tissue weighting factors characterizing the relative sensitivity of various tissues with respect to endpoints such as cancer induction and mortality [8]. The most appropriate method for ED calculation is the Monte Carlo simulation of radiography accompanied by measurements of entrance surface dose (ESD) or dose area product (DAP). Similar practices have been followed by many surveys [2,5] regarding the risk to children from simple X-ray examinations.

The aim of this study was to estimate the radiation dose for children and to compare

this dose with the radiation dose given to adultsduring Pediatric and adult periapical inter-oral dental X-Ray Examinations.

2. Methods

This study was carried out in the Dental College clinical hospitals in Erbil city. A total of 120 patients were divided into three age groups, (1-15),(16-30) and(31-60) and further divided based on sex, weight, height, thickness and technical parameters. Tube Voltage kVp, current-time product mAs ,FFD)were recorded. The Entrance Surface Dose (ESD) for each patient involved in periapical inter-oral dental X-Ray Examination was measured by using Thermolumence Dosimeter (TLD). In this study the Monte Carlo simulation was performed to estimate effective dose (ED) by using PCXMC Dose Calculation software copyright STUK 2004.

3. Result and Discussion

The technique factors kVp,mA and Time/sec with FFD focal to film distance, mean±SD for each patient age group as well as the overall mean ESD±SD for maxillary and mandibular intra-oral radiographies are shown in table (1). The distribution of ESDs measured at the center of the beam in intra-oral examinations for maxillary and mandibular is shown in figures (1) and (2), respectively.

The highest mean ESD±SDwere measured on the maxillary (3.678±1.868 mGy)formean age ±SDgroup (45.833±7.250 years) and the lowest mean ESD±SD were measured on the maxillary(2.775±0.822 mGy) for mean age±SD group (24.333±8.846 years). In addition, the highest mean ESD±SD were measured on the mandibular (2.304±1.328mGy) for mean age±SD group (26.833±6.645years) while the lowest mean ESD±SDwere measured on the mandibular(2.090±1.061mGy) for mean age±SD group (8.833±3.188years).Table (2) shows the range of maximum, minimum, Max/Min and median effective dose ED/μSv for maxillary and mandibular periapical inter-oral dental X-Ray Examination of three age groups (1-15, 16-30 and 31-60) years. Note that the maximum valuesrecorded were 4.998μSv for mandibular inter-oral X-ray examination for patients in the 1-15 years age group,and the minimum value of2.673μSv was recorded for mandibular inter–oral X-ray examination for patients 16-35 years age group.

The overall results of this study indicate that exposure of the patients at the Dental Radiology Department of Hawler University of Medical Sciences does not exceed the levels either reported by Gonzalez et al. [9] using thermoluminescent dosimeters, based on data collected from over 300 intraoral X-ray facilities. They proposed a provisional local reference level of 3.5 mGy entrance surface dose for intraoral radiology.As indicated before, IAEA has proposed a diagnosticreference level value

of 7 mGy for intraoral radiographies.Also, the ESD for maxillary molar is more than the ESD for mandibular molar for all age groups. In general a wide distribution of doses were obtained and all were in good agreement with other results, especially with EU[10,11].

Table(1): The technique factors kVp ,mA and Time/sec with FFD/cm focal to film distance, mean±SD for age of patient and the overall mean ESD (±SD) for maxillary and mandibular intraoral radiographies.

Age(year)		kVp	mA	Time/sec	FFD/cm	ESD(mGy)
8.833±2.562	Maxillary	65	20	0.5	23	3.148±1.298
8.833±3.188	Mandibular	65	20	0.5	23	2.090±1.061
24.333±8.846	Maxillary	65	20	0.6	23	2.775±0.822
26.833±6.645	Mandibular	65	20	0.6	23	2.304±1.328
45.833±7.250	Maxillary	65	20	0.6	23	3.678±1.868
48.000±9.402	Mandibular	65	20	0.6	23	2.210±1.351

Table (2):The rangeand median of effective dose ED/μSv for maxillary and mandibular periapical inter-oral dental X-Ray Examination of three age groups (1-15, 16-30 and 31-60) years.

Age Group	Typeof examination	Range Max	Min	Max/Min	Median
01-15 year	Maxillary	4.781	3.226	1.482	3.734
	Mandibular	8.695	2.428	3.581	4.998
	Maxillary	4.876	1.681	2.900	3.217
16-30 year	Mandibular	5.236	1.058	4.948	2.673
	Maxillary	8.54	2.625	3.253	4.873
31-60 year	Mandibular	6.274	0.906	6.924	2.997

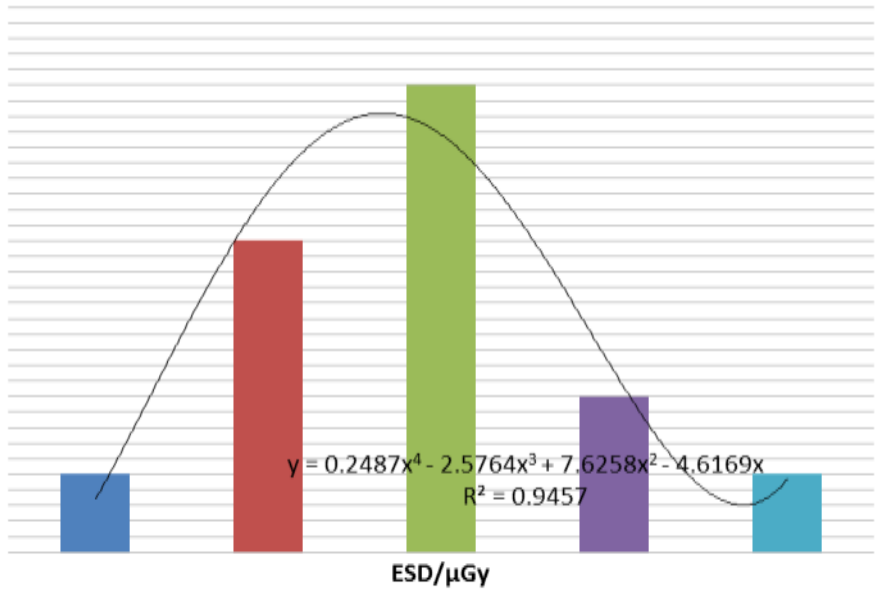

Figure(1):The distrbution of ESD/µGy for maxillary interoral radiography.

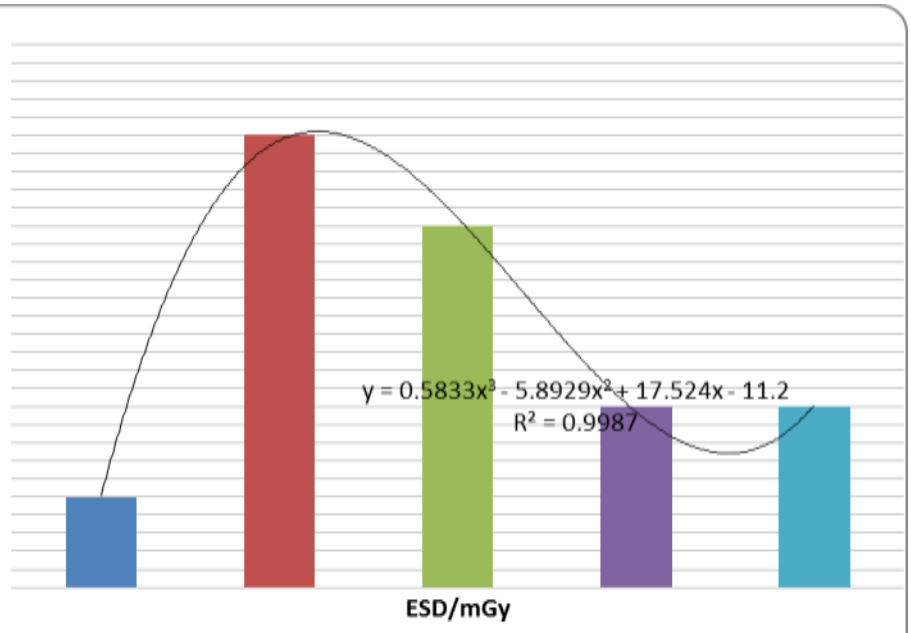

Figure(2): The distrbution of ESD/mGy for mandibular interoral radiography.

4. References

[1] Radiation Protection in Dentistry, Recommended safety Procedures for the Use of dental XRay Equipment, Published by authority of the Minister of Health, Canada, 1999.

[2]EbbaHelmrot, Gudrun AlmCarlsson, Measurment Of Radiation Dose In Dental *Radiology, Radiation Protection Dosimetry* (2005), 114, 1-3:. 168–171

[3] Gallagher A., A. Dowling, M. Devine, H. Bosmans, P. Kaplanis, U. Zdesar, J. Vassileva: *European Survey of Dental X-ray Equipment, Radiation Protection Dosimetry,*(2008), 129, 1-3: 284 – 287.

[4] International Atomic Energy Agency (IAEA). Dosimetry in diagnostic radiology: an international code of practice. Technical Reports Series No. 457. Printed by the IAEA in Austria, STI/PUB/1294. September (2007) ISSN 0074–1914.

[5]Looe H. K.,A. Pfaffenberger, N. Chofor, et. all. , Radiation Exposure To Children In Intra-oral Dental Radiology, *RadiationProtection Dosimetry* (2006), 121, 4 : 461–465.

[6] Alme´n, A. and Mattsson, S. On the calculation of effective dose to children and adolescents.*J. Radiol. Prot*. (1996),16(2),:81–89.

[7] European commission: "European guidelines on quality criteria for diagnostic radiographic images in paediatrics", European Commission EUR 161261 EN. Luxembourg, European Commission 1990.

[8] Stratakis J.,Damilakis J. and Gourtsoyiannis, "Organ And Effective dose Conversion Cofficients For Radiographic Examinations Of the Pediatric Skull Estimated by Monte Carlo Methods", *Eur Radial(*2005), 15:1948-1958.

[9] Gonzalez L., Vano E. Fernandez R.Reference doses id dental radiodiagnosticfacilities. *British Journal of Radiology*, (2001),74:153-156.

[10] European Commission, Radiation Protection 136. European guidelines on radiation protection in dental radiology (Luxembourg: Office for Official Publicationsof the European Communities) (2004) ISBN 92- 894-5958-1.

[11] Gibbs, S. J. Effective dose equivalent and effective dose: comparison for common projections in oral and maxillofacial radiology. *Oral Surg. Oral Med. Oral Pathol. Oral Radiol. Endod*, (2000), 90(4), 538–545.

LSBE055
Investigation of Protein-Protein Interaction and its Possible Role in the Formation of Amyloid Fibrils

Sheeren I. Hajee.
Biophysics Department,College of Medicine, Hawler Medical University,Krg, Iraq
Email :shereen_hajee@yahoo.com

Edrees M. T.Harki
Physics Department, College of Education,Salahadden-Hawler University,Krg, Iraq
Email :edreesharki1@yahoo.com

The corresponding author: Edrees M. T.Harki

Abstract
The main goal of this study is the investigation of protein-protein interaction and its effect on aggregation as well as amyloid fibril formation, and its possible role in controlling and inhibiting the formation of amyloid fibrils. To accomplish this, the study was done through the effect of temperature, trehalose, glycerol and L-arginine on BSA-BSA interaction by using SLS and Turbidity. It is observed that L-arginine takes the first place arrangement in reducing turbidity, followed by glycerin, with trehalose taking third place. Finally, a second step in this study was using Cong Red (CR) binding spectroscopy technique in detecting amyloid fibril formation. Amyloid fibril was formed from BSA under 70oC. In this part of the study,it was observed that arginine has a great ability to suppress BSA amyloid fibril when (L-arginine, glycerin, trehalose) were tested.
Keyword:protein-protein interaction,protein aggregation, SLS,Turbidity and amyloid fibril

[1] Introduction

Amyloidosis are protein deposition diseases of which the more well known are Alzheimer's disease, Huntington's disease, Bovine Spongiform Encephalopathy, familial amyloid polyneuropathy and Parkinson's disease [1,2].
It is generally accepted that amyloid formation is usually the result of misfolded and partially unfolded states acting in competition with the normal folding pathways. The best way to research amyloid formation is by studying the protein-protein interaction, and it has been known for many years that the osmotic second virial coefficients of $B_{22}$are very useful properties when studying the interaction between protein molecules in aqueous solutions [3,4], the osmotic second virial coefficients (B_{22}) of protein

solutions have generated a great deal of interest since George and Wilson showed the correlation between the ability of proteins to crystallize and B_{22}, which is a thermodynamic parameter that characterizes protein-protein interactions. Positive B_{22} values indicate predominantly repulsive intermolecular interactions and the protein in the native state, whereas negative values reflect predominantly attractive interactions and the protein will be unfolding or partially unfolded. B_{22} correlates to protein stability (as seen in aggregation behavior) and solubility by accounting for the contribution of electrostatics, Vander Waals interactions, excluded volumes, hydration forces, and hydrophobic effects, the same interactions that regulate protein phase behavior [5]. In addition to pH and ionic strength, there are several factors such as temperature, protein concentration in solution and the presence of additives that affect the value of B_{22}[6].

[2] Methods

A stock solution of 0.1M Sodium phophate buffer PH7 was prepared, filtered with a syringe (using 0.22μm, 4mm Millex Milipore syringe), and the concentration was determined spectrophotometrically (using ε (1%,1cm,280nm) = 6.67 for BSA. BSA stock solution was prepared in the buffer solutions at 5 different concentrations ranging from (1 -5) mg/ml. All concentration samples were heated for 60 min from (25 – 80) ̊c (5 degree interval). Static light scattering measurement for obtaining the second virial coefficient B22,were performed using a modulated photo detector with He-Ne laser(λ=632.8nm, 1mW) from PHYWE, model 08181.934#17530. Typically, 4-5 dilutions of a particular protein stock were filtered directly into the scattering cell. The incident light source was vertically polarized. Relative scattering intensities in excess of background (solvent, stray light) were converted to absolute scattering intensities(R_{90}) by calibrating the instrument response using toluene as calibration standard (R_{90}=14.0x10-6 cm-1 at 632.8nm).Static light scattering data was analyzed based on the classical Zimm equation (Eq.1) [7] :

$$\frac{K_0 C}{R_\theta} = \frac{1}{M_w} + 2B_{22}C + \text{.....,.....} \quad (1)$$

where R_θ is the Rayleigh ratio at angle θ (θ = 90°), Mw is the molecular weight of protein, and C its concentration in g/ml. The constant K0 is given by

$$K_0 = \frac{4\pi^2 n_o^2}{N_A \lambda_o^4} \left(\frac{dn}{dc}\right)^2 \text{.....} \quad (2)$$

where n_0 is the refractive index of the solvent, N_A is the Avogadro number, and (dn/dc) is the specific refractive index increment of the protein solution. Extrapolating the (dn/dc) values at 436 and 589 nm , using a linear regression (dn/dc) albumin at 632.8 nm was found to be 0.185 ml/g.

A plot of KC/R_{90} versus C (concentration g/ml) resulted in a straight line, and from

the slope of the straight line the value of B22 can be found. The intercept of this straight line ($1/M_W$) gives the molecular weight of the protein.The same steps as above were repeated in the presence of 0.5M L-arginine, 20% of glycerol, 0.2M trehalose. To measure turbidity an HACH 2100N turbidometer were used,and protein solution was prepared as follows: BSA protein was dissolved in 0.1M phosphate buffer containing 0.05% (w/v) sodium azide, filtering protein buffer solution with 0.22μm filter. The final BSA protein concentration was measured spectrophotometrically and was typically around 20 mg/ml. Next, an appropriate amount of trehalose, L-arginine, and glycerol was added into the solution separately and the solutions were stirred to ensure that the excipients were completely dissolved. Protein solution with and without excipients are prepared separately for each experimental run.Turbidity was measured for each sample after heating the sample for 60 min.

Finally,to study the formation of Amyloid fibril, the protein was prepared as follows:BSA was first dissolved in buffer at pH 7.0 containing 100mM NaCl to make a stock solution, which was diluted into buffer at pH 7.0 containing 100 mM NaCl and 0.05% (w/v) NaN3 in the absence or in the presence of glycerol 20%, trehalose 0.2M, and L-arginine 0.5M. Each protein solution was prepared separately in its own volumetric flask.20 ml of the protein at a final concentration of 20mg/ml in the absence and presence of glycerol 20%, trehalose 0.5M, L-arginine 0.5M were put in a glass vial with a tide screw cap and put in an incubator under various experimental conditions at 70oC for up to 20 days. After a daily 5min. stir, samples were taken out at intervals and stored on ice before adding CR solution.Congo red binding assay was done according to the procedure described in [8,9], the binding of CR to several purified amyloid like peptides having a β- plated sheet conformation was quantitatively examined. CR binds preferentially to the β-plated sheet conformation as CR does not bind nearly so well to native protein conformation. A stock solution of 200μM congo red was prepared in 0.1M phosphate buffer pH 7 containing 100mM NaCl and 10%(v/v) ethanol. The CR solution was filtered through a 0.22μm pore size filter before use. In a typical assay, the protein sample was mixed with a solution of CR to yield a final CR concentration of 10μM and a final protein concentration of 1-3μM, and then incubated at room temperature for at least 30min in the dark before recording the absorbance spectrum.

[3] Result and Discussion

Fig (1)and (2)show the results of B_{22} and molecular weight variation with changes in temperatures for BSA. It is observed that the repulsion between protein molecules decreases with increasing temperature when starting with native protein, in addition to reversing repulsive interaction between protein molecules to attraction. Two transition

temperatures werealso obtained. The first transition occurred below 55 o C and the second transition temperature occurred at a temperature of 70^{o}C. The first transition temperature is a minor transition, while the second transition is a major one, corresponding to the thermal unfolding of albumin. Multi transition temperature is an indication of the presence of intermediates in the melting profile of the protein. Population regression coefficient its 88.87 % temperature change, a very high and significant difference obtained due to the effect of temperature on B_{22} value.The result of the effect of an additive consisting of 0.5M L-arginine, 20% of glycerol, 0.2M trehalose on protein-protein interaction under the influence of temperaturewas studied.The population regression coefficient for B_{22} against temperature for a BSA solution containing 0.5M L-arginine, 20% of glycerol, 0.2M trehalose is 5.79%,69.33%,and82.94%,respectively. In addition, highly significant differences were obtained when changes in molecular weight against temperature for BSA solution in the presence of L-arginine were compared with BSA solution in the absence of arginine. No significant difference was obtained when an unpaired student t-test was used to compare molecular weight for BSA solutions with and without 20% glycerol and 0.2M trehalose, under the effect of temperature.

Another method used in this study to detect heat induced aggregation for BSA is by measuring turbidity at different temperatures. Fig (3)show the result of turbidity for BSA in 0.1M phosphate buffer pH 7, in the absence and presence of 0.5M L-arginine, 20% Glucose and 0.2M trehalose, heated from 35-800C, 5 degree intervals for 60 mins, the same condition as in SLS method. At the absence of additive It was observed that the turbidity is approximately constant at temperatures between 25-55^{o}C with a value of 3.89 at 25^{o}C; at temperatures greater than 55^{o}C the turbidity increases gradually till 70oC;and ata temperature of 70^{o}C the amount of turbidity increases more rapidly and reaches 46.7 at 80^{o}C. Turbidity results confirm those obtained from the SLS measurement showing the transition temperature as 55^{o}C and 70^{o}C, and it was also observed that heat induced aggregation occurs at temperatures of 70^{o}C and above. A highly significant difference of 65.95% confident, population regression coefficient its 65.95% temperature changes. Unpaired student t-test was used to compare the result of turbidity at (40-55)^{o}C and the amount of turbidity at temperatures between (55- 80)^{o}C, and significant differences were observed. As well, concerning 0.5M L-arginine, the results show no significant difference at temperatures of (40-55)^{o}C, but a very significant difference is seen at a temperature range of (60-80)^{o}C when compared with the turbidity of BSA in the absence of l-arginine at the same temperature. When glycerol is present, no significant difference at (40-60)^{o}C was obtained, while a highly significant difference was obtained at (65-80)^{o}C, indicating that increasing percentages of glycerol leads to decreases in aggregation percentage.

Congo red absorbance spectroscopy was utilized to probe for the presence of cross-β-pleated sheet structures associated with amyloid. It shifted the spectral properties of Congo red and exhibited a second shoulder peak at 540nm, which is indicative of strong binding between BSA and Congo red dye and the generation of an appreciable amount of amyloid fibrils. Identification of the amyloid-like fibrils- Congo red is a useful dye to detect the formation of amyloid fibril(s) [10]. Congo red has been shown to bind preferentially to aggregate peptides/proteins of amyloid but not to the native, unassembled forms [10]. We performed the Congo red binding experiments to see if the aggregates of BSA formed at higher temperatures (>50^{o}C) have amyloid fibril characteristics. The absorption intensity of Congo red at 487nm shifts to an absorption intensity of 540nm when BSA in 0.1M phosphate buffer was incubated at 70^{o}C for 30 days. Significant red shift is observed in the absorption spectrum when the dye binds to the protein in the order, intermolecular β-pleated sheet structure of the amyloid fibrils see Fig (4), which illustrates the intensity of the absorption peak of Congo red (487 nm), Congo red binding with incubated BSA (appearance of peak at 502nm with shoulder at 540 nm), and also when bonded Congo red was filtered the absorbance peak was 527 nm. The absorption peak of native BSA with CR was 497nm.

It is observed that the absorbance peak of CR decreases and reaches 498.17 nm at 20% glycerol, while the shoulder peak remains within the spectrum but with a lower value. The absorbance peak and the existence of shoulder are tabulated in Table (1).

In Fig (4) it was observed that the presence of L-arginine leads to a decrease in absorbance peak with a lack of shoulder peak at ~ 540 nm in the Congo red binding absorbance spectrum.No appreciable amount of amyloid was observed in the BSA sample with 0.5M L-arginine. No effect of trehalose was observed when added to protein solution as seen in Fig (4).

Nevertheless, it is our belief that the outcome of this work will enable us not only to comprehend the mechanism(s) of amyloid protein, disease-related or non-disease-related, self-association process, but also to aid in developing potential targets for molecular therapeutics in the prevention or retardation of amyloid formation implicated in amyloidogenic diseases.

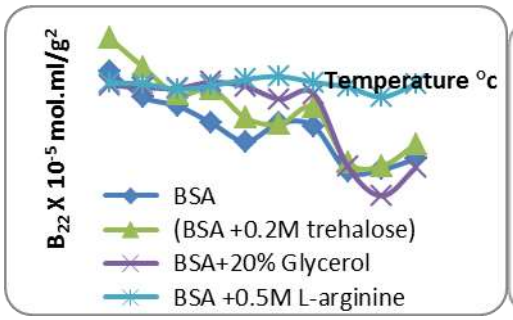

Fig (1) B_{22} value against Temperature, for BSA, BSA+0.2M trehalose, BSA+ 20%glycerol, and BSA+ 0.5M L-arginine.

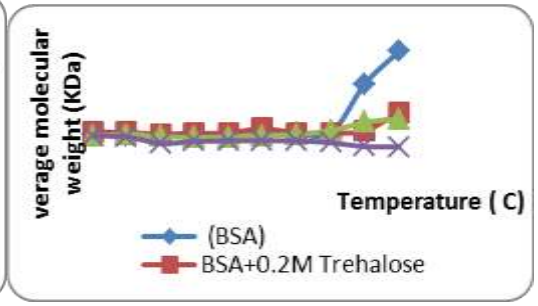

Fig (2) Molecular weight value against Temperature, for BSA, BSA+0.2M trehalose, BSA+

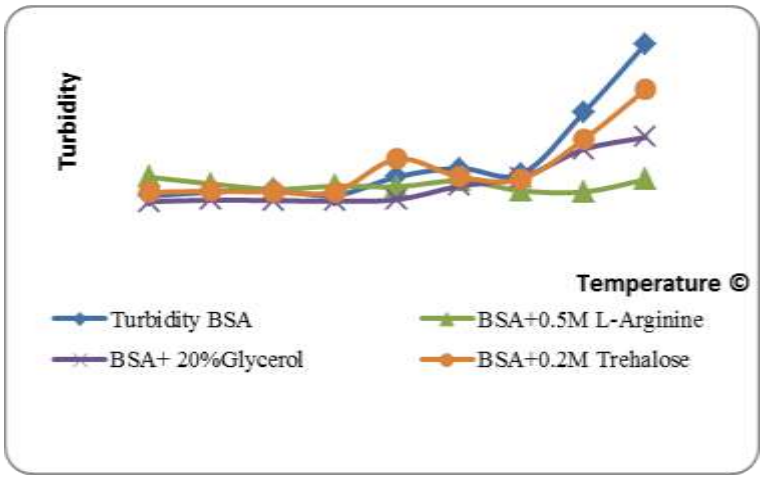

Fig (3) The value of turbidity against Temperature, for BSA, BSA+0.2M trehalose, BSA+ 20%glycerol, BSA+ 0.25M L-arginine and BSA+ 0.5M L-arginine.

Table [1]:Absorption spectrum peak of CR at different solution condition Absorbance peak (nm)

CR	487.52
CR+Native BSA	498.45
Filtered (CR+incubated BSA)	527.81
Unfiltered (CR+incubated BSA)	527.81+ shoulder peak at 540 nm
CR+incubated (BSA+0.2M Trehalose)	507.54 + shoulder peak at 540 nm
CR+incubated (BSA+ 20% glycerol)	498.17 with shoulder
CR+(BSA +0.5M L-arginine)	499.98 with small shoulder

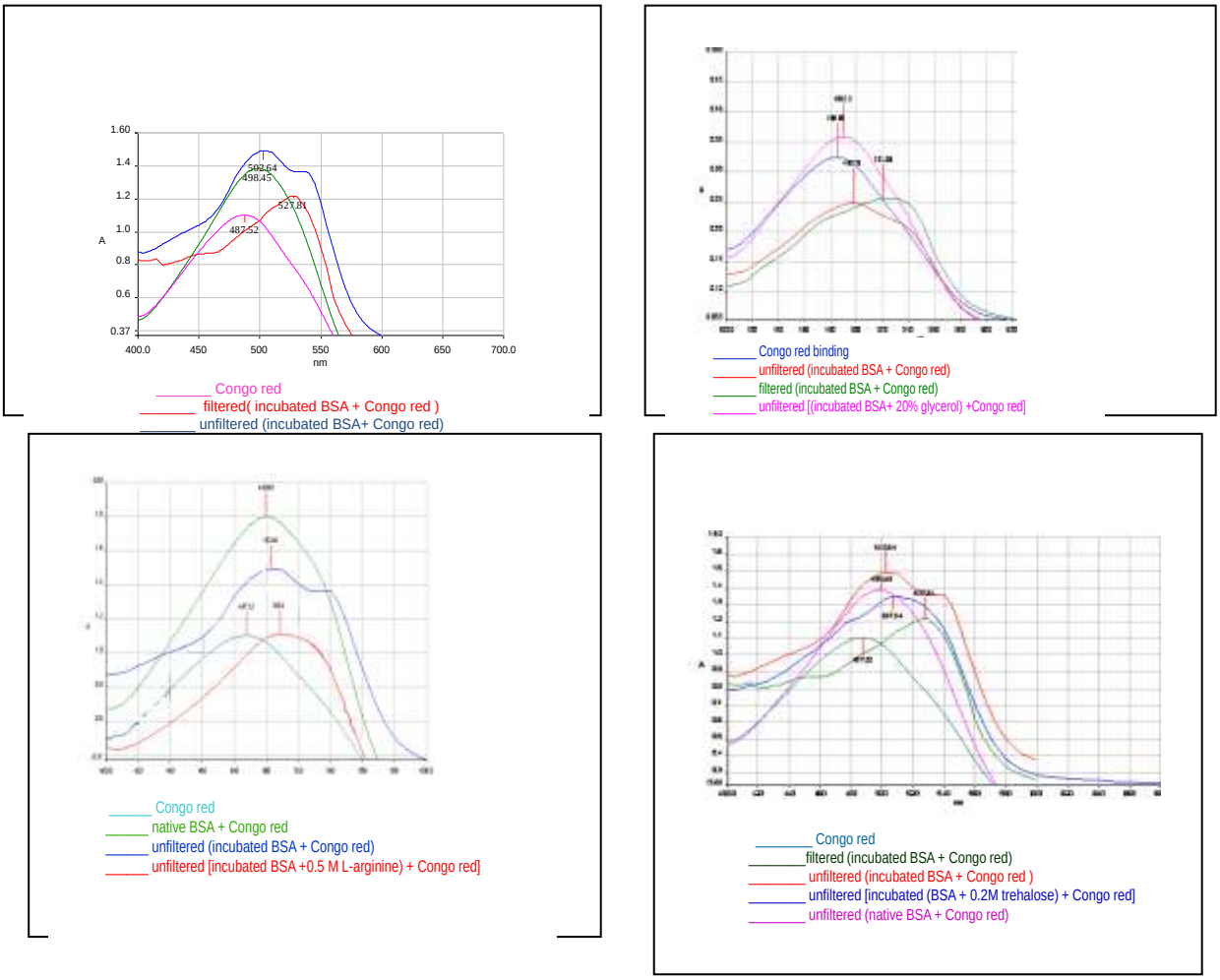

Fig (4)Congo red binding assays to characterize the effects of (20% glycerol, 0.5M L-arginine, and 0.2M trehalose) respectively on BSA amyloid fibrils

[4] References

[1] Uveresky VN, and Fink AL. Conformational constraints for amyloid fibrillation: the importance of being unfolded. *Biochim. Biophys. Acta*,(2004),1698: 131-153.

[2] Boss M, Gestwicki J E, Deasthali V, Grabtree G R, Graef I AMolecular mechanisms of neurodegeneration. Biochemical Socity Focused meeting: 543-547. Life Scinces Institute, University of Michigan, 210 Washtenaw Avenue, *Ann Arbur, MI*.(2005): 48109-2216.

[3] Winzor D J, Deszczynski M, Harding S E, Willis P R. Nonequivalence of second virial coefficient from sedimentation equilibrium and static light scattering studies of protein solutions. *Biophysical Chemistry*,(2007), 128: 46-55.

[4] Bonnete F, and Vivares D. Interest of the normalized second virial coefficient and interaction potentials for crystallizing large macromolecules," *Acta Crystallograpica, D*(2002) ,58 : 1571-1575.

[5] Dumetz A C, Chockla A M, Lenhoff A M. Protein phase behavior in aqueous solutions: Crystallization, liquid-liquid phase separation, Gels, and aggregates. *Biophysical Journal* (2008), 94:570-583.

[6] Wang Shun-Li; Lin Shan-Yang; Li Mei-Jane; Wei Yen-Shan; Hsieh Tzu-Feng. Temperature effect on the structural stability, similarity, and reversibility of human serum albumin in different states. *Biophysical chemistry*, (2005), 114: 205-212.

[7] Zimm, 1948 B.H. Zimm, The scattering of light and the radial distribution function of high polymer solutions, *J. Chem. Phys*, (1948), 16: 1093–1099.

[8] Flunk W E, Pettegrew J W, Abraham D J. Quantitative evaluation of Congo Red binding to Amyloid-like proteins with a Beta-pleated sheet conformation. *The Journal of Histochemistry and Cytochemistry*, (1989a) 37(8): 1273-1281.

[9] Flunk W E, Pettegrew J W, Abraham D J. Two simple methods for quantifying low-affinity dye-substrate binding. *The Journal of Histochemistry and Cytochemistry,*(1989b), 37(8): 1293-1297.

[10] Inoye H, and Kirschner D A. A beta fibrillogenesis: Kinetic parameters for fibril formation from Congo red binding. *J Struct. Biol.*,(2000) ,130(2-3): 123-129.

LSBE074

Reproductive success of *Eurytemora affinis* is unaffected during a diatom-dominated spring bloom

Roswati Md Amin

Present address: Department of Marine Science, Faculty of Maritime Studies and Marine Science, Universiti Malaysia Terengganu, 21030, Terengganu, Malaysia.

Umeå Marine Sciences Centre, Umeå University, Norrbyn 91020 Hörnefors, Sweden.

Email: roswati_ma@umt.edu.my

Ulf Båmstedt

Umeå Marine Sciences Centre, Umeå University, Norrbyn 91020 Hörnefors, Sweden.

Email: ulf.bamstedt@emg.umu.se

Carsten Paul

Institute of Inorganic and Analytical Chemistry, Bioorganic Analytics, Friedrich Schiller University Jena, Germany

Larysa Samchyshyna

Research Centre of Ecomonitoring and Biodiversity of Megalopolis NASU,Ukraine

Elin Lindehoff

Umeå Marine Sciences Centre, Umeå University, Norrbyn 91020 Hörnefors, Sweden.

Georg Pohnert

Institute of Inorganic and Analytical Chemistry, Bioorganic Analytics, Friedrich Schiller University Jena, Germany

The corresponding author: Roswati Md Amin

Abstract

Egg and naupliar production of copepod *Eurytemora affinis*, were determined over a period of 20 days (11–31 May, 2010) while fed water from 3 differently treated and untreated natural water. Two of the mesocosms were inoculated with *Skeletonema marinoi* strains producing different particulate polyunsaturated aldehydes (PUA) and one mesocosm with dissolved polyunsaturated aldehyde. The aim was to investigate if the potential effectscaused by different strains of the dominant diatom and/or only related to the level of metabolites (dissolved PUA) in the water. Egg production rate

of *Eurytemora affinis* mainly related to food availability, increased with increasing chlorophyll *a* concentration and mineral content of the water, but was not affected by the observed high particulate (up to 28 nmol L^{-1}) PUA production and dissolved (up to 278 nmol L^{-1}) metabolite in the water. However, the naupliar production was not affected by either aldehydes in the maternal diet or exposure to the dissolved aldehydes in the water. We suggest that *Skeletonema marinoi* did not play a significant role in determining the succession of *Eurytemora affinis* in the experiments.
Keywords: *Eurytemora affinis*, egg production, mesocosm, toxic aldehydes

LSBE386

The study on influence to the Cortisol concentration of dwellers for the indoor life space in the disaster prevention tents with causing environmental factors

Kazuo FUKUSHIMA
Graduate school of Design, Kyusyu University , Watanuki-Lab.
〒815-8540　Fukuoka city minami-ku siohara4-9-1,Japan
Post mail address :〒862-0922　Kumamto city higashi-ku　saburo 2-1-3
Uinhaitsu-105 , Japan
kazuoanimal1956@yahoo.co.jp

Takayuki NISHIMURA
Graduate school of Design, Kyusyu University , Watanuki-Lab.
〒815-8540　Fukuoka city minami-ku siohara4-9-1,Japan

Yosuke　Nisato
Graduate school of Integrated Frontier Sciences, Kyusyu University, Watanuki-Lab.
〒815-8540　Fukuoka city minami-ku siohara4-9-1,Japan

Midori MOTOⅠ
Graduate school of Integrated Frontier Sciences, Kyusyu University, Watanuki-Lab.
〒815-8540　Fukuoka city minami-ku siohara4-9-1,Japan

Shigeki WATANUKI
Study & Research for　Graduate school of Design, Kyusyu University, Watanuki-Lab.
〒815-8540　Fukuoka city minami-ku siohara4-9-1,Japan
watanuki@design.kyushu-u.ac.jp

The corresponding author: Kazuo FUKUSHIMA

Abstract

The purpose　of the study is to elucidate the　Cortisol concentration during the first day and the last day in the disaster prevention tents with improving the amenity of dwelling people.

And we analyzed the relation between　the　Cortisol concentration data and environmental factors.

As the methods, the different five types of the disaster prevention tents accommodated each five subjects with a sum of twenty five persons. On the morning of the first day

and the last day during ten days, we collected the saliva of dwellers to research the Cortisol concentration with ELISA analyzing kits(No:EA65,Oxford Biomedical Research ,USA) . And we measured the temperature, the humidity and the CO_2 concentration in each of the tents. Continuously we had dealt with two factors analysis of variance and got the data between the Cortisol concentration values and environmental factors. In case of interaction data we conducted multiple regression analysis for them.

Results were the followings.

We studied to effect the Cortisol concentration values of structural factors in tents. We dealt with two factors analysis of variance with the conditions(five types tents) and time factors(the first day, the last day).The time factors had main effect on Cortisol concentration We were confident that the Cortisol concentration significantly increased at the last day than the first day. On the case of detail Analysis, the Cortisol concentration had the interaction for environmental factors. In the multiple regression analysis between the independent variable of the environmental factors and the dependent variable of the Cortisol concentration, each of the humidity and the cubic capacity per person(m^3/a person) decreased with the Cortisol concentration increasing.

Consequently the cubic capacity per person(m^3/a person) and the humidity are important factors to improve the amenity of the disaster prevention tents on the condition of long time lapse and tent life. The humidity had influence to Cortisol concentration independently without the cubic capacity per person(m^3/a person).

Key words: tent , amenity, Cortisol, QOL

1. Introduction

In case of occurring the catastrophe, the disaster prevention tents will have the necessity of constructing temporary living space. Generally some researchers[1)–3)] have submitted the stress of long terms for tents lives with disadvantage environment and discomfort surroundings. The evaluation of ordinary houses and common rooms have been reported amenity and comfort by the several researchers[4)–7)].

But there are the difference structures and functions between the ordinary houses and the disaster prevention tents . We can't apply the evaluation of the ordinary houses.

We need the new evaluation standards of the comfort and stress for tents living space.

2. Objectives

The purpose of the study is to elucidate the Cortisol concentration during the

first day and the last day in the disaster prevention tents with improving the amenity and the stress for dwellers. We analyzed the relation between the Cortisol concentration as the physiological marker and the environmental factors. The environmental factors means the aspect ratio, the square capacity per person (㎡/a person),the cubic capacity per person (m^3 / a person), temperature, humidity and CO_2 concentration in the tents.

3. Methods

3.1 Subjects

The five types tents (A,B,C,D,E:Figure1) have each different environments and the conditions of living space. A type tent had thirty dwellers. B type tent had twenty dwellers. The each C,D,E types tents had each six dwellers . The total person of them are sixty eight persons. We chose each five persons subjects to each A,B,C,D,E tents within total persons. The total of twenty five persons subjects(29±5.4 years old) were not to drink alcohol and were not to smokers.

3.2 Experimental condition

The disaster prevention tents for the experiment were shown by Figure 1，they had each different sizes , structures and shapes of formation. These tents are the differences of 4 types. A type tents and B type tents were composed of three times of C type tents. Each type tents have the different conditions of tents which are sizes, structures, shapes.

There are dwellers with twelve persons more than standard capacity persons in A type tent. The dwellers of B type tent were more two persons than standard capacity persons. The dwellers of each C type, D type. E type tents had each six persons with the standard capacity persons. The table 1 shows the aspect ratio, the square capacity per person(㎡/a person) and the cubic capacity per person(m^3 / a person) in the tents. The table 2 shows temperatures, humidity and CO_2 concentration in the tents at the first day morning and last day morning.

3.3 The procedure of experiment(Protocol)

The terms of experiments had taken ten days from the last week of January to the middle week of February. The measurement of environmental factors and collecting saliva in the tents were conducted at seven o'clock in the morning of the first day and the last day. The subjects in the tents were to get up at six and thirty minutes o'clock in the morning. They gargled and sat down on the collapsible beds for twenty minutes .And then, they were collected the saliva.

3.4 The measurement of the environmental factors

The environmental factors include structural factors〔Table 1:the aspect ratio, the square capacity per person(㎡/a person) and the cubic capacity per person(m^3 / a person) 〕 and physical－chemical factors〔Table 2: temperatures, humidity and CO_2 concentration〕 in the tents. The temperature and the humidity in the tents were measured with automatic temperature and humidity measuring equipment(TR72,ST&D Inc.). The CO_2 concentration were measured with CO_2 concentration measuring test tube(GASTEC 1MO4GV100SJ1,Gastec Inc.). The location and position of measuring point for the temperature, humidity and CO_2 concentration was the center of the tents spaces.

3.5. The collection of saliva

We have used the salivette tube (salivette,No51,1534,Sarstdt,Numbrecht,Germany) to collect saliva of subjects persons for two minutes. After collecting the saliva,we had revolved the cyclone separator into the saliva to exclude microorganisms and cells from saliva. We dealt with the cyclone separator (at 3500rpm for 15 minutes). Continuously we weighed the salivas on the scales. We calculated the volumes of salivas(ml/minute).

3.6. The analysis of saliva－Cortisol concentration(Abbreviation :Cortisol concentration)

we analyzed Cortisol concentration (μg/ml) with ELISA Kit (Enzyme Immunoassay for Cortisol, Product No.EA65,Oxford Biomedical Research ,USA).

We made the 100 times dilution of the saliva and analyzed them.

3.7. The process of Data and statistics analysis

We analyzed the Data and statistics with SPSS ver,7.0 J(Japan Inc. Tokyo).

After having dealt with the Cortisol concentration ,we conducted two factors analysis of variance with the conditions (five types tents) and times factors(the first day, the last day). The Cortisol concentration had the interaction for structural factors. Continuously we conducted the multiple regression analysis between the independent variable of the environmental factors and dependent variable of the Cortisol concentration.

4. Result & Discussion

4.1. Result

The result of each environmental factors (structural factors, physical－chemical factors) in each tents shows Table 1 and Table 2.

There were difference values of measurement for temperatures, humidity, CO_2 concentration between the first day and the last day.

First of all, we conducted two factors analysis of variance with the conditions(five type tents) and times factors(the first day, the last day). The time factors on the Cortisol concentration had main effect〔$F(1, 23)=45.072$, $p<0.01$〕. We were confident that the

the Cortisol concentration significantly increased($p<0.01$) at the last day than the first day(Figure 2). On the case of detail analysis, the Cortisol concentration had the interaction for environmental factors〔$F(4, 20)=3.017$, $p<0.05$〕.

As we analyzed the interaction for the Cortisol concentration on times factors in detail and the relation of environmental factors. We elucidated the relation between the Cortisol concentration and the environmental factors〔the aspect ratio, the square capacity per person (m^2/a person),the cubic capacity per person (m^3 / a person), temperature, humidity and CO_2 concentration〕. We conducted the multiple regression analysis between the independent variable of environmental factors and the dependent variable of the Cortisol concentration. And then , the result showed Table 3. The Cortisol concentration had significantly each negative partial correlations with cubic capacity per persons (m^3 / a person)〔$Pr=-0.83$, $p<0.01$〕and humidity 〔$Pr=-0.39$, $p<0.01$〕.

4.2. Discussion

We had studied to improve the amenity and QOL of the disaster prevention tents, we measured the Cortisol concentration of the first day and the last day for ten days. We conducted two factors analysis of variance with the conditions(five types tents) and times factors(the first day, the last day).

The Cortisol concentration had main effect on the time factors〔$F(1, 23)=45.072$, $p<0.01$〕. As we found that the Cortisol concentration had interaction on environmental

factors significantly〔$F(4, 20)=3.017$, $p<0.05$〕. As we considered the relation between the Cortisol concentration and environmental factors.

We conducted the multiple regression analysis between the independent variable of environmental factors and the dependent variable of the Cortisol concentration.

Consequently The both of the cubic capacity per person (m^3 / a person) and humidity had decreasing with the Cortisol concentration increasing

significantly.

The partial correlation coefficient between the Cortisol concentration and the cubic capacity per person (m^3 / a person) is significantly negative value 〔Pr＝－0.83，p＜0.01〕(Table 3).

The partial correlation coefficient between the Cortisol concentration and humidity is significantly negative value〔Pr＝－0.39，p＜0.01〕(Table 3).

.

The previous papers of the study[8)−10)] were reported that the Cortisol were called stress hormone by many researcher generally, the Cortisol concentration had increased with human receiving the stress. Dr Taylor of USA Naval Health Research Center reported that the Cortisol concentration had increased with time factors. The much Cortisol concentration increasing with human exposing the severe stress is much variation of the rising value than the small increasing value of Cortisol concentration with the calm stress.

Therefore Tents lives of dwellers showed increasing the Cortisol concentration for ten days of the long terms. We think that the subjects persons remained chronic stress .

The result of two factors analysis of varaiance showed the interaction significantly.

And they showed the differences of the Cortisol concentration between the A type tent and E type tent. The difference of the Cortisol concentration showed the differences of structures, temperatures, humidity, dwellers persons in the tents.

The result of the multiple regression analysis between the Cortisol concentration and environmental factors shows significant partial correlation coefficient. The partial correlation coefficient between the Cortisol concentration and the cubic capacity per person(m^3 / a person) is significant negative value〔Pr＝－0.83，p＜0.01〕(Table 3).

The partial correlation coefficient between the Cortisol concentration and humidity is significantly negative value〔Pr＝－0.39，p＜0.01〕(Table 3).

The more the cubic capacity per person(m^3 / a person) was to decrease and the more the humidity was to decrease, the more the Cortisol concentration was to increase and to remain high value.

On another expression, as the physiological marker of chronic stress ,the decreasing the Cortisol concentration needed to increase the cubic capacity per person and needed to increase the value of humidity. In case of

increasing the cubic capacity per person , the dwellers were a few person and vacant space. The humidity for respiration and perspiration of subjects are to decrease with increasing cubic capacity per person.

Therefore the independent variable of cubic capacity per person intersected the independent variable of humidity. The humidity stands on the factor of the cubic capacity per person. But humidity were received the influence of the Cortisol concentration with independent physical factor of cubic capacity per person (m^3 / a person).

As the temperatures in tents didn't influence the Cortisol concentration. Generally they reported that the Cortisol concentration were to increase with cold temperature.

For instance, Dr Gerra[12] reported that Cold condition stress were studied two difference condition rooms between warm surrounding room(25℃) and cold surrounding room(4℃).Only the Cortisol concentration with cold temperature had increased .And the result shows that cold weather condition influences the Cortisol concentration values .

But On our study , the temperature didn't influence the Cortisol concentration, Increasing the Cortisol concentration were influenced by chronic stress without cold stress.

We add that the environmental factors of humidity is most important factor to keep comfort amenity in the disaster prevention tents .

Finally increasing humidity of environmental condition in winter season is important to improve amenity and QOL in the disaster prevention tents.

5. Conclusion

To improve the amenity and QOL in the disaster prevention tents, we elucidated the relation between the the Cortisol concentration and environmental factors.

Therefore we conducted the two factors analysis of variance with conditions(five types tents) and times factors(the first day, the last day),the result of two factors analysis shows main effect on time factors. The last day of the Cortisol concentration had increased than the first day of it significantly.

Consequently we were confident that dwellers of tents remained chronic stress with time lapse and tent life fatigue, strain and tiredness. From the result of multiple regression analysis between the independent variable of environmental factors and the dependent variable of the Cortisol concentration.

The Cortisol concentration increased significantly with humidity and cubic capacity per person(m^3 / a person) decreasing consequently. Therefore both humidity and cubic capacity per person are important factors to increase the Cortisol concentration for improving the amenity and QOL in the disaster prevention tents.

Especially humidity were to influence the Cortisol concentration without the relation of cubic capacity per person(m^3 / a person) . We were confident that humidity is important environmental factors to improve amenity and QOL in the disaster prevention tents.

6. Acknowledgments

We wish to thank the subjects for their involvement in this study ,in particular the volunteers of the logistic service support fellows of Japan.

7. References

[1] Shigaki T, Miyata M: Fundamental assessing trends in the Hyogo－ken Nanbu Earthquake－related diseases using Osaka city emergency ambulance service records, Japan Society of physical Anthropology 14(4),23－30,2009

[2] Kudo K, Shiozaki K ,et al: A study on the formative process of the informal evacuation enters on the Great H anshin Awaji Earthquake, Architectural Institute of Japan,Augst,375－376,1995

[3] Fukuhsima K ,Sakai K, Ishihara O:Study of thermal comfort and the psychological amenity for the tent life ,the 10th ICEE,thermal comfort out door,765 －769,2002

[4] Matumoto T, Mitsui I: The effect of heating of soles on thermal－sensation of subject in winter real void－space, Architectural Institute of Japan75(652),491 －497,2010

[5] Shintani H, Imatsuga A :A study on the space design for patients with stress－related diseases, Society for Mind－Body Science 6(1),111－125,1997

[6] Kikuta K,Enai M,et al:A study on thermal storage systems for highly insulated Buildings based on simplified predictive control, Architectural Institute of Japan 599(1),95－102,2006

[7] Maki F,Soki T :Changes of indoor Humidity in Various Living spaces,Mokuzai Gatkkai 52(1),37－43,2006

[8] Ito H, Fukuhara M, et al: Effect of localized pressure under an experimental acrylic plate covering the palatal mucosa on the concentration of salivary Cortisol and salivary α － amylase activity,Shika Igaku(J Osaka Odontol

Soc)72(1)Mar.,1-8,2009

[9] Vivia Ng, David K, et al: Salivary biomarkers associated with academic assessment stress among dental undergraduates.JDE(Oct.),1091－1094,2003

[10] Sebatian E, Heinrich S, et al:Psychobiology in psychoanalysis salivary Cortisol and secretory IgA as psychoanalytic process parameters,GMS psycho－Social－Med.2,1-11,2005

[11] Taylor,JP,Reia KP, et al:Trait anxiety and salivary Cortisol during free living and military stress, Aviat. Space Environ. Med.79(2),129－135,2008

[12] Gerra G, Volpi R, Manimetti L, et al:Sex－related responses of beta－endrphin,CATH,GH and PRL to cold exposure in human , Acta Endcrinol(126),24－28,1992

Table 1 The conditions of using tents

condition / type Of tent	w (	l (	height (m)	a ra (	amount of dweller (persons)	cubic capacity per person (m^3/person)	square capacity per person (m^2/person)	type of heater (stove)
Type A	5.	1	2.7	0.	30	5.3	2.5	open burner type
Type B	5.	1	2.7	0.	20	7.9	3.8	open burner type
Type C	5.	5	2.7	0.	6	8.8	4.2	close burner

								type
Type D	4.	4	3.1	0.	6	9.5	3.1	close burner type
Type E	4.	4	3.1	0.	6	10.0	3.2	close burner type

Table2 The measurement result of environment in tents

measurement of tent / type of tent	First Day temperature (℃)	Last Day temperature (℃)	First Day Humidity （%）	Last Day Humidity （%）	First Day CO_2 concentration （%）	Last Day CO_2 concentration （%）
Type A	23.8	22.5	71.2	52.5	0.32	0.35
Type B	22.5	17.5	44.4	23.4	0.17	0.19
Type C	20.6	18.3	48.0	46.0	0.07	0.09
Type D	20.2	19.4	47.6	32.1	0.10	0.13
Type E	11.4	12.2	65.6	42.8	0.15	0.17
outdoor	8.5	4.4	65.0	63.0	0.02	0.02

Table3 The partial correlation between Cortisol concentration and environmental facrors（The multiple regression analysis between the Cortisol concentration and

environmental factors)

(n=50、**： p <0.05、**： p <0.01)

independent variable / dependent variable	Aspect Ratio (－)	Square capacity Per person (㎡/person)	Cubic capacity Per person (m³/person)	Temperature (℃)	Humidity (%)	CO_2 Concentration (%)
Cortisol (μg/ml)	0.23	－0.18	－0.83**	－0.26	－0.39**	(－)
Multiple regression equation	$Y_{(Cortisol)}=16.47-1.03X_{(Cubic\ capacity\ Per\ person)}-0.04X_{(humidity)}$ （$R^2=0.69$）					

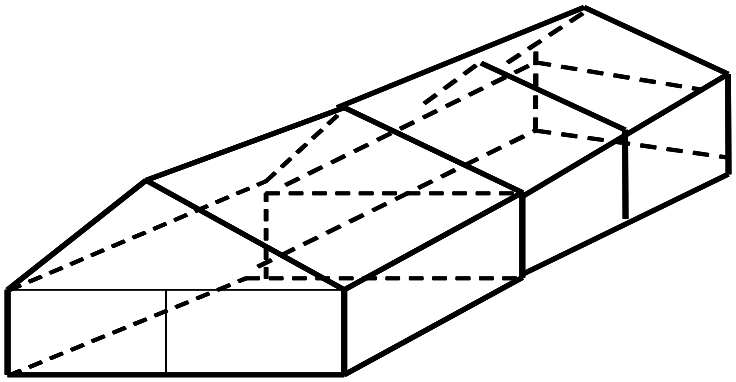

Type A、Type B

（ Three Type C tents connect in series make Type A or Type B）

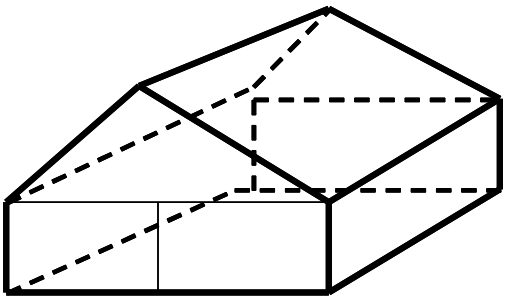

Type C

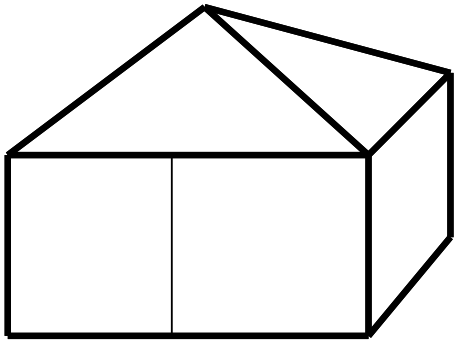

Type D（setting inside curtain）

Type E(setting no inside curtain)

Figure 1 the five condition of tents

Mean+S.D..(Each conditions of tents, n=5) *:p<0.05, **:p<0.01

Figure 2 the Cortisol concentration on each tents for the first day and the last day

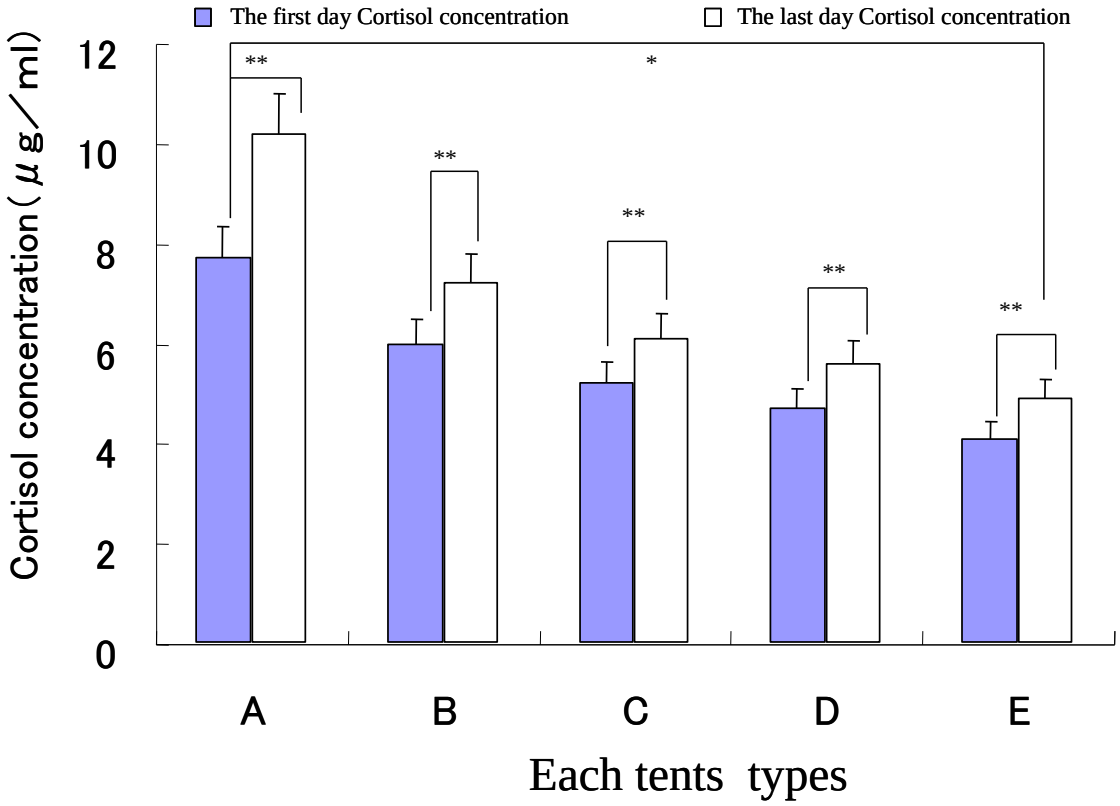

LSBE307
Changes of peripheral benzodiazepine receptor gene expression in major depressive disorder and methamphetamine dependence

Siriluk Weerasakul
Department of Anatomy and Centre of excellence in medical biotechnology, Faculty of Medical Science, Naresuan University, Phitsanulok, Thailand
e-mail: Siriluk_fowl@hotmail.com

Namtip Tubtimtong
Naresuan University Hospital, Faculty of Medicine, Naresuan University, Phitsanulok, Thailand
e-mail: namtipt@hotmail.com

Paritat Watiktinkorn
Synphaet Hospital, Bangkok, Thailand
e-mail: psy_forensic@yahoo.co.th

Samur Thanoi
Department of Anatomy and Centre of excellence in medical biotechnology, Faculty of Medical Science, Naresuan University, Phitsanulok, Thailand
e-mail: samurt@nu.ac.th

Sutisa Nudmamud-Thanoi
Department of Anatomy and Centre of excellence in medical biotechnology, Faculty of Medical Science, Naresuan University, Phitsanulok, Thailand
samurt@nu.ac.th
e-mail: sutisat@nu.ac.th , Tel: +668-9461-9243

The corresponding author: Sutisa Nudmamud-Thanoi

Abstract

Peripheral benzodiazepine receptor (PBR) plays a major role in steroidogenesis. An alteration of PBR density has been reported in psychiatric disorders. Therefore, the aim of this study was to investigate the alteration of PBR gene expression in psychiatric diseases such as major depressive disorder (MDD) and methamphetamine (METH) dependence. Twenty-two MDD patients (age 41±18 year) and fourteen METH dependent patients (age 33±7 years) were diagnosed by psychiatrists

according to Diagnostic and Statistical Manual of Mental Disorders fourth edition (DSM-IV). Control group for MDD consisted of thirty five positive mental health subjects (age 32±8 year) and control group for METH dependence consisted of thirty eight healthy subjects (age 32±5). Blood samples were collected for RNA extraction and followed by PBR gene amplification using semiquantitative reverse transcriptase polymerase chain reaction (RT-PCR). Moreover, serum was separated from blood sample for progesterone determination using electrochemiluminescenceimmuno assay. A significant decrease in PBR gene expression was found in MDD patients with suicide attempt when compared with both control group and non-suicide attempt group. On the other hand, a significant increase in PBR gene expression was found in METH induced psychosis compared with control group. The results in the present study suggest that PBR may play a critical role in MDD with suicide attempt as well as drug dependence and the alteration of PBR expression may be a biological marker for those diseases. However, the mechanisms of PBR expression in the MDD and drug dependence are needed to study further.

Keyword: peripheral benzodiazepine receptor, major depressive disorder, methamphetamine dependence, progesterone

1. Introduction

The peripheral benzodiazepine receptor (PBR) is located in peripheral organs such as spleen, testis, ovary and adrenal gland and in glial cells in the brain, involved in steroidogenesis and apoptosis [1]. Although, the functions of PBR within the CNS are not clear, there have been shown to regulate neurosteroid synthesis, mitochondrial functions including respiratory chain, ion channel activity, neuroinflammation in microglial cells and sensitive to endocrine changes and stress [1, 2, 3, 4, 5, 6]. Furthermore, several studies have reported that the density of PBR increases concomitantly with glial activation following neural injury induced by various insults such as inflammation, metabolic stress, trauma, transient global forebrain ischemia and chemically-induced brain injury [3]. An increase of PBR density was also found in other pathological situations, including sciatic nerve lesion, cerebral infarction, multiple sclerosis, Alzheimer'sdisease, and astrocytomas [4, 7]. Morover, an increase of PBR density was observed after exposure to acute stress, but a decrease of PBR density was found during exposure to chronic stressful condition [2, 8]. PBR, a biological marker of stress and anxiety, has also been used as a marker of microglia and astrocyte activation. It has also been described as a pharmacologically specific marker for neurotoxic amphetamine administration in mice [9, 10]. Therefore, the aim of this study was to investigate the alteration of PBR gene expression in psychiatric diseases such as major depressive disorder (MDD) and methamphetamine (METH) dependence.

2. Main Body

2.1 Materials and Methods

Subjects

Twenty-two patients (female; n=19, male; n=3, age 41±18 year) meeting DSM-IV criteria for major depression and 35 healthy subjects (female; n=18, male; n=17, age 32±8 year), free of psychiatric and drug abuse history, were recruited. Fourteen methamphetamine dependent patients (male, age 33±7 year) were diagnosed by a psychiatrist according to the DSM-IV and control group consisted of thirty eight healthy subjects (age 32±5).The experimental protocols were approved by the Human Ethics Committee of Naresuan University.

PBR and progesterone measurements

Peripheral blood was collected for RNA extraction and followed by PBR gene amplification using RT-PCR. PCR master mix of each reaction were composed of 1x Taq polymerase buffer (viviantis, USA), 0.2 mM of dNTPs (invitrogen, USA), 1.25 Units of Taq DNA polymerase (viviantis, USA), 0.2 mM $MgCl_2$ (viviantis, USA),20 μM primers of human PBR (target); F: 5'-AGG GTC TCC GCT GGT ACG CC-3', R: 5'-TGG GGC AAC CTC TGA AGC TC-3'and β-actin (internal control); F: 5'-CCC AGA GCA AGA GAG GCA TC-3', R: 5'-CTC AGG AGG AGC AAT GAT CT-3' and 4 ng of cDNA sample. The solution was incubated for 2 min at 94°C, followed by 30 cycles of 30 sec at 94°C, 30 sec at 58°C, 30 sec at 72°C with a final 10 min extension step at 72°C. The PCR products were then analyzed by agarose gel electrophoresis. PBR genes expression were measured by scion image software and normalized with house keeping ß-actin gene. Progesterone levels in the serum of all subjects were measured with Progesterone II kit (cobas, USA) according to manufacture's protocol. Differences between groups were analyzed by one-way analysis of variance (ANOVA).

2.2 Results

The result showed a significant decrease in PBR gene expression in major depressive patients with suicide attempt when compared with both controls and a non-suicide attempt group (fig. 1). A significant decrease in serum progesterone concentration was also observed in major depressive patients (table 1). There was significant increase in PBR mRNA expression of METH dependent patients (fig. 2). A significant increased in PBR mRNA expression of METH-induced psychosis (n=11) was found when compared with control subjects (fig. 3). There was no significant difference in progesterone level between METH dependent patients and control subjects (table 2).

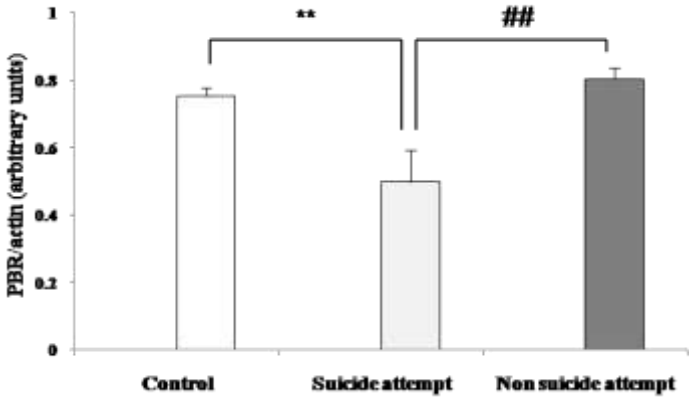

Figure 1 Comparison of PBR mRNA expression between control subjects, non suicide attempt and suicide attempt patients. Values are mean±SEM. ($^{**}p$ = 0.003 compared with control subjects, $^{\#\#}p$ = 0.001 compared with non suicide attempt patients; ANOVA post hoc Bonferroni tests)

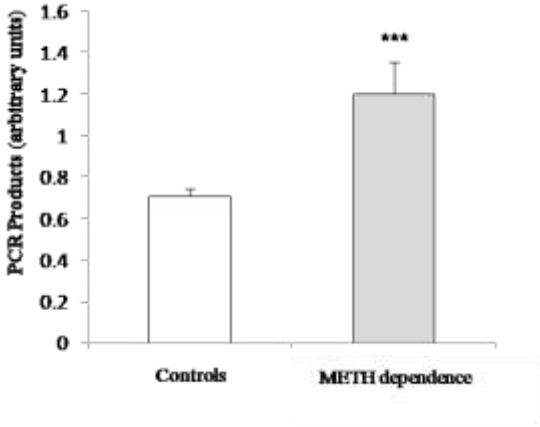

Figure 2 Comparison of PBR mRNA expression between METH dependent patients and control subjects. Values are mean±SEM. ($^{***}p$<0.001; Independent-Samples T Test)

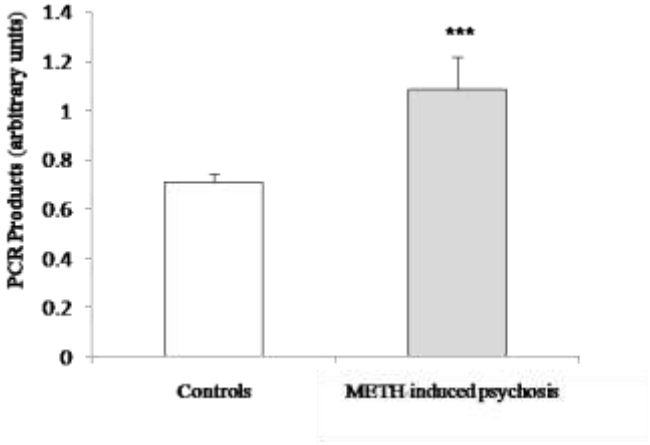

Figure 3 Comparison of PBR mRNA expression between METH-induced psychosis

patients and control subjects. Values are mean±SEM. ($^{***}p$ <0.001; Independent-Samples T Test)

Table 1. Progesterone serum levels of major depressive patients and controls.

Group	**Progesterone levels (ng/ml) (mean±SD)**
Controls (n=15)	2.64±4.56
Major depressive patients (n=15)	0.93±3.03*

* p = 0.049 t test of log-transformed data compared with control subjects.

Table 2. Progesterone serum levels of METH dependent patients and controls.

Group	**Progesterone levels (ng/ml) (mean±SD)**
Controls (n=16)	1.07±0.31
Major depressive patients (n=14)	0.98±0.27

2.3 Discussions

PBR gene expression was reduced in MDD with suicide attempt and reductions of progesterone levels were also observed in MDD. The results indicate that the attenuation of PBR expression found in suicide attempt may be induced from chronic stress. The result of low concentration of progesterone level provides an evidence to support PBR function and contributes a support of neurosteroid deficit in major depression. Moreover, an up-regulation in PBR mRNA expression was found in METH dependence. This result provides a strong support of PBR function after METH induced neurotoxicity in human. An increase of PBR expression may reflect to the activation of glial cells to protect brain from METH induced neurotoxicity. The result of progesterone level in METH dependence may be because of an adaptation of progesterone to normal level after drug withdrawal symptoms.

The results in the present study suggest that PBR may play a critical role in suicide attempt and drug dependence and the alteration of PBR expression may be a biological marker for those diseases.

2.4 Acknowledgments

This research was supported by Naresuan University Research Fund and TRF-Master Research Grant . The authors also gratefully acknowledge the patients in the Psychiatric Clinic, Naresuan University Hospital and the Central Correctional Institutional for Drug Addicts, Bangkok, Thailand, and all subjects in the study..

3. References

[1] Papadopoulos V, Lecanu L, Brown R C, Han Z, Yao Z-X. Peripheral-Type Benzodiazepine Receptor in Neurosteroid Biosynthesis Neuropathology and Neurological Disorders. *Neuroscience,* 2006, 138: 749-756.

[2] Soreni N, Apter A, Weizman A, Don-Tufeled O, Leschiner S, Karp L, et al. Decreased platelet peripheral-type benzodiazepine receptors in adolescent patients with repeated suicide attempts. *Biological Psychiatry,* 1999, 46: 484-488.

[3] Casellas P, Galiegue S, Basile A S. Peripheral benzodiazepine receptor and mitochondrial function. *Neurochemistry International,* 2002, 40: 475-486.

[4] Ferzaz B, Brault E, Bourliaud G, Robert P J, Poughon G, Claustre Y, et al. SSR180575(7-chloro-*N*,*N*,5-trimethyl-4-oxo-3-phenyl-3,5-dihydro-4*H*-pyridazino[4,5-*b*]indole-1-acetamide), a Peripheral Benzodiazepine Receptor Ligand, Promotes Neuronal Survival and Repair. *Pharmacology and Experimental Therapeutics,* 2002, 301: 1067-1078.

[5] Venneti S, Lopresti B J, Wiley C A. The peripheral benzodiazepine receptor (Translocator protein 18 kDa) in microglia: From pathology to imaging. *Progress n Neurobiology,* 2006, 80: 308-322.

[6] Weizman A, Burgin R, Hare Y, Karp L, Gavish M. Platelet peripheral-type benzodiazepine receptor in major depression. *Journal of Affective Disorders,* 1995, 33: 257-261.

[7] Chen M K, Guilarte T R. Translocator protein 18 kDa (TSPO): molecular sensor of brain injury and repair. *Pharmacol and Therapeutic,* 2008, 118: 1-17.

[8] Johnson M R, Marazziti D, Mintzer O B, Emmanuel N P, Ware M R, Morton, W A, et al. Abnormal Peripheral Benzodiazepine Receptor Density Associated with Generalized Social Phobia. *Society of Biological Psychiatry,* 1998, 43: 306-309.

[9] Chelli B, Pini S, Abelli M, Cardini A, Lari L, Muti M, et al. Platelet 18kDaTranslocator Protein density is reduced in depressed patients with adult separation anxiety. *European Neuropsychopharmacol,* 2008, 18: 249-254.

[10] Fantegrossi W E, Ciullo J R, Wakabayashi K T, De la Garza R, Traynor J R, Woodes J H. A Comparison of the Physiological, Behavioral, Neurochemical and Microglial Effects of Methamphetamine and 3, 4-

[11] Methylenedioxymethamphetamine in the Mouse. *Neuroscience,* 2008, 151: 533-543.

LSBE262
Leaf Anatomy and Pollen Studies of Zingiberaceae in Lambusango Wildlife Reserve, Buton Island, Indonesia

Gufrin[1,2*], Indrawati[2], Rita Ningsih[2], Mohd Nazip Suratman[1], Nurun Nadhirah Md Isa[3], and [4]Axel Dalberg Poulsen

[1]Faculty of Applied Sciences, Universiti Teknologi MARA, 40450 Shah Alam, Malaysia

[2]Department of Biology, Faculty of Mathematic and Natural Sciences, Haluoleo University, Kendari 93117, Indonesia

[3]Faculty of Applied Sciences, Universiti Teknologi MARA, 26400 Jengka Pahang, Malaysia

[4]Natural History Museum, University of Oslo, PO Box 1172, Blindern, No-0318 Oslo, Norway

Corresponding author: gufrinamlin@gmail.com

Abstract

The documentation of flora in Sulawesi is far from complete. The general lack collection is confounded on Zingiberaceae. Besides, the enigmatic of the *Amomum melichroa* and *Alpinia melichroa* from Sulawesi is still under discussion. Studies on leaf anatomy and pollen have solved many problems in plant taxonomy. In this research, the characteristics of leaf anatomy and pollen were studied to correct the taxonomy of plants. The procedure for leaf anatomy analysis was in accordance to the method suggested by Johansen (1940) modified, whereas the pollen analysis was performed according to the chlorination method as suggested by Erdman (1952; 1954). From the study, eight species of ginger collected are found belong to be the family of Zingiberaceae namely *Alpinia galanga*, *Alpinia melichroa*, *Alpinia monoplora*, *Alpinia* sp., *Etlingera* sp.1, *Etlingera* sp.2, *Amomum testaseum*, and *Curcuma domestica*. The leaf anatomy such as stomata index, stomata density, and stomata length are varies between all species. However, pollen unit, shape, and size are seemed to be uniform in all species. Meanwhile, the combination between pollen symmetry, structure, e*xine* ornamentation, *exine* thickness and *Aperture* appeared to be different among species and thus can be used as specific characters for the species. An interesting result was found on pollen of *A. melichroa* that is different from other species within the same genus, which prompts question about botanical status of *A. melichroa* by Schumann. From the study it is concluded that the leaf anatomy and pollen data can be used as keys for identification of ginger at species level.

Keyword: Leaf Anatomy, Pollen, Ginger, Zingiberaceae, Taxonomy

1. Introduction

Sulawesi is one of the islands that are included in the Wallacea Line established by Alfred Russel Wallace [1]. Wallacea Line was established between Asia Oriental Region and Australian Region due to the in differences animals and plants from these reas. Based on these differences, research on plants in this area becomes very important to be conducted including on Zingiberaceae. Zingiberaceae is one the largest families in plant kingdom [2] belonging to the Zingiberales order. The family has about 52 genera and is estimated to contain about 1200-1400 species [3, 4, 5, 6]. It is documented that Zingiberaceae is distributed in tropical and sub-tropical areas [2], particularly in Asia from India to New Guinea [7]. Zingiberaceae is herb plant with leafy shoot, and its entire group has rhizome that grow horizontal in the ground. Leaves arrangement are *distioceus* and its sheath formed *pseudo-stem*. Flowers arrangement formed a bunch with a bractea that supports one flower. Generally, their inflorescences are terminal on the leafy shoot and rhizome; and few among of them have flowers that emerge from the middle of leafy shoot [8].

The exploration of flora in Sulawesi is far from complete [9]. The general lack collection is confounded on Zingiberaceae [8]. Besides, there has been an on-going discussion about revision of genus *Etlingera* in Sulawesi. Moreover, the verification of the *Amomum melichroa* and *Alpinia melichroa* by Schumann also is being finalized [9]. Studies on leaf anatomy and pollen grain have been used on plant taxonomy approach for many species and have succeeded to solve many problems in plant taxonomy that difficult to distinguish with the morphological characteristics.

Generally, the plant taxonomy uses the morphological characteristics to identify the plant species. However, development of sciences and technologies have increased the interest of taxonomists to find the other evidences in plant identification such as plant anatomy, pollen [10] and DNA data. According to Shukula and Misra [11] there are many anatomical characteristics that can be used to proof the morphological character in plant taxonomy. These include the size of stomata, shape of stomata, type of stomata, and index of stomata, type of trichoma, beam transporter arrangement, papilla, and ergastic substances.

Many researches have been conducted on anatomical studies and have successfully solved the taxonomy problems, such as Setyawan [12] on *Alpinia*, *Costus* and *Hedychium*, Nkem et al [13] on two species eggplant and Damayanti [14] on six species of bananas in Borneo, Indonesia. Besides anatomic character, the pollen morphology is one of the important data that can be used in plant taxonomy. The general pollen character that can be used in plant systematic are, pollen size, pollen shape, pollen type, structure of the pollen wall, pollen architecture, number of

aperture, aperture position, and aperture shape [15]. Therefore, the objective of this studied is to examine the leaf anatomy and pollen morphological characters that can to be used as evidences in plant taxonomy especially in Zingiberaceae.

2. Material and Method

2.1 Sampling Method

Materials of the research were collected from Lambusango Wildlife Reserve, Buton Island, Indonesia. Sampling area was located in Kakenauwe, Kaweli, Wagari and Wakangka Vilages. Samples were collected between July to September 2010 by exploration method. The flowering and fruiting Zingiberaceae plant were collected as samples. The anthers for each plant were collected from the flowers and kept in the bottle with glacial acid for pollen characterization in the Laboratory. The leaf for anatomical characterization was collected from the third leaf to the youngest for every leafy shoots. The leaf samples were collected in 3 replicates for all species from different leafy shoot, and then were preserved in the bottles with 70 % alcohol.

2.2 Leaf Anatomical Characterization

The slide preparation for leaves anatomic study was in accordance to the method suggested by Johansen [16] modified. The slide was observed by Nikon Eclipse Microscope with Nis Element Imaging Software (NEIS). Analysis of different characters of each sample was done with three repetitions. The repetition of slide was taken from different leaf that was collected from other leafy shoot from the same species. Every character such as the length of stomata was measured as many as ten replications and the mean value was recorded. This step was repeated on different slide from different leaf as replication as many as three times for all *abaxial* and *adaxial* epidermis of all samples. The epidermis for each slide was observed under the microscope beginning from low magnification (100X) to medium magnification (400X) to identify the general character and then high magnification (1000X) was used to measure the length of the stomata.

2.3 Pollen Characterization

The slide preparation for pollen characterization was done by chlorination method as suggested by Erdman [15]. Identification of pollen characters was observed by Nikon Eclipse Microscope (NEIS). The characters of pollen for every species were done by three repetitions on different slide. In each repetition as many as 30 pollens were measured to ensure the accuracy of characters that were identified. Similarly observations of pollens under the microscope were conducted with low magnification (40X) for general characters, followed as high magnification (1000X) for specific

characters. On high magnification, oil immersion was applied to enhance the focus to the objects identified.

3. Results and Discussion

3.1 Results

From the observation, all type of stomata for both leaves surfaces are identified as Paracytic, in which one or more of the subsidiary cells that flank the stoma are parallel with the long axis of the guard cells. As can be seen (Table 1 and Figs 1-8) the shape of cell epidermis is dominantly elongated-hexagonal for both *adaxial* and *abaxial* epidermis, except *A. galanga* and *C. domestica* is polygonal on *adaxial* suface. The stomata index for all species is different for every leaf sample in each species. The greatest stomata index value for *adaxial* epidermis was found in *Etlingera* sp.1 (1.636), and the lowest in *A. Monoplora* (0.149). For the *abaxial* epidermis greatest was found in *Etlingera* sp.1 (8.58), and the lowest in *C. domestica* (4.213). The highest density of stomata on *adaxial* epidermis is *Alpinia* sp (102.74), and the lowest is *Etlingera* sp.2 (7.52), whereas the highest density of stomata for *abaxial* epidermis is *Etlingera* sp.1 (862.1), and the lowest is *C. domestica* (80.98). The result from the observation the length of stomata found that the largest stomata for *adaxial* epidermis is *C. domestica* (30. 24) and smallest is *A. monoplora* (17.14), whereas the largest for the *abaxial* epidermis is *C. domestica* (33.04) and the smallest is *Etlingera* sp.1 (13.6). Trichomes on leaves surface in this study was only found as *adaxial* type in species *A. monoplora.*

The results from the measurement of the pollen grain showed that all pollen units are monad with shape for Index (P/E) is *prolate spheroidal* (Table 2 and Figs 9-16). There was a variation in the size of pollen grain for all species; for instance *Etlingera* sp.1, its pollen size is in medium category (46 µ) and for *Etlingera* sp.2 in big category (56 µ), while the others are in a very big category (>100 µ). The types of pollen symmetry are generally radial in five species i.e, (*A. melichroa, Alpinia* sp, *Etlingera* sp.1, *Etlingera* sp.2 and *C. domestica),* while three other species i.e, (*A. galanga, A. monoplora,* and *A. testaceum*) are bilateral. All pollen structures are *tectate* with the *ektexine* is *psilate* except for *A. melichroa* which is *intectate*; where it has spine on its *ektexine* with length size of (4.5µ).

Five samples have been found to have *endexine* which include *Verrucate* (*A. melichroa, A. galanga, Etlingera* sp.1, *Etlingera* sp.2 and *A. testaceum*), whereas three other samples are *reticulate* i.e, (*A. melichroa, Alpinia* sp, and *C. domestica*). The thickness of *ektexine* and *endexine* are varies for all species sample, the thickest of *ektexine* is *A. melichroa* (23.98 µ) and *endexine* is *A. monoplora* (5.4 µ), while the thinnest of *ektexine* is *A. melichroa* (5.22 µ) and *endexine* is *Etlingera* sp.1 (1.1 µ). There are two from eight samples that have aperture namely *A. galanga* with *polypore*

aperture type (7 *aperture*), and *A. monoplora* with *polypore aperture* type also (5 *aperture*), while the other are none *aperture* pollen. The data observation of leaf anatomy and pollen morphology of Zingiberaceae in Lambusango Wildlife Reserve, Buton Island, Indonesia was compiled in the Table 1 and Table 2 below.

Table 1 Comparison of the leaves anatomical character of Zingiberaceae in Labundobundo Wildlife Reserve Buton Island, Southeast Sulawesi, Indonesia

No	Species	Epidermis	Type of Stomata	Shape of epidermis cell	Stomata Area Index (mm^{-1})	density of Stomata (mm^{-2})				Length of stomata (µm)				Trichoma	
						Repetition			Average	Repetition			Average	Type of Cell	Size (µm)
						1	2	3		1	2	3			
1	*A. melichroa*	AD	Paracytic	Elongated-hexagonal	0.558	20.08	17.85	20.08	19.34	23.478	24.009	23.717	23.73	-	-
		AB	Paracytic	Elongated-hexagonal	6.273	133.92	109.37	120,53	121.27	21.417	20.147	18.494	20.01	-	-
2	*A. galanga*	AD	Paracytic	Polygonal	1.199	39.51	37.5	30	35.61	21.3	21.971	22.507	21.92	-	-
		AB	Paracytic	Elongated-hexagonal	7.898	355.97	356.77	353.36	355.37	18.774	19.384	19.846	19.33	-	-
3	*A. monoplora*	AD	Paracytic	Elongated-hexagonal	0.149	8.92	12.01	12.01	10.98	17.356	17.057	17.035	17.14	-	-
		AB	Paracytic	Elongated-hexagonal	6.631	200	208.33	210.67	206.33	15.982	16.737	15.959	16.22	unicellular	155.82
4	*Alpinia* sp	AD	Paracytic	Elongated-hexagonal	0.172	89.28	110.29	108.69	102.75	20.394	17.943	18.493	18.94	-	-
		AB	Paracytic	Elongated-hexagonal	8.8	468.75	517.24	666.67	550.88	15.323	16.985	16.394	16.23	-	-
5	*Etlingera* sp.1	AD	Paracytic	Elongated-hexagonal	1.636	45.18	45.28	53.57	48.01	19.102	19.327	18.759	19.06	-	-
		AB	Paracytic	Elongated-hexagonal	8.958	885.41	875	825.89	862.10	13.318	13.477	14.026	13.60	-	-
6	*Etlingera* sp.2	AD	Paracytic	Elongated-hexagonal	0.247	6.94	8.92	6.69	7.52	22.053	23.682	22.659	22.79	-	-
		AB	Paracytic	Elongated-hexagonal	6.978	337.5	331.63	291.67	320.26	18.907	17.551	18.485	18.31	-	-
7	*A. testaseum*	AD	Paracytic	Elongated-hexagonal	0.358	13.58	7.81	11.90	11.10	24.115	21.797	21.858	22.59	-	-
		AB	Paracytic	Elongated-hexagonal	6.757	172.79	167.61	163.46	176.95	22.485	23.703	22.979	23.05	-	-
8	*C. domestica*	AD	Paracytic	Rhomboid, hexagonal to polygonal	1.452	15.62	17.85	8.92	14.13	29.031	31.256	30.458	30.24	-	-
		AB	Paracytic	Elongated-hexagonal	4.213	73.86	71.42	97.65	80.98	32.493	35.7	31.266	33.04	-	-

Table 2 Comparison of the pollen characteristic of Zingiberaceae in Labundobundo Wildlife Reserve Buton Island, Southeast Sulawesi, Indonesia.

No	Species	Indicator												
							Exine Ornamentation			Exine thickness		Aperture		
		Pollen Unit	Shape of pollen (P/E)	Size of Pollen (µm)	Symmetry of pollen	Structure of Pollen	Ektexine	Length of spine	Endexine	Ektexine	Endexine	Shape	No.	Type
1	*A. melichroa*	Monad	Prolate spheroidal	(118) Very big	Radial	Intectate	Echinate	4.50	Verrucate	23.98	3.77	-	-	None aperture
2	*A. galanga*	Monad	Prolate spheroidal	(148) Very big	Bilateral	Tectate	Psilate	-	Verrucate	7.72	2.71	Porat	7	Polypore
3	*A. monoplora*	Monad	Prolate spheroidal	(160) Very big	Bilateral	Tectate	Psilate	-	Reticulate	14.41	5.40	Porat	5	Polypore
4	*Alpinia* sp	Monad	Prolate spheroidal	(116) Very big	Radial	Tectate	Psilate	-	Reticulate	13.67	3.46	-	-	None aperture
5	*Etlingera* sp.1	Monad	Prolate spheroidal	(46) medium	Radial	Tectate	Psilate	-	Verrucate	5.22	1.10	-	-	None aperture
6	*Etlingera* sp.2	Monad	Prolate spheroidal	(56) Big	Radial	Tectate	Psilate	-	Verrucate	6.53	1.19	-	-	None aperture
7	*A. testaseum*	Monad	Prolate spheroidal	(131) Very big	Radial	Tectate	Psilate	-	Verrucate	21.76	3.54	-	-	None aperture
8	*C. domestica*	Monad	Prolate spheroidal	(130) Very big	Bilateral	Tectate	Psilate	-	Reticulate	17.60	1.95	-	-	None aperture

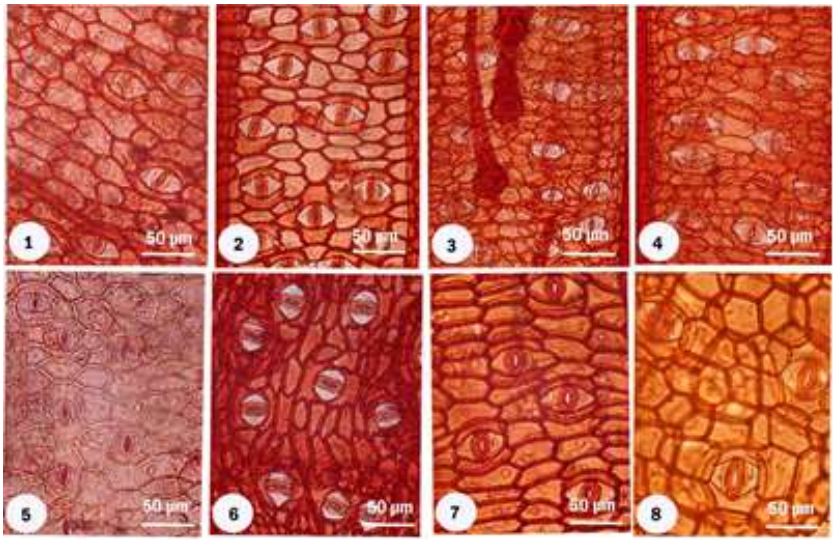

Figs. 1-8. The stomata micrographs of Zingiberaceae species in Lambusango Wildlife Reserve, Buton Island, Indonesia. **(1)** *A. melichroa* **(2)** *A. galanga* **(3)** *A. monoplora* **(4)** *Alpinia* sp **(5)** *Etlingera* sp.1 **(6)** *Etlingera* sp.2 **(7)** *A. testaceum* **(8)** *C. domestica*. Magnification = 400X

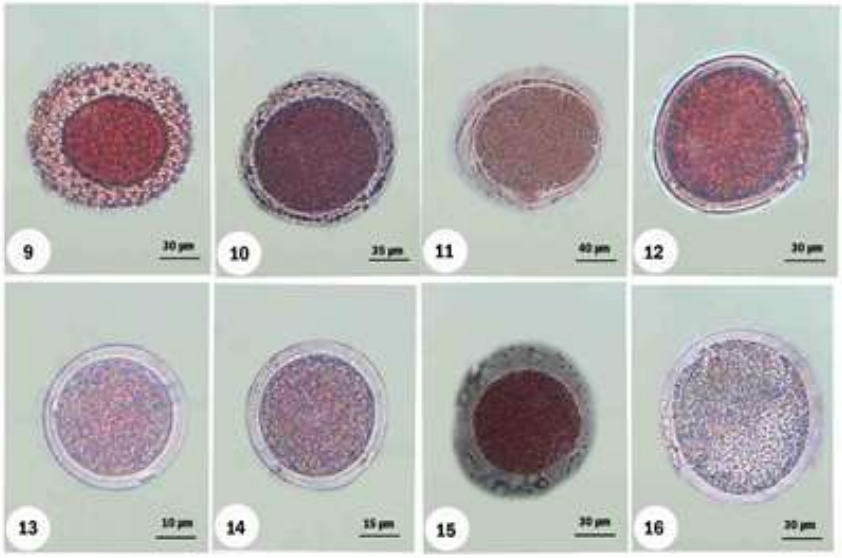

Figs. 9-16. The pollen micrographs of Zingiberaceae species in Lambusango Wildlife Reserve, Buton Island, Indonesia. **(1)** *A. melichroa* **(2)** *A. galanga* **(3)** *A. monoplora* **(4)** *Alpinia* sp **(5)** *Etlingera* sp.1 **(6)** *Etlingera* sp.2 **(7)** *A. testaceum* **(8)** *C. domestica*. Magnification = 400X

3.2 Discussion

According to Rarford [10] and [17], stomata type on leaf is one of the characters that can be used in plant classification. The result of this study was found that all stomata type is *paracytic* (Figs 1-8). The same results have been found from the study of six of bananas in west Kalimantan by Damayanti [14]. The shape of epidermis cells is uniform for all species except *A. galanga*, in which its *adaxial* epidermis cell is *polygonal*, and *C. domestica* is *rhomboid, hexagonal* to *polygonal*, and these characters only can be used as character for family as well as for order levels. Based on the results from the observation, the characters that can be used to identify Zingiberaceae are the stomata index, stomata density, stomata length and trichoma.

The results have been supported by Rarford [10], that these characters are useful to be used to distinguish the plant taxon in species level.

The same results as reported by Damayanti [14]; where these characters were also used to distinguish six species of bananas, and Nkem *et al* [13], who used this data to distinguish eggplant species in Nigerian. Data of pollen symmetry, pollen structure, *exine* ornamentation (*ektexine* and *endexine*), *exine* thickness and pollen *aperture* can be used to distinguish the species in the same genus. Consideration of those characters as pollen characters to distinguish the species was supported by Erdtaman [15] and Radford [10]; in which, all of these characters can be used to identify the plant taxon at family, genus, and species levels.

An interest on result pollen characterization was found on *A. melichroa*; in concept of its pollen which is different as compared to the other three species in the same genus (Table 2). Three species from genus *Alpinia* have ornamentation *psilate* on its *ektexine*, except *A. melichroa* has ornamentation *echinate;* in which the length of its spine was measured about 4.5 µm. If the ektexine structure can be considered for specific character for genus level on *Alpinia* as well as on species, this data may raise up questions about *A. melichroa* K. Schum. in which the status still under discussion until now. In the first time, *A. melichroa* and *A. chrynogynia* were described by K. M. Schumann (1904) to maintain *Amomum* in Vietnamese. In (1990) R. M. Smith excluded *A. melichroa* and *A. chrynogynia,* from genus *Alpinia* and suggesting that they might better placed in *Amomum* (9). The latest study of Zingiberaceae in Sulawesi was conducted by A. D. Poulsen (2008-2009), and declared that *A. chrynogynia* K. Schum is a species of *Etlingera*. However, *A. melichroa* K. Schum still not clear in his manuscript (9), and consider it as the species that is not reported until now.

4. Conclusion

Eight species of Zingiberaceae were collected namely: *A. melichroa, A. galanga, A. monoplora, Alpinia* sp, *Etlingera* sp.1, *Etlingera* sp.2, *A. testaceum,* and *C. domestica*. All stomata index, stomata density, and length of stomata are varies for all species, and trichoma on the leaf was only found in *A. monoplora.* The pollen characters such as pollen unit, shape, and size seemed to be uniform for all species. Meanwhile, the combination between pollen symmetry, structure, e*xine* ornamentation, *exine* thickness and *Aperture* appeared to be different among species and thus can be used as specific characters of species. An interesting result was found in the pollen of *A. melichroa* which was different from other species in the same genus, which prompts to a question about botanical status of *A. melichroa* by Schumann. We conclude that the leaf anatomy and pollen data can be used as a key for identification of Zingiberaceae in species level.

5. Acknowledgement

The authors Thanks PT. Antam tbk. For awarding a scholarship for conducting this study, to Haluoleo University for the use of Laboratory facilities, and the Staff officers of Lambusango Wildlife Reserve for their guidance during the exploration and collection of samples,

6. References

[1] Corlett, R T. The Ecology of Tropical East Asia. Oxford University Press. New York, United States, 2009, ISBN: 978-0-19-953245-2.

[2] Sirirugsa, P. Thai Zingiberaceae: Species and Their Uses. The International Conference on Biodiversity and Bioresource: Conservation and Utilization, Phuket Thailand, November 23-27, 1997. pp. 1-8.

[3] Bajaj, Y P S. Biotechnology in Agriculture and Forestry *40,* Spriner-Verlag, Berlin Heidelberg, 1997. pp.12-111.

[4] Kubutzki, K. Flowering Plants Monocotyledons, Springer- Verlag, Berlin Heidelberg, 1998. pp. 11-18.

[5] Clayton, W D and Dassanayake, M D. Flora of Ceylon, National Herbarium, Departement of Agriculture, Srilanka, 2000. pp.

[6] Simpson, M G. Plant Systematics, Dana Dreibelbis, Canada, 2006. pp.

[7] Kress, W J. Stone, D E. Williams, K J. The Phylogeny and new Classification of the ginger (Zingiberaceae): Evidence of Molecular data. Am. J. Bot, 2002. (89) pp. 1682-1696.

[8] Poulsen, A D. Gingers of Sarawak. Natural History Publications (Borneo). Kinabalu, 2006. pp.

[9] Sharp, N J. Newman, M F. Santika, Y. Gufrin and Poulsen, A D**.** The enigmatic ginger *Alpinia melichroa* rediscovered in SE Sulawesi. Nordic Journal of Botany (in press). 2012. pp. 1-5.

[10] Radford, A E. Fundamental of Plant Systematic. Harper and Row. Publisher. Inc. New York, 1986. pp.

[11] Shukula, P and Misra, S P. An Introduction to Taxonomy of Angiosperms, Vicas Publishing House. PVT. LTD, New Delhi, 1982. pp.

[12] Setyawan, A D. Anatomi Sistematik Pada Anggota Familia Zingiberaceae. BioSMART, , 2001 3(2). pp. 36-44.

[13] Nkem, M F, Udodi, Nwachukwu C, Olivio O. Comparative Leaf Epidermal Stidies on Solanum macrocarpon and Solanum nigrum, Nature and Science, 2007. 5(3). Pp. 1-4.

[14] Damayanti, F. Analisis Jumlah Kromosom dan Anatomi Stomata pada Beberapa

Plasma Nutfah Pisang *(Musa sp.)* Asal Kalimantan Timur, Bioscientiae, ., 2007. 4(2). pp. 53-61.

[15] Erdtman, G. Pollen Morphology and Plant Taxonomy. Chronica Botanical Company. Waltham Mass U.S.A, 1952. pp.

[16] Johansen, D A. Plant Microtechnique 1st Edition. Mc Graw. Hill Book Company,Inc. New York & London, 1940. pp.

Stuessy, T F. Case Study In Plant Taxonomy. Columbia University Press, New York, 1994. pp.

Civil Engineering I

2013/3/16 Saturday 09:00-10:30 Room 604

Session Chair: ***Prof. Mohammed Enamul Haque***

ACCMES 113

Multilayer Perceptron Back-Propagation Artificial Neural Network Model to Predict Failure Loads on Reinforced Concrete Slabs

Mohammed Enamul Haque｜*Texas A&M University*

ACCMES 63

Factors Affect the Strength Development of Repaired Pavement Using Recycling Technique

Avirut Chinkulkijniwat｜*Suranaree University of Technology*

ACCMES 96

Numerical Analysis to Better Understand the Failure Mechanism and Reinforcements on the Tunnel Face of an Earth Pressure Balance Shield - A Case Study of Mashhad Metro Line 2

Saba Gharedashi｜*Amir Kabir University of Technology*

Milad Barzegar｜*Amir Kabir University of Technology*

ACCMES 109

Simulations of Control Characteristics of Tuned Liquid Column Damper Using an Elliptical Flow Path Estimation Method

Passagorn Chaiviriyawong｜*Prince of Songkla University*

Suchart Limkatanyu｜*Prince of Songkla University*

ACCMES 148

Response Analysis of Strike-Slip Fault Movement on Buried Pipeline

Md Aftabur Rahman｜*Saitama University*

Hisashi Taniyama｜*Saitama University*

ACCMES 153

Optimum Cross-Sectional Floating Structure

Du Ho Lee｜*Korea Institute of Construction Technology*
Youn Ju Jeong｜*Korea Institute of Construction Technology*
Young Jun You｜*Korea Institute of Construction Technology*
Min Su Park｜*Korea Institute of Construction Technology*

ACCMES 155

Hydraulic Conductivity of Various Shapes of Sands

Nurullah Akbulut｜*Hasan Kalyoncu University*
Ali Firat Cabalar｜*University of Gaziantep*

ACCMES 113
Multilayer Perceptron Back-Propagation Artificial Neural Network Model to Predict Failure Loads on Reinforced Concrete Slabs

Dr. Mohammed E. Haque, P.E.
Professor
Department of Construction Science (MS-3137)
Texas A&M University
College Station, TX 77843-3137, USA
Email: mhaque@tamu.edu

Abstract

In order to minimize the extensive calculations required to predict the failure loads of reinforced concrete slabs, this paper describes an artificial neural network (ANN) based training model to predict failure loads. To create training and model validation data, several square/rectangular slabs with varying edge support conditions, slab thicknesses, and reinforcements were analyzed to determine failure loads using a virtual work method for yield-lines failure mechanism. When a slab fails in flexure, the rebar yields first in the region of highest moment, and this portion of slab acts as a plastic hinge. With additional loads, the hinging region will rotate plastically, and moments will be redistributed to neighboring regions, causing them to yield as well. Eventually, enough yield lines will be developed to cause the slab to deformed plastically and collapse without any additional loads. The ANN model was developed with NeuroShell-2 software using a multilayer perceptron (MLP) back-propagation (BP) architecture. The ANN model was trained with a set of 450 concrete slab analysis data, and the trained model was validated using a new set of 54 slabs analysis data. The ANN predicted values of slab failure loads were found to demonstrate very good agreement with the calculated values.

Keyword: Artificial Neural Network, yield-line analysis, reinforced concrete slab, failure load.

1. Introduction

The yield line analysis of reinforced concrete slab uses rigid plastic theory to compute the failure loads corresponding to plastic moment resistances in various parts of the slab. The concept of yield line analysis was first proposed by A. Ingerslev in 1921-1923, and it was subsequently extended to modern yield line theory by K.W. Johansen [1]. When the yield line pattern is formed in regions of maximum moment, it divides the slab into a series of elastic plate segments. Once the yield lines have formed, all further deflections due to additional loads are concentrated along the yield

lines, and the slab deflects as a series of rigid plates connected together by long hinges along the yield lines (Figure 1). The external work done by the loads to cause a small arbitrary virtual deflection (δ) must equal the internal work done as the slab rotates at the yield lines to accommodate this deflection. In the virtual work method of analysis, by giving a virtual displacement to slab the rotations at various yield lines can be calculated. By equating the internal and external work, the relationship between the ultimate loads and the resisting moments of the slab can be obtained. The elastic rotations and deflections are not considered in the work calculation since their values are negligible compared to plastic rotation and deflection. There are several textbooks available where virtual work method of analysis has been discussed in details [2, 3].

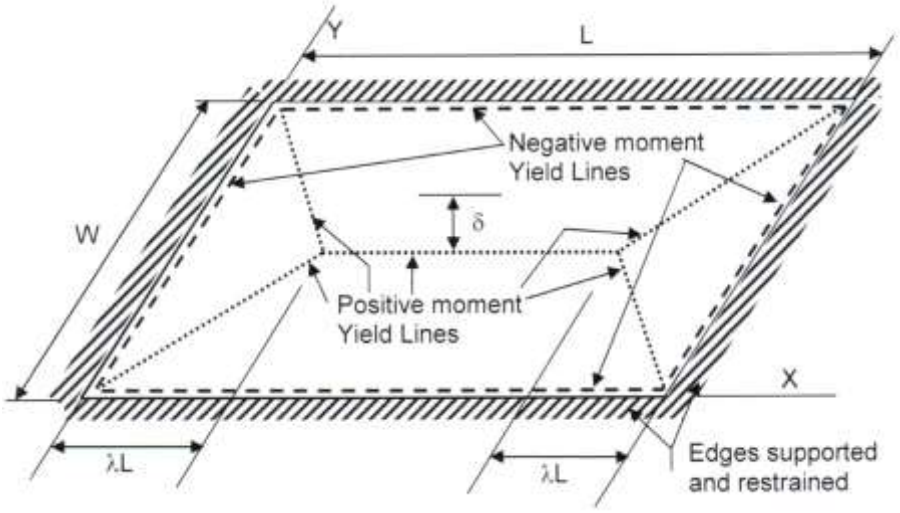

Figure 1. Plastic Mechanism for a rectangular slab with moment resistant edges

The objective of this paper was to develop an artificial neural network (ANN) based trained model to predict failure loads on two-way rectangular reinforced concrete slab. In order to create training data, several square/rectangular slabs with different edge support conditions, slab thickness, and slab reinforcements (positive and negative) were analyzed to determine failure loads using a virtual work method for yield-lines failure mechanism.

ANN is one of the artificial intelligence algorithms that relates to the class of machine learning. It mimics the natural human brain's process of acquiring and retrieving knowledge. It models the biological neuron, which consists of nodes (cells) and links (axon). It is defined as a computing system made up of a number of simple, highly interconnected processing elements, which process information through their dynamic state responses to external input [4]. Each processing element (PE) or artificial neuron has an input and an output side. The connections are on the input side correspond to

the dendrites of the biological original and provide the input from other PEs while the connections on the output side correspond to the axon and transmit the output. Network training is an act of continuously adjusting their connection weights until they reach unique values that allow the network to produce outputs that are close enough to the desired outputs. The learning ability of a neural network is determined by its architecture and by the algorithmic method chosen for training. Currently, back-propagation is the most popular, effective, and easy to learn model for complex networks [5, 6]. Figure 2 depicts a schematic representation of an ANN with multiple layers or slabs, i.e. a MLP. The BP training algorithm consists of two main steps, a forward step which involves generating a solution to the classification problem in question, and then a back propagation of the error to modify the weights in the direction of minimum error. The forward step presents the inputs as training examples to the ANN, which is passed to each hidden node in the hidden layer where the activation at that node is calculated using a sigmoidal transfer function [7] in order to yield an output which is transferred to the output layer. In the back-propagation step, the difference in error between the ANN output and the target output is calculated and used to adjust the values of the connecting weights, from the output, through the hidden layer, to the input layer [8]. These steps are repeated until a minimum error between the ANN predicted output and the target output value is reached.

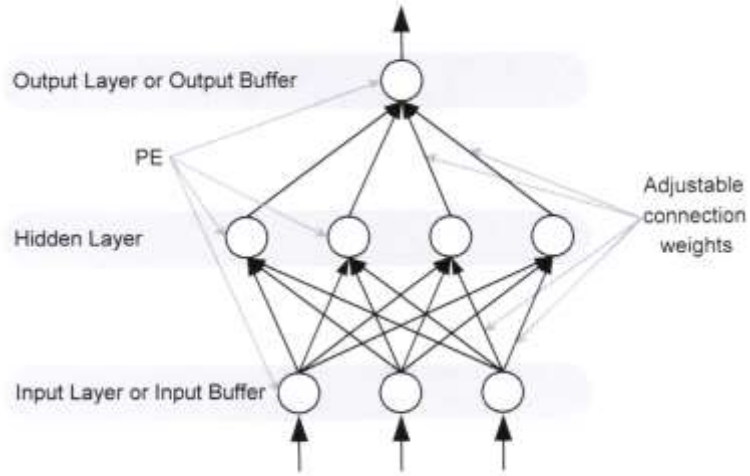

Figure 2. Schematic Representation of MLP

2. ANN Model Development Methodology

A set of 450 rectangular and square reinforced concrete slabs analysis data for training of an ANN model was created by manually performing virtual work method of analysis. In addition, another set of 54 slabs data was created manually in order to validate the trained ANN model. Using several sets of slab thickness, concrete strength (f_c'), reinforcing steel yield strength (f_y), rebar size and spacing were

considered to calculate various sets of moment strength per unit width of slab (Figure 3).

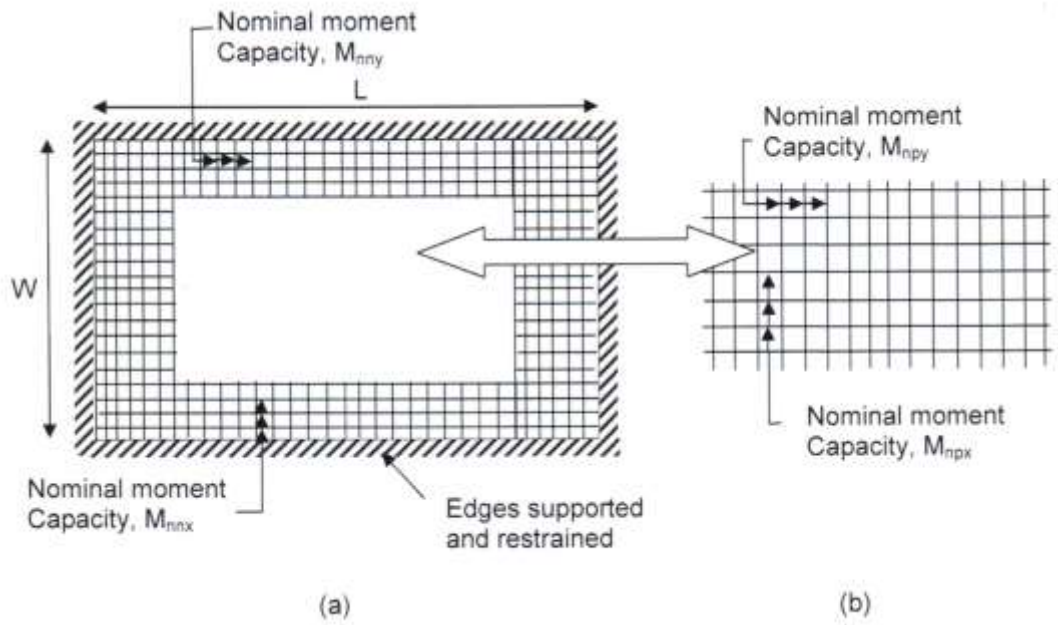

Figure 3. (a) Top reinforcement, Negative Nominal Moment Capacities, M_{nnx}, M_{nny}; (b) Bottom reinforcement, Positive Nominal Moment Capacities, M_{npx}, M_{npy}

Depending on the aspect ratio of the rectangular panel and moment strengths, there are three possible yield line patterns can be formed (Figure 4). For a given set of data, slab length (L), width (W), thickness (h), nominal moment strengths (M_{npx}, M_{nnx}, M_{npy}, M_{nny}), and by iteratively changing the value of γ ($0<\gamma\leq0.5$) or solving for γ by means of differential calculus the failure load (q_f) was calculated by equating the external and internal work done. The value of factored load, q_u was calculated by multiplying qf with reduction factor, ϕ (where ϕ =0.9). The training data included six inputs – L, W, M_{npx}, M_{npy}, M_{nnx}, and M_{nny}, one output – q_u.

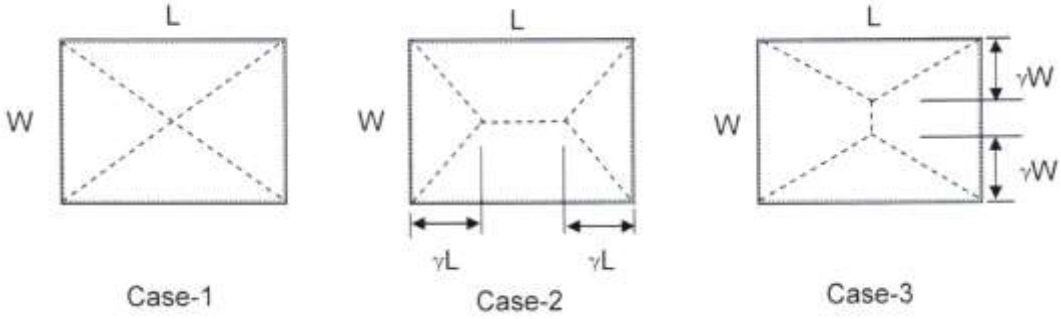

Figure 4. Three possible yield line patterns

The ANN model was developed with NeuroShell-2 software using a multilayer perceptron (MLP) back-propagation (BP) architecture [9]. The Ward network

architecture is shown in Figure 5. A total of five layers of neurons with one input layer, three hidden layers, and one output layer were used. Different activation functions were applied to hidden layer slabs that led to a better prediction. Activation functions - Logistic, Gaussian, symmetric-logistic, Gaussian-complement, and Logistic were used in Slabs 1 through 5 respectively. The hidden neurons: 6, 8, 8, 8, 1 were used in Slabs 1 through 5 respectively. For the BP training criteria, "Rotation" was used for pattern selection, which selects training patterns in the order they appear in the input file, and "TurboProp" was selected for weight updates. "TurboProp" is simpler to use than the other methods because the user does not have to set learning rate and momentum. The training criteria also included fixing the maximum and minimum absolute errors, minimum average error, and the number of learning epochs since minimum average error. When the given training criteria were met, training of the model was stopped.

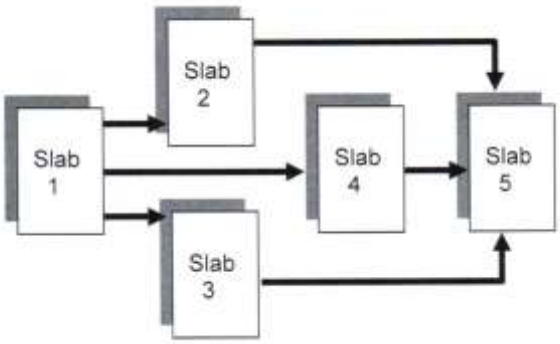

Figure 5. Architecture of MLP BP Ward Neural Networks [9]

3. Results and Discussion

The training data set of 450 reinforced concrete slabs was randomly divided into two sets: (1) 80% data for training the network, and (2) 20% data for testing the network during training, and continuously correct the training by adjusting the weights of the network links. Figure 6 demonstrates the scattered plot of ANN predicted q_u and calculated q_u during the training phase of the model. Another set of 54 reinforced concrete slab data was used for validate the trained model. This validation set data was not used during training. For validation, this set of data was presented to the trained model to predict the output. Figure 7 demonstrates the scattered plot of the predicted and calculated q_u values during validation phase. Both of these figures clearly demonstrate a very good agreement between the calculated values of q_u and ANN predicted q_u.

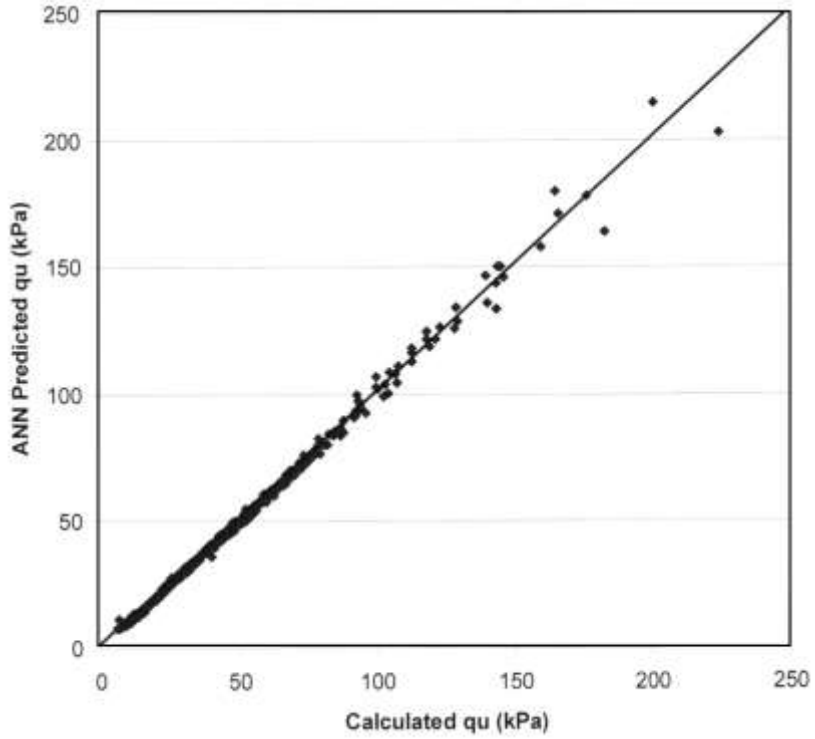

Figure 6. Scatter plot of ANN predicted vs. calculated q_u (kPa) – Training Phase

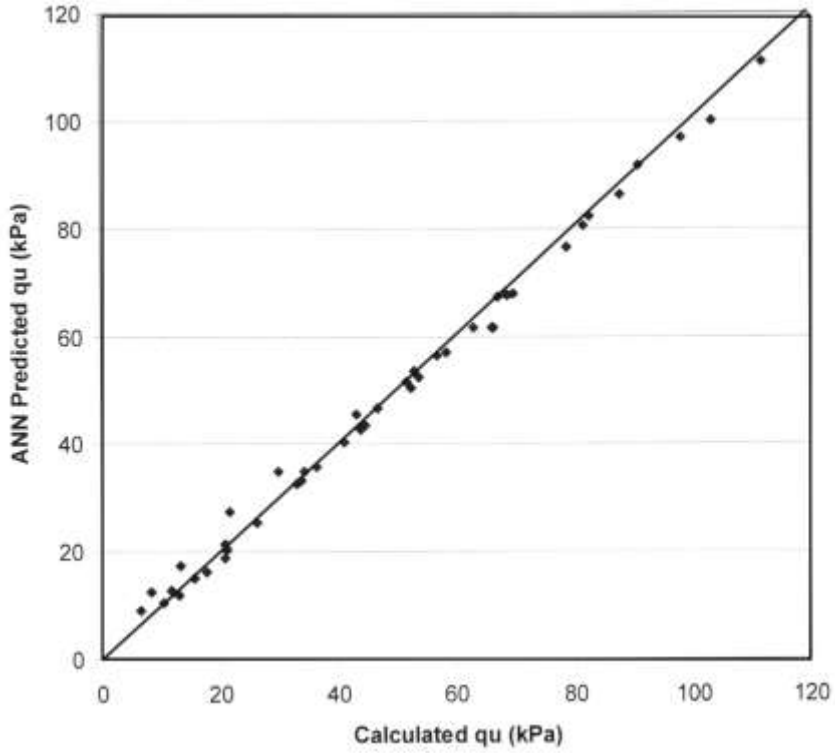

Figure 7. Scatter plot of ANN predicted vs. calculated q_u (kPa) - Trained model validation phase.

The neural network used for the presented model demonstrated an excellent statistical

performance as shown in Table 1 for the training model and the validation of the trained model. In Table 1, R squared is a statistical indicator usually applied to multiple regression analysis. It compares the accuracy of the model to the accuracy of a trivial benchmark model wherein the prediction is just the mean of all of the samples. A perfect fit would result in an R squared value of 1, a very good fit near 1, and a very poor fit near 0. The correlation coefficient, r is a statistical measure of the strength of the relationship between the actual vs. predicted outputs. The r coefficient can range from -1 to +1. It will show a stronger positive linear relationship when r is closer to +1, and a stronger negative linear relationship when r is closer to -1. Table 2 illustrates a set of rectangular slabs that are analyzed for failure loads using yield line theory, and compared with the ANN model predicted values. It shows that the ANN predicted values are in very good agreement with the calculated values.

Table 1. Network system performances

	Network training	Network validation
N	450	54
R squared	0.9961	0.9954
Correlation coefficient, r	0.9981	0.9983
Mean squared error (kPa)	0.096	0.0.096
Mean absolute error (kPa)	1.101	1.436

Table 2. Calculated and ANN Predicted q_u

L (m)	W (m)	M_{npx} (kN-m)	M_{nnx} (kN-m)	M_{npy} (kN-m)	M_{nny} (kN-m)	Calculated q_u (kPa)	Predicted q_u (kPa)	Difference (kPa)
6.10	6.10	16.27	27.12	16.27	27.12	82.74	82.24	0.50
6.10	6.10	10.85	13.56	10.85	13.56	46.54	46.67	-0.13
6.10	6.10	8.14	0.00	8.14	0.00	15.51	15.17	0.34
6.10	6.10	10.85	0.00	10.85	0.00	20.68	21.36	-0.68
6.10	4.88	18.98	27.12	18.98	27.12	111.90	110.87	1.03
6.10	4.88	16.27	21.70	18.98	27.12	103.47	100.03	3.44
7.63	6.10	16.27	21.70	18.98	27.12	66.22	61.47	4.74
7.63	6.10	4.07	4.41	2.71	2.71	10.34	10.48	-0.14
7.63	6.10	4.07	6.78	2.71	2.71	11.78	12.88	-1.10

4. Conclusions

It is demonstrated in this paper that the Artificial Neural Network (ANN) based trained model can be applied to determine failure loads for reinforced concrete slabs. An ANN model was developed with NeuroShell-2 software using a multilayer perceptron (MLP) back-propagation (BP) architecture. Several square/rectangular slabs with different edge support conditions, slab thickness, and slab reinforcements (positive and negative) were analyzed for failure loads using a virtual work method of yield-lines failure mechanism, and the analyzed data set was used to train the ANN model. The trained model was then validated using a new set of data that unused during training, and compared with the calculated values. The ANN model demonstrated an excellent statistical performance in the network training as well as in the validation of the trained network. The ANN predicted values were found to demonstrate very good agreement with the calculated values. The application of an ANN model in similar real-world applications will certainly minimize the need for extensive manual calculations.

5. References

[1] Johansen K W. Yield-Line Theory, Cement and Concrete Association, London, (1962).

[2] Wang C K, Salmon C G, Pincheira J A. Reinforced Concrete Design, 7th Ed., John Wiley & Sons, Inc., USA, 2007.

[3] Wight J K, MacGregor J G. Reinforced Concrete Mechanics & Design, 6th Ed., Pearson, New Jersey, USA, 2012

[4] Caudill M. Neural Network Primer: Part 1. AI Expert, Dec. (1987), 46-52.

[5] Haque M E. Reinforced Concrete Beam-Column Design: An Artificial Neural Network Approach, In: *Proc. of the American Concrete Institute* – 5th International Conference, ACI SP 209-41, (2002), 757-769.

[6] Haque M E, Mund A. An Artificial Neural Network Model for Construction Loads on Shores, Reshores and Slabs, In: *Proc. of the Fifth Alexandria International Conference on Structural and Geotechnical Engineering (AICSGE 5)*, Vol. II, pp. RC- 87-94, Alexandria, Egypt, December 2003.

[7] Rumelhart D E, McClelland J L. Parallel distribution processing: Explorations in the microstructure of cognition, Volume 1: Foundations. MIT Press. Cambridge, MA, USA, 1986.

[8] Basheer I A, Hajmeer M. Artificial neural networks: fundamentals, computing, design, and application. *J. Microbiol.Methods* 43: (2000), 3-31.

[9] Ward Systems Group Inc., NeuroShell 2 User's Manual, Ward Systems Group, Inc., Frederick, Maryland, USA (1996).

ACCMES 63

Factors Affect Strength of Repaired Pavement Using the Recycling Technique

Avirut Chinkulkijniwat and Suksun Horpibulsuk
School of Civil Engineering, Suranaree University of Technology,
111 University Avenue, Muang District, Nakhon-Ratchasima 30000, THAILAND

Abstract

The pavement recycling technique is a way to effectively repair damaged pavements. In this study, statistical analysis shows that the field strength is significantly lower than the laboratory strength. The mixing process used in the pavement recycling technique does not significantly affect the field strength reduction as indicated by the small variation of the field hand-compacted strength (q_{ufh}) and the laboratory strength (q_{ul}). The curing condition does significantly control the field strength development. A factor of safety of 2.0 is recommended for design.

1. INTRODUCTION

The pavement recycling technique is widely used in various countries, including Thailand, to restore damaged pavements. However, the field strength development is generally found to be lower than the laboratory strength (e.g., Horpibulsuk et al., 2004; Horpibulsuk et al., 2006; Horpibulsuk et al., 2011a). Understanding the mechanism that controls the field strength development is vital to improve the mixing process and field quality controls to obtain the strongest recycled pavement at a low construction cost. Also, this understanding helps determine the appropriate factor of safety, which is the ratio of the field strength to laboratory strength. The difference between laboratory and field strength is possibly due to the non-uniformity in mixing in-situ soil with cement and differences in the compaction method and curing condition (Horpibulsuk et al., 2006). The objective of this paper is to statistically analyze the field strength data to understand the mechanism controlling the field strength development and thus suggest the best practice for pavement recycling in Thailand. This study is fundamental, and the results could possibly be applied in other tropical countries.

By default, a significance level (p-value) of 0.05 was used throughout this study. If the significance level in the test output is less than 0.05, the assumption of equality of the two strength data sets (null hypothesis) is not valid with a probability of 95%. However, if the significance level is greater than 0.05, then with a probability of 95%, the two strength data sets are similar.

2. MATERIALS AND METHODS

2.1 Laboratory Investigation

Two different soils, which represent typical coarse-grained materials often used in earth work, were used in this laboratory study: lateritic soil and crushed rock. The lateritic soil was taken from a borrow pit in the Nakhon-Ratchasima Province, Thailand. The lateritic soil was composed of 28.5% fine-grained particles and 71.5% coarse-grained particles and was non-plastic with a liquid limit of 22.5%. The crushed rock was taken from a quarry in the Phetchabun Province, Thailand. The crushed rock was composed of 91% coarse-grained particles and the rest were fine-grained particles. Based on the Unified Soil Classification System, the lateritic soil and crushed rock were classified as silty sand (SM) and well-graded silty gravel (GW-GM), respectively. Several basic properties of these soils are presented in Table 1.

Table1. Basic properties of soils used for establishing and verifying the model

Soil	LL	PI	Group Symbol	Source
Soils used for establishing the model				
Lateritic soil	22.5	NP	SM	Horpibusuk et al. (2006)
Crushed rock			GW-GM	Horpibusuk et al. (2006)
Soils used for verifying the model				
Lateritic soil	36	20	GC	Ruenkrairergsa and Charatkorn (2001)
Lateritic soil	NP	NP	SW-SM	Sirilertwattana (2006)
Lateritic soil	21.5	6.8	GW-GM	Sirilertwattana (2006)

Both soils were passed through a 19-mm sieve to remove coarser particles. The water content of the soils was adjusted to 0.6, 0.8, 1.0, 1.2 and 1.4 times the OWC. The soils at their respective water contents were thoroughly mixed with Type I Portland cement at cement contents varying from 1 to 7%. The soil cement mixture was compacted according to ASTM D696-91 in a standard 100-mm diameter mold under four compaction energy levels (296.3, 592.5, 1346.6 and 2693.3 kJ/m^3). After 24 hours, the samples were dismantled, wrapped in vinyl bags and stored in a humidity chamber at a constant temperature (25±2^{o}C). Unconfined compression tests

were run after the samples cured for 7, 14, 28, 60 and 120 days. For each curing time and each combination of water content and cement content, at least 3 samples were tested under the same condition to check for consistency. The strength of these samples will be referred to as the laboratory strength (q_{ul}).

2.2 Field Investigation

The field strength data of the stabilized pavement materials were gathered from 4 roadway sites (3 sites in the Phetchabun Province and 1 site in the Utaradit Province) using the pavement recycling technique. The input cement for each site was obtained from trial modified Proctor tests at the OWC to attain 7-day strengths of 2750 kPa for Phetchabun 1, Phetchabun 3 and Utaradit, and 3500 kPa for Phetchabun 2. Damaged pavement at a thickness of approximately 20 cm was dug up and mixed with the cement and water by the recycling machine. At each station, which were 150 meters apart, the soil-cement mixture was collected from the machine and manually compacted in the laboratory. These samples are herein referred to as the *"field hand-compacted samples"*.

Immediately after mixing, the soil-cement mixture was field compacted by a vibratory roller, going back and forth for 3 passes and followed by a pneumatic roller for 5 passes and a smooth wheel roller for 3 passes. The frequency of the vibratory roller was 1500 cycles per minute. The pneumatic roller consisted of 6 rubber tires with a contact pressure under the tires of approximately 600 kPa. The smooth wheel roller used 2 smooth metal rollers with a ground contact pressure of approximately 350 kPa. This field compaction results in a ratio of the dry unit weight ($\gamma_{dfr} / \gamma_{dfh}$) at each station greater than 95%, where γ_{dfr} is the dry unit weight of the field-mixed and roller-compacted samples, which was obtained from a sand cone test within 1 hour after field compaction. The γ_{dfh} is the dry unit weight of the field hand-compacted sample at each station. A high $\gamma_{dfr} / \gamma_{dfh}$ value indicates high field quality controls. For each station, the field-mixed and roller-compacted samples were taken by a coring cutter from the improved pavement after 7, 14 and 28 days of curing to conduct the unconfined compression test. These samples were trimmed to a diameter to height ratio of 1.0, matching those prepared in the laboratory. These samples are herein referred to as the *"field roller-compacted samples"*. Because the samples are hard, carefully cored and trimmed, the effect of the sample disturbance on the strength can be neglected.

3. ANALYSIS OF THE FIELD STRENGTH DEVELOPMENT

The unconfined compressive strengths from the three different cement-stabilized sample sets, the field hand-compacted strength (q_{ufh}), the field roller-compacted strength (q_{ufr}) and the laboratory strength (q_{ul}) were statistically analyzed to evaluate the mechanism influencing the field strength development. The SPSS software was used for this objective. The variation of these three strengths at the different test sites is illustrated in Fig. 1. By setting q_{ul} as a reference, the difference between q_{ufh} and q_{ul} is likely attributed to the non-uniformity in the mixing cement with the dug pavement materials in the mixing machine, whereas the difference between q_{ufr} and q_{ufh} is due to the differences in the compaction and curing methods. The dashed line represents the laboratory design strength (q_{ul}).

A t-test was performed to compare the mean values of q_{ufh} and q_{ufr} (Table 2). The results indicate that the variances between q_{ufh} and q_{ufr} are homogeneous at a significance level of 0.123 based on Levene's test. Thus, a t-value with equal variance was used. A significance level of 0.000 was found for the 2-tailed test, which indicates that the strength of the field hand-compacted samples (mean value = 2872.43 kPa) had a significantly higher strength than that of the field roller-compacted samples (mean value = 2243.22 kPa).

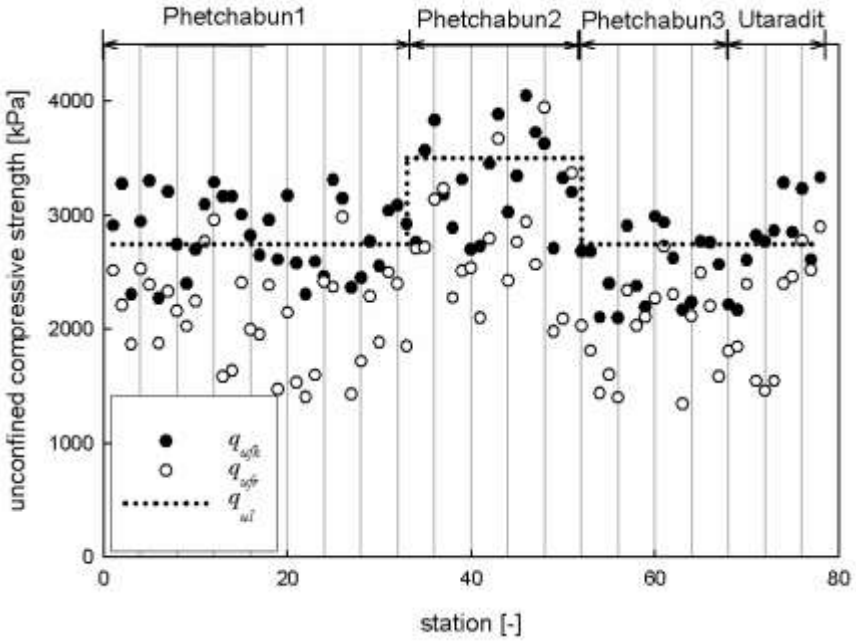

Fig.1. Field roller-compacted and field hand-compacted strength after 7 days of curing

Table2. Independent samples test to compare means of the q_{ufh} and q_{ufr}

	Levene's test for equality of variances		t-test for equality of means				
	F	Sig.	t	df	Sig. (2 tailed)	Mean difference	Std. error difference
Equal variances assumed	2.404	.123	7.952	154	.000	629.212	79.122
Equal variances not assumed			7.925	147.437	.000	629.212	79.122

The variation of q_{ufh} compared with q_{ul} for each site was studied. The t-test result (Table 3) shows that the significance (2-tailed) levels are greater than 0.05 at most of the sites, i.e., Phetchabun 1, Phetchabun 2 and Utaradit, which indicates the equality between q_{ul} and q_{ufh} at most of the sites. Only one site from the four studied sites showed that q_{ul} and q_{ufh} were not equal at a probability of 95%.

It is a well-known fact that mixing results in relative movement among the components in the mixture and thereby affects the strength and deformation properties of the stabilized soil (e.g., Hayashi and Nishikawa, 1999; Larsson et al., 1999). From the equality between q_{ul} and q_{ufh}, it can be concluded that the in-situ mixing by the machine is generally uniform and acceptable. Therefore, it can be assumed that the mixing process does not significantly affect the field strength reduction when the pavement recycling technique is used. This conclusion contradicts the results in the case of deep-mixed columns (Horpibulsuk et al., 2004; Horpibulsuk et al., 2011b, Larsson et al., 2005) In fact, uniformity of deep mixing is rarely achieved due to the viscosity of the clay and the very high in-situ effective overburden stress. The flow ability of the cement admixed coarse-grained soil is much higher than that of fine-grained soil. Therefore, the shallow stabilization of the coarse-grained soil is more uniform.

Table 3. Equality test between q_{ul} and q_{ufh} at each studied site

Sites	N	Mean	Std. deviation	Test value (q_{ul})	t	df	Sig. (2-tailed)

		(q_{ufh})					
Phetchabun1	33	3834.170	332.629	2750	1.454	32	0.156
Phetchabun2	18	3294.484	431.120	3500	-2.023	17	0.059
Phetchabun3	19	2498.558	310.580	2750	-3.634	18	0.002
Utaradit	8	2968.750	270.420	2750	2.288	7	0.056

The large difference between q_{ufh} and q_{ufr} (Table 3) indicates that the compaction and curing conditions greatly affects the field strength development. In terms of the compaction condition, the compaction method and the compaction effort might affect the field strength. However, the compaction was performed by vibratory and pneumatic rollers, which is a widely used method for highway and pavement works. These rollers are known to be effective in compacting granular material and are generally used in field compaction processes. Moreover, the compaction was well controlled as indicated by the very high relative densities, over 95%. Hence, the compaction condition should not be a concern. Thus, the curing condition is the only major factor that should be taken into account.

Field curing is performed by spraying water on the recycled pavement a couple of times a day without covering the remedied pavement with saturated cover material, such as burlap or rugs, or adding a curing compound. Unless the concrete were to attain a greater field strength, this practice seems inadequate, particularly in a hot country such as Thailand.

To determine the influence of the curing method, the difference between the laboratory and field strengths was investigated using q_{ufr} to q_{ul} ratios. The distribution of the strength ratios at the test sites is illustrated in Fig. 2. The descriptive statistics for q_{ufr}/q_{ul} ratios are presented in Table 4. The 95th percentile was 1.05, indicating that the magnitude of q_{ufr} was less than the magnitude of q_{ul} for most of the populations. The 5th percentile was 0.52, meaning that 95% of the population had a magnitude of q_{ufr} greater than $0.52q_{ul}$; in other words, the field strength was almost half the laboratory strength.

In the mix design process, many laboratory trial mixes are performed to acquire the laboratory strength so that the field strength reduction can be compensated. For the current practice in Thailand, a safety factor of 2.0 is suggested. In addition, it is recommended to cure

4. CONCLUSIONS

The laboratory and field strength development of cement-stabilized coarse-grained soils when the pavement recycling technique is used was statistically analyzed. The field strength was significantly lower than the laboratory strength. A ratio between the field and laboratory strengths was normally distributed. The field strength reduction was mainly caused by the insignificant amount of curing water due to the hot weather in Thailand. With this curing condition, the 5th percentile of the field to laboratory strength ratio was 0.52. Hence, it is logical to assign a factor of safety of 2.0 when determining the input of cement.

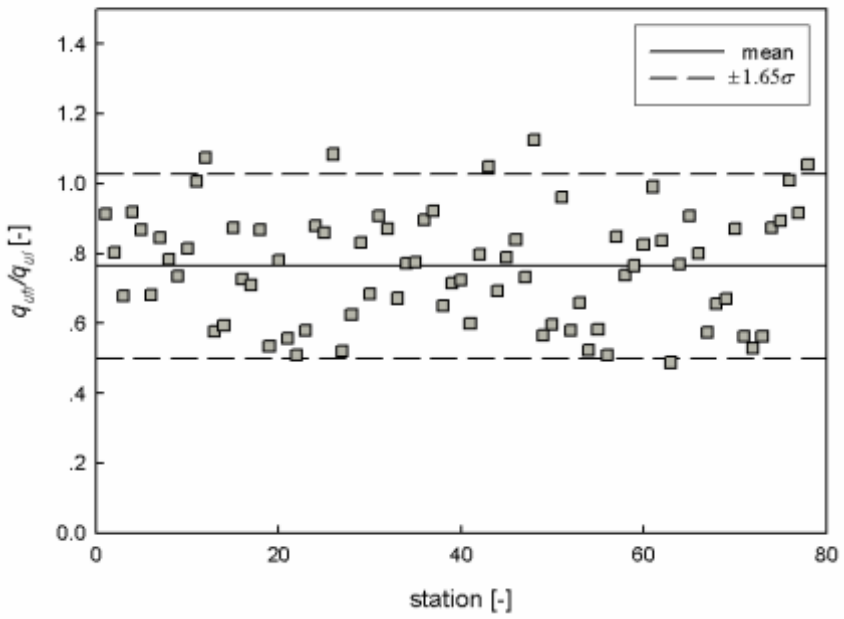

Fig.2. Distribution of the strength ratio, q_{ufr} / q_{ul}

Table 4. Descriptive statistics for q_{ufr} / q_{ul}

Statistics	Values
N	78
Mean	.7640
Std. Deviation	.1599
Kolmogorov-Smirnov Z	.805
Asymp. Sig. (2-tailed)	.536
5th Percentile	0.5194
95th percentile	1.0547

5. acknowledgement

The authors would like to acknowledge the financial support and facilities provided by the Suranaree University of Technology.

6. REFERENCES

[1] ASTM D698-91, 1995: Test method for laboratory compaction characteristics of soil using standard effort [12400 ft-lb/in3 (600 kN-m/m3]. Annual Books of ASTM Standards, ASTM International, West Conshohcken, PA., pp. 69-76

[2] Consoli, N.C., Foppa, D.,o, L. and Heineck, K.S. (2007). Key parameters for strength control of artificially cemented soils, Journal of Geotechnical and Geoenvironmental engineering, Vol. 133, No. 2, pp. 197-205.

[3] Consoli, N.C., Rosa, D.A., Cruz, R.C. and Rosa, A.D. (2011). Water content, porosity and cement content as parameters controlling strength of artificially cemented silty soil, Engineering Geology, Vol. 122, pp. 328-333.

[4] Hayashi, H. and Nishikawa, J. (1999). Mixing efficiency of dry jet mixing method applied to peaty soft ground. Proc. Int. Conf. on Dry Mix Methods for Deep Stabilization. Stockholm, pp. 333-338.

[5] Horpibulsuk, S. and Miura, N. (2001). A new approach for studying behavior of cement stabilized clays, Proc. 15th ICSMGE, Istanbul, Turkey, Vol. 3, pp. 1759-1762

[6] Horpibulsuk, S., Miura, N. and Nagaraj, T.S. (2003). Assessment of strength development in cement-admixed high water content clays with Abrams' law as a basic, Geotechnique, Vol. 53, No. 4, pp. 439-444

[7] Horpibulsuk, S., Bergado, D.T. and Lorenzo, G.A. (2004a). Compressibility of cement admixed clays at high water content, Geotechnique, Vol. 54, No. 2, pp. 151-154

[8] Horpibulsuk, S., Miura, N., Kago, H. and Nagaraj, T.S. (2004b). Analysis of strength development in in-situ cement admixed columnar inclusion – A field study, Ground Improvement, Vol.8, No.2, pp. 59-68

[9] Horpibulsuk, S., Miura, N. and Nagaraj, T.S. (2005). Clay-water/cement ratio identify of cement admixed soft clay, J. Geotech. Geoenviron. Engrg., ASCE, Vol. 13, No. 2, pp. 187-192

[10] Horpibulsuk, S., Katkan, W., Sirilerdwattana, W. and Rachan, R., (2006). Strength development in cement stabilized low plasticity and coarse grained soils: Laboratory and field study. Soils and Foundations, Vol. 46, No. 3. pp. 351-366

[11] Horpibulsuk, S., Rachan, R., and Suddeepong, A. (2011a), Assessment of strength development in blended cement admixed Bangkok clay, Construction and Building Materials, Vol.25, No.4, pp.1521-1531.

[12] Horpibulsuk, S., Phochan, W., Sudeepong, A., Chinkulkijniwat, A. and Liu, M.D. (2011b), Strength development in blended cement admixed saline clay, Applied Clay Science, doi:10.1016/j.clay.2011.10.003.

[13] Horpibulsuk, S., Rachan, R., Suddeepong, A., and Chinkulkijniwat, A. (2011c), Strength development in cement admixed Bangkok clay: laboratory and field investigations, Soils and Foundations, Vol.51, No.2.

[14] Larsson, S., Rehnman, S-E. and Walter, M. (1999). Laboratory method for design and development of the dry jet mixing method. Proc. of the 12th ECSMGE, Amsterdam, Vol. 3, pp. 1533-1538.

[15] Larsson, S., Dahlstrom, M. and Nilsson, B. (2005). Uniformity of lime-cement columns for deep mixing: A field study. Ground Improvement, Vol. 9, No. 1, pp. 1-15

[16] Miura, N., Horpibulsuk, S. and Nagaraj, T.S. (2001). Engineering behavior of cement stabilized clay at high water content, Soils and Foundations, Vol. 41, No. 5, pp. 33-45

[17] Ruenkrairergsa, T. and Charatkorn, S. (2001). Compressive strength of soil-cement under different density, Report of Research and Development Center, epartment of Highway, Thailand.

[18] Sirilertwattana, W. (2006). Factors influencing compressive strength of repaired roads by recycling technique of pavement materials, Master Thesis, Suranaree University of Technology, Nakhon-Ratchasima, Thailand.

ACCMES 96

Numerical analysis to better understand the failure mechanism and reinforcements on the tunnel face of an Earth Pressure Balance shield - *A case study of Mashhad metro line 2*

Saba Gharedashi
Department of Mining and Metallurgical Engineering, Amirkabir University of Technology, Tehran, Iran.
milisaba.46@gmail.com

Milad Barzegar
Department of Mining and Metallurgical Engineering, Amirkabir University of Technology, Tehran, Iran.
milad.b1984@gmail.com

The corresponding author: Saba Gharedashi

Abstract
In order to understand the mechanism of the effects of varying face support pressures on tunnel stability, numerical simulations are conducted using the three-dimensional numerical modeling for the Mashhad metro line 2 project. Measurements were performed in the earth pressure balance TBM. Vertical pressure gradients were measured when the tunnel face encountered with global failure in collapse and blow-out. The loads acting on the tunnel face were estimated according to the active and passive earth pressure principles. It is found that the use of varying face support pressure causes the size of the disturbed zone in proximity to the face is affected. Detailed discussions are given considering tunnel face displacements (extrusion).
Keyword: Earth pressure balance (EPB) shield, numerical modeling, finite difference method (FDM), Mashhad metro, Face extrusion

1. Introduction

High portion of soil deformation and surface settlement during the tunnel excavation process can be associated with the inward movement of the tunnel face. If the geological conditions are unfavourable in tunneling, such as soft or granular soil, an additional means for the tunnel face support has to be employed. This can be achieved by applying the supporting pressure to the tunnel face by pressurized slurry or compressed air. After this, a series of papers dealing with the tunnel stability, tunnel face stability and the failure mechanism of the face could be found in various journals (for example [1]). Several authors have tried to model the effect of shield using a

numerical modeling tools [2,3]. Some machines show low flexibility as to geometry shape and curvatures in the tunnel line. The main purpose of the research program presented in this paper was to investigate the stability of the tunnel face supported by the earth pressure balance TBM, to determine the supporting pressure at the collapse and blow-out to observe the failure mechanism and to identify the critical zone ahead of the tunnel face. The objective was achieved by numerical modeling. The earth pressure of working face is classified into two kinds of types. The first class is active earth pressure, which is from the active action of earth pressure to the shield structure if the thrust force of shield is less than composite force of active earth pressure. The second class is passive earth pressure, which is from the active action of shield structure to the earth mass in front of working face if the thrust force of shield is greater than composite force of active earth pressure. To investigate the behavior of the Mashhad metro tunnel face subjected to support pressures (ranging from 10% to 200% of lateral earth pressure, $\frac{\sigma_x}{\sigma_y}$) a numerical study was carried out to examine the effect of face support pressure on the size of the disturbed zone in proximity to the face.

2. Mashhad metro project

Excavation of a long tunnel is a major component of Mashhad metro project. The excavation of the tunnels is to be performed by an earth pressure balance shield machine with an outside diameter of 9.15 m. The shallowest ground section is a cover-to-depth ratio (C/D) of 1.17, where C and D are the cover depth and diameter of the tunnel. Because of the unfavorable geological conditions and the dimension of the excavating face, the face stability of the tunnel is one of the key technical aspects in this project. For the detailed design of the tunnel, a comprehensive geotechnical investigation was completed, which consisted of undisturbed sampling, cone penetration tests, standard penetration tests and pressuremeter tests. According to the site investigation results, Mashhad soils can be differentiated into a number of well-defined strata based on physical properties and soil types, as illustrated in Table 1.

Table 1. Physical and Mechanical Properties of the Tunnel Host Media

Layer	Soil type	K_o	E	ν	φ	C	γ_{bulk}
		-	MPa	-	degree	KPa	KN/m^2
I	SC-SM	0.43	80	0.3	35	0	19.6
II	GC-GM	0.36	100	0.28	40	11	19.8
III	CL-ML	0.61	30	0.34	20	25	18.2

3. Numerical modelling of face stability

In order to demonstrate the fundamental three-dimensional aspect of the problem a comprehensive numerical study was conducted employing the FLAC3D code [4].

The soil layers are assumed to be an elastoplastic material conforming to the Mohr-Coulomb failure criteria. It is assumed the tunnel is driven by means of an earth pressure balance TBM in soft soil. Figure 1 shows the different components of the constructed numerical model. Neglecting the deformations of the shield skin, the TBM was modelled as a rigid contact body. The length of the shield was assumed to be 10 m with regard to the TBM specifications. The step-by-step excavation process was modelled by repeated rezoning of the element mesh at the cutting face and repeated insertion of elements representing the tunnel lining and the tail void grout, respectively. Furthermore, the boundary conditions for the face support and the grouting pressure were adjusted according to the progress of the simulated tunnel advance. The elements of the grout are directly connected to the elements of the tunnel lining on the inner side and the soil on the outer side. The concrete lining was ,therefore, modelled in a simplified way as a continuous, isotropic, elastic tube. Grouting pressure distribution is complicated. The grouting pressure was modelled by pore pressure boundary conditions on the grout element nodes at the shield tail according to the assumed grouting pressure with a variation of 15 KN/m2/m over the height. In table 2 the vertical soil pressures at the largest and shallowest depths are presented. This in order to get an idea of the pressures needed to inject the annular void during excavation. In this paper, P_{in} denotes grouting pressure. Table 3 shows the mechanical properties of encountered materials used in the model.

Table 2. Boundary Pressures for Grout Injection

Tunnel	***Top***
	Bottom
Depth (m)	**+ 1022**
	+ 1013
σ_v (kN/m2)	**± 149**
	± 318
Grout pressure (bar)	**3.5**
	5.2

Table 3. Material Models and Parameters Used

Type	**Constitutive model**	**Thickness**	**E**	**ν**	**φ**	**C**	**ρ_{bulk}**
		cm	**MPa**	**-**	**degree**	**KPa**	**Kg/m^3**
Shield	elastic	10	210000	0.17	-	-	7850
grout	Mohr-coulomb	12	40	0.25	35	600	1500
lining	elastic	35	30000	0.2	-	-	2600

Fig. 1. a) 3-D Finite Difference Mesh, b) Representation of the Different Shield Tunneling Components in the Model

(a)

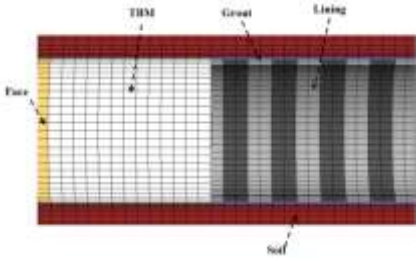

(b)

3.1. Simulation result

The focus of the analysis was on the face failure mechanism ahead of the TBM. The freshly excavated soil pressure acting on the tunnel face was considered as a linearly distributed pressure, which increases with depth according to the density of the conditioned muck in the excavation chamber. The initial conditioned muck pressure at the level of the center of the tunnel face is equal to the earth pressure at rest. The conditioned muck pressure will be increased (or decreased) in every construction phase, until blow-out (or collapse) occurs. The support pressure acting at the tunnel face can be seen as a combination of an absolute pressure and the vertical pressure gradient. The paper deals with the pressure gradients measured, the possible failure mechanism that determine the size of the disturbed zone in proximity to the face found. The failure criterion is defined as follows: the construction phase is considered as the beginning of failure, where for the first time considerable value of unbalanced force (not equal to 0) is observed, as shown in Figure 2.

Fig.2. The Failure Criterion of Numerical Modeling

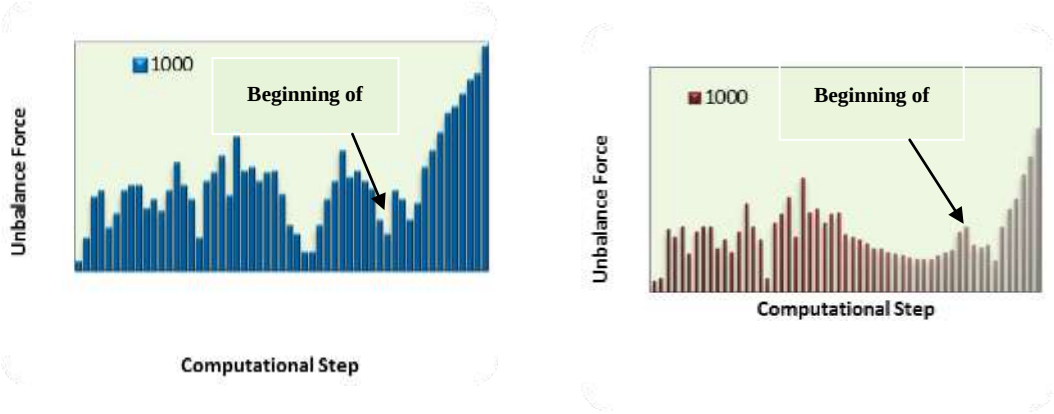

Figure 3 shows the pressure measurement inside the tunnel for the actual face pressures are lower than the free field horizontal stresses. There was a sudden drop in the measured pressure as the construction phase i, was initiated. This is attributed to a very small deformation of the ground around the tunnel face at the early stage of the unloading. The ground deformation, due to the high stiffness at very small strain level, did not compensate for the volume lose caused by the excavation being driven from the tunnel. The moment of the collapse is also indicated in Figure 3. There is a sudden increase in the tunnel face displacements (extrusion), which can be clearly identified. The collapse pressure ranged from 50 to 75 kPa measured at the center of the tunnel.

Figure 3. Numerical Measurements at the Moment of the Collapse

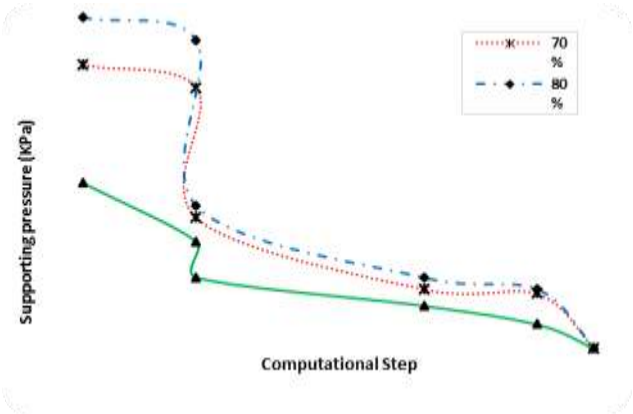

The following measurements where performed at the tunnel face. The total pressure was measured at the tunnel face at 9 locations, see Figure 4.

Figure 4. Position of Different Points at the Tunnel Face

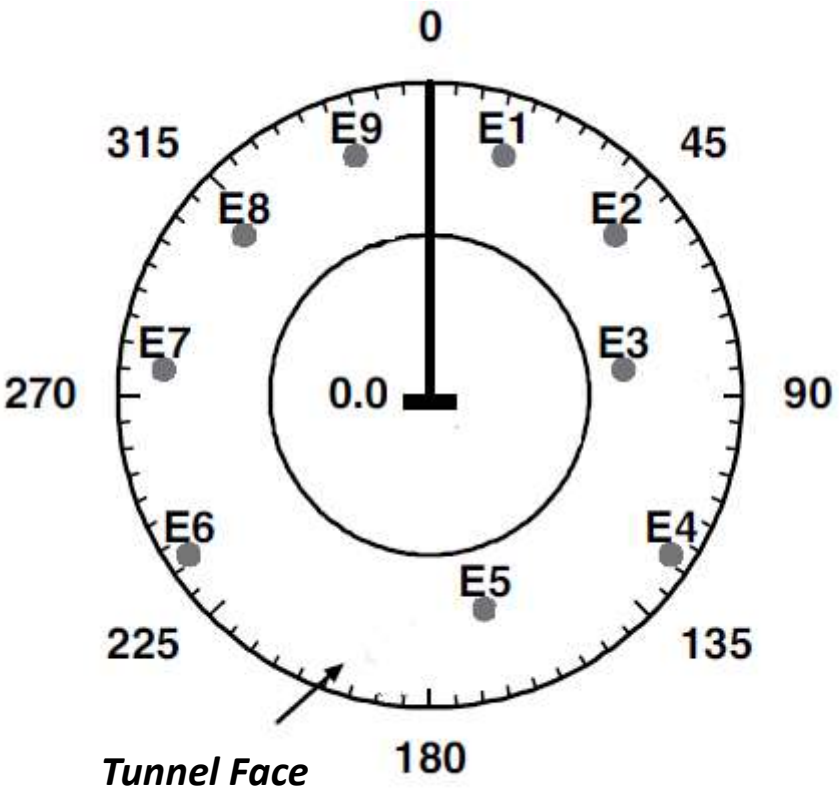

The vertical pressure gradients determined from these varying face support pressures are shown in Figure 5. It shows that the gradient can be high during excavation when the actual face pressure is more than the free field horizontal stresses but decreases when the actual face pressure is lower than the free field horizontal stresses. The values measured for the vertical gradient at varying face support pressure can be put in perspective realizing that the gradient of the total vertical pressure in the not yet excavated soil approximately 13kPa/m. The measurements showed that the measured gradients can higher than 15kPa/m, but also lower than 10kPa/m. Unlike in the active state ($\sigma_T/\sigma_y = 60\%$), the face support pressure decreases during the failure of the ground (Figure 5b). But the varying vertical gradient in the both of the passive and active state is similar (Figure 5c). The measurements showed that the measured gradients can higher than 15kPa/m, but also lower than 10kPa/m.

Figure 5. (a) Pressures measured at the tunnel face in the passive state $\sigma_T/\sigma_y = 200\%$, (b) Pressures measured at the tunnel face in the active state $\sigma_T/\sigma_y = 60\%$, (c) and the gradient determined from the pressure measured at the tunnel face in the passive and active state . All readings (E1-E9) are used to calculate the gradient

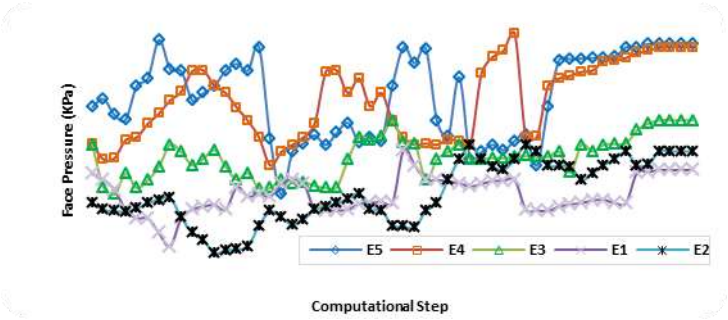

(a)

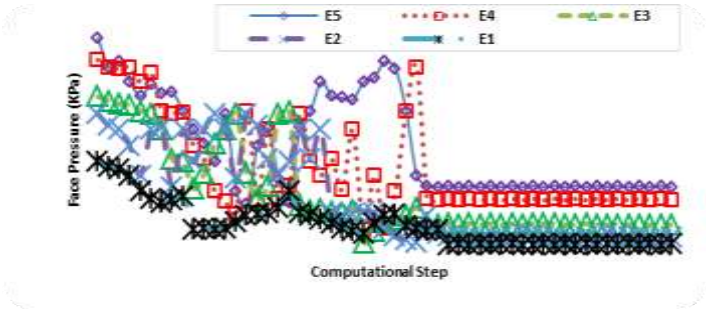

(b)

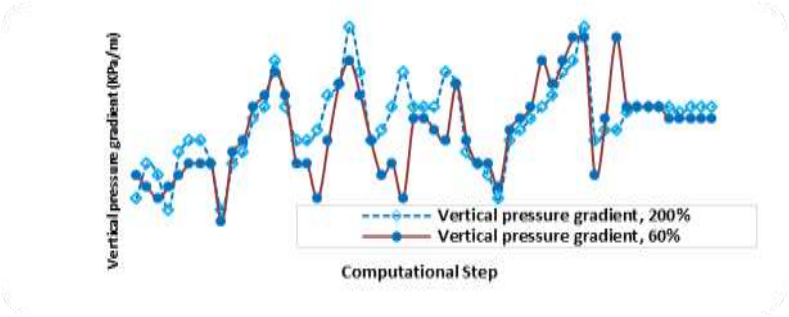

(c)

3.2. Tunnel face extrusion

Lunardi [5] has shown that the deformations of the tunnel face can be a useful indicator to evaluate the ground response. In Lunardi's approach, deformations associated with the tunnel excavation are classified as: (1) pre-convergence, (2) face extrusion and (3) radial convergence. Figure 6 shows developing extrusion for varying face support pressure, which were then to become widespread in tunneling as an accompaniment to more traditional convergence measurements. 15m long into the face with measurement points fitted at 1metre intervals. The results of the extrusion measurements taken, significantly increased our theoretical knowledge of the stress-strain behavior of a tunnel at the face and confirmed the effectiveness of the face support pressure in controlling deformation behaviour. As shown in Figure 6 the use of varying face support pressure causes the different size of the disturbed zone in proximity to the face is affected. In the both of the passive and active state the size of the disturbed zone in proximity to the face increases, but it is more significant for the active state, see Figure 6b. For passive state 15m long size of the disturbed zone and

active state 20m measured (see horizontal axis Figure 6a,b).

Figure 6. (a). Extrusions Along Horizontal Distance from Tunnel Face for Different Face Pressure

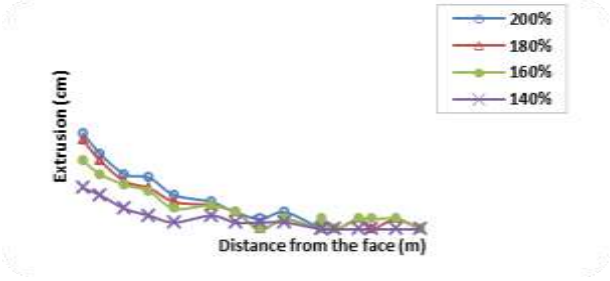

(a)

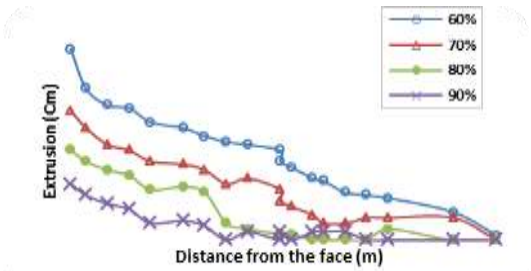

(b)

Figure 7 shows the extrusion measurements at a distance from the face. The figure illustrates that there is a plastic zone surrounded by an elastic zone (also known as confined yield zone). As the face support pressure decreases, the confined yield zone extends from the tunnel face to the surrounding soil mass. It shows good agreement with the fact that the largest plastic strains (passive and active state), and hence the largest displacements (extrusions), develop around the tunnel face.

Figure 7. Face Extrusion for Different Face Support Pressure

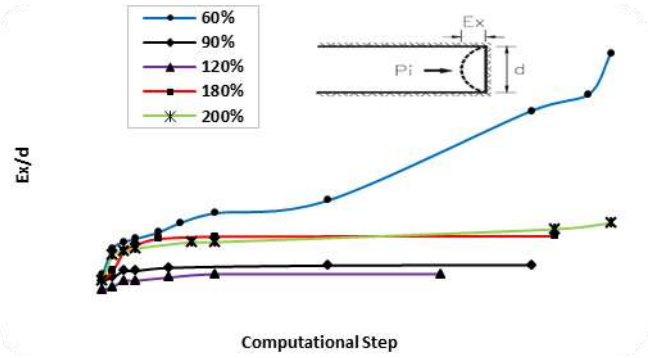

3. Conclusion

The obtained results from the conducted analyses demonstrate the complexity of the various interactions involved in shield tunneling.

- The zone affected by the collapse was found to be between 1.5D ahead the tunnel face and 2D in the passive state.
- It appears that the uniformly disturbed pressure acting on the tunnel face is a very efficient stabilizing tool. However, in the event of a sudden lost of

supporting pressure, the collapse will occur suddenly without any warning, affecting a relatively large zone immediately after the commencement of the ground movement at the face.

- The vertical pressure gradient isn't to a certain extend influenced by the different face support pressure.
- The vertical pressure gradient can be lower or higher for a EPB than for a slurry shield.

5. References:

[1] Leca E, Dormieux L. Upper and lower bound solutions for the face stability of shallow circular tunnels in frictional material. Geotechnique, 1990, 40(4): 581-606.

[2] Guglielmetti V, Grasso P, Mahtab A, Xu S. Mechanized tunnelling in urban areas-design methodology and construction control. Taylor and Francis, 2008: 507–515.

[3] Xu Y, Sun D, Sun J, Fu D, Dong P. Soil disturbance of Shanghai silty clay during EPB tunnelling. Tunn Undergr Space Technol, 2003, 18(2003):537–545.

[4] Itasca Consulting Group. Inc. FLAC3D Manual, third ed, 2006, (FLAC3D Version 3.1).

[5] Lunardi P. Design and construction of tunnels using the approach based on the analysis of controlled deformation in rocks and soils. in : davis, j (trans), springer pubpp, 2008: 8-22.

ACCMES 109

Simulations of Control Characteristics of Tuned Liquid Column Damper Using an Elliptical Flow Path Estimation Method

Passagorn Chaiviriyawong
Department of Civil Engineering, Faculty of Engineering, Prince of Songkla University, Songkhla, Thailand
cpassagorn@eng.psu.ac.th

Suchart Limkatanyu
Department of Civil Engineering, Faculty of Engineering, Prince of Songkla University, Songkhla, Thailand
Suchart.l@psu.ac.th

The corresponding author: Passagorn Chaiviriyawong

Abstract

The simulations of tuned liquid column damper (TLCD) and its variation known as liquid column vibration absorber (LCVA) are presented in this study. The numerical simulation carried out in this paper is based on the elliptical flow path estimation method. This newly proposed numerical model is capable of representing the vibration characteristics of the TLCDs and LCVAs with relatively large transition zone between the vertical columns and the cross-over duct. A series of tests on a shaking table are also conducted. Based on correlation studies between numerical and experimental results, it is shown that the proposed numerical model is able to emulate the experimental results. This feature is essential in the control problem for optimum performance of a tall building. Furthermore, the elliptical flow path estimation method can be utilized to investigate their efficiency as a vibration absorber.

Keyword: LCVA, TLCD, Shake table, Elliptical flow path estimation method, Natural frequency

ACCMES 148

Response analysis of strike-slip fault movement on buried pipeline

Md. Aftabur Rahman
Graduate student, Department of Civil and Environmental Engineering, Saitama University
Email: aftabur028@yahoo.com

Hisashi Taniyama
Faculty, Department of Civil and Environmental Engineering, Saitama University
Email: taniyama@mail.saitama-u.ac.jp

Corresponding author: Md. Aftabur Rahman

Abstract

A 3D distinct element method (DEM) and finite element method (FEM) analysis has been carried out to examine the response of buried pipeline accounting for fault displacement. Around 0.62 million spherical particles are used to create the model and DEM simulation has been performed for the stabilization of granular assemblies. Subsequently strike slip fault movement is applied to the model. Pipe is represented as three dimensional beam element and fixed boundary condition are applied at the anchored point of the pipeline. Dynamic behavior of pipes and particles has also been thought in the analysis. The deformation responses of the pipeline are analyzed in this paper. Force-displacement relationship between pipes and soil particles play an important role for the modeling and design of buried pipes. In this study, the relationship between force and displacement are well thought out. The interaction between soil particles and pipe elements are understandable from this numerical simulation. The effect of particle movement on pipe deformation responses are also studied and found that the particle shows greater effect near the fault crossing point. Finally a parametric study has been performed to understand the effect of different pipe properties for the same strike slip movement.

Keywords: Buried pipe, Soil-pipe interaction, Strike-slip, Force-displacement, Discrete element method.

1. Introduction

Pipeline systems, served as water supply and wastewater facilities, natural gas and liquid fuel lines, power and communication lines, generally play an important role in the daily life system. These pipelines are referred to lifeline systems as they are essential for the support of life and maintenance of property. Seismic behavior of buried pipeline is entirely different from the above ground structures. Surface faulting

has been a major cause of pipe damages during past earthquakes [1-2]. Damage of structures by seismic fault is attracting concern for many researchers in recent times [1].

Seismic response analysis of buried pipes is a complex phenomenon including three dimensional dynamic analysis of soil-structure system. A rigorous analysis satisfying all the conditions is almost impossible; hence different degrees of simplifications are made to obtain a good estimate of the response quantities of interest. Researchers have been presented different types of models and analytical techniques to obtain the response of buried pipelines owing to fault movement depending upon types of model and response quantities of interest [3-6]. However a number of researchers performed numerical study of buried pipe for different fault rupture and also done parametric study to fully understand the behavior of the pipe for fault slip using commercially available analytical tools [7-9]. Apart from the numerical simulation some large scale experimental investigations [1, 10-11] like centrifuge test and shaking table test has also been performed to identify the vulnerability parameters and failure criterion of pipes subjected to fault displacement.

Almost all the researches in buried pipes were carried out by using finite element method (FEM) in which pipe was considered either beam or shell element or soil surrounding the pipeline was modeled using non linear springs, which support the pipeline at discrete points. Conversely soil pipe interaction is the main concern in the field of buried structures. Apart from using simple spring system, distinct element method (DEM) is a powerful tool for representing the granular media and has been proved by many researchers [12-13]. This research study used DEM technique for the more rational analysis of granular materials and numerical simulation has been performed to obtain the response of pipelines subjected to strike slip fault. The behavior of force-displacement has also been described in detail in this research paper.

2. Numerical Modeling

An important tool in modeling the behavior of granular assemblies is the discrete element model (DEM), developed in 1970's by Cundall and Strack [14]. DEM simulations can be used to determine all kinds of properties of granular assemblies. Particles are connected to their adjacent particles using normal and shear springs and dashpots. The rheological elements of DEM are illustrated in Figure – 1(a).

(a) (b)

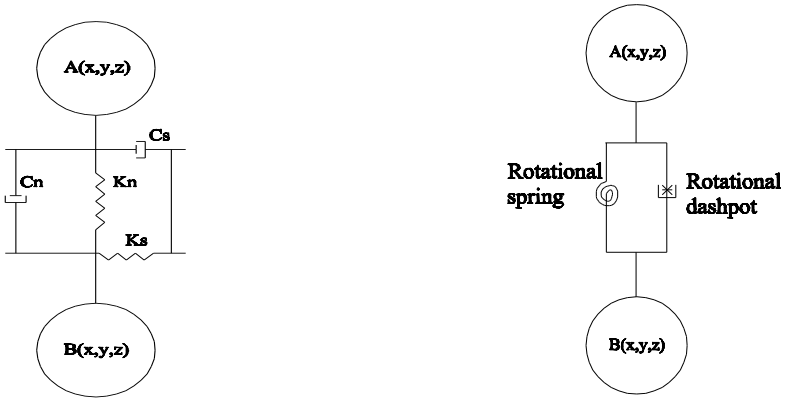

Figure-1: (a) Rheological model of DEM, (b) Schematic illustration of rolling resistance

Iwashita and Oda [15] proposed additional rotational spring-slider system in parallel with the normal contact spring. This contact model is schematically presented in Figure–1(b). Spherical particles with normal, shear & rolling springs and normal and shear dashpots [16] were exploited in this research. Normal forces are calculated when particle overlap and maximum shear force and moment are given in the following:

$$F_{max} = \mu F_n \quad \ldots\ldots\ldots (1)$$

$$M_{max} = \alpha B F_n \ldots\ldots\ldots (2)$$

Where, F_n is the normal force, μ is frictional coefficient, B is contact area, α is a parameter which determines the rolling resistance.

Pipe is placed in shallow depth in this analysis. Particles contact with pipes during the DEM simulation and force between pipes and particles are calculated using principle of mechanics. Pipe is modeled as 3D beam element and there are six degrees of freedoms at each nodal point. Stiffness matrix, mass matrix and damping matrix are formulated and the fundamental equation for the pipeline is given in equation 3.

$$F = Ku + C\dot{u} + M\ddot{u} \quad \ldots\ldots\ldots (3)$$

3. Proposed Model

Deformation of buried pipeline is analyzed by developing a three dimensional modeling of soil and pipes. 618460 spherical particles with diameter 1.0 cm are used to build up the model and represented the soil assemblies. The basement and sidewalls are also made of spherical particles of 1.0 cm diameter and assumed to be rigid in the analysis. Periodic boundary conditions are given at outer edges in X direction so that any particle goes beyond the boundary is placed at the opposite edge. The size of the

model after the preparation process are 61cm x 181 cm x 48.5 cm. Pipe was placed in shallow depth in this model in such a way that it remained fully buried condition after the sedimentation process. As this research study intended to use the realistic properties of pipes and particles, a number of literature review and design guideline are necessary to fix the pipe properties. Afterward ductile iron pipe (DIP) having diameter, d= 10 cm and elastic modulus, E=1.6 x 10^{11} N/m^2 are selected for this model. Pipe is divided into 15 equal elements and completely fixed boundary conditions are imposed. Seismic fault plane is considered perpendicular to the pipe horizontal axis and divides the whole model in two equal parts. After the sedimentation of soil particles, strike slip fault movement has been pertained on the model. Properties of sandy soil have been used to calculate the stiffness of the particles for this numerical simulation. Density of the particles is assumed as 2.4 g/cm^3 in the analysis and void ratio of the model after the sedimentation process is found to be, e = 0.194. The parameters used for the particles are shown in Table-1. Layout of the proposed numerical model is outlined in Figure-2.

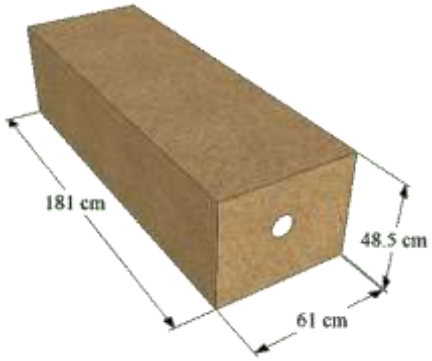

Figure- 2: Layout of proposed model

Table-1: Parameters of the analysis

Parameters	Value
Normal stiffness constant	2.2 x 10^5 N/m
Tangential stiffness constant	6.1 x 10^4 N/m
Normal damping constant	3.5 N.s/m
Tangential damping constant	2.0 N.s/m
Time step	0.000008

4. Result

4.1 Deformation response of buried pipeline

Deformed profile of the pipeline for different fault displacement is illustrated in the Figure-3. Fixed boundary conditions are given at the far end of the anchored point of the pipeline and preset displacements are given to those points as the same magnitude of fault slip.

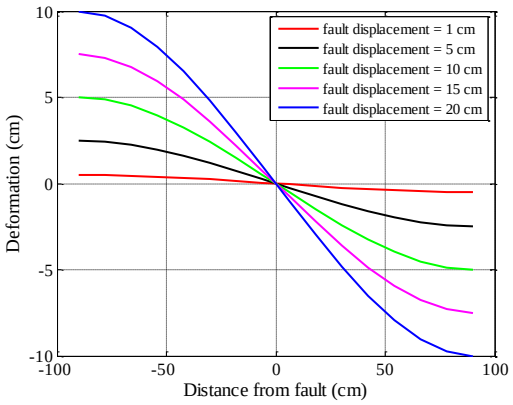

Figure-3: Deformation response of pipe

The above statement can be clearly elucidated in Figure-4. Horizontal axis represents the distance from fault plane and vertical axis shows the force between pipes and particles. The forces are higher near the fault crossing points stated the effect of particles on pipe deformation i.e. particles near the crossing point pushes the pipes to deform more. The particles show finer effect on pipes up to the fault displacement of 10 cm. Subsequently, the much less effect of particles is seen and boundary conditions can contribute to the pipe displacement. However, the specific aim of this research is to investigate the particle movement & its effect on pipe responses and the results presented in Figure-3 & 4.

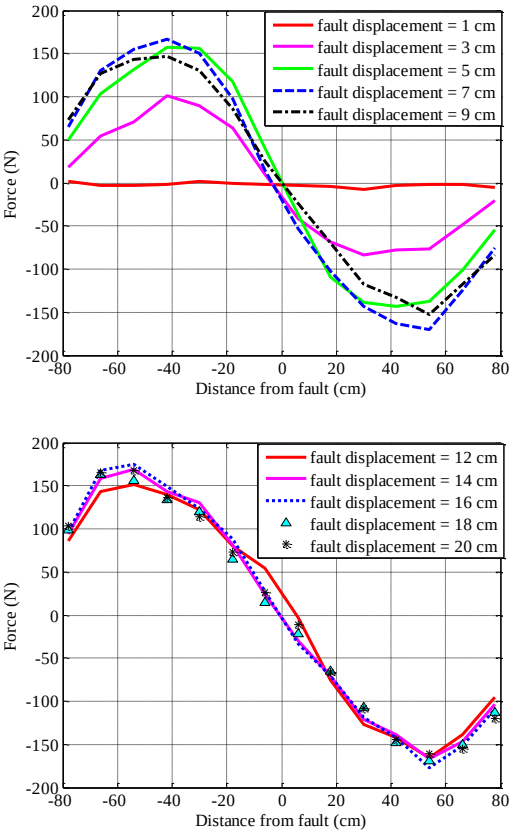

Figure-4: Force between pipes and particles

The maximum force between pipes and particles at different nodal points of pipe elements for different fault displacement are observed at a distance 20-50 cm from the fault line and are opposite magnitude on either side of the fault plane and exhibits lower contribution near the boundary of the model.

4.2 Force displacement relationship

One of the key points of this research study is to describe the soil pipe interaction. Soil pipe interaction is described by the force displacement relation between pipes and particles. The conventional force-displacement correlation of soil springs in axial, horizontal and vertical direction follows the linear relation up to the yield point and beyond that constant force appears. Most of the research work in buried pipe analysis uses this type of soil springs to represent the soil behavior. This research study established the load-deformation relation between pipes and particles which comes from the movement of particles and contacting forces between the particles. Force-displacement relations at different nodal points of the pipelines are outlined in Figure-5 where horizontal axis represents the nodal displacement and vertical axis corresponds to the force between pipes and particles.

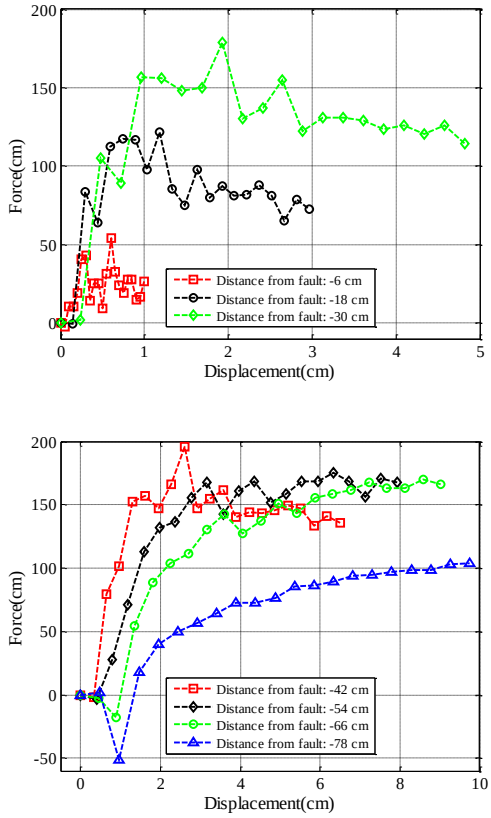

Figure-5: Force-displacement relation between pipes and particles

Force-displacement curve near the fault line shows the initial rising up the force with the displacement and after the peak, force value goes down and exhibits strain softening behavior. Movement of soil particles with the fault slip governs the characteristics of the force response between pipes and particles. The decreasing trend of the force near the fault crossing point enhances the possibility of brittle failure of the particles whereas away from the fault crossing point shows the gradual increment of forces. In Figure-5, load deformation behavior of the pipes greater than 42 cm from the fault line exemplify the gradual rising up of force rather initial rising up and show signs of strain hardening behavior. Thus at the far away from the fault line, particle deformation shows ductile behavior rather than brittle nature. Typical load deformation curve only explain the behavior up to the yield points though this research study includes the natural behavior of particles and relies on the naturally occurring load –deformation relation.

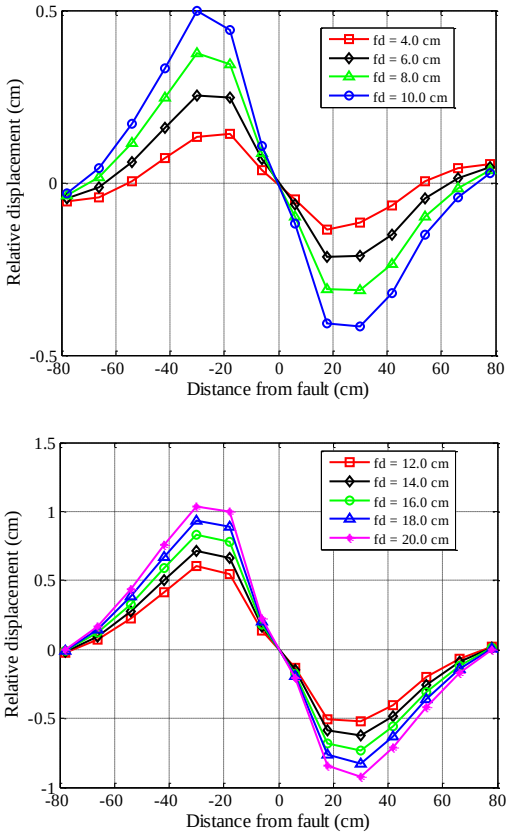

Figure-6: Displacement of particles

Displacement of contacting particles with the pipes is also observed and shown in the Figure-6 where horizontal axis gives the distance from fault and vertical axis represents relative displacement between pipes and particles. Legend ‘fd’ in the figure explains the amount of fault slip given to the model. Particle movement plays an important role in this analysis. Maximum relative particle movement observed near

the fault rupture up to the distance of 40 cm from the fault line and particle moves in the strike direction up to the fault movement of 10 cm. Subsequently displacements of particles are fewer with the increment of strike slip. Figure-6 can explain the load –deformation behavior of the pipes more clearly showing the initial increment of particles relative displacement and beyond that the decrement of the particle displacement resulting the force responses between pipes and particles. Instead of using the predetermined spring to represent the soil, this type of analysis considering the contact between pipes and particles may give better understanding of the relation between soil and pipes.

5. Parametric Study

Vulnerability of buried pipeline due to surface faulting is a vital factor in designing and installing underground pipeline for practical uses. Underground pipeline generally extends over long distance through the wide variety of soils, geological conditions and regions with different seismicity. Consequently there are some influence factors on the response of pipeline account for fault rupture propagation. The critical factors are burial depth, soil properties, fault angle, nature of rupture propagation, position of water table and pipe properties etc. To understand the above parameters clearly, a series of parametric study is necessary. Most of the researchers are concerned about the variety of soil properties, burial depth, fault angle etc. But effects of different pipes properties are playing an important function of the parametric study. This research study includes a short parametric study using different pipe properties.

5.1 Pipe properties

For this parametric study, four different models are considered with different types of pipe properties. Herein these four different types are used for the same model and responses of the pipes are compared for same strike slip fault movement. Typical properties of those commercially available pipes are taken for the analysis and presented in Table-2.

Table-2: Parameters for different model

Pipe types	Density (kg/m^3)	Elastic modulus (N/m^2)
Model-1 (DIP)	7850	1.6×10^{11}
Model-2 (PVC)	1300	3.4×10^{9}
Model-3 (HDPE)	950	8.0×10^{8}
Model-4 (Concrete)	2400	3.0×10^{10}

5.2 Result of parametric study

Axial strains with the incremental fault displacement for the four models are illustrated in Figure-7. HDPE pipes give higher strain in compare with the other models. This may happen due to the low density and elasticity of the HDPE pipes. DIP pipe shows much stiff behavior among these four models under the identical condition of strike slip faulting.

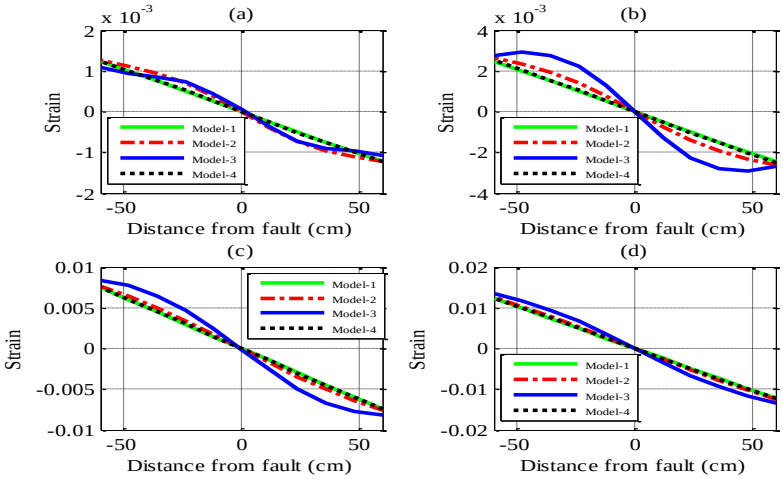

Figure-7: parametric study for strain, (a) fault displacement =2 cm, (b) fault displacement = 4cm, (c) fault displacement = 12 cm, (d) fault displacement =20cm

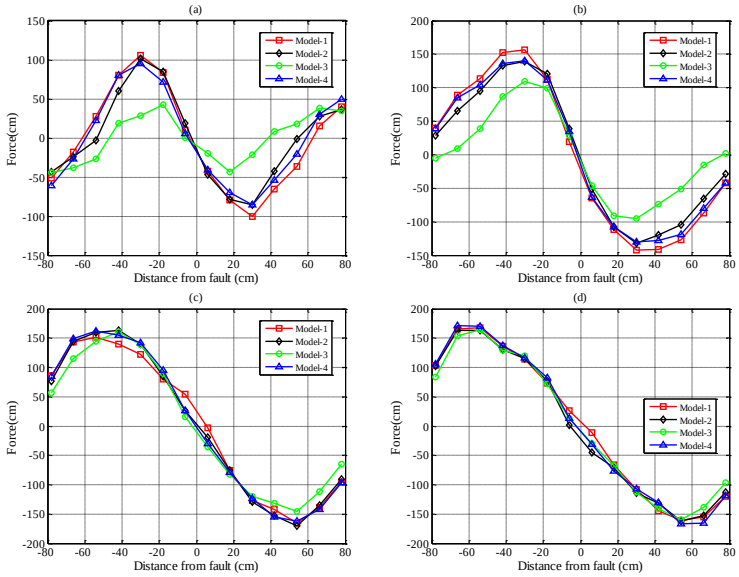

Figure-8: Force responses (a) fault displacement =2 cm, (b) fault displacement = 4cm, (c) fault displacement = 12 cm, (d) fault displacement =20cm

The effect of forces between pipes and particles for different models describes the response of the four models. Maximum forces are observed near the fault line for all types of models but with different force magnitude. The force responses are varied with the different stiffness of the pipes accordingly. The above mentioned statements are graphically presented in Figure-8 where horizontal axis represents the distance from fault and vertical axis corresponds to the force between pipes and particles. Larger force observed for the Model -1 with the increment of fault displacement whereas in case of Model-4, the force response is lower than other models. The effect of low stiffness of the pipes leads to much deformation for Model-2 and Model-3.

Force-displacement behavior of pipes at different nodal points is also studied in this research and some are given in Figure-9. DIP gives the higher yield value in compare

with the other models. As the particle properties remain unchanged in all four models, the variation of the responses among these four models thus govern by their properties i.e. stiffness of the pipes. However, HDPE pipe gives the smaller yield value than other type of models. Strain softening may observed after the yield near the fault line whereas away from the fault line pipe responses shows much ductile behavior in all cases.

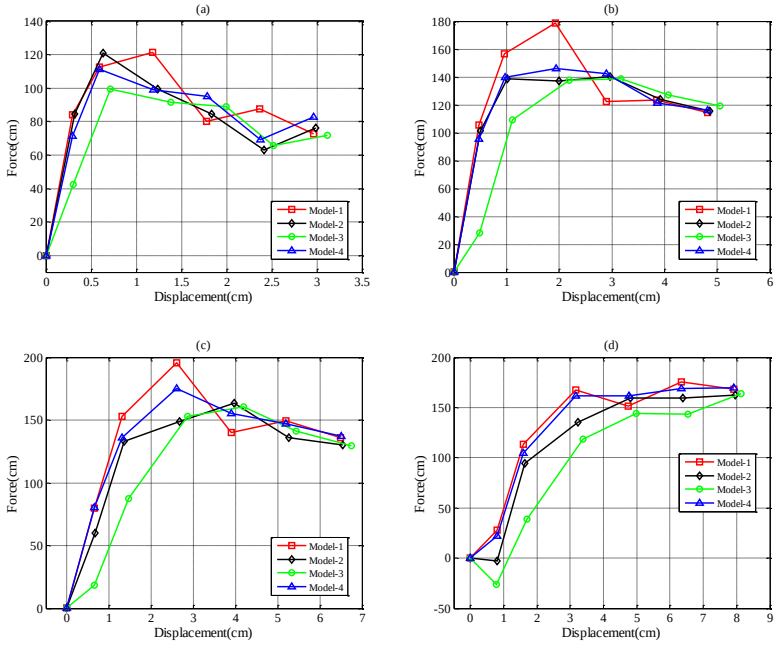

Figure-9: Force-displacement relation, (a) Distance from fault: -18 cm, (b) Distance from fault: -30 cm, (c) Distance from fault: -42 cm, (d) Distance from fault: -54 cm

6. Conclusion

A three dimensional numerical simulation of buried pipe has been performed for the response analysis of pipes buried in shallow depth. Pipe deforms with the movement of particles at the time of fault rupture and exhibits strain increment accordingly with the fault slip. Particles near the fault line shows greater effect on the pipeline. Load-deformation relation between pipes and particles are also observed and discussed in this paper. The relation seems to be understandable and compatible with the typical load –deformation curve. Afterward a short parametric study has been performed with different commercially available pipe types and in the analysis DIP pipe shows better performance against ground rupture. However, limitation of computational time may be an obstacle for more rigorous analysis of this simulation. Simulation of larger model with smaller size particle can overcome the current obstacle of the simulation and be a more rational analysis.

7. Acknowledgement

The first author greatly acknowledges to the Asian Development Bank-Japan Scholarship Program (ADB-JSP) for its support by providing scholarship for this research work.

8. References

[1] W.W.Sim, I.Towhata, S.Yamada, G.J.-M.Moinet. Shaking table tests modeling small diameter pipes crossing a vertical fault. Soil Dynamics and Earthquake Engineering, 2012,Vol. 35, pp. 59-71.

[2] McCaffrey, M.A and O'Rourke, T.D. Buried pipeline response to reverse faulting during the 1971 san fernando earthquake, earthquake behavior and safety of oil and gas storage facilities, buried pipelines and equipment, pvp-77. American Society of Mechanical Engineers, 1983, pp. 151-159.

[3] N.M. Newmark and W.J.Hall. Pipeline design to resist large fault displacement. Proceedings of the US national conference on earthquake engineering. Ann Arbor, University of Michigan, 1975, pp.416-425.

[4] Kennedy RP, Chow AW, Wlliam RA. Fault movement effects on Buried oil pipeline. Transportation Engineering Journal, ASCE, 1977, Vol. 103, pp.617-633.

[5] Leon Ru-Liang Wang, Yaw-Huei Yeh. A refined seismic analysis and design of buried pipeline for fault movement. Earthquake Engineering and Structural Dynamics, 1985, Vol. 13, pp. 75-96.

[6] Shiro Takada, Nemat Hassani and Katsumi Fukuda. A new proposal for simplified design of buried steel pipes crossing active faults. Earthquake Engineering and Structural Dynamics, 2001, Vol. 30, 1243-1257.

[7] Joshi Shantanu, Prashant Amit, Deb Arghya, Jain Sudhir K.. Analysis of buried pipelines subjected to reverse fault motion. Soil Dynamics and Earthquake Engineering, 2011.

[8] Vazouras, Karamanos Spyros A., Dakoulas Panos. Finite element analysis of buried steel pipelines under strike-slip fault displacements, Soil Dynamics and Earthquake Engineering, 2010, Vol. 30, pp. 1361-1376.

[9] Ogawa Yasuo, Yanou Yasunari, Kawakami Makoto, Kurakake Takeshi. Numerical study for rupture behavior of buried gas pipeline subjected to seismic fault displacement. Proceedings of 13th WCEE, Vancouver, B.C., Canada, 2004.

[10] Abdoun Tarek H., Ha Da, O'Rourke Michael J.. Behavior of moderately buried HDPE pipelines subject strike-slip faulting. Proceedings of the 12th International Conference of International Association for Computer Methods and Advances in Geomechanics (IACMAG), Goa, India, 2008.

[11] Yoshizaki Koji, O'Rourke Thomas D., Hamada Masanori. Large scale experiments of buried steel pipelines with elbows subjected to permanent ground deformation. J. Struct. Mech. Earthquake Eng. , JSCE, 2003, No. 724/I-62.

[12] C. Pascal. Interaction of faults and perturbation of slip: influence of anisotropic stress states in the presence of fault friction and comparison between Wallace–Bott and 3D Distinct Element models. Tectonophysics , 2002, Vol. 356, pp. 307-322.

[13] Abbas Soroush, Behrooz Ferdowsi. Three dimensional discrete element modeling of granular media under cyclic constant volume loading: A micromechanical perspective, Powder Technology,2011, vol. 212, pp. 1-16.

[14] Cundall P.A, Strack O D L. A discrete numerical model for granular assemblies. Geotechnique, 1979, vol. 29, no. 1, pp. 47-65.

[15] Iwashita, K && Oda, M. olling resistance at contacts in simulation of shear band development by DEM, Journal of Engineering Mechanics, ASCE, 1998, 124:3, pp. 285-292.

[16] Taniyama, H. Numerical analysis of overburden soil subjected to strike-slip fault: Distinct element analysis of Nojima fault. Engineering Geology, 2011, 123, pp. 194-203.

ACCMES 153

Optimum Cross-Sectional Floating structure

Du-Ho, Lee.
Structual Engineering Research Division, KICT, Go-yang, Korea.
ldh0067083@kict.re.kr

Youn-Ju, Jeong.
Structual Engineering Research Division, KICT, Go-yang, Korea.
yjjeong@kict.re.kr

Young Jun, You.
Structual Engineering Research Division, KICT, Go-yang, Korea.
yjyou@kict.re.kr

Min Su, Park.
Structual Engineering Research Division, KICT, Go-yang, Korea.
mspark@kict.re.kr
The corresponding author: Du-Ho, Lee.

Abstract

In the present study, numerical analysis of pontoon-type, combination-type and hybrid-type floating structures(240*240*14) are carried out through ANSYS AQWA in water depth 35m. The six degree motions of structure such surge, sway, heave, roll, pitch, yaw is investigated for fifth cases, which divided the wave period from 5sec to 15sec in regular wave. Since the structure is a square shape, the numerical analysis is only performed in case of incident wave angle 0 and 45 degrees. From the comparison between pontoon and hybrid floating structure, it is found that the combination-type floating structure is very effective to reduce the motion of structure for all cases.

Keyword: Floating structure, Hybrid, Hydrodynamic analysis, ANSYS AQWA, RAOs.

1. Introduction

In recent years, construction practices of floating structures such floating offshore structures as floating LNG terminals, container terminals, oil production and storage facilities, and floating breakwaters have increased around the world, resulting in active progress of researches on the floating structures. The structural type of the floating structures can be divided into pontoon type and semi-submergible type. First, the pontoon type makes it easy to secure buoyance, and its internal space can be

utilized as storage use. In addition, it has widely been applied worldwide due to its advantages of simple structure and economic (Allen et al., 2006; Haveman et al., 2006; Jeong et al., 2010). However, the pontoon-type floating structure can't absorb the impact energy of wave load due to the closed sides, which generates severe

(a)Pontoon type **(b) Hybrid type**

Figure 1. Shape of unit modules

hydrodynamic motion resulting by the wave loads (Jeong et al., 2010; Zijian, 2007). In case of semi-submergible type, the flow of seawater is possible due to the installation of air gap in the floating structures, because of this, advantage of its insta llation and utilization even under extreme wave environment. However, it has the disadvantage of increase in the height of the structure itself due to the obtainer of buoyancy and installation of an air gap. To complement the problems of the two types, a hybrid floating structure was developed, and furthermore, a combination floating structure was proposed. In case of the combination floating structure, its disadvantage was complemented through combination with a pontoon-type floating structure to obtain buoyancy.

Table 1. Dimension of unit module

	Pontoon	Hybrid
Length(m)	30	30
Breath(m)	30	30
Height(m)	14	14
Cylinder Diameter(m)	None	20
Thickness		
Top/Bottom Slab(m)	0.65	0.65
External Wall(m)	0.65	0.50
Internal Wall(m)	0.30	None

In this study, an analysis on the pontoon-type, hybrid-type and combination-type floating structures with size of 240(L)×240(B)×14(H) was conducted, targeting the coast with water depth of 35m. The hydrodynamic motion characteristics under

different 50 wave loads at 5 to 15 seconds of wave period that can occur in the targeted coast were investigated. In case of the wave angle of incidence, an analysis on the two directions of 0° and 45° was conducted in consideration of a square-shaped floating structure. The wave-induced motion were identified through hydrodynamic analysis, and its analysis was carried out using ANSYS AQWA, the universal analysis program.

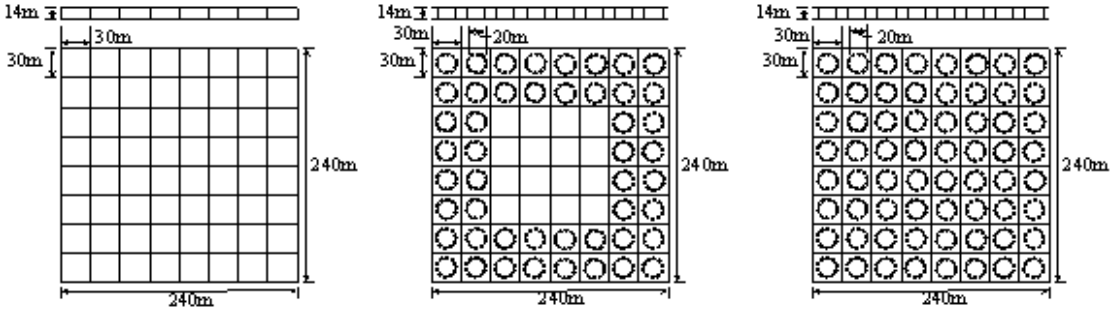

(a) Pontoon-type (b) Combination-type (c)Hybrid-type

Figure 2. Analysis model

2. Numerical Analysis

2.1 Hydrodynamic Analysis Program ANSYS-AQWA

The analysis software AQWA used in this study is a program that performs dynamic behavior analysis of offshore structures like vessels and floating objects against external forces of marine environment such as wave, wind and current as a universal program of ANSYS Inc. and it enables various kinds of analyses, including LINE, LIBRUM, FER, NAUT and DRIFT. First, LINE analysis is a three-dimensional diffraction and radiation analysis program, and it is used to calculate wave force and structure response. LIBRUM analysis performs eigen-mode and dynamic stability analysis, and FER, NAUT and DRIFT analyses conduct mooring tension analysis and movement of structures.

In this study, the RAO(Response Amplitude Operator) on the each direction of pontoon-type and hybrid-type floating structures against wave loads applied through AQWA LINE analysis was deduced, and analytical verification on the movement reduction effects of Optimum Cross-Sectional floating structure was conducted through a comparative analysis on the analysis results..

2.2 Analytical Model

The analysis target structure of this study is a concrete floating quay wall, and detailed specifications of the concrete floating structure is based on the cross-section derived from the actual design(KICT, 2010). The basic specifications of the unit

modules that constitute the target floating structure are shown in Figure 1 and Table 1. The size of the floating structure is length(Ls) 240m, breadth(Bs) 240m and height(Hs) 14m, and the shapes of floating structures, the analysis models in this study are shown in Figure 2. As identified in figure 2, (a) pontoon-type floating structure is a floating structure whose entire structure is composed of pontoon-type unit modules of Figure 1 (a), and (c) hybrid-type floating structure is a structure in which only hybrid modules of Figure 1 (b) are combined. In addition, the combination-type floating structure of Figure 3 (b) is the one whose central part is 120*120 pontoon-type and outer part is made of hybrid-type. An analysis on the coast with water depth of 35m was carried out under marine environmental conditions for the hydrodynamic analysis, and among various external forces of the marine environment, only the effect on the wave loads that have the most impact on the motion of floating structures was examined.

The wave loads applied to the hydrodynamic analysis, the 50 wave loads at 5 to 15 seconds of wave period were applied. In addition, an incidence angle (β) of wave length was considered toward the two directions of 0and 45 degrees and the hydrodynamic motion of each floating structure according to the incidence angle were compared. The hydrodynamic motion of each floating structure were identified through a comparative analysis of RAOs that occur in the floating structures. In this study, an analysis was carried out using ANSYS AQWA, the hydrodynamic universal analysis program, and the target floating structure was modeled with 3D-Shell elements.

3. Analysis Results and Discussion

The AQWA-LINE analysis on the 50 wave loads of 5 to 15 seconds that can occur in the coast with water depth of 35m was carried out. In addition, the hydrodynamic motion of floating structure on the each angle of incidence was compared. First, hydrodynamic force that causes motion of floating structures was investigated.

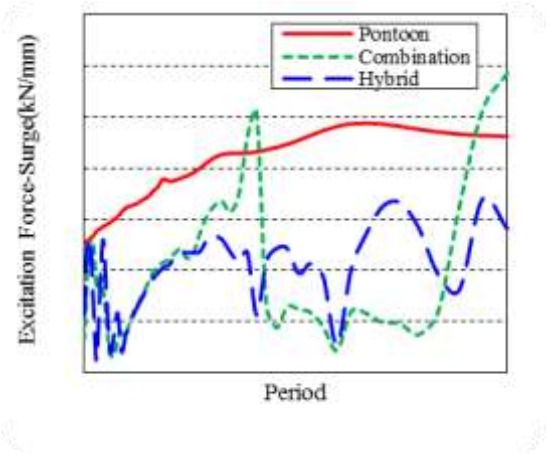

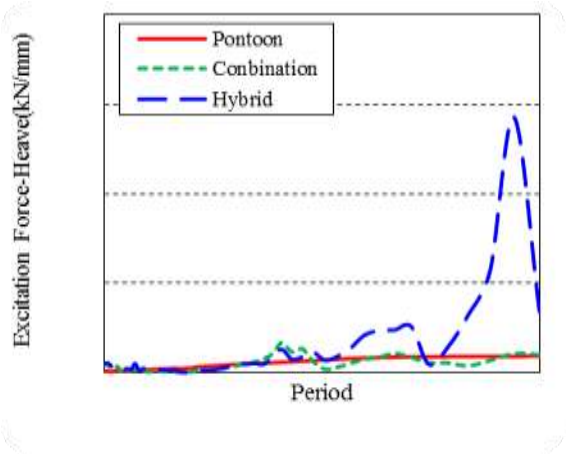

(a) surge (b) heave

Figure 3. Excitation force at incidence angle 0 degree

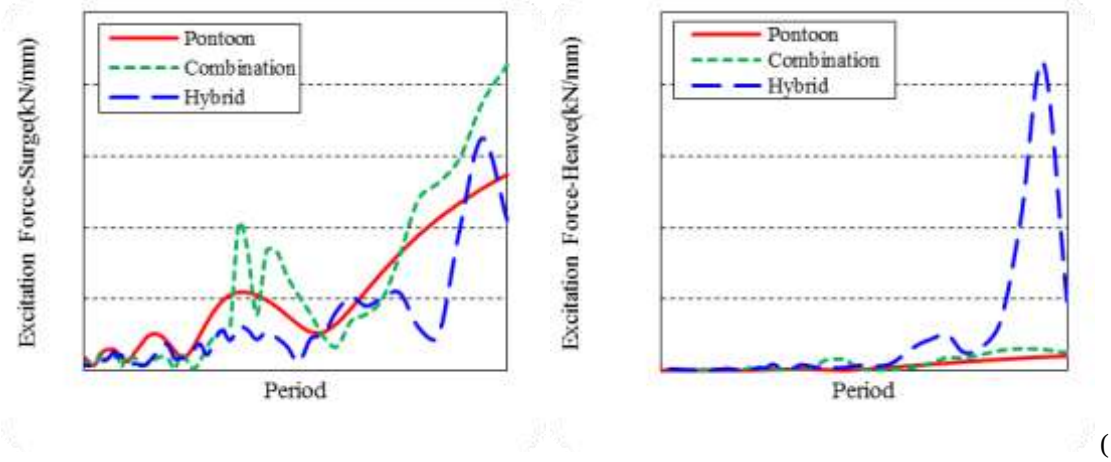

(

a) surge (b) heave

Figure 4. Excitation force at incidence angle 45 degree

Figure 3 represents the excitation force that occurs when the incidence angle is 0 degree.As shown in Figure 3 (a), small excitation force against a surge occurred compared topontoon-type floating structure. In particular, the wave excitation force of a combination type greatly decreased between 9 and 13 seconds. Figure 3 (b) shows the excitation force on the heave, and represents the maximum excitation force in a hybrid floating structure at 14 seconds of wave period. In addition similar excitation force occurs in both pontoon-type and hybrid-type. Figure 4 shows the excitation force that occurs in the floating structures when an incidence angle is 45. Figure 4 (a) represents excitation force on the surge, and all 3 analytical models show similar excitation force trends. In addition, the excitation force increased at more than 12 seconds of wave period in case of combination-type floating structure.

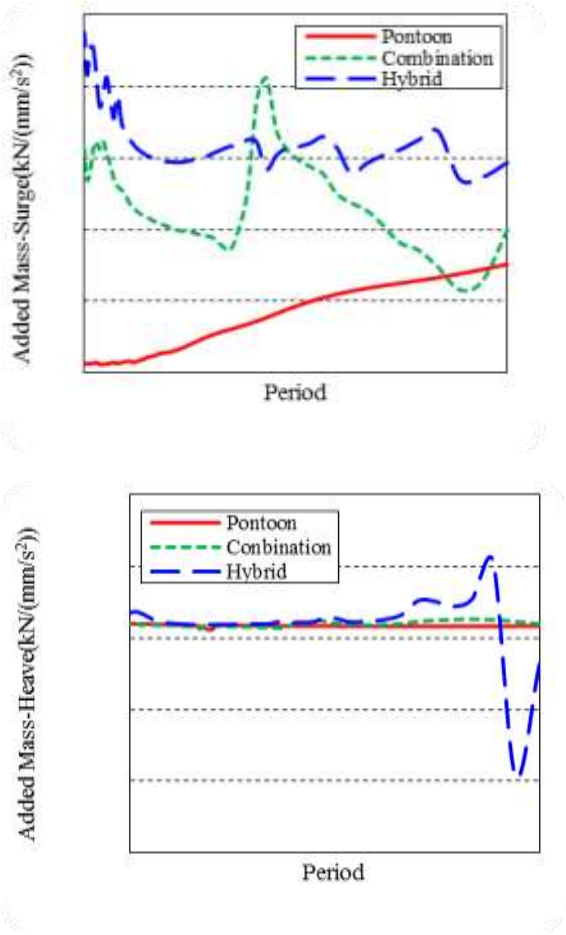

(a) surge (b) heave

Figure 5. Added mass

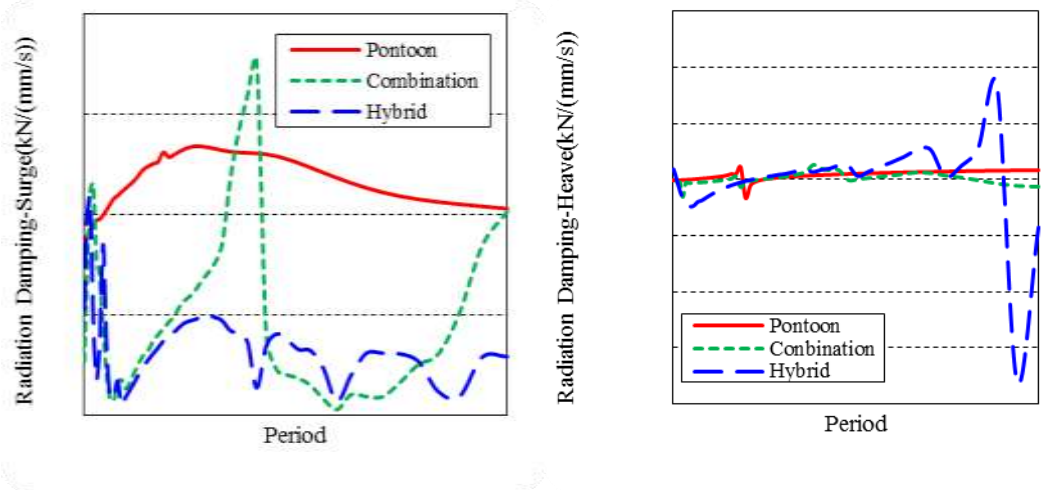

(a) surge (b) heave

Figure 6. Radiation damping

Among hydrodynamic forces that occur in floating structures, added mass and radiation damping are shown in Figure 5 and 6. Figure 5 (a) represents added mass in surge, and the smallest added mass appears in pontoon-type floating structure as

shown in the Figure. Figure 5 (b) shows the added mass of heave, and it turned out that all three analytical models indicate similar levels in general, but a sharp decrease in added mass occurs in hybrid-type floating structure at about 13 seconds.

Figure 6 (a) represents radiation damping on the surge, and the largest radiation damping appears in pontoon-type floating structure as shwon in the Figure. Figure 6 (b) shows the radiation damping of heave, and it turned out that all three analytical models indicate similar levels in general, but a sharp decrease in radiation damping occurs in hybrid-type floating structure at about 13 seconds. Such a result is consid-

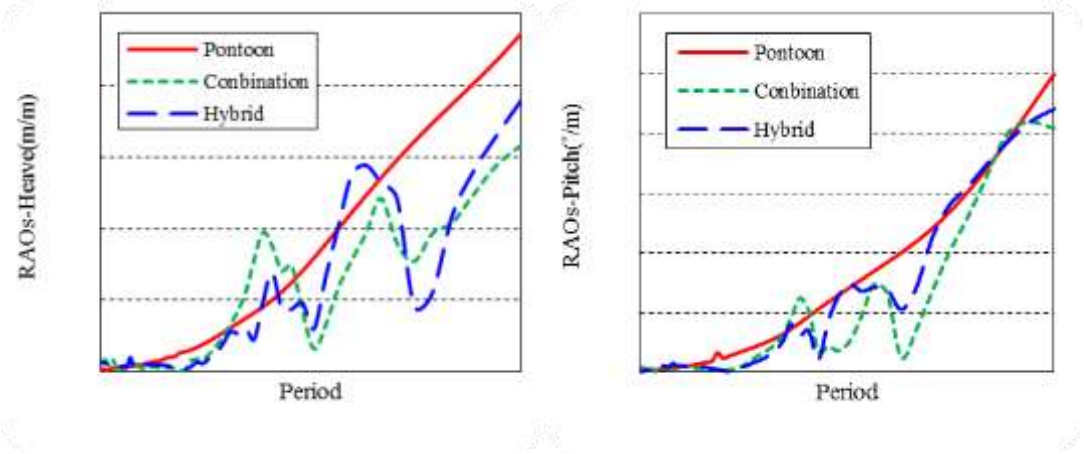

(a) heave(b) pitch

Figure 7. RAOs at incidence angle 0 degree

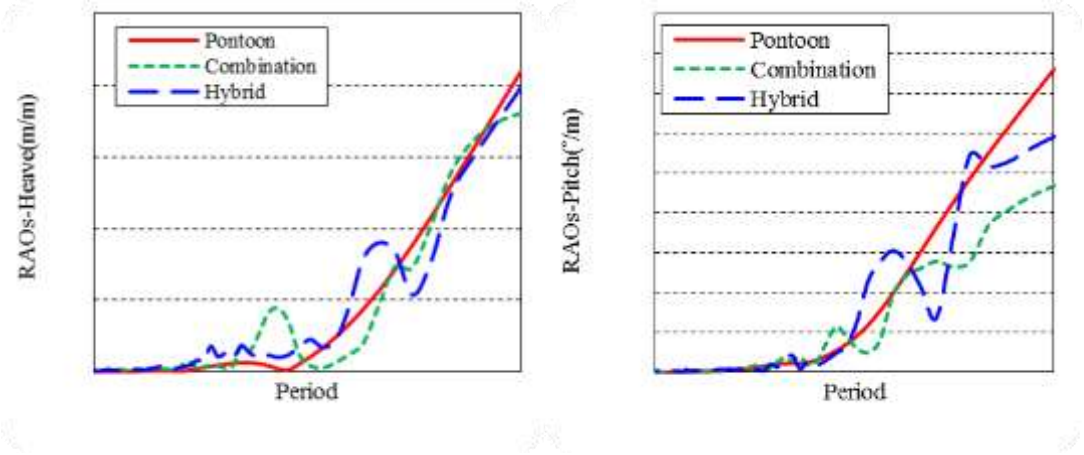

(a) heave(b) pitch

Figure 8. RAOs at incidence angle 45 degree

ered to occur due to the interaction between the fluid and cylinder of a hybrid in case of the long period wave.

The motion of floating structures was examined through a comparative analysis of RAOs that occur in the floating structures. Among 6 degrees of freedom, an analysis on the heave and pitch was carried out. Figure 7 and 8 shows the results of analytical

models that occur when the angle of incidence is 0 and 45, respectively.

As identified in Figure 7 (a), microscopic motion reduction effects appear under short-period wave loads with wave period of less than 10 seconds, and the larger motion than pontoon-type floating structure occurs temporarily in case of the heave. However, the motion of hybrid and combination floating structures decreased in long period wave with more than 10 seconds. In addition, it was found that the reduction in motion of combination floating structure is greater compared to that of hybrid floating structure. Figure 7 (b) represents the motion characteristics of the pitch, and the distinct motion reduction effects appear in long period wave with wave period of more than 9 seconds. In addition, the most obvious motion reduction effects were found in combination floating structure.

Figure 8 represents the heave and pitch RAOs of floating structures when the angle of incidence is 45°. Figure 8 (a) shows the motion by the heave, and all analytical models show almost similar motion characteristics. However, microscopic motion reduction appeared in long period wave with of more than 10 seconds in case of combination floating structure. Figure 8 (b) represents the motion by the pitch, and the motion reduction effects of hybrid and combination floating structures can be identified in long period waves of more than 10 seconds.

4. Conclusion

In this study, a comparative analysis on the motion reduction effects according to shape of floating structures was carried out, and based on this, the optimum cross-sectional shape of the floating structures was reviewed. In addition, a combination- type floating structure was proposed in this study, and its excellent motion reduction effects by combining the advantages of pontoon-type and hybrid-type were verified.

1. The motion reduction effects of combination-type and hybrid-type floating structures turned out to be greater compared to those of general pontoon-type floating structure.
2. The combination-type floating structure showed the most excellent motion characteristics of all three analytical models.
3. The combination-type floating structure boasts its easiness of securing buoyancy due to pontoon-type floating structure in the center.
4. Due to the presence of pontoon-type floating structure in the center, the combination-type floating structure is subjected to less force caused by the interaction between the structure-fluid in long period waves compared to the hybrid-type floating structure.
5. It is considered that the motion reduction effects appear since seawater passes through a air gap of the floating structure due to hybrid unit modules.

5. Acknowledgements

This study was supported by the Korea Institute of Construction Technology through the research project "Development of construction technology for concrete floated offshore infrastructure".

6. Reference

[1] Allen, E., Dees, D., Hicks, S., Hollibaugh, R., Martin, T., and Starling, T.(2006) Design of a Floating Production Storage and offloading Vessel for offshore Indonesia- Final Report, Texas A&M University, Texas.

[2] ANSYS Inc.(2010) ANSYS Uer's Manual

[3] Haveman, C., Parliament, J., Sokol, J., Swenson, J., and Wangner, T.(2006) Design of a Floating Production Storage and offloading Vessel for Operation in the South China Sea-Final Report, *Texas A&M university*, Texas.

[4] Korea Institute of Construction Technology,Development of Application Technology for Concrete Floating Structure, 2010.

[5] Korea Institute of Construction Technology,Development of Structural System of Hybrid Floating Structure, 2011.

[6] Jeong, Y.J., Cho, J.Y., You, Y.J., and Na, S.W. (2010) Stability and Wave-induced Bending Moment for Design of offshore Floating Terminal, *9th Pacific Structural Steel Conference 2010*, Beijing, China, pp. 369-374.

ACCMES 155
Hydraulic conductivity of various shape of sands

Nurullah Akbulut[1], Ali Firat Cabalar[2]

[1]Hasan Kalyoncu University, Department of Civil Engineering, 27100, Gaziantep, Turkey,

[2]University of Gaziantep, Department of Civil Engineering, 27310, Gaziantep, Turkey

ABSTRACT

This study aims to investigate the effects of shape of sands on the coefficient of permeability (k). The paper presents the results of an extensive series of experimental investigation carried out in permeablity tests on sands having various shapes. A particle size range (1.18- 0.6 mm) of five different sands (Leighton Buzzard Sand, Trakya Sand, Narli Sand, Crushed Stone Sand, Fly Ash Pellets) having distinct shapes were tested in a constant head permeability testing apparatus at a relative density (R_d) of about 35% and constant room temperature (20^{o}C). Experimental results showed a clear relation between the shape of the sands and the hydraulic conductivity values obtained. Pictures taken show the physical differences/ similarities among the sands used during this investigation. A comperative study on the tests results and estimated hydraulic conductivity values using emprical equations derived by numerous researchers for coefficient of permeability prediction of soils are also presented.

Keywords: Sand, shape, permeability.

1. INTRODUCTION

Water is free to flow through the pores between soil particles in accordance with the Darcy's emprical law ($q=Aki$). The coefficient of permeability (k) or hydraulic conductivity depends basically on the average size of the pores through the soil matrix, and temperature of the environment. In general, the smaller the soil grains the lower is the coefficient of permeability. The presence of a fines content in a coarse grained soil results in a k value significantly lower than that for the same soil without fines. For a given soil, the k value is affected by stratification. For example, if a soil deposit is stratified, the permeability for flow parallel to the direction of stratification is higher than that for flow perpendicular to the direction of stratification. The k value also changes with temperature, upon which the viscosity of the water is dependent. Such as, if the k value measured at 20°C is taken as 100%, then the k values at 10°C and 0°C would be 77% and 56% respectively (Craig, 1997; Powrie, 2004; Das, 2008). From clay to cobbles, the k value increases over many orders of magnitude. The typical k values for different soils are within the ranges shown in Table 1.

To obtain the *k* value in laboratory studies, two common laboratory test methods of constant head for coarse grained soils and falling head for fine graines soils are employed. In some cases, the *in-situ* determination of coefficient of permeability may be required. Such as, well pumping test, which involves continuous pumping from a well, can be used in homogenous coarse grained soil strata. In borehole in-situ method, water is allowed to flow into the stratum under constant head. The k value of coarse grained soil can also be determined from in-situ measurements of seepage velocity, which involves excavating pits at two different points and taking measurements between them (Craig, 1997; Powrie, 2004; Das, 2008).

Table 1. Coefficient of permeability, k (m/s), (BS 8004: 1986).

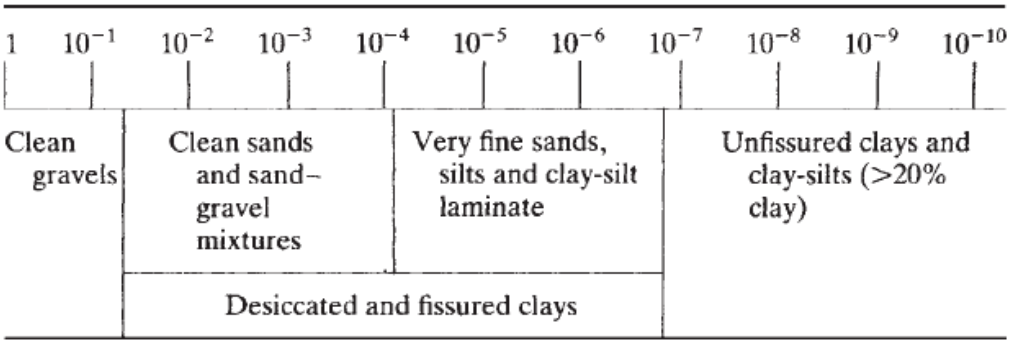

For sandy soils, Hazen, 1892, 1911; Taylor, 1948; Terzaghi and Peck, 1964; Lambe and Whitman, 1969; Holtz and Kovacks, 1981; Das, 1997; and Coduto, 1999 estimated the approximate *k* value by various emprical equations. Kozeny (1927) and Carman (1956) developed a semiemprical/theoritical formula for predicting the permeability of porous media. Furthermore, certain geotechnical textbooks cite many more empirical equations developed for permeability prediction of soils; including Kenney et al. (1984), Vukovic and Soro (1992), Alyamani and Sen (1993), USBR, (1990), Slichter (1898) and Chapuis (2004). Actually, these formulas are constrained with some limitations.

Here in this study, it is aimed to investigate the influences of shape of sands having the same gradation characteristics (C_c, C_u, D_{10}, D_{30}, D_{50}, D_{60}) on the coefficient of permeability using a series of experimental results. The paper also aims to present a comperative study of Kozeny-Carman, Hazen, Terzaghi, Slichter, USBR, Alyamani & Sen, and Chapuis methods employed for predicting the coefficient of permeability (*k*) of soils.

2. EXPERIMENTAL STUDY

The materials used in the tests described in this study were Leighton Buzzard Sand (LBS), Trakya Sand (TS), Narli Sand (NS), Crushed Stone Sand (CSS), and Fly Ash

Pellets (FAP), having the distinct shapes falling between 1.18 and 0.6 mm. Figure 1 shows the gradation curve of the specimens. D_{10}, D_{30}, D_{50}, and D_{60} sizes are around 0.64, 0.73, 0.84 and 0.90 respectively. Thus, the coefficient of uniformity (C_u) and the coefficient of curvature (C_c) have been calculated as 1.41 and 0.93. Pictures given in Figure 2 show the physical differences/similarities among the sands used during this investigation. The sands were tested in a constant head permeability testing apparatus at a relative density (R_d) of about 35% and constant room temperature (20^{o}C). Maximum and minimum void ratio values (e_{max}, e_{min}) were found to be 0.842 and 0.525 for Leighton Buzzard Sand, 0.931 and 0.679 for Trakya Sand, 0.795 and 0.543 for Narli Sand, 1.013 and 0.668 for Crushed Stone Sand, and 1.280 and 0.916 for fly ash pellets respectively.

The specimens, at the required relative density (35%), are placed in a perspex cylindrical cell of about 50 cm^2 cross-sectional area (A). The specimens rest on a wire mesh at bottom of the cell. The volume of the water (q) flowing during a certain time (t) is measured, when a steady vertical water flow, under a constant head, is maintained through the soil specimen. Then, k values of the specimens tested were calculated using Darcy's law ($k=ql/Ah$).

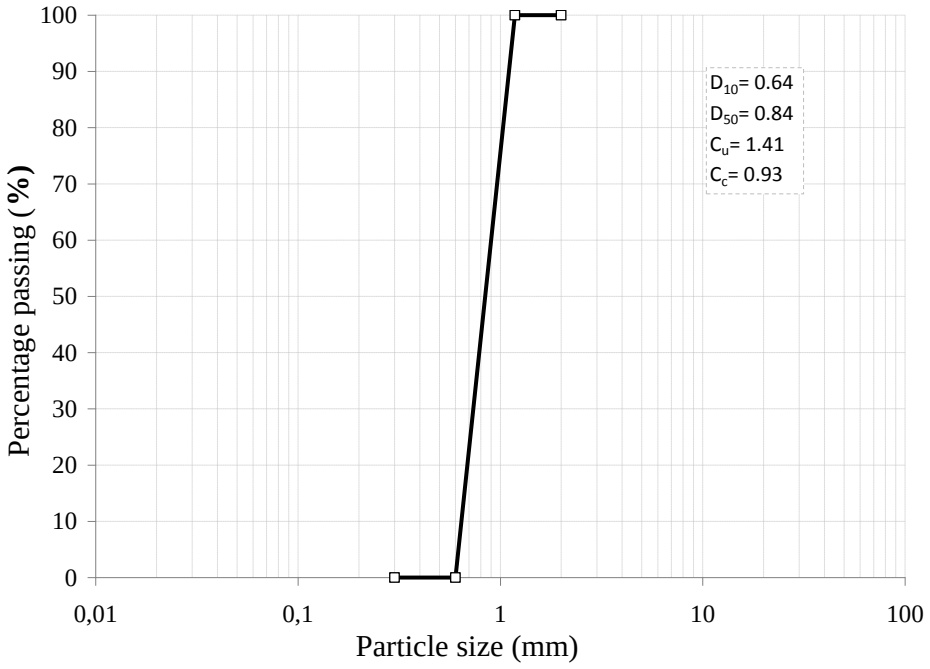

Figure 1. Particle size distribution for the geomaterials used during the experimental study.

(a) (b)

(c) (d)

(e)

Figure 2. Pictures of the geomaterials used during the experimental study (a- Leighton Buzzard Sand, b- Trakya Sand, c- Narli Sand, d- Crushed Stone Sand, e- Fly Ash Pellets).

3. RESULTS AND DISCUSSION

Table 2 gives a summary of the specimens used in the tests reported here. The initial relative densities of all specimens were kept around 35%. The specimens were loose to medium dense.

Table 2. Summary of the specimen data

	G_s	e_{max}	e_{min}	$e_{specimen}$	$d_{specimen}$ (g/cm^3)	ϕ (^{o})	k (cm/sec)
Leighton Buzzard Sand	2.65	0.842	0.525	0.731	1.530	33	0.322
Trakya Sand	2.65	0.931	0.679	0.843	1.438	36	0.375
Narli Sand	2.68	0.795	0.543	0.707	1.570	38	0.296
Crushed Stone Sand	2.66	1.013	0.668	0.892	1.406	41	0.417
Fly Ash Pellet	1.75	1.280	0.916	1.152	0.813	39	0.597

Figure 3 shows the variation of coefficient of permeability (k) values and void ratio (e) for the geomaterials tested. The higher k values can be seen for the geomaterials having higher e values. In general, a mixture of various grain sizes results in lower void ratio. However, in this study, void ratios depend on the shape of soil grains, as the sands with different shapes have the same gradation curves. Soil grains exist in many shapes and these shapes pack together in a variety of ways that may increase or decrease void ratio. Although, soil packing is effected by many physical properties, perhaps the simplest to discuss is grain shape. It has been already demonstrated the effect of grain shape on void ratio (e), internal friction angle (ϕ), and shear strength (τ) values (Zelasko et al.,

1975; Santamarina and Cascante, 1998; Shinohara et al., 2000; Sukumaran and Ashmawy, 2001). In general, if the void ratio is high, particle are free to rotate which results in lower frictional resistance to shearing, and higher *k* values. In densely packed soils with low void ratio, higher number of contacts per particle results in an increase in shearing and lower *k* values. It is thought that the granular packing in more angular soil grain samples have a more open fabric than those in relatively rounded soil grain samples. Grain texture also may affect the permability to a certain extent. Grains with a rough surface texture can cause more frictional resistance to flow than smooth textured grains. However, the result obtained here in this study is not consistent with this statement. The author's interpretted that the reason of that could be due to the dispersion of fly ash particles on the pellet grains during saturation phase and testing, or because of the lower specific gravity value of pellet grains.

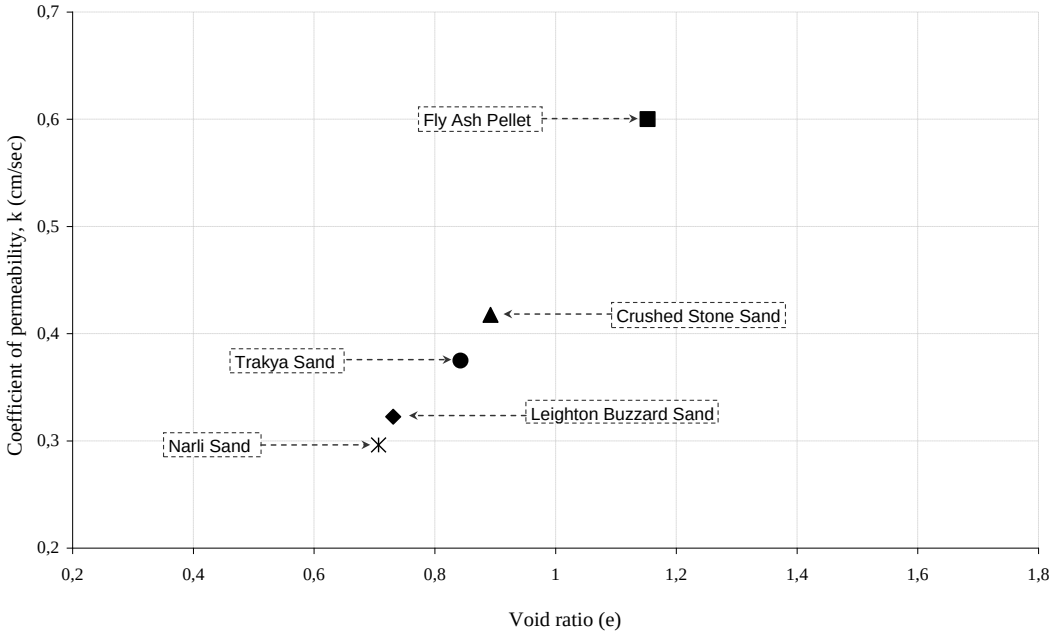

Figure 3. Coefficient of permeability for various sands at 35% of R_d.

Figure 4 is presented based on the information given by Taylor (1948), which is an widely accepted illustration between *k* and $e^3/(1+e)$. This approach had been previously developed by Terzaghi (1925) for clayey soils.

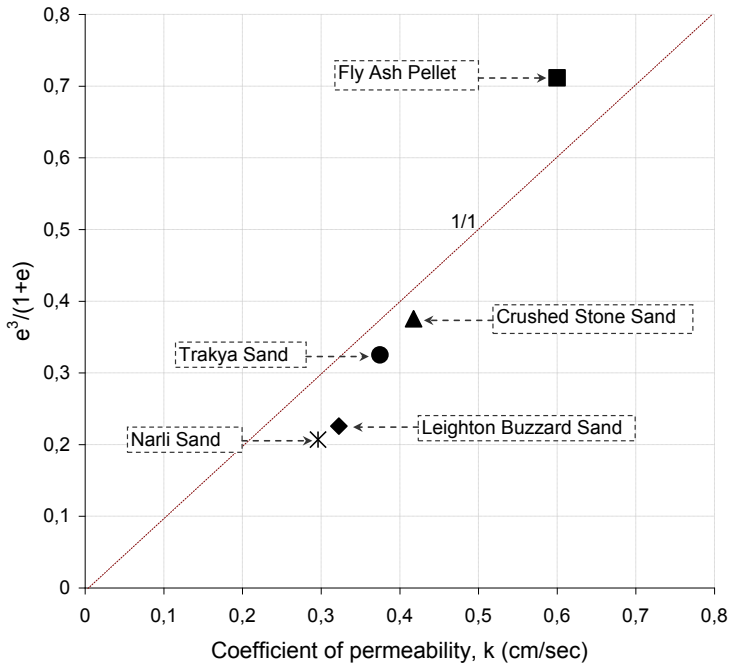

Figure 4. Relationship between *k* and $e^3/(1+e)$ for the sands tested.

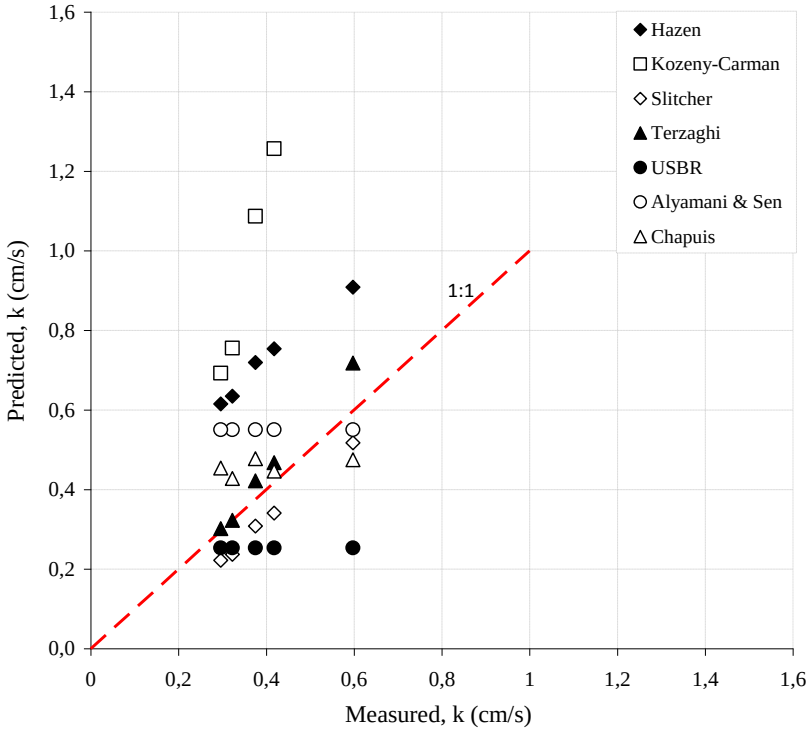

Figure 5. Predicted vs measured *k* values for the sands tested using various methods.

It is seen from the Figure 5 that Kozeny-Carman's formula can be of the interesting approach to focus on since its *k* values fall away above of the equality line on the plot. Likewise, Hazen method gave similar high values, may be because of the sorting

coefficient value (*C*) in the formula. Although it was intended to verify these approaches for the purpose of the present study, it is difficult to expect that Kozeny-Carman and Hazen methods are likely to be consistent with shape of the sands having same grain size described here. USBR, and Alyamani & Sen's approaches give the same *k* values for all measurements (0.2535, and 0.5691). Actually, the authors realized that these two methods are not very sensitive to the shape of soil grains classified as poor graded (*SP*). That could be because of the limited parameters employed in the equations. It is also interesting to note from the study by Odong (2007) that the Vukovic and Soro (1992) method, from which the emprical equations were derived, is dependent on a unique parameter, the coefficient of uniformity (C_u). Thus, the authors have postulated that *k* values of all the sands tested in this study have been remain as a constant value; however, in fact they all have different *k* values. Accordingly, it may give insight that any system of permability analysis which neglects the effect of the grain shape will be incomplete. Estimations by Chapuis are more accurate than the Hazen, and Kozeny-Carman. Overall results showed that Terzaghi and Slitcher methods are more useful equations to predict fairly well the *k* values of the soil samples tested in this investigation. The emprical equations used during this investigation, and results on the sands tested are presented in Table 3.

Table 3. Emprical equations and their implications on the sands tested in this paper.

Researcher/ Organization	**Equation**	**Sample**	**k (cm/sec)**
Hazen	$k = 6x10^{-4} x \frac{g}{v} x[1 + 10(n - 0.26)]x(d_{10})^2$	LBS*	0.6349
		TS-	0.7196
		NS+	0.6151
		CSS†	0.7540
		FAP‡	0.9087
Kozeny-Carman	$k = 8.3x10^{-3} x \frac{g}{v} x \left[\frac{n^3}{(1-n)^2}\right] x(d_{10})^2$	LBS	0.7556
		TS	1.0872
		NS	0.6926
		CSS	1.2566
		FAP	2.3808
Terzaghi	$k = 0.0084x \frac{g}{v} x \left[\frac{n - 0.13}{\sqrt[3]{1-n}}\right]^2 x(d_{10})^2$	LBS	0.3229
		TS	0.4220
		NS	0.3022
		CSS	0.4676
		FAP	0.7181
Chapuis	$k = 1.5x(d_{10})^2 x \frac{e^3}{1+e} x \frac{1 + e_{max}}{(e_{max})^3}$	LBS	0.4279

		TS	0.4776
		NS	0.4541
		CSS	0.4466
		FAP	0.4751
Slichter	$k = 1x10^{-2}x\frac{g}{v}xn^{3.287}x(d_{10})^2$	LBS	0.2372
		TS	0.3082
		NS	0.2224
		CSS	0.3408
		FAP	0.5175
USBR	$k = 4.8x10^{-3}x\frac{g}{v}x(d_{20})^{0.3}x(d_{20})^2$	LBS	0.2535
		TS	0.2535
		NS	0.2535
		CSS	0.2535
		FAP	0.2535
Alyamani & Sen	$k = 1300x[I_0 + 0.025(d_{50} - d_{10})]^2$	LBS	0.5691
		TS	0.5691
		NS	0.5691
		CSS	0.5691
		FAP	0.5691

LBS[*]:Leighton Buzzard Sand; **TS**[-]:Trakya Sand; **NS**[+]:Narli Sand; **CSS**[†]:Crushed Stone Sand; **FAP**[‡]:Fly Ash Pellet.

4. CONCLUSIONS

In this investigation, a particle size range (1.18- 0.6 mm) of five different sands having distinct shapes have been tested in a constant head permeability testing apparatus at a relative density (R_d) of about 35%. Also, already available empirical permeability equations have been briefly discussed for the estimation of coefficient of permeability values (k). Experimental results have showed a clear relation between the shape of the sands and the hydraulic conductivity values obtained. Differences between the predicted and measured k values conclude that the methods employed here are capable but not sufficient for correct prediction of k values. The tests results reported, and the readily available equations compared here in this paper show the followings:

(i) Sands having different shapes with the same grading characteristics (C_c, C_u, D_{10}, D_{30}, D_{50}, D_{60}) result in different k values.

(ii) Different e_{max} and e_{min} values for the sands having a same gradation curve have been obtained, due to the properties of grain shape.

(iii) Relatively rounded soil grains tested (apart from the fly ash pellets) have lower *k* values than the angular soil grains have.

(iv) Estimating the *k* values of soils by using grading characteristics can lead to underestimation or overestimation, unless the grain shape properties (roundness, sphericity) are taken into account.

(v) Empirical equations by Terzaghi and Slitcher give more accurate results than the other equations (Chapuis, USBR, Alyamani and Sen, Hazen, and Kozeny-Carman) employed to predict the *k* values of the soil samples tested in this investigation.

5. References

[1] Alyamani M.S., Sen Z. (1993). Determination of Hydraulic Conductivity from Grain-Size Distribution Curves. Groundwater, 31(4): 551-555.

[2] Carman, P.C. (1956). Flow of Gases through Porous Media. Butterworths Scientific Publications, London.

[3] Chapuis RP (2004) Predicting the Saturated Hydraulic Conductivity of Sand and Gravel Using Effective Diameter and Void Ratio. Can Geotech J 41: 787-795.

[4] Coduto, D. P. (1999). Geotechnical engineering: Principles and practice, Prentice-Hall, Upper Saddle River, N.J.

[5] Craig, R. F. (1997). *Craig's Soil Mechanics,* 2nd ed. Taylor and Francis, London.

[6] Das, B. M. (1997). *Advanced soil mechanics,* Taylor & Francis, Washington, D.C

[7] Das, B. M. (2008). *Advanced Soil Mechanics,* 3rd ed. Taylor and Francis, London.

[8] Hazen, A. 1892. Some Physical Properties of Sands and Gravels, with Special Reference to their Use in Filtration. 24th Annual Report, Massachusetts State Board of Health, Pub.Doc. No.34, 539-556

[9] Hazen, A. 1911. Discussion: dams on sand foundations. Transactions of the American Society of Civil Engineers, 73: 199–203.

[10] Holtz, R. D., and Kovacs, W. D. (1981) An introduction to geotechnical engineering, Prentice-Hall, Englewood Cliffs, N.J.

[11] Kenney, T.C., Lau, D., and Ofoegbu, G.I. 1984. Permeability of compacted granular materials. Canadian Geotechnical Journal, 21(4): 726–729. doi:10.1139/t84-080.

[12] Kozeny, J. 1927. Uber Kapillare Leitung Des Wassers in Boden. Sitzungsber Akad. Wiss.Wien Math.Naturwiss.Kl., Abt.2a, 136,271-306 (In German).

[13] Lambe, T.W., and Whitman, R.V. (1969). Soil mechanics. Wiley, New York

[14] Odong J (2007) Evaluation of the empirical formulae for determination of hydraulic conductivity based on grain size analysis. J Am Sci 3: 54-60.

[15] Powrie, W. (2004). *Soil Mechanics Concepts & Applications*, 2nd ed. Taylor and Francis, London.

[16] Santamarina, J.C. and Cascante, G. (1998), Effect of Surface Roughness on Wave Propagation Parameters, Geotechnique, vol. 48, no. 1, pp. 129-137.

[17] Shinohara, K., Oida, M., Golman, B. (2000). Effect of particle shape on angle of internal friction by triaxial compression test. Powder Technology. Vol. 107, pp.131-136.

[18] Slichter, C.S. (1898). Theoretical investigation of the motion of ground waters. 19th Annual Report.U.S. Geology Survey, USA.

[19] Sukumaran, B. and Ashmawy, A. K. (2001). Quantitative characterisation of the geometry of discrete particles. Geotechnique. Vol. 51, No. 7, pp. 619-627.

[20] Taylor, D. W. (1948). *Fundamentals of soil mechanics*, Wiley, New York

[21] Terzaghi, K. (1925). Principles of soil mechanics: V- Physical differences between sand and clay. Engineering News Records, Vol. 95, No. 23, pp. 912-915.

[22] Terzaghi, K., Peck, R.B. (1964). *Soil Mechanics in Engineering Practice*. Wiley, New York.

[23] USBR (1990). Earth Manual-Part 2, U.S. Department of the Interior Bureau of Reclamation, Denver, 1270 p.

[24] Vukovic M, Soro A (1992). Determination of Hydraulic Conductivity of Porous Media from Grain-Size Composition. Water Resources Publications, Littleton, Colorado.

[25] Zelasko, J.S., Krizek, R.J., and Edil, T.B. (1975). Shear Behavior of Sands as a Function of Grain Characteristics. Istanbul Conference on Soil Mech. Found. Eng., 1, 55-64.

Electrical Engineering I

2013/3/16 Saturday 09:00-10:30 Room 605

Session Chair: ***Prof. Ansgar Kern***

ICEAS 965

Differential Search Algorithm for Economic Dispatch with Valve-Point Effects

Mohd Herwan Sulaiman | *Universiti Malaysia Pahang*

ICEAS 1002

Development of Line Following Car using CCD Camera

Wan Rahiman | *Universiti Sains Malaysia*

Amre Puasa | *Universiti Sains Malaysia*

ICEAS 1038

Difference Grey Sliding-Mode Control of a UPS Inverter for Robust Output Voltage Tracking

En-Chih Chang | *I-Shou University*

Lung-Sheng Yang | *Far East University*

Rong-Ching Wu | *I-Shou University*

EECS 391

A FPGA-based Space Vector Controller With Power Stage

Ansgar Kern | *Technische Hochschule Mittelhessen*

EECS 438

Performance of Grid-connected Hybrid Photovoltaic/Fuel Cell/Battery Distributed Generation System

Ahmad M. Eid | *Aswan University*

ICEAS 965

Differential Search Algorithm for Economic Dispatch with Valve-Point Effects

MohdHerwanSulaiman
Sustainable Energy & Power Electronics Research (SuPER) Group
FakultiKejuruteraanElektrik&Elektronik
Universiti Malaysia Pahang
mherwan@ieee.org, herwan@ump.edu.my

Abstract

This paper introduces a new method for determining the feasible optimal solution of Economic Dispatch (ED) problems which is using the recently developed Differential Search (DS) algorithm. DS algorithm simulates the *Brownian-like random-walk* movement used by an organism to migrate. DS will seek for the optimal generation scheduling when the specific load is known so that the cost can be minimized without violating any constraints. The cost minimization also will give the significant impact to the total system losses. To demonstrate the effectiveness and feasibility of DS in solving ED, two well-known ED test systems with non-convex solution features have been tested and compared with some of the most recently published ED solution methods in literature. The results of this research show that DS is able to find more economical solution than those determined by other methods.

Keyword: Differential search algorithm (DS), economic dispatch, valve-point effects

1. Introduction

Power system is one of the complex systems of human's invention. One of the most important issue emerged in power system complexity is Economic Dispatch (ED) problem. ED is the fundamental problem which aims to find the optimal power generation to match with the demand at minimum cost by satisfying all the system constraints. In addition, the practical ED problems which are involving non-convex objective functions with equality and inequality constraints including the practical operation constraints of generators such as ramp rate limit, prohibited operating zones and generation limits make it harder to solve the global optimum using conventional methods, especially for larger systems. Small improvements in determining the optimal output scheduling can contribute to significant cost savings. Thus, there are a lot of researches and techniques have been proposed to solve ED problem.

In recent years, various methods have been proposed to solve ED problem in power systems: from analytical technique [1, 2] to artificial intelligence approaches[3-7]. Recently, new computational technique called swarm intelligence becoming the choice of many researchers in solving ED problem, such as particle swarm

optimization (PSO) [8, 9], firefly algorithm (FA) [10] and artificial bee colony (ABC) [11, 12]. The modification of PSO namely quantum-behaved PSO (QPSO) [13] and self-organizing hierarchical PSO (SOH-PSO) [14]also have been tempted to solve ED.

Although the said methodologies have been developed for ED, the complexity of the task reveals the necessity for development of efficient algorithms to accurately locating the optimum solution [10].This paper presents an application of Differential Search (DS) algorithm for solving non-convex ED problems with the valve loading effects. In this paper, DS is adopted to find the global optimum results of ED. DS algorithm simulates the Brownian-like random-walk movement used by an organism to migrate.

The layout of this paper is organized as follows: The ED problem is briefly discussed in Section 2. It followed by an overview of DS in Section 3. The proposed DS algorithm for solving ED is presented Section 4, followed by the case study results and discussion which are shown in Section 5. Finally, the conclusion is given in Section 6.

2. Economic Dispatch

In the economic dispatch (ED) problem with valve-point effects, the cost function takes the following form:

$$\min f = \sum_{i=1}^{n} F_i(P_i) \tag{1}$$

$$F_i(P_i) = \alpha_i P_i^2 + \beta_i P_i + \gamma_i + \left|\varepsilon_i \times \sin\left(\delta_i \times \left(P_i^{\min} - P_i\right)\right)\right| \tag{2}$$

where n is the number of generator units, $P_i^{min}$is the lower bound of P_i, α_i, β_i, and γ_i are coefficients of generator i, and ε_i and δ_i are parameters reflecting the valve-point effects. The cost function in (2) is subject to the power balanced constraints and individual generation limits as follow:

$$\sum_{i=1}^{n} P_i = P_D + P_L \tag{3}$$

$$P_{i(\min)} \le P_i \le P_{i(\max)} \quad i = 1, 2,\ldots,n \tag{4}$$

where$P_D$is the total load demand, $P_L$is the total loss and n is the total number of committed generator during the dispatched hour. Since the power loss is cannot avoided in interconnected power system, it must be taken into account to achieve as closed as practical economic dispatch by using the B-coefficient method [15], as follows:

$$P_L = \sum_{i=1}^{n}\sum_{j=1}^{n} P_i B_{ij} P_j + \sum_{i=1}^{n} B_{0i} P_i + B_{00} \tag{5}$$

3. Differential Search Algorithm

DS algorithm is inspired by migration of living beings which constitute superorganisms during climate change of the year. Migration behavior allows them to move from one habitat to more efficient habitat. They start to change their position by moving toward more fruitful areas. The movement of superorganism can be described by a *Brownian-like random-walk* model [16].

It is assumed that random solution of population is corresponding to the artificial-superorganism migration to global optimum solution of the problem. During the migration, the artificial-superorganism tests whether some randomly selected position are suitable for temporarily basis. If the position tested is suitable to stop over for a temporary during the migration, the members of the artificial-superorganism that made the discovery immediately settle at the discovered position and continue their migration from this position. DS search strategy may simultaneously use more than one individual and no inclination to correctly go towards the *best* solution of the problem which makes it has a successful search strategy for finding the solution of multimodal functions. Pseudo-code of DS algorithm can be obtained in [16].

4. Economic Dispatch Using DS

In solving ED using DS, a member of an artificial-organism firstly will be initialized. This comprises of the number of generations of the system that will be optimized which resulted a minimum cost by fulfilling all the constraints. The mechanism of finding stopover site at the areas is using a random searching process. Various random processes are utilized in DS until the optimal results are found by the migration of artificial-organisms.

Equations (1)-(2) were applied in the evaluation process of the ED problem. In order to deal with the inequality constraint: upper and lower limits of each generator, normally when the solutions obtained out of these boundaries, the algorithm will choose the boundary values. For equality constraint: power balance constraint, the penalty method has been used. The penalty value is reflected to the power balance mismatch and embedded in the cost function (1) as follows:

$$F = (F) + PF * abs[(\sum_{i=1}^{n} P_i) - P_D - P_L] \quad (3)$$

where*PF* is the penalty factor.

The advantage of DS is it has only two control parameter i.e. $p_1$and $p_2$which is normally are set to 0.3 [16] which provides the best solution. DS also is very simple. Nevertheless, to obtain good results, large number of iterations needs to be set in this

algorithm.

5. Simulation Results and Discussions

The proposed method has been applied to two test systems: a power system with 13-units and TAIPOWER 40-unit systems. The proposed method is compared with the recent techniques reported in literature.

5.1 13-units system

This test case consists of 13 generating units. The load demand of this test system is 1800 MW. The same parameters data of all units as given in[6] is utilized. Table 1 shows the best, average and worst results of different ED solutions methods. The outcomes of other methods shown in Table 1 have been directly quoted from the corresponding references. It can be seen that the best result of proposed method is slightly better compared to FA.Nevertheless, the overall performance of DS in term of average and worst is much better among the others reported. A detailed power generated by individual unit for proposed method and FA is shown in Table 2.

Table 1: The best, average and worst of different ED solution methods for the 13-units test system

Methods	Best ($/h)	Average ($/h)	Worst ($/h)
CEP [6]	18,048.21	18,190.32	18,404.04
PSO [9, 10]	18,030.72	18,205.78	NA
MFEP[6, 10]	18,028.09	18,192	18,416.89
HS [7]	17,965.62	17,968.563	18,070.176
FA[10]	17,963.83	18,029.16	18,168.80
DS	17,963.8292	17,966.6968	17,968.9467

Table 2: Individual power generation in the best result of proposed DS versus FA for the 13-units system

Unit	DS	FA
	Power (MW)	Power (MW)
1	628.3185307	628.31852
2	149.5996165	149.59952
3	222.7491063	222.74912
4	109.8665494	109.86655
5	60	109.86655
6	109.8665498	109.86655
7	109.8665484	109.86655
8	109.8665493	60
9	109.8665496	109.86655
10	40	40
11	40	40

12	55	55
13	55	55.00009
Total generation (MW)	1800	1800
Cost ($/h)	17963.829207639	17963.8307965424

5.2 TAIPOWER 40-units system

This test case consists of 40 generating units with non-convex fuel cost function incorporating valve loading effects. The required load demand to be met by all 40 generators is 10500 MW. Again, the detailed information of generating units of test system can be obtained in [6]. This test system is more complex than the previous case and any difference between ED solution methods can be better revealed in this test case. The DS has been executed for twenty times with various initialization of starting points. The obtained results of the proposed DS to resolve ED problem for this test system are tabulated in Table 3. In this table, the detailed comparisons of the best, average and worst solutions of the proposed DS and most recently published ED solution methods are shown by referring to the [10]. As seen from Table 3, the best solution of proposed method is better than those of all methods, indicating DS's higher efficiency to solve ED problem comparing with the other methods. Thus, the proposed method is proved to be the best among all methods so far. Due to the space constraint, the detailed results of the optimal solution of the proposed method including generation output of each unit for this test system isnot given.

Table 3: The best, average and worst of different ED solution methods for the TAIPOWER 40-units test system

Methods	Best ($/h)	Average ($/h)	Worst ($/h)
HGPSO	124,797.13	126,855.70	NA
PSO	124,350.40	126,074.40	NA
SPSO	123,930.45	124,154.49	NA
CEP	123,488.29	124,793.48	126,902.89
HGAPSO	122,780.00	124,575.70	NA
FEP	122,679.71	124,119.37	127,245.59
MFEP	122,647.57	123,489.74	124,356.47
IFEP	122,624.35	123,382.00	125,740.63
TM	122,477.78	123,078.21	124,693.81
EP–SQP	122,323.97	122,379.63	NA
MPSO	122,252.26	NA	NA
ESO	122,122.16	122,558.45	123,143.07
HPSOM	122,112.40	124,350.87	NA
PSO–SQP	122,094.67	122,245.25	NA
PSO-LRS	122,035.79	122,558.45	123,461.67

Improved GA	121,915.93	122,811.41	123,334.00
HPSOWM	121,915.30	122,844.40	NA
IGAMU	121,819.25	NA	NA
HDE	121,813.26	122,705.66	NA
DEC(2)-SQP(1)	121,741.97	122,295.12	122,839.29
PSO	121,735.47	122,513.91	123,467.40
APSO(1)	121,704.73	122,221.36	122,995.09
ST-HDE	121,698.51	122,304.30	NA
NPSO-LRS	121,664.43	122,209.31	122,981.59
APSO(2)	121,663.52	122,153.67	122,912.39
SOHPSO	121,501.14	121,853.57	122,446.30
BBO	121,479.50	121,512.06	121,688.66
BF	121,423.63	121,814.94	NA
GA–PS–SQP	121,458.00	122,039.00	NA
PS	121,415.14	122,332.65	125,486.29
FA	121,415.05	121,416.57	121,424.56
DS	**121,414.6185**	**121,414.8449**	**121,418.8120**

6. Conclusions

In this paper, a new approach to non-convex ED problems based on the DS has been presented. Two well-known test systems have been studied and comparisons of the quality of the solution and performance have been conducted against several of most recently published ED solution methods. Based on simulation study, it can be seen that the quality and reliability of the proposed DS was superior compared to other methods. In future, the proposed DS can be used to solve ED with more practical and complex constraints including prohibited zones, ramp rate limits and etc.

7. References

[1] M. Madrigal and V. H. Quintana, "An analytical solution to the economic dispatch problem," *Power Engineering Review, IEEE,* vol. 20, pp. 52-55, 2000.

[2] J. An, Y. Liu, H. Zhang, and Y. Sun, "Analytical study on economic dispatch," in *Control and Decision Conference (CCDC), 2010 Chinese*, pp. 583-585.

[3] T. Yalcinoz and H. Altun, "Power economic dispatch using a hybrid genetic algorithm," *Power Engineering Review, IEEE,* vol. 21, pp. 59-60, 2001.

[4] T. Yalcinoz, H. Altun, and M. Uzam, "Economic dispatch solution using a genetic algorithm based on arithmetic crossover," in *Power Tech Proceedings, 2001 IEEE Porto*, 2001, p. 4 pp. vol.2.

[5] S. Baskar, P. Subbaraj, and M. V. C. Rao, "Hybrid real coded genetic algorithm solution to economic dispatch problem," *Computers & Electrical Engineering,* vol. 29, pp. 407-419, 2003.

[6] N. Sinha, R. Chakrabarti, and P. K. Chattopadhyay, "Evolutionary programming techniques for economic load dispatch," *Evolutionary Computation, IEEE Transactions on,* vol. 7, pp. 83-94, 2003.

[7] L. d. S. Coelho and V. C. Mariani, "An improved harmony search algorithm for power economic load dispatch," *Energy Conversion and Management,* vol. 50, pp. 2522-2526, 2009.

[8] S. Ahmed Yousuf, "Economic dispatch using particle swarm optimization with bacterial foraging effect," *International Journal of Electrical Power & Energy Systems,* vol. 34, pp. 38-46, 2012.

[9] T. A. A. Victoire and A. E. Jeyakumar, "Hybrid PSO–SQP for economic dispatch with valve-point effect," *Electric Power Systems Research,* vol. 71, pp. 51-59, 2004.

[10] X.-S. Yang, S. S. Sadat Hosseini, and A. H. Gandomi, "Firefly Algorithm for solving non-convex economic dispatch problems with valve loading effect," *Applied Soft Computing,* vol. 12, pp. 1180-1186, 2012.

[11] S. K. Nayak, K. R. Krishnanand, B. K. Panigrahi, and P. K. Rout, "Application of Artificial Bee Colony to economic load dispatch problem with ramp rate limits and prohibited operating zones," in *Nature & Biologically Inspired Computing, 2009. NaBIC 2009. World Congress on*, 2009, pp. 1237-1242.

[12] S. Ozyon, C. Yasar, B. Durmus, and D. Aydin, "The application of artificial bee colony algorithm for the economic power dispatch with prohibited operating zone," in *Innovations in Intelligent Systems and Applications (INISTA), 2012 International Symposium on*, 2012, pp. 1-5.

[13] M. Ke, W. Hong Gang, D. ZhaoYang, and W. Kit Po, "Quantum-Inspired Particle Swarm Optimization for Valve-Point Economic Load Dispatch," *Power Systems, IEEE Transactions on,* vol. 25, pp. 215-222, 2010.

[14] K. T. Chaturvedi, M. Pandit, and L. Srivastava, "Self-Organizing Hierarchical Particle Swarm Optimization for Nonconvex Economic Dispatch," *Power Systems, IEEE Transactions on,* vol. 23, pp. 1079-1087, 2008.

[15] C. Po-Hung and C. Hong-Chan, "Large-scale economic dispatch by genetic algorithm," *Power Systems, IEEE Transactions on,* vol. 10, pp. 1919-1926, 1995.

[16] P. Civicioglu, "Transforming geocentric cartesian coordinates to geodetic coordinates by using differential search algorithm," *Computers & Geosciences,* vol. 46, pp. 229-247, 2012.

ICEAS 1002

Development of Line Following Car using CCD Camera

Wan Rahiman and Amre Puasa
School of Electrical and Electronic Engineering
Universiti Sains Malaysia,
Pulau Pinang, Malaysia
Email: wanrahiman@eng.usm.my

Abstract

A new era of autonomous vehicle or self driving is getting closer to reality in order to reduce traffic accident and improve mobility system, i.e. traffic efficiency. Therefore, the development of 1-10 scale prototype based on dynamic line tracking of a car within a visual environment by an intelligent control is developed. The line follower car is a mobile machine that can detect and follow the line along the track or road. This motion control is using visual servoing techniques to reduce computational overhead. The visual information received are extracted from horizontal line of each frame and then passed into a proportional steering system. This research paper demonstrates a prototype development of intelligent line follower control based on the intensity line profile is analysed using Design of Experimentals (DOE). The experimental approach to development and testing uses a small scale test track designed to imitate a real environment. DOE has the ability to discover the presence of interaction between the variables of the line profile. The discovery of interacting variables has led to breakthrough improvements in the efficiency of the detecting intensity of the line on the track.

Keywords: Analogue and Digital, Intelligence Systems, DOE

1. INTRODUCTION

The increasing rate of road accidents has become a major concern in the world especially during the festive seasons. It believes to have connection with the way we drive cars and also the rapid growth in population and motorisation encountered by the country. Therefore, driverless car technology is solutions are being worked out. Apart from this, the development of autonomous vehicle has been widely used in various fields like industries, research and development, academic, militaries and others. In order to make a fully automated driverless car that will use on the highway or for other applications, research of the development of integration vision data using small size mobile robot as prototype is coming to a point where the approaches,

algorithms and models need to be applied for further understanding of their usefulness and applicability towards any given project for a driverless car [1].

Nowadays, it has far outgrown the capabilities in terms of high end technologies solutions in the autonomous vehicle. With the fast growing costly development but yet with economic restraint, need for highly effective and efficient integrated between autonomous vehicle and details information about the path required intensive research efforts to create new intelligence algorithm for path following vehicle [2][3]. Particularly, intelligent system synthetically considers all sorts of different path sections, combining with communication means, transfers the information allocated rationally, balanced and interacted between vehicle sensors and surrounding infrastructure, to vehicle device for providing drivers with path to be chosen [5][6]. Therefore, the autonomous driving has become a hot and focus in the intelligent system. At present, the control theory and control technology, driven by the rapid development on the information technology and integrated circuit manufacturing technology, make a significant progress, such as the improved PID algorithm, adaptive control, neural networks and fuzzy control, robust control, sliding mode control, optimal control, as well as many other modern control algorithms have been widely used.

Visual information plays an important role in almost all areas in robotic applications. Vision sensors such as camera are mainly used for mapping and obstacles detection and usually object-referenced by other sensors [7][8][9]. For these reasons, we are focusing on the development in line follower car using Charge-Coupled Device (CCD) camera as detection sensor. Various techniques of extracting data from camera are available to meet the requirement of this particular application, which provides a flexible enhancement to the data collection technique. The study of visual sensor based on two basic issues. One is to determine on how to obtain raw data received correspondence from image sequences, and the other is to optimise collected data and use them as control input.

This development is a subset of the potential application of autonomous car capabilities but is well quantified. To improve the efficiency of the experiment that is to reduce or to remove the experimental bias, according to DOE method, it is suggested to use three basic principles of DOE. They are randomisation, replication and blocking [10][11].

2. SYSTEM DESCRIPTION

The car is a standard model kit that was used in the Freescale Cup Intelligent Car Racing competition. The model is equipped with a Futaba steering servo and MC9S12XS128 microcontroller. The model has been chosen because it gathers several advantages:

- *light weight and portable*: The basic element of the model is very light and portable that allow us to easily assemble electronic devices and light enough to be handled at the testing area. The chassis of the model is supplied with the 7.2V battery pack.
- *steering servo*: The servo motor is the most important part in this model and it is used to improve the steering. The front wheels are steered by a powerful servo motor in order to position the model on the track.
- *interface software*: There are continuing image data input capture from CCD camera through interface circuits to the microcontroller unit. Important sensory information such as steering wheel angle and wheels velocities and car status are directly accessible. The microcontroller unit will need to communicate with the camera to follow the path and speed of the car.

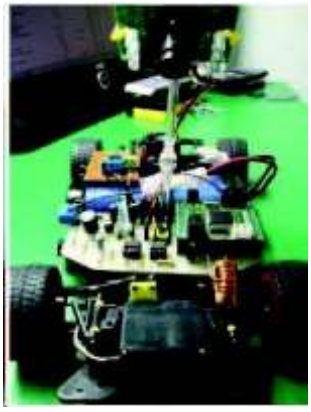

Fig. 1. Model Kit

All these features facilitate the process of modifying this model for autonomous driving. The fully equipped model is depicted in Fig 1. This mobile robot consists of two major control modules; speed control module and direction control module. Both control modules are responding based to the PWM signal generated by HCS12 MCU which is Freescale's MC9S12XS128 16-bit MCU. PWM value to control direction and speed are determined by heuristically. The overall system includes a chassis 1-10 scale and one CCD camera supplied by Axiom and Sparkfun, respectively.

A. Model modification

The model was competed in smart-race competition organize by FreeScale (Malaysia). Originally the model is a simple chassis and a servo with nothing special in its functions. In order to enhance the original model kit for autonomous driving, several modifications have been performed on the model. This section describes the mechanical and electrical changes that were necessary.

Since the model's tyres interact directly with the track surface, it will affect directly the model's stability and speed [12]. The tyres are provided by the organiser and we will follow and comply with term and regulation set for competition where modifications on the tyres are prohibited, we emphasise more to the existing tyre adjustment.

During the adjustment process, the new tyres after used for some time, will make the model grasping ability to the track surface increase and then decrease gradually. This is because after the tyres used for some time, the surface become rough and the

central part of the tyre are worn out, thus; the overall tyre's surface becomes more flat and grasping ability to the road surface increase. Thus, the tyre configurations are needed to accurately quantify the effect of wornness during the turn taken at sharp corner.

Correct alignment of the wheels maximise the ability of vehicle to run straight with a little steering effort. Adjustments on this parameter are made to enable the model to move in a straight line on track, increase the stability, enable wheels back to initial position automatically after turning, and reduce the spare parts' and tyre wear.

The CCD camera is attached to the mobile robot that acts as a sensor must made strong requirement such as mechanical robustness, selection angle of the camera for optimal visual, and dust proofness.

B. Mircocontroller

We re-engineered a standard model car that used for competition to autonomously navigate through a track. The autonomous car must be able to interpret its environment by gathering information from the CCD camera. A microcontroller of 16-bit embedded processor may then access communication reading from CCD camera and the servo motor to determine and control the position of the car. Plus, this information also is used to adjust the speed as needed. The block diagram of the overall system as shown in Fig. 2 illustrates the integration vision environment.

The microcontroller unit interfaces with an analogue camera to receive image through the general purpose I/O port. Then, IC LM1881 is used to extract video sync from the composite video data so that the microcontroller unit can sample the video data at the right time.

To allow the car to detect the black line on the track, CCD camera is used to scan the image and transporting a NTSC signal to microcontroller. Interfacing circuit between microcontroller and other devices such as camera, servo motor and DC motor are need to achieve project's objectives. Once the CCD camera receives start command, the onboard microcontroller initialises a scanning algorithm and records up in a set of registers. Thus, the microcontroller will receive inputs from cameras and will generate commands to the system.

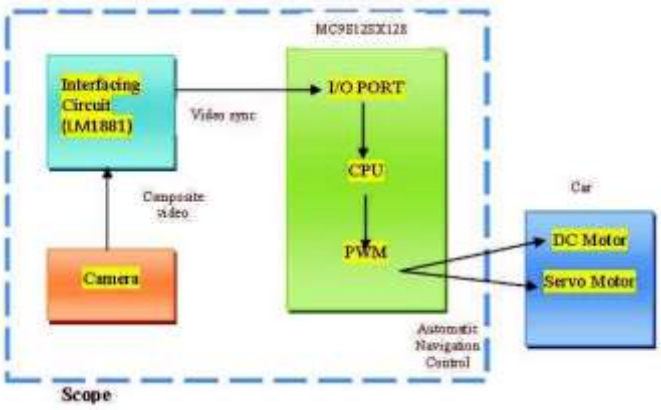

Fig. 2. Scope of Work

By using LM1881 video chips, analogue video signals can be extracted out and the image signal synchronisation can be identified. By inputting these signals and analogue video signals to the microcontroller, the right timing of the digital image information can be collected. Fig. 3 shows the video signal separation circuit schematic. Therefore, this microcontroller unit can be used to generate the automotive applications such as a controller for the intelligence car which is same as in this project.

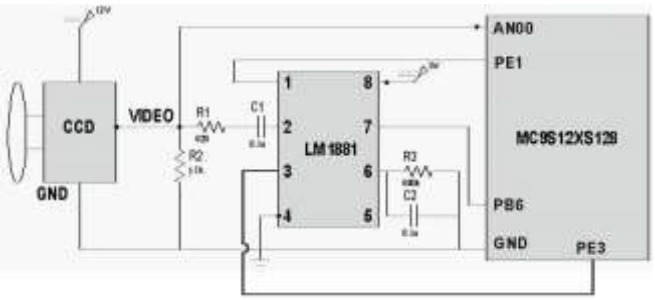

Fig. 3. Video Signal Separation Circuit Schematic

C. Scanning and track characteristic

Scanning is the method to break down the scene into picture elements and reassembling them on the screen. It is like human eye's motion when reading. The scene is divided into a series of horizontal lines during scanning and this is illustrated in Fig. 4. Camera will start to read the topmost of the horizontal line from left to right. It will produce a series of analogue signals that based on to the intensity of lights and shadows along that horizontal line. After finishing each horizontal line, it will retrace back to the left end of the next line below and follows process in the same way. By repeating this process, camera will reads the whole area of the scene, line by line, until to the bottom of the picture. Then the camera will scan the next image, and process continually repeated. So now, the camera has produced a rapid sequence of analogue impulses which is corresponding to the order of every picture lines for all images that had been captured. This visual technique is used in order to detect the line and follow it by using image processing for interpretation.

Fig. 4. The Principle of Scanning

The experimental track setup of the line follower car is depicted in Fig. 5. The mechanism design in the steer of the car is according to Ackerman principle. Thus, this principle provides the car to rotate and the wheels roll smoothly along the single transformation centre in order to stay on the test track. The track was made from three centimetre wide curves cut from white and secured to the field surface with black colour masking tape. The

masking tape on the paper provided high contrast path, which was easy to distinguish by thresholding of the image.

Using this track allowed us to obtain image information from CCD camera. Then process the information, calculates corresponding to control input and sends these back to the servo motor. Line follower car are dynamically unstable and require constant control input to prevent it from diverging from the test track. The main concern in any navigation system is safety. While car runs on the track, following car conditions have to be met:

CC1 Stay on the track and running smoothly; It is vital for the car to stay on its track to avoid any accident occurs.

CC2 Speed and break based on track conditions; If the car moves too fast, it will lose its grip on the track and thus will out of control and if the car moves too slow, more time is needed to reach the destination it will waste the time.

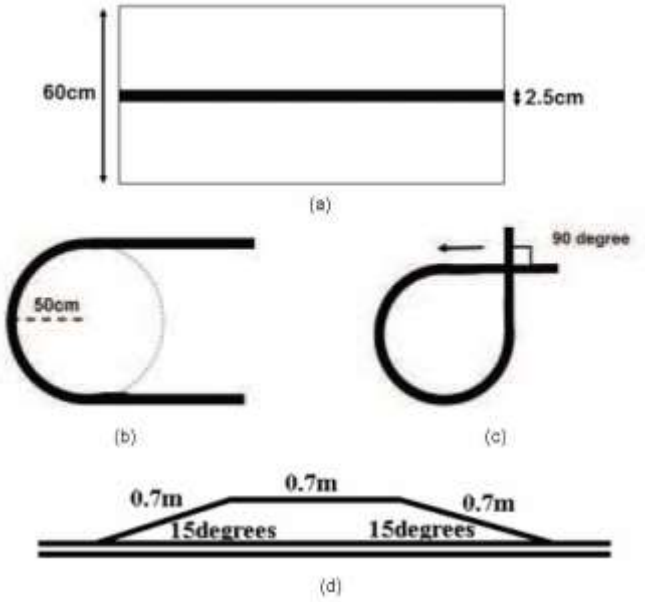

Fig. 5. (a) Surface of the track is white base plate with continuous black line. (b) The bending radius of the track should not be less than 50cm. (c) The track can intersect with a crossing angle

ollowing are the track conditions:

ΓC1 As shown in Fig. 5(a), the surface of the track is a white base plate with a continuous black line. The width of the track is 60cm while the width of the black line is 2.5cm. The black line is at the center of the track.

ΓC2 The minimum bending radius of the track is 50cm. As shown in Fig. 5(b), the condition is applied in every curve in the track.

TC3 Referring to Fig. 5(c), the track can be cross line with angle of 90◦.

TC4 There is an up-slope and down-slope on the track. According to Fig. 5(d), the maximum angle of the slope is 15° where slope will be in a straight section of the track.

The track is designed to have several challenging areas for the line follower car, including the hill climb, uneven surface (rattle track), S-conners, and sharp turn after a relatively long straight section where the car builds up speed.

3. THE TRACKING ANALYSIS VIA IMAGE SIGNALS

The car uses the CCD camera as an image sensor to trace the racing track. The image sensor produces the NTSC standard analogue video signals. The A/D converter of the S128 MCU is used, and with corresponding to the sub video signal produced by the original signal, image signal can be collected within the RAM of the microcontroller. By going through the algorithm software for image signal processing, the actual path of the black line can be known.

Analogue signal output from the CCD camera is a NTSC standard signal where horizontal scanning frequency is about 15.734kHz and vertical scanning frequency is 59.94Hz. Odd field scans first and then followed by even field to complete one cycle field which means that if scanning frequency of odd field and even field is approximately 30Hz, then the scanning frequency for one field is 59.94Hz.

By referring the NTSC standard specification on National Instrument datasheet, scanning period can be calculated by

$$f_0 = \frac{1}{T} \tag{1}$$

where f_0 is the fundamental frequency and T is the fundamental period of a cycle. As expressed by Eq. 1, cycle period is the reciprocal of frequency. That is, the product of frequency or number of cycle per second and the cycle period equals one second. It is important to note that for analogue standard colour NTSC, the line frequency for horizontal line rate is 15,734 line per second and by using Eq. 1 we obtain

$$T_H = \frac{1}{15.734 \times 10^3}$$

$$= 63.6\mu sec$$

However, based on NTSC specification on video format, active line duration for NTSC format is only $52.2\mu sec$. For now, all calculation for data sampling will be used active line duration which is $52.2\mu sec$. And vertical scanning period is

$$T_V = \frac{1}{59.94}$$

$$= 16.68\mu sec$$

By using LM1881 video sync separator, the odd even field can be identified by the microcontroller through the detection of logic 1 or 0 of digital I/O. Using A/D convertor of the microcontroller, the NSTC signal from the camera is converted to digital format. The complete A/D process need 14 cycles. In order to sample more data from the NTSC signal, phase-locked loop (PLL) circuit is used to boost up the A/D conversion clock. The setting of the PLL module is adjusted to boost the bus clock frequency from 8MHz to 10MHz. From that signal, a locking range in Voltage Controlled Oscillator, f_{VCO}, and a reference clock, f_{REF}, as well as bus frequency, f_{BUS}, are calculated [13] as follows

Table 1

Determination of Centre Point

Num. of array	P1	P2	P3	P4	P5	P6	P7	P8	P9	P10
ATD value	74	75	74	74	42	43	75	75	74	74
Illustration										

$$f_{VCO} = 2 \times f_{osc} \times \frac{SYNDIV + 1}{REFDIV + 1} \quad (2)$$

$$f_{PLL} = \frac{f_{VCO}}{2 \times POSTDIV} \quad (3)$$

$$f_{BUS} = \frac{f_{PLL}}{2} \quad (4)$$

Number of data sampling A/D is performed through Eqs. (2),(3) and (4). The frequencies in units of MHz are picked from the frequency list-box [13]. The frequencies are wrote synthesizer register (SYNR) that initialises into the lock detector bit with PLL and Bus sample rate of 64MHZ and 32MHz, respectively. The A/D conversion time of the measurement signal can be defined as

$$A/D\ conversion\ time = \frac{1}{f_{BUS}} \times 14 \quad (5)$$

In the calculation, the relative total number of sample data of a particular image with respect to one horizontal scanning means the A/D of S12XS MCU can be sampled around 119 data. After determining the number of sample data, the program started by initialising the PLL module and also the PWM channels. After that, the program will wait for the first vertical sync of the video data before entering an infinite loop. The program will always acquire the video data from an odd field. There are 262.5 video lines per field. The program will enter a nested 'for' loop to count the number of video lines gone through until there are 240 lines, which means a complete odd field has been scanned. The video data are the input from AN00, which are stored in a one-dimensional array, namely Cdata[118].

At the even field, data store in array elements is accessed to determine the track position. Then, the relative position of the centre point in the array is calculated. The relative position will be used to calculate the new PWM value to control the car steering. After that, the new PWM value to control the car speed will be determined.

The system will wait for the odd field of the next frame to sample the new video data again. The process of getting video data and calculate the new PWM value will go on as it is an infinite loop.

CCD camera is used to identify the pattern of the track. Since signal of the camera changes rapidly, the signal is needed to be stimulated separately. The IC LM1881 circuit is therefore being designed where it is used to extract odd/even field information of the camera. LM1881 also allows the output from the CCD camera to be collected in a normal timing. Based on the analysis of the data for the A/D of

MC9S12XS128 using BDM from the Code Warrior development tool, it is clearly that the value of the dark line varies with the changes of the surrounding. For example, if the data of the dark line are collected in a darker area, the value in the MC9S12XS128 will be around 43. If the data is collected in a bright area, the value in the MC9S12XS128 will be around 75.

Therefore, to allow MC9S12XS128 to differentiate the dark line efficiently regardless of the surrounding conditions, the threshold value is being determined each time after the data from the camera is being collected by using Eq. 6. Values lower than the threshold is considered as the dark line. The threshold value is determined by

$$TLV = k(min + max) \tag{6}$$

where TLV is the threshold limit value, k the constant value, min is the minimum value data and max is the maximum value data from one-dimensional array.

The constant value must be smaller than 0.5 and it is set at 0.5. The system will store single horizontal scan line data input in one-dimensional array which is named as Cdata in this project and this data is stored in digital value. Fig. 6 shows part of the video data stored in one-dimensional array Cdata [118] where the Analogue to Digital (ATD) value of video line can be seen when it is expanded. The value is subjected to change depending on the threshold and brightness of the area covering the track.

4. EXPERIMENTAL AND DISCUSSION

The goal of calculation using the methods of finding minimum and maximum value in a one-dimensional problem of sites is to find the threshold values of point set when the image processing unit configured the output of image data supplied. In this work, the system will search and store the minimum and maximum value within the input range. For instance, in one horizontal line scanning, we can determine the maximum ATD value is 75 and the minimum value is 42 (refer Table I). Thus, by using Eq. 6, the threshold value of this system is 59. This value will be compared to each of the input values. When ATD value is lower than the threshold value, the system will consider as a black surface or black line. At this particular line, *P5* and *P6* are lower than the threshold value, it considers as black lines. So, the system can detect bright-to-dark transitions (*P5*) as well as dark-to-bright transitions (*P6*). Centre point of black line can be determined by using

$$Centre\ point = \frac{P5 + P6}{2} \tag{7}$$

Based on Eq. 7, the centre point is *P6*. Calculation in this system is in an integer value and the centre point value is 5.5. Thus, system will consider black line at *P6*. *P6* is slightly close to *P7* which is not the black line anymore. As a result, value for PWM will affect as well as servo motor that turning the front wheel. In the case of number of black detected increase, error in the system will be reduced. So, to reduce error in

the system, Design of Experiment (DOE) is used to determine highest black line can be detected.

There are three major factors that can be considered as a factor to the number of black lines, n, detected; the delay time after 1 data store in Cdata [118], horizontal line that system take from camera image, and angle of the camera to take an image. All data collected and all analysis has been done by using Minitab software.

Table II

ANOVA For Each Factors

Source	DF	Seq SS	Adj SS	Adj MS	F	P
Delay	4	298.4400	298.4400	74.6100	239.13	0.000
Angle	4	53.3200	53.3200	13.3300	42.72	0.000
Line	4	12.5600	12.5600	3.1400	10.06	0.000
Delay*Angle	16	18.8400	18.8400	1.1775	3.77	0.000
Delay*Line	16	6.2000	6.2000	0.3875	1.24	0.246
Angle*Line	16	7.7200	7.7200	0.4825	1.55	0.094
Delay*Angle*Line	64	21.9200	21.9200	0.3425	1.10	0.325
Error	125	39.0000	39.0000	0.3120		
Total	249	458.0000				

In Analysis of Variance

$$H_0 : \mu_i = \mu_j \quad (8)$$

$$H_1 : \mu_i \neq \mu_j \quad (9)$$

where the subscripts i and j represent two different population called treatment. The null hypothesis, H_0, and alternative hypothesis, H_1. The null hypothesis is assumed all factors have same number of black detected. Alternative hypothesis where there has some variation of mean on the number of black detected. The Eqs. (8) and (9) have to satisfy the rejection condition of H_0 if $|\bar{X}_i - \bar{X}_j| > T$. The T value is computed using Eq. (10).

It is clearly shows that at Table II, P-value are less than 0.05 for each of the factors that use in this evaluation. Hence, H_0 is rejected and it can conclude that the treatment means differ; that is, the delay, angle and line setting significantly affect the meaning of black detected. The interaction between delay and angle is also a significant (P-value < 0.05) and other interaction is not significant.

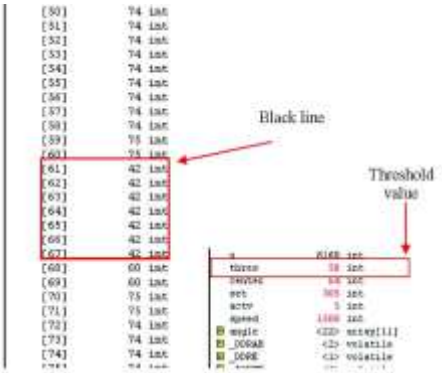

Fig. 6. Part of Video Data Stored in One-dimensional array

Based on Fig. 7, for the delay factor, it can show clearly that there is extremely different from delay 0 and delay 1 compared to others level in same factor. However, based on this figure only, conclusions cannot be made either the difference is significant or not. Therefore, it needs to compare each mean value using Tukey's test to show the difference between levels.

Here an example of Tukey's test for Delay factor. The T - value of delay factor is:

$$T = q_{\alpha}(a,f)\sqrt{\frac{MS_E}{m}} \quad (10)$$

where value from attached studentized range table, q, mean square error from ANOVA table, MS_E, the upper α percentage of point q, the number of degrees of freedom associated with the MS_E, f, and number of replicates per treatment, m. To use a fix significance level approach, we select α is 0.05 and f is 245 degrees of freedom error. By using Table Percentage Points of the Studentized range [14] gives T-value is 2.2022. This value needs to compare with every difference between levels in delay factor. Any pairs of treatment averages that differ in absolute value by more than 2.2022 would imply that the corresponding pairs are significantly different. Again, on Table II, there are factors that having an interaction that affects the number of black detected, they are angle and delay factors. The contour levels are plotted in the curves and the area between the curves is coloured to indicate interpolated values.

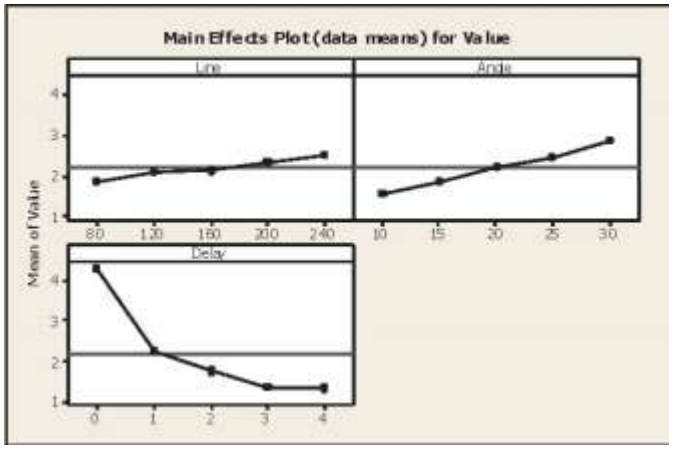

Fig. 7. Main Effect Plot

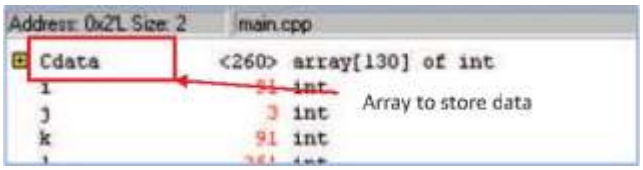

Fig. 8. One-dimensional Array Data

Based on three contour plots calculated using DOE analysis, the best setting of the camera to capture an image is when 0 delay, 30 angle and line 240.

A. Pre-run Image Scanning on Track

Fig. 8 shows the video data that are stored in a one-dimensional array Cdata [118], where the data of video line can be seen by expanding the row. When Cdata is expanded, the values in the array of size 118 are shown. The array element number is getting bigger as the video line goes from left to right. The array elements with 11 of the numbers from leftmost do not take into consideration. This is because there is front porch of a video line respectively.

A range of white pixel is $70 < white < 80$ and for black pixel is $40 < black < 50$. The black pixel is within array element number 55 to 76 (refer to Fig. 6). By comparing the threshold value and calculation of centre point of the black line detected, it is shown that the next condition of the track is in a straight line. PWM value to the servo motor should also be changed so that the car can steer towards the position.

5. CONCLUSION

In this project, the car is successfully run on the track and finishes the line. The proposed system of autonomous car using video processing to follow the black line on the track has been presented. Two modules and several techniques applied based on vision sensor have been shown that the system will react based on continuity input image data through interface circuits to the microcontroller to store in one-dimensional array (Cdata [118]). The system consists of two major control modules which is speed control module and direction control module. Both control modules are responding based to the PWM signal generated by HCS12 MCU which is Freescale's MC9S12XS128 MCU.

However, the limitation on this system where the system does not have any feedback for speed control module. It is an open-loop control system. There is a possibility that output speed is not linear with the PWM that generated by the MCU. If there is no linearity between car model speed and the PWM duty cycle, the stability of the car will be affected.

6. ACKNOWLEDGEMENT

We are very grateful to Universiti Sains Malaysia for providing funding under the RUI grant (1001/PELECT/814170) in order to pursue our research in autonomous car technology.

7. REFERENCES

[1] U. Franke, D. Gavrila, A. Gern, R. Janssen, F. Paetzol, and C. Wohler,"From door to door. Principles and applications of computer vission for driver assistant systems", in *L. Valcic, F. Harashima, M. Parent (Eds.), Intellligent Vehicles Technologies, Butterworth Heinemann, Oxford*, pp. 131-188, 2001.

[2] H. Weiser, P. Schulenberg, H. G¨ollinger, and T. Michler, "Autonomous Driving on Vehicle Test Tracks: Overview, Implementation and Vehicle Diagnostics", in *Proceddings of the IEEE Conference on Intelligent Vehicles*, vol. 2, pp. 62-67, 1998.

[3] F. Pin, and Y. Watanabe, "Driving A Car Using Reflexive Fuzzy Behaviours", in *IEEE International Conference on Fuzzy Systems*, vol. 2, pp. 1425-1430, 1993.

[4] T. Yamaguchi, E. Sato, and Y. Takama, "Intelligent Space and Human Centered Robotics", in *IEEE Trans. Ind. Electron*, vol. 50, pp. 881-889, 2003.

[5] R.C. Luo, and T.M. Chen, "Autonomous Mobile Target Tracking System Based On Grey Fuzzy Control Algorithm", in *IEEE Trans. Ind. Electron*, vol. 47, no. 4, pp. 920-931, 2004.

[6] O. Khatib, "Real-time Obstacle Avoidance For Manipulators and Mobile Robots", in *The International Journal of Robotics Research*, vol. 5, no. 1, pp. 90-98, 1986.

[7] E.D. Dickmanns, "Vision for Ground Vehicles: History and Prospects", in *International Journal of Autonomous Systems 1*, vol. 5, pp. 1-44, 2002.

[8] J. M. Armingol, A. de la Escalera, C. Hilario, J. M. Collado, J. P. Carrasco, M. J. Flores, J. M. Pastor, and F. J. Rodrguez, ”IVVI: Intelligent Vehicle based on Visual Information”, in *Robotics and Autonomous Systems*, vol. 55, no. 12, pp. 904-916, 2007.

[9] A. de la Escalera, J. M. Armingol, F. Rodriguez, and J. M. Pastor, ”Visual sign information extraction and identification by deformable models for intelligent vehicles”, in *IEEE Transactions on Intelligent Transportation Systems*, vol. 5, no. 2, pp. 57-68, 2004.

[10] J. Antony, *Design of Experiments for Engineers and Scientists*, Elsevier Science & Tecnology Books, 2003.

[11] D.C. Montgomer, *Design and Analysis of Experiments*, 8Ed, John Wiley & Son, 2013.

[12] Yao Li, Jianwu Zhang, and Xiqiang Guan, ”Estimation of Vehicle Parameters and Road Friction Using Steering Torque and Wheel Speeds” *WSEAS Transactions Systems*, vol. 1, no. 1, 2012.

[13] “Microcontroller MC9S12XS256 Reference Manual” *Freescale MC9S12XS Family Manual*, rev. 1.13,2012

[14] D.C. Hoaglin, F. Mosteller, and J.W. Tukey, *Fundamentals of Exploratory Analysis of Variance*, John Wiler & Son, 1991.

ICEAS 1038

Difference Grey Sliding-Mode Control of a UPS Inverter for Robust Output Voltage Tracking

En-Chih Chang
Department of Electrical Engineering, I-Shou University, Kaohsiung City 84001, Taiwan, R.O.C.
enchihchang@isu.edu.tw

Lung-Sheng Yang
Department of Electrical Engineering, Far East University, Tainan City 74448, Taiwan, R.O.C.
yanglungsheng@yahoo.com.tw

Rong-Ching Wu
Department of Electrical Engineering, I-Shou University, Kaohsiung City 84001, Taiwan, R.O.C.
rcwu@isu.edu.tw

The corresponding author: enchihchang@isu.edu.tw

Abstract

In this paper, a sliding-mode control (SMC) with difference grey prediction is proposed and applied to UPS inverters. Though the SMC is insensitive to system uncertainties within expected limits, the chattering and steady-state errors may occur when uncertainty values are overestimated or underestimated. The chattering and steady-state errors will cause inexact tracking control, and even deteriorate the system performance. Thus, to alleviate the chattering and steady-state errors, a mathematically simple and computationally fast difference grey prediction is employed for SMC and therefore low distorted voltage in UPS inverter output can be obtained. Experimental results for the UPS inverters are performed in support of the proposed method.

Keyword: Sliding-mode control (SMC), Difference grey prediction, UPS inverters, Chattering, Steady-state errors

1. Introduction

The limitation of low distortion in the output voltage of the uninterruptible power supplies (UPS) and fast dynamic response when feeding distorting loads are the challenging issues, which have stimulated the development of a variety of different methods. Control of UPS inverter is a tracking control problem, which achieves a sinusoidal AC output voltage tracking and minimizes the total harmonic distortion in the presence of disturbances and plant parameter variations. Conventionally, when the system has external load variations and other disturbances, a PI controller is used in

the UPS inverter for the improvement of the system operating characteristics. However, the PI controller can not overcome the sensitiveness for system parameters variation [1], [2]. Thus, to avoid the system uncertainties, robust nonlinear control strategy can be used, i.e., sliding-mode control (SMC). Essentially, the SMC utilizes a high speed switching control law to force the state trajectory of the plant which is held in the sliding surface and then the state trajectory was along this surface to the origin [3], [4]. Consequently, the expected control target to the nonlinear system can be attained by the selection of the appropriate sliding surface. The benefits of SMC are insensitive to the parameter variations of the plant and the external disturbances. However, in the SMC, the upper/lower bound of the system uncertainties is supposed as the maximum/minimum value. The chattering and steady-state errors may occur. In order to overcome the chattering and steady-state errors, previous works have used adaptive or observer controllers to estimate the bound of the external load disturbance by complex mathematical models or complex calculation [5], [6]. The grey theory has been proposed by Deng., and many applications in a variety of fields have been developed [7], [8]. The grey model is built based on first-order differential equation, and used some hypothesis and mathematical approximation to transfer a continuous form into discrete form. Such a transformation will confront some unconquerable problems, such as the limited sampling frequency, sample/hold effects and discretization errors. Using difference equation replaces differential equation to build grey model that is a reasonable and precise method [9]. This paper employs a mathematically simple and computationally efficient difference grey prediction to alleviate the chattering/ steady-state errors when the upper/lower of the system uncertainties is overestimated/ underestimated. The grey prediction requires only several output data to achieve a grey model and to forecast a future value without complex calculation. Thus, the proposed method will yield a closed-loop UPS inverter with low THD, fast dynamic response, chattering elimination, and steady-state errors reduction under different types of load. The organization of this paper is as follows: Section 2 describes the mathematical modeling of the UPS inverter. The proposed SMC with difference grey prediction is designed in Section 3. Section 4 shows the experimental results. Section 5 concludes the paper.

2. Mathematical Modeling of UPS Inverter

A single-phase UPS inverter is shown in Fig. 1, consists of a LC filter and a load resistance. The LC filter and the load can be considered as the plant of a control loop.

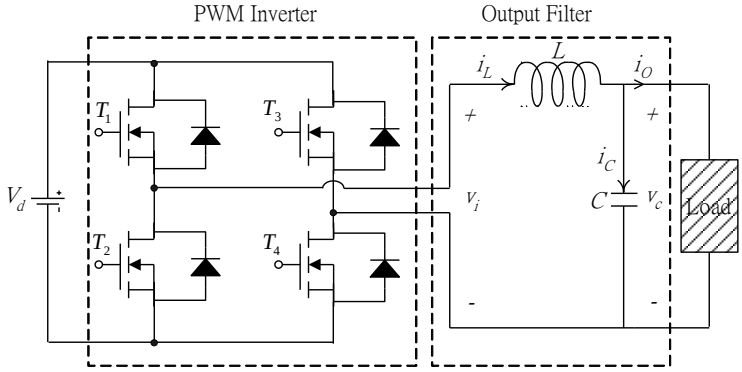

Fig. 1 UPS inverter with LC filter

Fig. 2 shows the block diagram of the LC filter. Thus, the state space equation of the LC filter can be represented in the following state space form.

$$\begin{bmatrix} \dot{v}_C \\ \dot{i}_L \end{bmatrix} = \begin{bmatrix} 0 & \frac{1}{C} \\ -\frac{1}{L} & 0 \end{bmatrix} \begin{bmatrix} v_C \\ i_L \end{bmatrix} + \begin{bmatrix} 0 \\ \frac{1}{L} \end{bmatrix} v_i + \begin{bmatrix} 1 \\ 0 \end{bmatrix} \left(\frac{1}{C} \dot{i}_O \right) \tag{1}$$

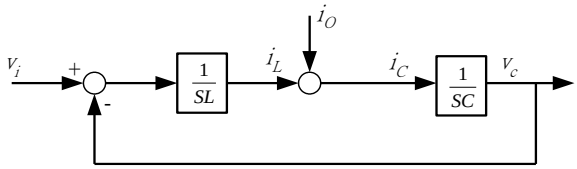

Fig. 2 The block diagram of the LC filter

We use the state vector $\begin{bmatrix} \dot{v}_C & \ddot{v}_C \end{bmatrix}$ to replace of the state vector $\begin{bmatrix} \dot{v}_C & \dot{i}_L \end{bmatrix}$, and the state space form is rewritten as follows.

$$\begin{bmatrix} \dot{v}_C \\ \ddot{v}_C \end{bmatrix} = \begin{bmatrix} 1 & 0 \\ -\frac{1}{LC} & 0 \end{bmatrix} \begin{bmatrix} v_C \\ \dot{v}_C \end{bmatrix} + \begin{bmatrix} 0 \\ \frac{1}{LC} \end{bmatrix} v_i + \begin{bmatrix} 0 \\ 1 \end{bmatrix} \left(-\frac{1}{C} \dot{i}_O \right) \tag{2}$$

From Fig. 2, the output voltage, $v_o = v_c$ is expected to track a sinusoidal ac voltage, v_{ref}. If the output voltage, v_O tracks a reference voltage, v_{ref} strictly, the difference measure, between v_o and v_{ref} can be converged to zero. Thereby, define $e_1 = v_{ref} - v_O$ and $e_2 = \dot{e}_1$. Then, the error dynamic state space equation is derived as

$$\begin{bmatrix} \dot{e}_1 \\ \dot{e}_2 \end{bmatrix} = \begin{bmatrix} 0 & 1 \\ -a_2 & -a_1 \end{bmatrix} \begin{bmatrix} e_1 \\ e_2 \end{bmatrix} + \begin{bmatrix} 0 \\ -b \end{bmatrix} u + \begin{bmatrix} 0 \\ f \end{bmatrix} \tag{3}$$

where $a_1 = \frac{K_C K_{PWM}}{L}$, $a_2 = \frac{1}{LC}$, $b = \frac{K_C K_{PWM}}{LC}$, $f = d + \Gamma$, $d = \frac{1}{C} \dot{i}_O$, $\Gamma = a_1 v_{ref} + a_2 \dot{v}_{ref} + \ddot{v}_{ref}$.

3. Control Design

3.1 Sliding-mode control

The sliding surface, σ is selected as

$$\sigma = c_1 e_1 + e_2 \tag{4}$$

where c_1 is constant.

As a consequence of (4), it is also

$$\dot{\sigma} = c_1 \dot{e}_1 + \dot{e}_2 \tag{5}$$

Substituting the system state equation (3) into (5), we have

$$\dot{\sigma} = c_1\dot{e}_1 + \dot{e}_2 = c_1 e_2 - a_2 e_1 - a_1 e_2 - bu + f \tag{6}$$

Let $a_i = a_{i0} + \Delta a_i$, $i = 1, 2$, $b = b_0 + \Delta b$.

where a_{i0} and b_0 are nominal values of a_i and b_0 , and Δa_i and Δb are the deviations, respectively.

Then, decompose the control function, *u* into

$$u = u_{eq} + u_s \tag{7}$$

where u_{eq}, called the equivalent control, is used to control the overall behavior of the system. The equivalent control is defined as follow:

$$\dot{\sigma}\big|_{u=u_{eq},\, a_1=a_{10},\, a_2=a_{20},\, b=b_0,\, \dot{i}_O=0} = 0 \tag{8}$$

When in sliding motion, let $\sigma = 0$, then

$$e_2 = -c_1 e_1 \tag{9}$$

$$\therefore u_{eq} = \frac{-a_{20}e_1 + c_1 a_{10}e_1 - c_1^2 e_2 + a_{20}v_{ref} + a_{10}\dot{v}_{ref} + \ddot{v}_{ref}}{b_0} \tag{10}$$

The u_s is used to suppress the parameter variations. This function is constructed in the following:

$$u_s = \Phi_1 e_1 + \Phi_2 e_2 + \Phi_3 \tag{11}$$

The condition for the existence of sliding motion is

$$\sigma\dot{\sigma} < 0 \tag{12}$$

Substituting (10) and (11) into (12), one has

$$\begin{aligned}
\sigma\dot{\sigma}\big|_{u=u_{eq}+u_s} &= c_1 e_2 - a_2 e_1 - a_1 e_2 - b_0 u_{eq} - \Delta b u_{eq} - b u_s \\
&\quad + d + a_2 v_{ref} + a_1 \dot{v}_{ref} + \ddot{v}_{ref} \\
&= c_1 e_2 - a_2 e_1 - a_1 e_2 - \left[\left(1 + \frac{\Delta b}{b_0}\right)\cdot(-a_{20}e_1 + \right. \\
&\quad \left. + c_1 a_{10}e_1 - c_1^2 e_1 + a_{20}v_{ref} + a_{10}\dot{v}_{ref} + \ddot{v}_{ref}\right) \\
&\quad - b\Phi_1 e_1 - b\Phi_2 e_2 - \Phi_3 + d \\
&\quad + a_2 v_{ref} + a_1 \dot{v}_{ref} + \ddot{v}_{ref} \\
&= \left[-\Delta a_2 e_1 + (c_1^2 - c_1 a_{10})\cdot\left(1 + \frac{\Delta b}{b_0}\right) + \right. \\
&\quad \left. + \frac{\Delta b}{b_0} a_{20} - b\Phi_1\right] e_1\sigma + (c_1 - a_1 - b\Phi_2) e_2\sigma \\
&\quad + \left[\Delta a_2 v_{ref} + \Delta a_1 \dot{v}_{ref} - \left(1 - \frac{\Delta b}{b_0}\right)\cdot(a_{20}v_{ref} + \right. \\
&\quad \left. + a_{10}\dot{v}_{ref} + \ddot{v}_{ref}) + d - b\Phi_3\right]\sigma < 0
\end{aligned} \tag{13}$$

Thus,

$$\Phi_1 = \begin{cases} \alpha_1 < \inf\left\{\left[\Delta a_2 e_1 - (c_1^2 - c_1 a_{10})\cdot\left(1 + \frac{\Delta b}{b_0}\right) - \right.\right. \\ \qquad \left.\left. - \frac{\Delta b}{b_0} a_{20}\right] \Big/ b\right\} \quad \text{if} \quad e_1\sigma > 0 \\ \beta_1 > \sup\left\{\left[\Delta a_2 e_1 - (c_1^2 - c_1 a_{10})\cdot\left(1 + \frac{\Delta b}{b_0}\right) - \right.\right. \\ \qquad \left.\left. - \frac{\Delta b}{b_0} a_{20}\right] \Big/ b\right\} \quad \text{if} \quad e_1\sigma < 0 \end{cases} \tag{14}$$

$$\Phi_2 = \begin{cases} \alpha_2 < \inf[(a_1 - c_1)/b] & \text{if} \quad e_2\sigma > 0 \\ \beta_2 < \sup[(a_1 - c_1)/b] & \text{if} \quad e_2\sigma < 0 \end{cases} \tag{15}$$

$$\Phi_3 = \begin{cases} \alpha_3 < \inf\left\{\left[-\Delta a_2 v_{ref} - \Delta a_1 \dot{v}_{ref} + \dfrac{\Delta b}{b_0} \cdot (a_{20} v_{ref} + \right.\right. \\ \qquad \left.\left. + a_{10}\dot{v}_{ref} + \ddot{v}_{ref}) - d \right] / b \right\} & \text{if} \quad \sigma > 0 \\ \beta_3 > \sup\left\{\left[-\Delta a_2 v_{ref} - \Delta a_1 \dot{v}_{ref} + \dfrac{\Delta b}{b_0} \cdot (a_{20} v_{ref} + \right.\right. \\ \qquad \left.\left. + a_{10}\dot{v}_{ref} + \ddot{v}_{ref}) - d \right] / b \right\} & \text{if} \quad \sigma < 0 \end{cases} \tag{16}$$

where the symbols inf and sup denote infimum and supremum, respectively.

3.2 Difference Grey Prediction

The basic idea of the grey system is to establish an approximation model of the unknown or partially known system. By the accumulated generating operation (AGO) and according to the measurable original data, the grey modeling procedure can be described as follows:

Step 1: Gather the original sample data sequence

$$x^{(0)} = \left\{ x^{(0)}(k), \quad k = 1, 2, ..., n \right\}. \tag{17}$$

Step 2: Mapping generating operation (MGO)

The data sequence of the system may be positive or negative. We use the MGO to map the negative data to the relative positive data.

$$x_{new}^{(0)} = \left\{ x^{(0)}(k) + bias, \quad k = 1, 2, ..., n \right\} \tag{18}$$

where *bias* is constant.

Step 3: Take Accumulated generating operation (AGO) for $x_{new}^{(0)}$

$$x_{new}^{(1)}(k) = \sum_{i=1}^{k} x_{new}^{(0)}(i) \ , \quad k = 1, 2, ..., n \ . \tag{19}$$

Step 4: Construct the difference equation model

The linear difference equation grey prediction model is established as

$$x_{new}^{(1)}(k+2) + M x_{new}^{(1)}(k+1) + N x_{new}^{(1)}(k) = 0 \tag{20}$$

where M and N are the coefficients of the difference equation grey prediction model that needs to estimate their values.

The (20) is rewritten as the following matrix form

$$\left[-x_{new}^{(1)}(k+1) \quad -x_{new}^{(1)}(k) \right] \begin{bmatrix} M \\ N \end{bmatrix} = \left[x_{new}^{(1)}(k+2) \right]. \tag{21}$$

Let $k = 1, 2, ..., n-2$ and (21) will be

$$\begin{bmatrix} -x_{new}^{(1)}(2) & -x_{new}^{(1)}(1) \\ -x_{new}^{(1)}(3) & -x_{new}^{(1)}(2) \\ \vdots & \vdots \\ -x_{new}^{(1)}(n-1) & -x_{new}^{(1)}(n-2) \end{bmatrix} \begin{bmatrix} M \\ N \end{bmatrix} = \begin{bmatrix} x_{new}^{(1)}(3) \\ x_{new}^{(1)}(4) \\ \vdots \\ x_{new}^{(1)}(n) \end{bmatrix}. \tag{22}$$

Suppose

$$Y=\begin{bmatrix} x_{new}^{(1)}(3) \\ x_{new}^{(1)}(4) \\ \vdots \\ x_{new}^{(1)}(n) \end{bmatrix},\quad B=\begin{bmatrix} -x_{new}^{(1)}(2) & -x_{new}^{(1)}(1) \\ -x_{new}^{(1)}(3) & -x_{new}^{(1)}(2) \\ \vdots & \vdots \\ -x_{new}^{(1)}(n-1) & -x_{new}^{(1)}(n-2) \end{bmatrix},\quad \Theta=\begin{bmatrix} M \\ N \end{bmatrix}.$$

The estimated parameters M and N can be solved by the least square estimation method.

$$\Theta=[M,N]^T=(B^TB)^{-1}B^TY. \tag{23}$$

Next, we need to find the solution of (22).

Let $x_{new}^{(1)}(k)=\xi^k$, $x_{new}^{(1)}(k+1)=\xi^{k+1}$, and $x_{new}^{(1)}(k+2)=\xi^{k+2}$, the following equation can be obtained:

$$\xi^{k+2}+M\xi^{k+1}+N\xi^k=\xi^k(\xi^2+M\xi+N)=0 \tag{24}$$

The roots to satisfy (24) are given as

$$\begin{cases} \xi_1=\dfrac{-M+\sqrt{M^2-4N}}{2} \\ \xi_2=\dfrac{-M-\sqrt{M^2-4N}}{2} \end{cases}. \tag{25}$$

Therefore, there are three cases for (25) as follows: $\xi_1\neq\xi_2$; 2) $\xi_1=\xi_2$; 3) ξ_1 and ξ_2 are complex conjugate.

Step 5: Take Inverse accumulated generating operation (IAGO)

$$\hat{x}_{new}^{(0)}(k)=\hat{x}_{new}^{(1)}(k)-\hat{x}_{new}^{(1)}(k-1) \tag{26}$$

Step 6: Inverse mapping generating operation (IMGO)

Applying IMGO for $\hat{x}_{new}^{(0)}$, the predicted value of the original data sequence $\hat{x}^{(0)}$ is obtained as

$$\hat{x}^{(0)}(k+1)=\hat{x}_{new}^{(1)}(k+1)-\hat{x}_{new}^{(1)}(k)-bias \tag{27}$$

3.3 The Combination of Sliding-mode control and Difference Grey Prediction

Because the upper/lower bound of the system uncertainties is supposed as the maximum/minimum value, the system loses robustness and causes the chattering and steady-state errors in the SMC. To alleviate the chattering and steady-state errors, a sliding-mode control with difference grey prediction is derived.

The classic control input, $u(t)$ is redefined as

$$u=u_{eq}+u_s+u_{dgy} \tag{28}$$

where u_{eq} is the equivalent control, u_s is used to alleviate the influence due the plant parameter variations, and u_{dgy} offers the compensation with difference grey prediction due to the external disturbances.

$$u_{dgy}=\begin{cases} 0 & ,\ |\hat{\sigma}|\geq\Phi \\ \dfrac{\kappa_2\hat{\sigma}}{\hat{b}}\mathrm{sgn}(\sigma\hat{\sigma}) & ,\ |\hat{\sigma}|\leq\Phi \end{cases} \tag{29}$$

where "^" denotes the forecast value with grey prediction, κ_2 is a constant, and Φ is the system boundary. Thus, if (29) is employed as this proposed method control input, the system is asymptotically stable.

Proof: The Lyapunov function is defined as

$$V = \frac{1}{2}\sigma^2 \tag{30}$$

Differentiating V with respect to time yields

$$\begin{aligned} \dot{V} &= \sigma\dot{\sigma} \\ &= \sigma\left[\frac{\kappa_1}{b}\mathrm{sgn}(\sigma) - \frac{\kappa_2\hat{\sigma}}{\hat{b}}\mathrm{sgn}(\sigma\hat{\sigma}) - (\Delta b u + d)\right] \\ &\le 0 \end{aligned} \tag{31}$$

where κ_1 is a constant. Therefore, the dynamic system is asymptotically stable.

4. Experimental results

The system parameters of UPS inverter are listed as follows: V_d =250 V; v_o=110 V_{rms}; switching frequency=18 kHz; L=1 mH; C=30 μF; rated load R=10 Ω. Figure 3 shows the output voltage and the load current obtained using the proposed method at a full resistive load and Fig. 4 shows that obtained using the classic SMC at the same load condition. These output voltages are nearly sinusoidal with negligible distortion. Figure 5 and Fig. 6 show the output voltage and the load current obtained using the proposed method and the classic SMC under step load change from no load to full load, respectively. Inspection of the waveforms indicates a smaller voltage dip in Fig. 5, as compared with Fig. 6. It is obvious that the proposed method has better robustness when an external disturbance is suddenly applied to UPS inverter. Table 1 gives the percentage of THD under these testing conditions. From Fig. 5 and Table 1, we observe that the proposed method can compensate inverter output-voltage dip very quickly, and the percentage of THD when the load sudden change is lower than the classic SMC. It is very clear that the proposed method is successful to alleviate the chattering and steady-state errors, thus yielding robust system performance.

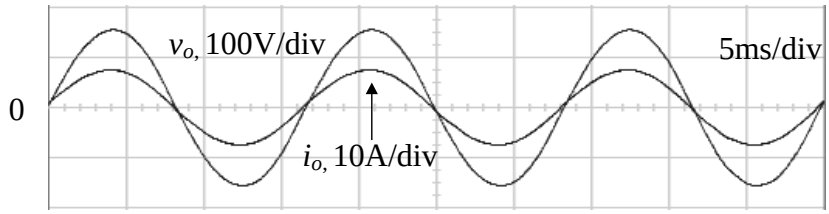

Fig. 3 Output voltage with resistive load (R=10Ω) for proposed method

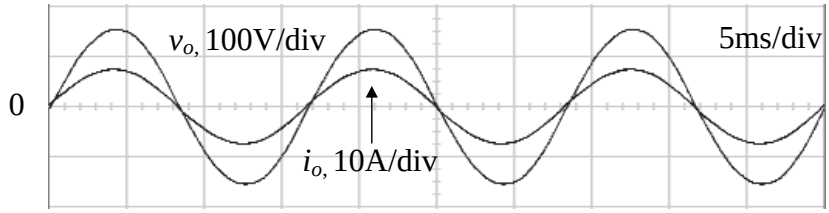

Fig. 4 Output voltage with resistive load (R=10Ω) for classic SMC

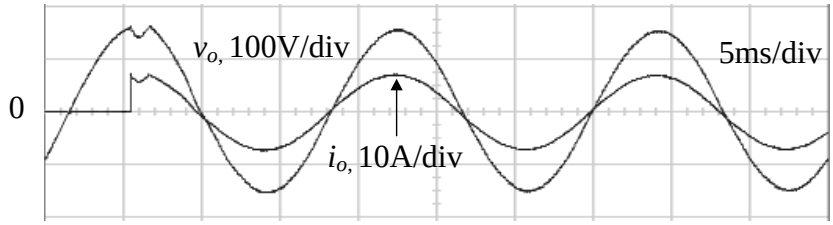

Fig. 5 Output voltage with sudden step load from ∞Ω to 10Ω for proposed method

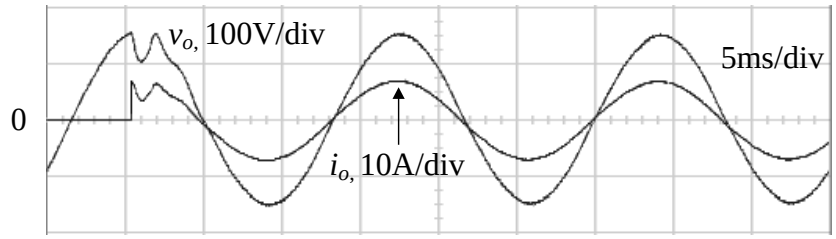

Fig. 6 Output voltage with sudden step load from ∞Ω to 10Ω for classic SMC

1.1.1. Table 1 Output voltage %THD

	Proposed method	Classic SMC
Resistive Load	10Ω	10Ω
%THD	0.32%	0.71%
Step load change	From ∞Ω to 10Ω	From ∞Ω to 10Ω
%THD	2.61%	7.43%

5. Conclusions

In this paper, a difference grey prediction compensated sliding-mode controller is applied to the UPS inverter. The upper/lower bound of system uncertainties do not require high accuracy by difference grey prediction. Thus, grey prediction alleviates the chattering and steady-state errors, which exist in classic SMC system. The experimental results verify that the proposed method can obtain high-quality and high-accuracy AC voltage and low THD in the UPS inverter output.

6. Acknowledgement

This work was supported by the National Science Council of Taiwan, R.O.C., under contract number NSC 101-2221-E-214-054.

7. References

[1] Caceres R, Rojas R, Camacho O. Robust PID control of a buck-boost DC-AC converter. *Proc. IEEE Int. Conf. Telecommunications Energy*, 2000, pp. 180-185.

[2] Astrom K J, Hagglund T. PID controller: theory, design and tuning. Research Triangle Park, 1995NC:ISA.

[3] Itkis U. Control system of variable structure. New York, Wiley, 1976.

[4] Chiang S J, Tai T S, Lee T S. Variable structure control of UPS inverters. *IEE Proc. Electr. Power Appl.*, 1998, 145(6): 559-567.

[5] Lee J U, Yoo J Y, Park G. T. Current control of a PWM inverter using sliding mode control and adaptive parameter estimation. *Proceedings of the IEEE International Conference on Industrial Electronics*, 1994, 1, pp. 372-377.

[6] Yokoama T, Kawamura A. Disturbance observer based fully digital controlled PWM inverter for CVCF operation. *IEEE Trans. Power Electronics*, 1994, 5: 473-480.

[7] Deng J L. Introduction to grey system theory. *J. Grey Syst.*, 1989, 1: 1-24.

[8] Deng J L. Control problems of grey system. *Systems and Control Letters*, 1982, 5: 288-294.

[9] Wen K L, Chen F H, Huang M L. Existence of grey model GM(2,1). *J. Grey Syst.*,1998, 1: 209-214.

EECS 391
A FPGA-based Space Vector Controller With Power Stage

Ansgar Kern
Fachbereich IEM, Technische Hochschule Mittelhessen
Wilhelm-Leuschner Str. 13
61169 Friedberg, Germany

Abstract
This paper will introduce a FPGA-based space vector controller with communication interface and power space designed for educational purposes. Frequency inverters employing space vector controllers are usually complex and interdisciplinary devices which are difficult to cover completely in one semester. They require the knowledge of electrical machines, power electronics and control theory. In this paper a different approach is proposed based on methods derived form information technology. Using programmable devices in conjunction with a communication interface it is possible to depict a space vector controller as a software entity which can be described accordingly. The paper will describe the application topology, methods used and the results obtained so far.
Keywords: space vector controller, FPGA, I2C-interface, VHDL

1. Introduction

Many frequency inverters use space vector based algorithms to control their power stages in order to drive the attached induction or synchronous motors. They also include elaborate methods to identify the attached machines. In order to familiarise students with the workings of a modern frequency inverter the complex system has to be stripped down to its essential components. These are the space vector controller and the power stage. Machine identification is an add-on which can be explained in sufficient detail separately and the closed loop control algorithm for the frequency inverter is of only secondary interest in this context.
The focus therefore is on an easy to understand and handle implementation of a space vector controller. The power stage will be added later on to verify the theoretical results. Also a means of measuring the workings of the controller has to be established. All this should be accomplished using a minimal hardware configuration, preferably based on a laptop computer or PC.

2. Development environment

As the basis for the development environment tools have been selected in such a way, that every development step can be executed using a standard laptop

computer. All tools are provided with a free software licence. The complete environment can therefore be used by students not just in the classroom but anywhere without additional license fees.

The environment consists of a FPGA development suite, in this case Xilinx based [1], software for communicating with an I2C-interfac, which later on establishes communication with the space vector controller and software for a PC based oscilloscope to monitor the controller output (Fig. 1).

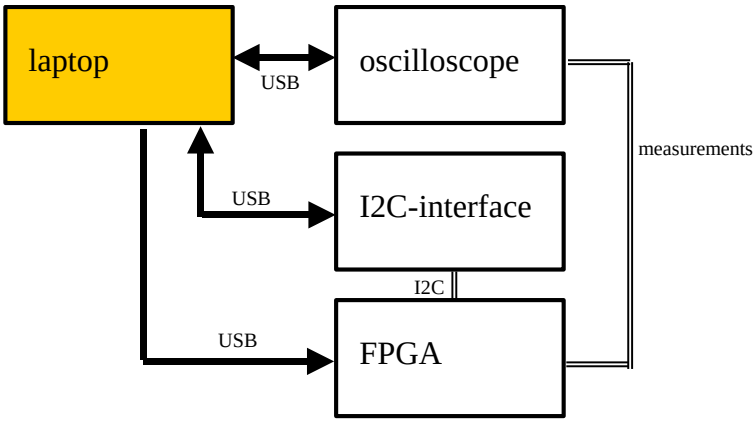

Fig. 1: Development environment

In this scenario the FPGA is host to the space vector algorithm. It is configured via the USB interface using the laptop computer. No information is fed back by the FPGA directly to the computer once the space vector has been implemented. The I2C-interface is used to communicate with the space vector controller and represents higher level control components from the controller point of view. All parameters and data are exchanged via the I2C-interface. The oscilloscope represents an external observer of the system monitoring the control signals for driving the power electronics.

Oscilloscope, I2C-interface and FPGA board are actual hardware components attached to the computer via a USB interface. They are not required for the actual development process of the space vector controller.

2.1 I2C-Interface

Frequency inverters and other power electronics related equipment are usually controlled via various bus systems like PROFIBUS [2] or industrial Ethernet. They require a complex protocol to be handled by the devices attached to the bus which adds a further layer of complexity. In this case, in order to keep things simple and transparent, the I2C-bus was chosen as a means to communicate with the controller. Since no protocol has to be implemented, parameters can be transmitted to and read from the controller directly. Students can therefore

observe immediately the effects of single bytes of information sent. As a disadvantage it has to be noted that the I2C-interface has to be implemented on the FPGA besides the space vector controller too. This makes the design process of the FPGA more complex. Practical results however have shown, that the I2C-Interface can be separated form the space vector controller quite neatly and can thus be treated as a black box which just provides parameters or stores data.
Since the I2C-interface is not the main focus of this work, a concise example of its workings will be given only to demonstrate its advantages (Fig. 2).

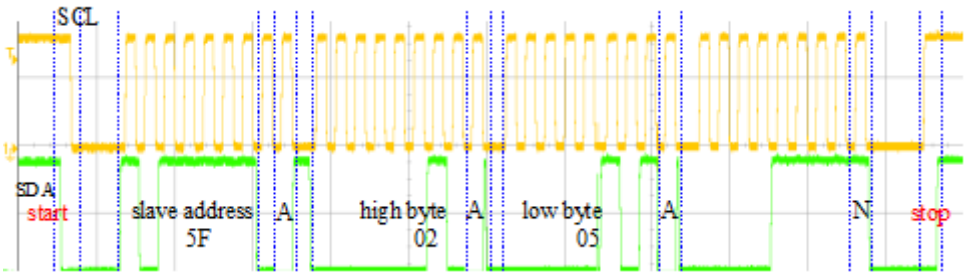

Fig. 2: I2C-interface operation

The I2C-interface requires only two lines called clock (SCL) and data (SDA) [3]. At first the slave address is sent via the bus by the master, in this case the PC. It consists of eight bits after which the slave sends an acknowledge (A). After receiving the acknowledge from the slave the master continues sending data bytes to the slave addressed until no acknowledge (N) is send by the slave. After that the transmission ends. No further protocol handling is required and the bytes sent to the slave directly correspond with actions to be executed by the slave. The first byte sent represents the slave address, the second byte addresses a 16 bit register of the space vector controller. The values of several registers determine the behaviour of the controller. The controller can thus be influenced by simply changing the values of its associated registers (Fig. 3). The bus layer of the I2C-interface and the application layer of the space vector controller are clearly separated and in theory the controller would be able to work as a stand alone device provided the proper initial values are stored in its registers. So in theory the functionality of the controller could even be demonstrated to students without an I2C-interface present.

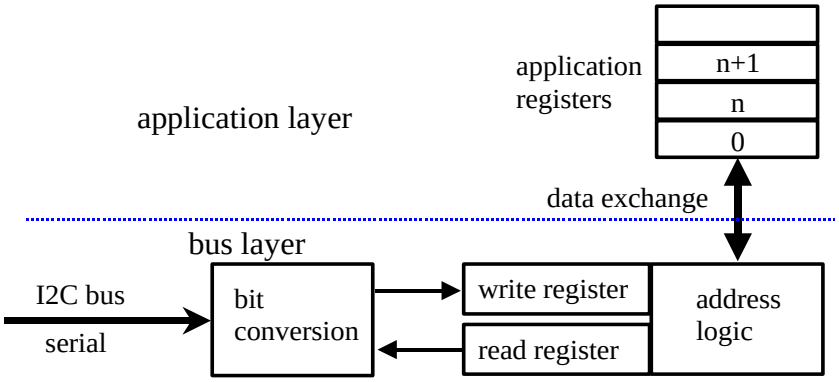

Fig. 3. I2C interface

3. Application topology

The principal workings of a space vector controller are widely know and will therefore be only touched upon with regards to the implementation specific points [4]. The theory is based on a continuously moving vector where vector length and speed can be adjusted in a quasi continuous manner. For the implementation as a digital system certain limitations apply depending on the platform used. With the FPGA based implementation mathematically complex operations like divisions and sinus-functions have to be ruled out, since they are to complex and time consuming to implement. Therefore the vector can not be depicted as a quasi continuously moving entity but rather like an entity which can only assume a limited number of positions in the complex number plane (Fig. 4).

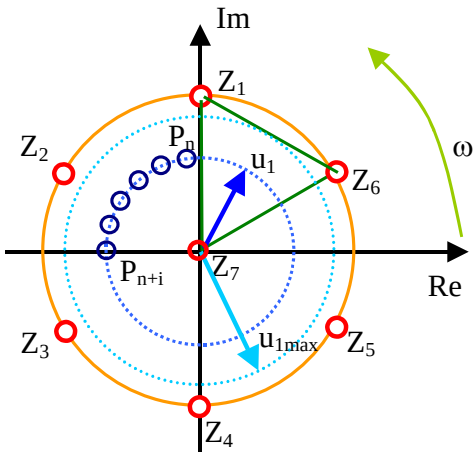

Fig. 4. Possible position in the complex number plane

The number of possible positions P_n depends on the binary representations of the

possible controller values. In this case, 127 positions P_n have been sampled per 90 degrees at a resolution of eight bits. That results in 255 different vector lengths and a total of 502 positions per 360 degrees. In other words, 128010 different space vector positions are possible. The sample values are implemented via a look up table which is initialised at start-up time.

The space vector algorithm has further been simplified by implementing a single phase version and phase shifting that version 120 and 240 degrees to generate the required three phased system. The pulses obtained for a single phase system are shown in Fig. 5 and the implemented topology in Fig. 6.

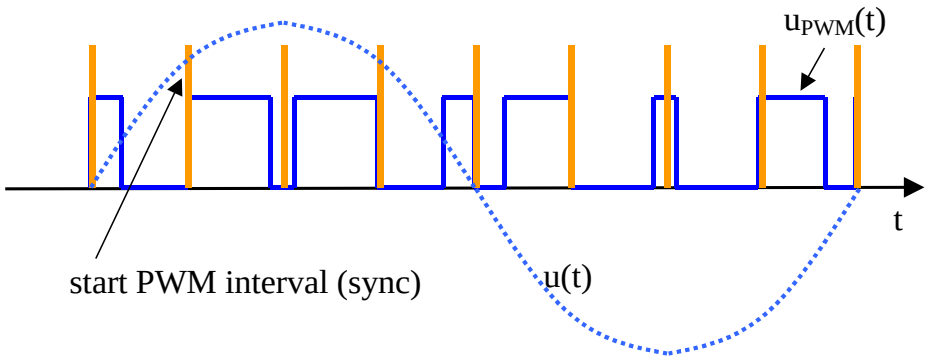

Fig. 5. Single phase voltage and digital equivalent

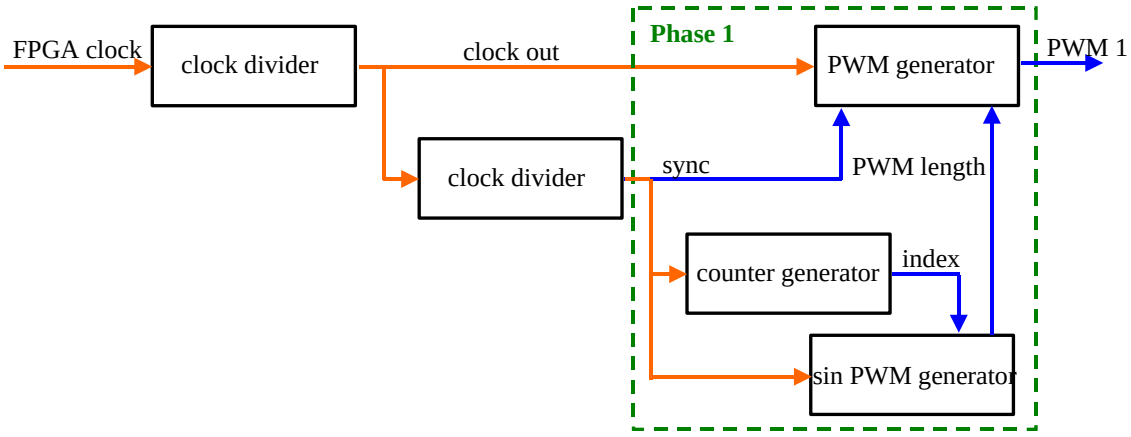

Fig. 6. Block diagram of a single phased sinusoidal PWM generator

At the start of each PWM interval a synchronisation pulse is generated in order to synchronise the three phases. Please note that in Fig. 5 in order to simplify matters only 8 sample values at a resolution of eight bits have been used to generate a vector rotation of 360 degrees. That would result in only 2040 possible positions. It should also be noted that the smallest circle obtainable with a length of only one is of no

practical value since the output voltage would be of purely rectangular shape.
The block diagram in Fig. 6 is implemented three times on the FPGA, once for each phase.

3.1 Application implementation

The space vector controller is implemented of an FPGA board running at a 50MHz clock. The fastest space vector speed f_S at maximum resolution can be calculated according to Eq. 1.

$$f_S = \frac{50MHz}{502 * 255} = 390Hz \tag{1}$$

That of course is to fast for ordinary electrical drives. Therefore the first clock divider in Fig. 6 can be used to slow down the base frequency f_B of the system according to Eq. 2. Please note that N in Eq. 2 will always be an integer number ranging from 1 to 65535, the largest 16 bit number possible.

$$f_B = \frac{50MHz}{N} \tag{2}$$

As a result only vector speeds of 390Hz over N are possible. That of course results in significant gaps in the speed spectrum of the attached drive. To minimise these gaps, sample values can be skipped or repeated in order to influence the vector speed. This will result in distortions of the generated output voltages and additional losses in the form of higher harmonics.

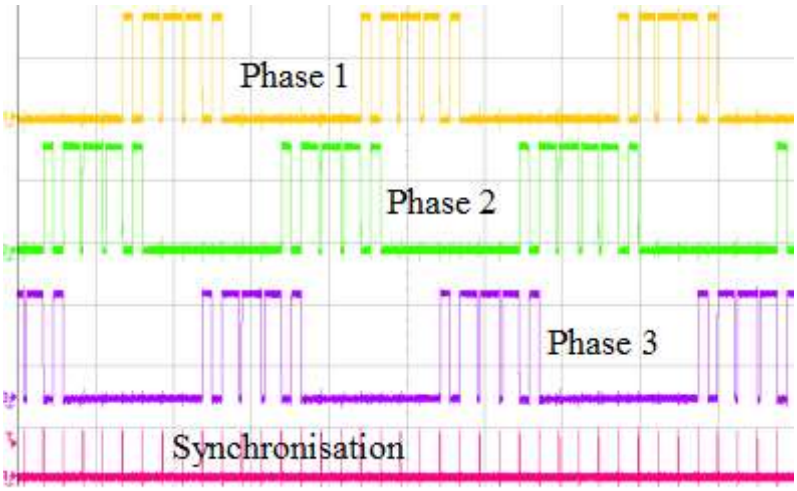

Fig. 7. Three phases in a half-bridge mode, angle increment set to 30 degrees

Fig. 7 shows a simple example of the switching pulses generated if an operation mode called half bridge mode.
In so called half bridge mode two times three control signals are generated. Within

each set the signals are phase shifted 120 degrees and the two sets are phase shifted 180 degrees to each other. Of the six signals generated Fig. 7 shows only three.
In full bridge mode only three control signals are generated. They are phase shifted 120 degrees and can be used to control a three phased inverter. Fig. 8 shows an example of these control signals.

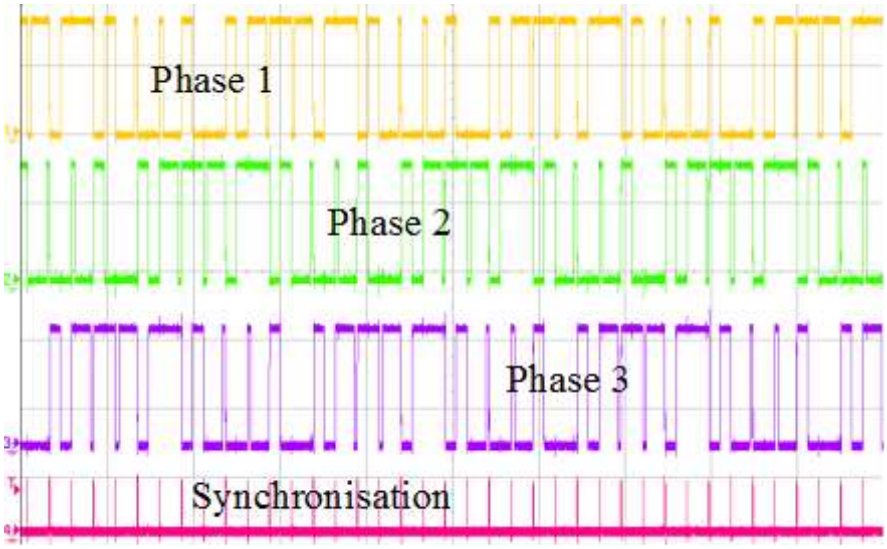

Fig. 8. Three phases in full-bridge mode

In full bridge mode each signal is repeated basically every 180 degrees, every second time it is inverted however. Again all three signals are phase shifted by 120 degrees.

5. Conclusion and outlook

The introduced concept was designed to familiarise students with the principle concept of space vector control. The approach taken was from a point of view which heavily relied on the concepts taught during informatics sessions. In that view, space vector control is just another application and not something specific to power electronics or electrical drives.
The approach proved to be increasing the understanding of students with regards to the application of space vector control. It also showed to them the close connection of informatics and control algorithms in current technology. It also enabled students from other areas of engineering, especially mechatronics, to approach the subject matter in a standardised way using familiar concepts.
The concept is basically scalable, meaning that an approach using only software components can be used and extended gradually by introducing various hardware components such as bus-interfaces, oscilloscopes and finally power stages. Also the use of software which relies of a cost free licensing scheme proved to be of great

advantage, enabling the distribution of the software via virtual machines to everyone interested.

The final step of designing an easy to use and robust power stage is already on the way and will hopefully be concluded in the near future enabling students to observe not just the switching pulses generated but also voltages and currents in real world applications.

4. References

[1] Xilinx, Spartan-3A/3AN FPGA Starter Kit Board User Guide, Xilinx Corporation 2008.

[2] Max Felser, PROFIBUS Manual: A collection of information explaining PROFIBUS networks, epubli GmbH 2011, pp. 30-39.

[3] Philips Semiconductors, The I2C-bus and how to use it, Philips 1992.

[4] Nguyen Phung Quang, Jörg-Andreas Dittrich, Vector Control of Three-Phase AC Machines: System Development in the Practice, Springer-Verlag 2008, pp. 18-22.

EECS 438
Performance of Grid-Connected Hybrid Photovoltaic/Fuel Cell/Battery Distributed Generation System

Ahmad Eid, Member, IEEE
Electrical Engineering Department,
Aswan Faculty of Engineering,
Aswan University, Egypt
ahmadeid@ieee.org

Abstract

In this paper, the performance of grid-connected hybrid distributed generations isstudied. The hybrid system includes Photovoltaic (PV) panels, Fuel Cells (FC) and Battery Energy Storage System (BESS).The PV module operates at maximum power of 20kW regardless of the environmental conditions using P&O MPPT control method. The FC model provides a maximum power of 40kW using a current controlled DC/DC boost converter. The BESS consists of a battery, a bidirectional DC/DC converter and a controller. The BESS is responsible for smoothing and regulating the DC voltage bus at 400Vduring off-grid mode by charging/discharging the battery.A PQ-controlled bidirectional PWM inverter connects the hybrid generations to the grid.The adopted control methods show good performance of the micro-grid at transient and steady state operations in terms of the quality of the DC and AC bus voltages.

Keywords: Photovoltaic, Fuel Cell, Battery, DC Micro-grid, Converters.

1. Introduction

Distributed energy resources including distributed generation (DG) with distributed energy are sources of energy located near local loads and can providea variety of benefits including improved reliability, self-healing and load control if properly operated in theelectrical distribution system. Micro-grids are systems that have at least one distributed energyresource, associated loads, and can form intentional islands in the electrical distributionsystems. Numerous benefits arise from thisability to island for events like faults and voltage sags.Smart islanding can greatly enhances the value propositionfor the utility and the customer. Within micro-grids, energy sources can be disconnected and reconnectedto electric power system with minimal disruption to the local loads [1]. DG technologies typicallyinclude photovoltaic (PV), wind, fuel cells, micro-turbines,and reciprocating internal combustion engines with generators.Most of the DGtechnologies require a power electronics interface in order toconvert the energy into grid-compatible AC power. Theoutput of the main inverter should be compatible in voltage and frequency with themain grid.Different DC/DC converters

are used for regulating the voltage at the main DC bus to which DC loads are connected.

DC micro-grids appears recently due to the development anddeployment of renewable DC power sources and their inherentadvantage for DC loads in commercial, industrial andresidential applications. The DC micro-grids have beenproposed [2-4]. However, AC sources have to be convertedinto DC before connected to a DC micro-grid and DC/ACinverters are required for conventional AC loads.Multiple reverse conversions in an individual AC or DCgrid reduce the efficiency of power utilization and increase thecomplexity and cost of equipment due to the embeddedAC/DC and AC/DC converters.

2. Micro-Grid Configuration and Modeling

2.1 DC Micro-Grid System Structure

The studied hybrid DG system, wherevarious DC sources and loads are connected to the DC buswhilethe main grid and AC loads are connected to AC bus, is shown in Fig. 1. The DC and ACbuses are connectedtogether through a bidirectional three-phase 6-pulse PWM inverter. To simulate the system operations andcontrols, the hybrid micro-grid is built in PSIMsoftware. Twenty kW PV arrays and 40 kW fuel cell are connected to DC bus through DC/DC boost converters to simulate DC sources.

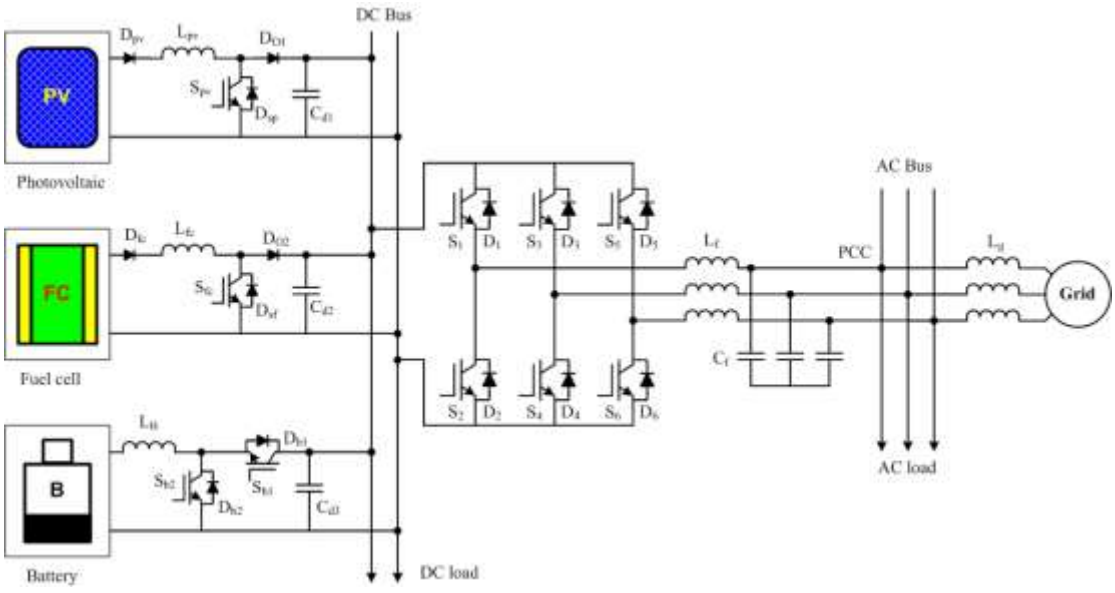

Fig. 1: Proposed hybrid DC micro-grid system.

The battery as energy storage is connected tothe DC bus through a bidirectional DC/DC converter. Variable DCand AC loadsare connected toDC and AC buses respectively to test the system capabilities and control during transient states when

connecting/disconnecting loads in the system. The rated voltages for DC and ACbuses are 400 V and 200 V rms respectively. A three-phase high pass LC filter is connected at the output of the bidirectional PWM inverter to mitigate the high frequency ripples generated due to the action of the PWM inverter. All the converters have the minimum number of switches to decrease the total cost of the micro-grid.

2.2PV Array Model

The single-diode PV array is modeled by the following three equations [5].

$$I_{pv} = n_p I_{ph} - n_p I_{sat}\left[e^{\frac{q}{AkT}\left(\frac{V_{pv}}{n_s}+\frac{I_{pv}R_s}{n_p}\right)} - 1\right] - \frac{n_p}{R_{sh}}\left(\frac{V_{pv}}{n_s}+\frac{I_{pv}R_s}{n_p}\right) \quad (1)$$

$$I_{ph} = \frac{S}{1000}\left(I_{sc} + k_i(T - T_r)\right) \quad (2)$$

$$I_{sat} = I_{rr}\left(\frac{T}{T_r}\right)^3 e^{\frac{q E_g}{Ak}\left(\frac{1}{T_r}-\frac{1}{T}\right)} \quad (3)$$

where $I_{pv}$and $V_{pv}$are the PV array output current and voltage, $n_s$is the number of cells connectedin series, n_p is the number of modules connectedin parallel, q is the charge of an electron, k is Boltzmann'sconstant, A is the p-n junction ideality factor,$I_{ph}$is the cell photo-current, Tand T_r are the cell and reference temperatures (K), I_{sat} is the cell reverse saturationcurrent,I_{sc} is the cell short-circuit current at reference temperatureand radiation, ki is the short circuit current temperaturecoefficient, and S is the solar radiation inW/m^2,$I_{rr}$is thereverse saturation current at T_r, $R_s$and R_{sh} are the series and shunt equivalent resistances and E_g is the band-gapenergy of the semiconductor used in the cell.The parameters used in the PV module are listed in Table 1 and its equivalent circuit is shown in Fig. 2-a.

Table 1 Parameters of PV model

Parameter	Value	Parameter	Value
Referenced solar irradiance	1 000 W/m^2	Referenced cell temperature	298 K
Maximum power	20 kW	Band-gap energy	1.12eV
Number of cells in parallel	29	Number of cells in series	12
Cell internal series resistance	$1x10^{-4}\Omega$	Cell internal shunt resistance	$1k\Omega$
Ideality factor	1.2	Temperature coefficient	0.0702 A/K
Short circuit current	108 A	Reverse saturation current	$2.528x10^{-6}$ A
Number of modules	36	Rated output voltage	200 V

2.3Fuel Cell Model

The voltage of a fuel cell $V_{fc}$is defined as the sum of the theoretical open circuit voltage and the different over-voltages as [6]:

$$V_{fc} = 1.229 + \frac{RT}{2F}\left[\ln\left(P_{H_2}\right) + \ln\left(P_{O_2}\right)\right] - A\ln(i_c) - i_c\, r_s - m\exp(n i_c) \quad (4)$$

Where F is the Faraday constant (96485C), R is the universal gas constant (8.314 J/K.mol), T is the temperature in Kelvin, P_{H2}, P_{O2} are the hydrogen, oxygen partial pressure in bar, respectively, i_c is the cell current density (A/m^2) and A is constant, r_s is the area-specific resistance, the value of m is typically about $3x10^{-5}$V, and n about $8x10^{-3}cm^2/mA$. Anequivalent circuit model of the fuel cell is shown in Fig. 2-b [7] with its parameters is listed in Table 2.

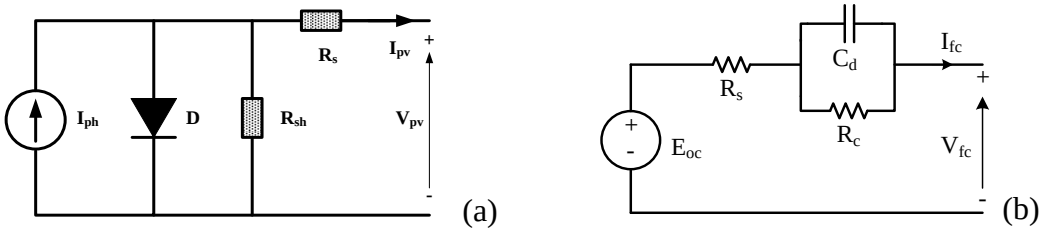

Fig. 2:Electric circuit models of (a) PV cell, (b) fuel cell.

2.4Battery Model

Battery model can usually be divided into experimentalmodel, electrochemical model and equivalent electric circuit model.The equivalent circuit model is most suitable for the dynamicsimulation.Assuming the internal resistance of the batteryconstant during both charge and discharge cycles, the output voltage is given as [8]:

$$E = E_o - \left[E_f - E_n + \left(E_f - E_x\right)\left(e^{\frac{-3Q_n}{Q_x}} - 1\right)\right]\left(\frac{Q(Q - Q_n)}{Q_n(Q - \int i_b dt)}\right) + \left(E_f - E_x\right)e^{\frac{-3\int i_b dt}{Q_x}} \quad (5)$$

where, E_o is battery constantvoltage (V), Q is batterycapacity (Ah),E_f is the fully charged voltage, E_n, Q_n are the end of nominal zone voltage and capacity while E_x and Q_x arethe end of exponential zone voltage and capacity, Q is the capacity at any time and i_b is the output battery current.

Table 2 Parameters of battery model

Parameter	Value	Parameter	Value	Parameter	Value	Parameter	Value
E_f	234V	E_x	210V	Q_n	240Ah	Q_r	300Ah
Q_x	60Ah	E_n	200V	E_o	216.5V	r_b	0.017Ω

3. Hybrid DC Micro-Grid Controls

3.1 Control of PV

The PV source is connected to DC bus through a boost DC/DC converter. The PV output power depends on the environmental conditions (solar irradiation and

temperature). In order to generate the maximum allowable power from the PV (20 kW), its DC/DC converter is controlled using Perturb and Observation (P&O) Maximum Power Point Tracking (MPPT) method. P&O isused most widely since it is much simpler and needs fewermeasured variables [5]. P&O algorithm operates by constantlymeasuring the terminal voltage and current of the PV array,then constantly perturbing the voltage by adding a smalldisturbance, and then observing the changes of the outputpower to determine the next control signal. If the powerincreases, the perturbation will continue in the same directionin the following step, otherwise, the perturbation directionwill be inversed, as shown in Fig. 3-a.

3.2 Control of FC

The control of the fuel cell converter is illustrated in Fig. 3-b. The FC and PV supply the required powers for the DC load (P_{dc}), AC load (P_{ac}) as well as the considered power loss of the system (P_{ls}). The limiter limits the maximum power of FC to 40 kW. The required FC current is calculated by dividing its reference power by its voltageas shown in Fig. 3-b. The reference current is used in a PI current-controlled loop to provide the required gate signal for DC/DC boost converter.

3.3 Control of Battery

The main objective of the battery converter is tomaintain the common DC bus voltage constant at 400V. When charging/discharging, switch S_{b1}/S_{b2} is activatedand the converter works as a buck/boost circuit, respectively, Fig. 3-c. The battery converter control includes twoloopsexternal voltage control and internal current control.

3.4 Control of Inverter

The PQ control method is used to control the 3-phase PWM inverter by regulating the d- and q-axis current components [8]. The control strategy, see Fig. 3-d, mainly consists of two cascadedloops, namely a fast internal current loop and an externalvoltage loop. The proposed multi-level control scheme isbased on the concept of instantaneous power on thesynchronous-rotating dq reference frame.

4. Simulation Results and Discussions

4.1 Autonomous Mode

The hybrid DC micro-grid is simulated in autonomous mode to verify the used control methods. The battery converter maintains the DC bus voltage at 400V. The simulation starts with the DC load power (P_{dc}) of 40kW and it descends to 30 kW at 0.5s, while the

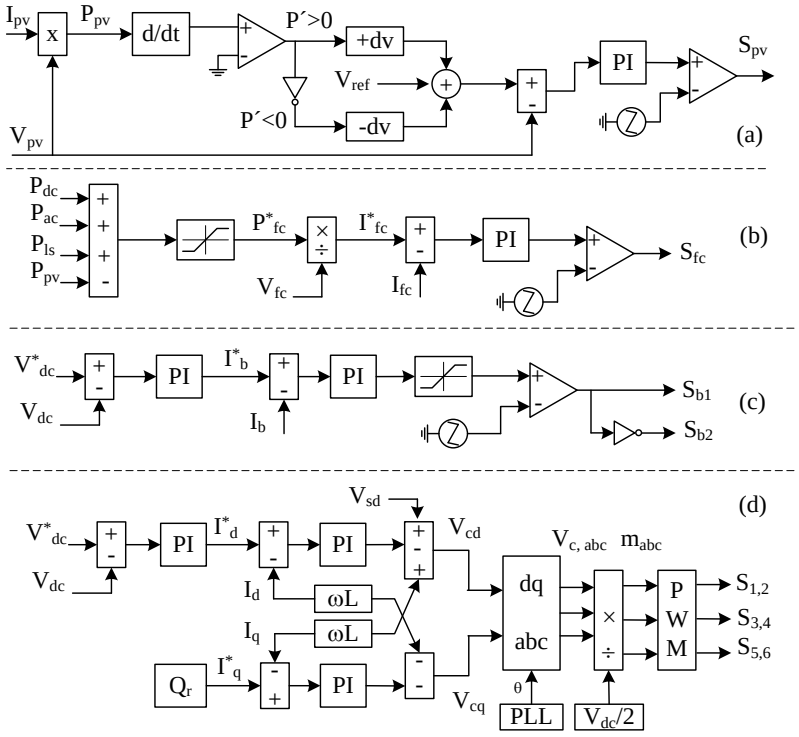

Fig. 3:Control of hybrid sources (a) PV, (b) FC(c) battery and (d) invertercontrollers.

AC load power (P_{ac}) is 20kW and steps to 40kW at 1s as shown in Fig. 4-a. The output power of the fuel cell (P_{fc}) is maintained at 40kW all time while the PV power (P_{pv}) is changing from 16-20kW according to the solar irradiation of 800-1000W/m^2, Fig. 4-d. Meanwhile, the battery power is changing its value and polarity, Fig. 4-b, according to the required power for the load and for keeping the DC voltage constant. The corresponding DC bus current (I_{dc}) and battery current (I_b) are shown in Fig. 4-c. The voltage of the DC bus (V_{dc}) and the battery terminal voltage (V_b) are shown in Fig. 4-d. The phase voltage of the inverter (V_{ai}) and current (I_{ai}) are shown in Fig. 4-e. The THD values of the voltage and current are much less than 5%.

4.2 Grid-Connected Mode

The DC micro-grid is simulated in the case of grid-connected mode as shown in Fig. 5. The DC load power steps at 1s and makes another step at 1.5s. The AC load power starts at 30kW and steps to 60kW at 0.5s, as shown in Fig. 5-a, as well as the inverter exchange power (P_i) from the DC bus to the AC bus. The DC sources reactions and the grid power to supply the different loads are shown in Fig. 5-b. Until time of 0.5s, the power direction is from the inverter to the grid, as the total DC generated power from the FC and PV exceeds the total load. When the total load becomes 60kW (maximum power of DC sources), the generated power from the grid is zero. When the load power exceeds 60kW, the grid supplies the excess power.

The corresponding DC currents of the PV, FC and DC bus are shown in Fig. 5-c. The terminal voltages of the PV and FC are shown in Fig. 5-d. The controlled voltage of the DC bus is shown in Fig. 5-e. It is regulated by the inverter at 400V and the shown transient points are due to the changing of loads. The output voltage of the inverter for phase a is shown in Fig. 5-f. The THD of the voltage is much less than the 5% due to the presence of the well-designed LC filter.

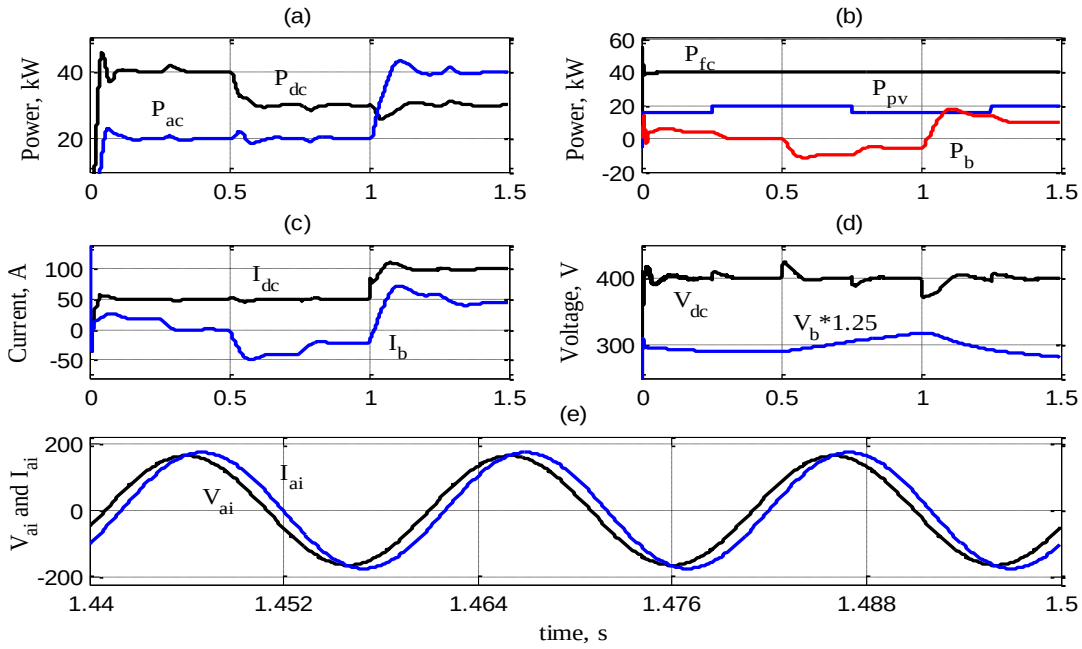

Fig. 4: Performance of the DC micro-grid at autonomous operation.

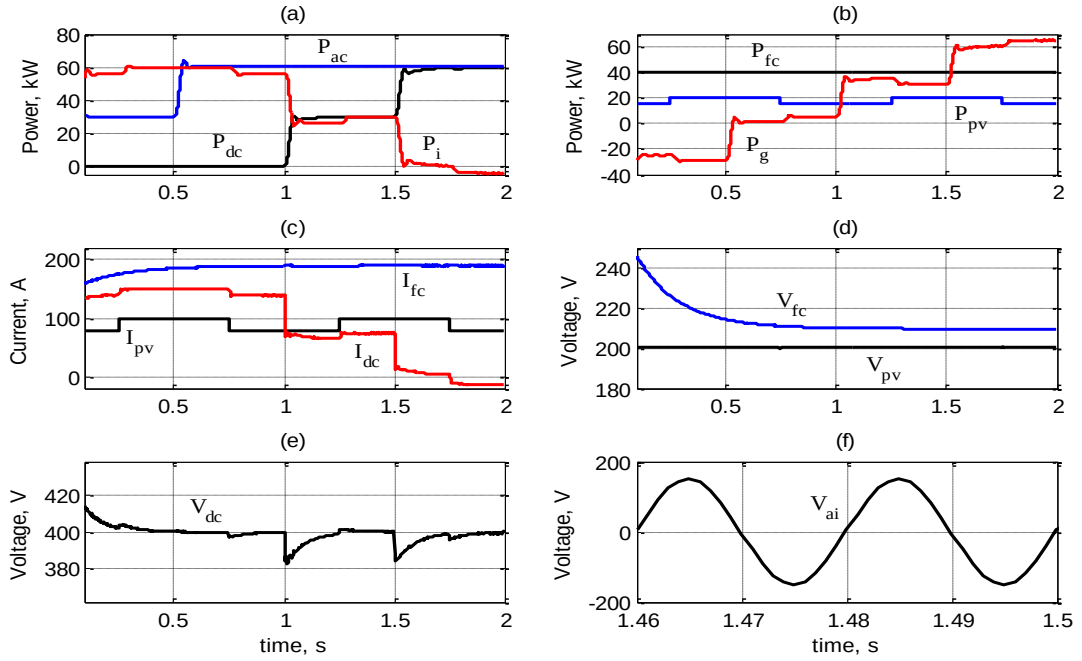

Fig. 5: Performance of the DC micro-grid at grid-connectedoperation.

5. Conclusions

A hybrid DC micro-grid of photovoltaic, fuel cell and energy storage battery is analyzed and simulated under autonomous and grid-connected modes of operations.The PV module is controlled to operate at maximum power using P&O MPPT method. The FC provides a maximum power of 40kW using a current controlled DC/DC boost converter. The BESS is responsible for smoothing and regulating the DC bus voltage at 400 V during autonomous mode. The inverter is controlled using PQ control method to provide the necessary output voltage that is in-phase with the grid voltage with the help of a PLL circuit. The adopted control methods show good performance of the grid at transient and steady state operations in terms of the quality of the DC bus voltage and AC voltage.

6. References

[1] B. Kroposki, R. Lasseter, T. Ise, S. Morozumi, S. Papatlianassiou and N. Hatziargyriou, "Making microgrids work", *IEEE Power and Energy Magazine*, May-June 2008, 6(3): 40-53.

[2] M. Baran and N. Mahajan, "DC distribution for industrial systems: opportunities and challenges," *IEEE Trans. on Industry Applications*, Nov. 2003, 39(6): 1596-1601.

[3] A. Sannino, G. Postiglione, and M. Bollen, "Feasibility of a dc network for commercial facilities," *IEEE Trans. on Industry Applications*, Sep. 2003, 39(5): 1409-1507.

[4] D. Salomonsson and A. Sannino, "Low-voltage DC distribution system for commercial power systems with sensitive electronic loads," *IEEE Trans. Power Delivery*, Jul. 2007, 22(3): 1620-1627.

[5] K.H. Hussein, I. Muta, T. Hoshino and M. Osakada, "Maximum photovoltaic power tracking: an algorithm for rapidly changing atmospheric conditions", *IEE Proceedings-Generation, Transmission and Distribution*, Jan. 1995, 142(1): 59-64.

[6] J. Larminie, A. Dicks, "Fuel cell systems explained", 2nd edition, John Wiley & Sons, England, 2003.

[8] X. Liu, P. Wang and P. C. Loh, "A hybrid AC/DC microgrid and its coordination control", *IEEE Trans. Smart Grid*, Jun. 2011, 2(2): 278-286.

[7]A. Eid, H. El-Kishky, M. Abdel-Salam and T. El-Mohandes, "Modeling and characterization of an aircraft electric power system with a fuel cell-equipped APU connected at HVDC bus", *International Power Modulator and High Voltage Conference*, Atlanta, GA, May 23-27, 2010, pp. 639-642.

Life Science II

2013/03/16 Saturday 10:45-12:15 Room 603

Session Chair: ***Chong Kim Wong***

LSBE 119

Effect of Chitosan and Modified Atmosphere Packaging on Quality Changes of Giant Perch (Lates calcarifer) Meat during Cold Storage

Vilailak Klompong | *Thaksin University*
Pidtayanan Kaewkwanpet | *Thaksin University*
Supamas Chumanee | *Thaksin University*

LSBE 405

Biosynthesis of value-added green material from renewable resources using a marine Bacillus megaterium isolate KB-1

Kesaven Bhubalan | *Universiti Malaysia Terengganu*
Maizatul Nuzi Othman | *Universiti Malaysia Terengganu*
Ishak Muhammad Syafiq | *Universiti Malaysia Terengganu*
Mohd Effendy Abdul Wahid | *Universiti Malaysia Terengganu*
Al-Ashraf Abdullah Amirul | *Universiti Sains Malaysia*

LSBE 416

Characterization of allergenic compounds from Pleurotus ostreatus and Pleurotus sajor caju

Elbatrawy Nasr Eman | *Virginia Commonwealth Univ*
Ghonimy Abdouallah Eglal | *Al Azhar Uni. Cairo*
Wu Fang Sheng | *Virginia Commonwealth Univ*

LSBE 137

Functional Physicochemical Properties and Their Application in Food Processing of Thai Indigenous Red Rice Varieties

Rutrada Sompong | *Thaksin University*

LSBE 322

Nutrient reduction and the marine plankton in Tolo Harbour, Hong Kong

Chong Kim Wong | *The Chinese University of Hong Kong*
Alle A.Y. Lie | *The Chinese University of Hong Kong*
Guangtao Zhang | *Chinese Academy of Sciences*
Y. Kit Yung | *Hong Kong Environmental Protection Department*
Qingchao Chen | *Chinese Academy of Sciences*

LSBE 309

Methamphetamine Administration on Alterations of Sperm Quality and Hormone receptors in Rat testis

Sutisa Nudmamud-Thanoi | *Naresuan University*
Wanvipa Sueudom | *Naresuan University*
Nareelak Tangsrisakda | *Naresuan University*
Samur Thanoi | *Naresuan University*

LSBE 300

Rubber Stand Volume Model Applications using Segmentation and Pixel-Based Classification on Landsat TM in Selangor, Malaysia

Mohd Nazip Suratman | *Universiti Teknologi MARA*

LSBE 119
Effect of Chitosan and Modified Atmosphere Packaging on Quality Changes of Giant Perch (*Lates calcarifer*) Meat during Cold Storage

Vilailak Klompong
Department of Food Science and Technology, Thaksin University, Papayom, Phattalung 93110 Thailand
klompong@hotmail.com

Pidtayanan Kaewkwanpet
Department of Food Science and Technology, Thaksin University, Papayom, Phattalung 93110 Thailand
freedom_bloodza@hotmail.com

Supamas Chumanee
Department of Food Science and Technology, Thaksin University, Papayom, Phattalung 93110 Thailand
boss_zaa_8@hotmail.com

The corresponding author: Vilailak Klompong

Abstract

Effect of chitosan and modified atmosphere packaging on quality changes of Giant Perch meat during storage at 4°C for 15 days was investigated. Sample was divided into four treatments including control, Giant Perch meat added with chitosan (5 mg /g fish), Giant Perch meat packed by modified atmosphere (O_2 10%, CO_2 80%, N_2 10%) and Giant Perch meat added with chitosan (5 mg /g fish) and packed by modified atmosphere (O_2 10%, CO_2 80%, N_2 10%). As the storage time increased, moisture loss, pH, conjugated dienes, thiobarbituric acid reactive substances (TBARS), Trimethylamine (TMA), Total volatile bases (TVB), total plate count, psychrophiles and *Pseudomonas* spp. in Giant Perch meat increased ($P<0.05$). The highest moisture loss, pH, conjugated dienes, TBARS, TMA, TVB and total plate count was observed in control ($P<0.05$), followed by Giant Perch meat packed by modified atmosphere, that added with chitosan, and that added with chitosan and packed by modified atmosphere, respectively. However, the highest psychrophiles was detected in control, followed by Giant Perch meat added with chitosan, that packed by modified atmosphere and that added with chitosan and packed by modified atmosphere ($P<0.05$), respectively. Acceptance scores from sensory evaluation decreased ($P<0.05$) as the duration of storage increased ($P<0.05$). However, the highest stability from

sensory evaluation was observed in Giant Perch meat added with chitosan and packed by modified atmosphere. Thus, natural and safe chitosan could be used together with modified atmosphere packaging to extend the shelf life of Giant Perch meat during cold storage.

Keyword: Chitosan, Giant Perch Meat, Modified Atmosphere Packaging

1. Objectives

To investigate the effect of chitosan and modified atmosphere packaging on quality changes of Giant Perch meat during storage.

2. Methods

Sample was divided into four treatments including control, Giant Perch meat added with chitosan (5 mg /g fish), Giant Perch meat packed by modified atmosphere (O_2 10%, CO_2 80%, N_2 10%) and Giant Perch meat added with chitosan (5 mg /g fish) and packed by modified atmosphere (O_2 10%, CO_2 80%, N_2 10%) and then storage at 4°C for 15 days.

3. Results

As the storage time increased, moisture loss, pH, conjugated dienes, thiobarbituric acid reactive substances (TBARS), Trimethylamine (TMA), Total volatile bases (TVB), total plate count, psychrophiles and *Pseudomonas* spp. in Giant Perch meat increased ($P<0.05$). The highest moisture loss, pH, conjugated dienes, TBARS, TMA, TVB and total plate count was observed in control ($P<0.05$), followed by Giant Perch meat packed by modified atmosphere, that added with chitosan, and that added with chitosan and packed by modified atmosphere, respectively. However, the highest psychrophiles was detected in control, followed by Giant Perch meat added with chitosan, that packed by modified atmosphere and that added with chitosan and packed by modified atmosphere ($P<0.05$), respectively. Acceptance scores from sensory evaluation decreased ($P<0.05$) as the duration of storage increased ($P<0.05$). However, the highest stability from sensory evaluation was observed in Giant Perch meat added with chitosan and packed by modified atmosphere (Fig. 1-4).

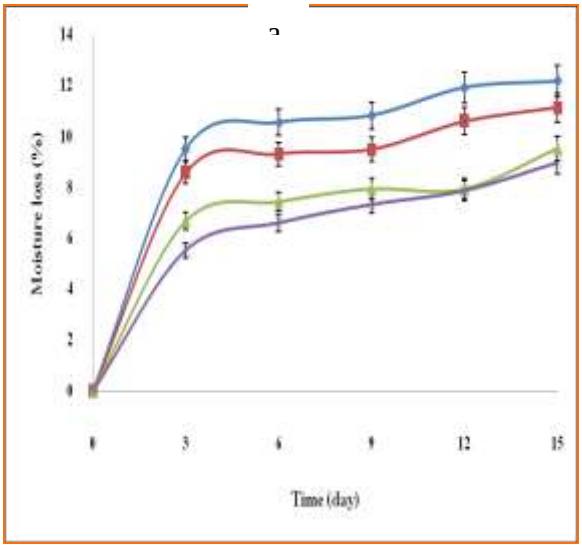

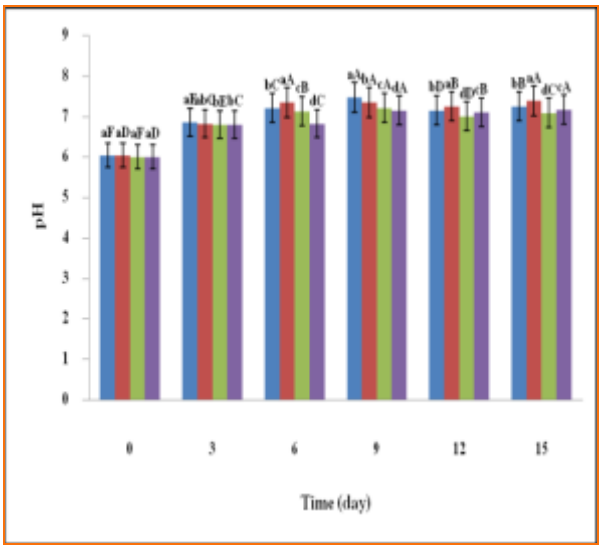

Figure 1 Moisture loss (a) and pH (b) of Giant Perch meat during storage at 4°C for 15 days; control ( ), modified atmosphere packaging ( ), added with chitosan ( ) and added with chitosan and modified atmosphere packaging ( ). Bars represent the standard deviation from triplicate determinations. Different capital letters on the bars within the same treatment indicate the significant differences ($P<0.05$). The different letters on the bars within the same storage time indicate significant differences ($P < 0.05$).

a

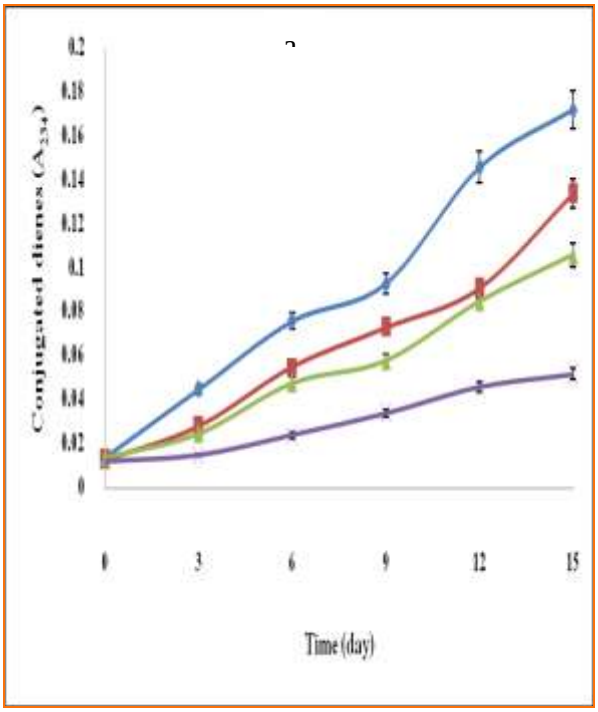
Conjugated dienes (A_{234})
0.2
0.18
0.16
0.14
0.12
0.1
0.08
0.06
0.04
0.02
0
0
3
6
9
12
15
Time (day)

b

c

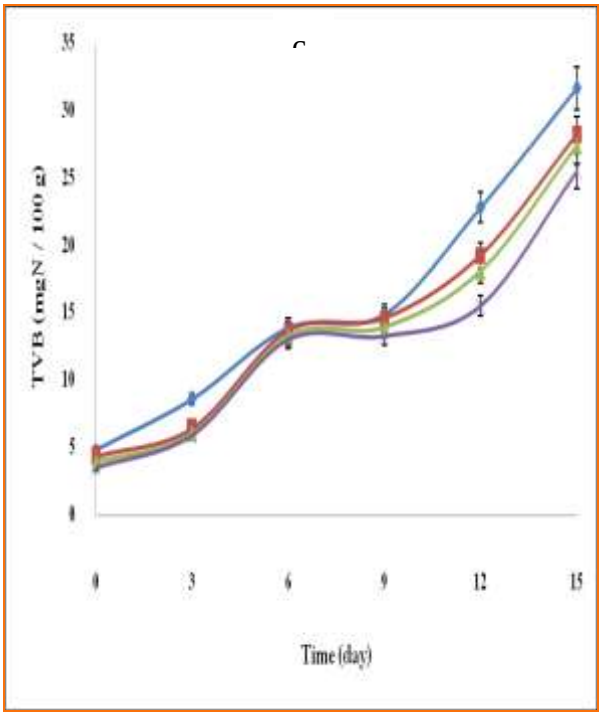
TVB (mgN / 100 g)
35
30
25
20
15
10
5
0
0
3
6
9
12
15
Time (day)

d

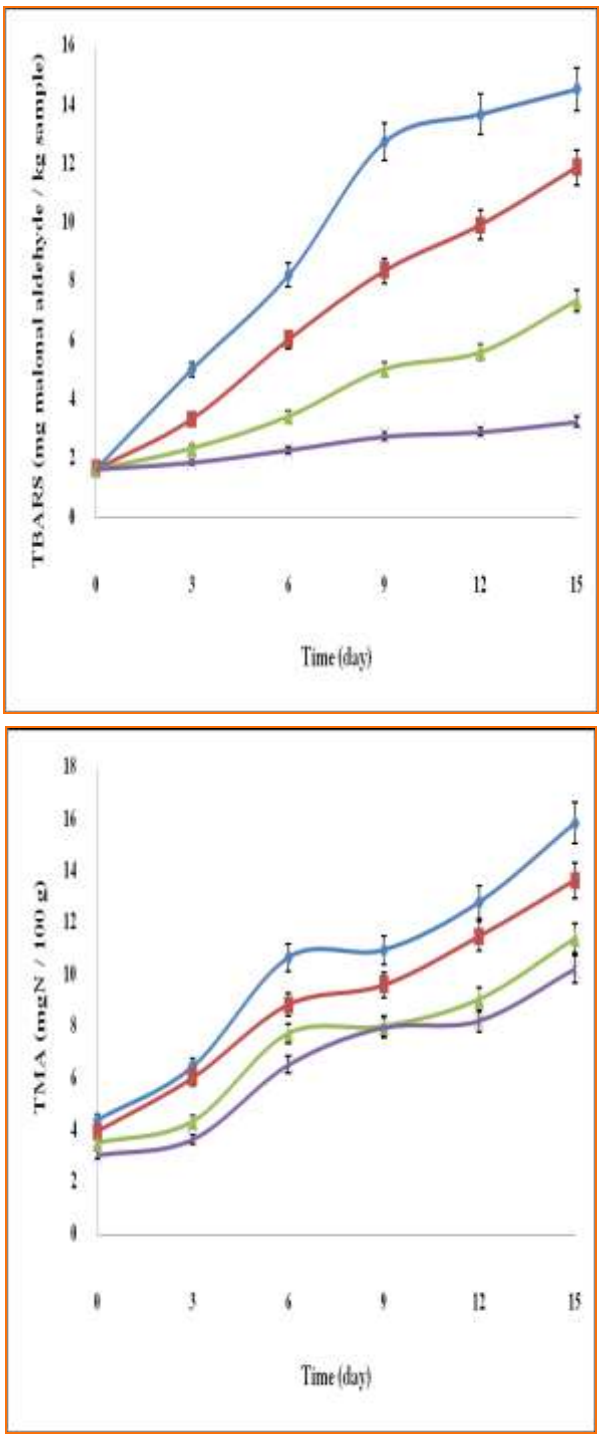

Figure 2 Conjugated dienes (a), Thiobarbituric acid reactive substances (TBARS) (b), Trimethylamine (TMA) (c) and Total volatile bases (TVB) (d) of Giant Perch meat during storage at 4°C for 15 days; control (◆), modified atmosphere packaging (■), added with chitosan (▲) and added with chitosan and modified atmosphere packaging (✖).Bars represent the standard deviation from triplicate determinations. Different capital letters on the bars within the same treatment indicate the significant differences ($P<0.05$). The different letters on the bars within the same storage time indicate significant differences ($P < 0.05$).

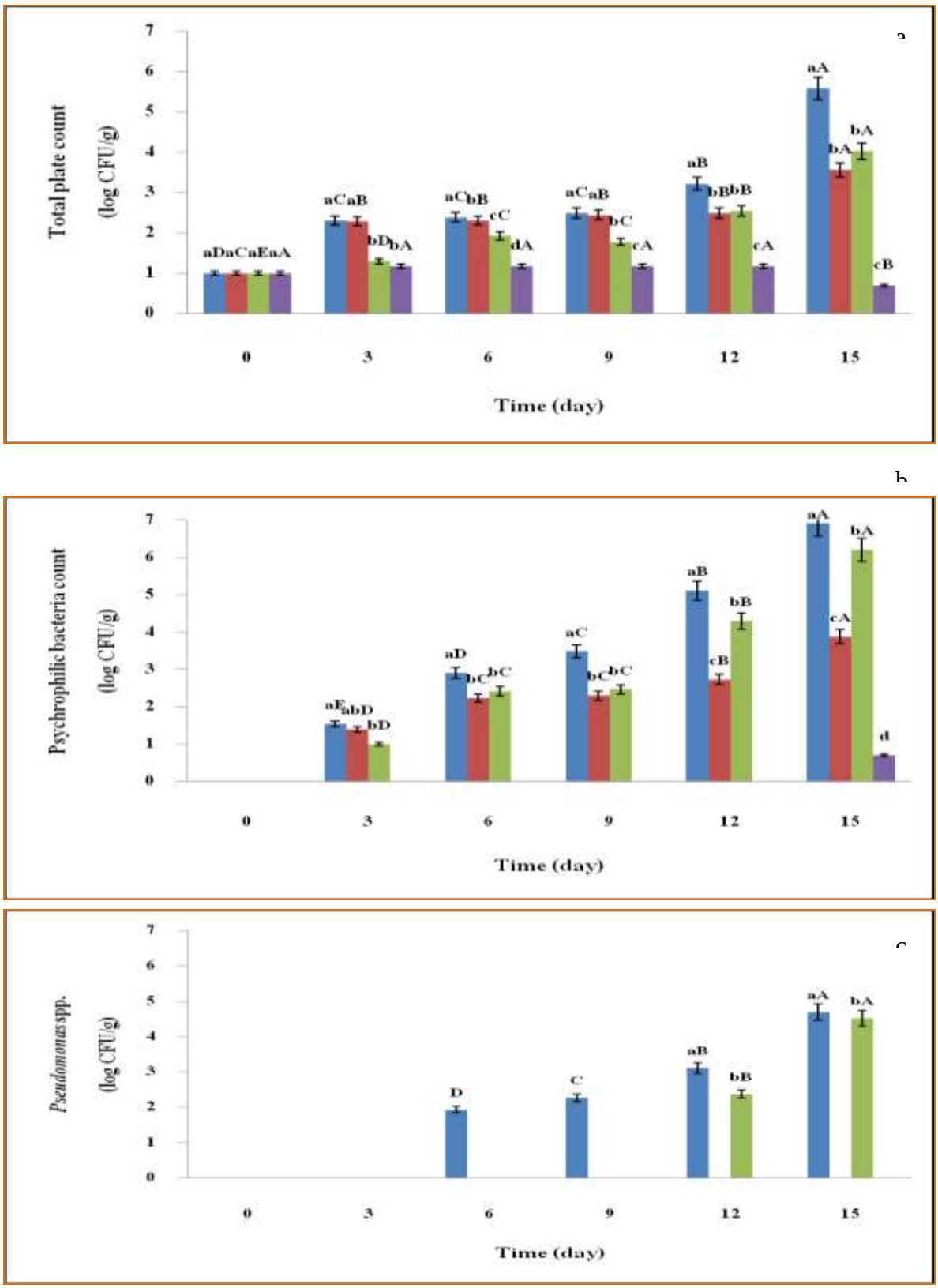

Figure 3 Total plate count (a), Psychrophilic bacteria (b) and *Pseudomonas* spp. (c) of Giant Perch meat during storage at 4°C for 15 days; control (◆), modified atmosphere packaging (■), added with chitosan (▲) and added with chitosan and

modified atmosphere packaging (✱). Bars represent the standard deviation from triplicate determinations. Different capital letters on the bars within the same treatment indicate the significant differences (P<0.05). The different letters on the bars within the same storage time indicate significant differences (P < 0.05).

a b

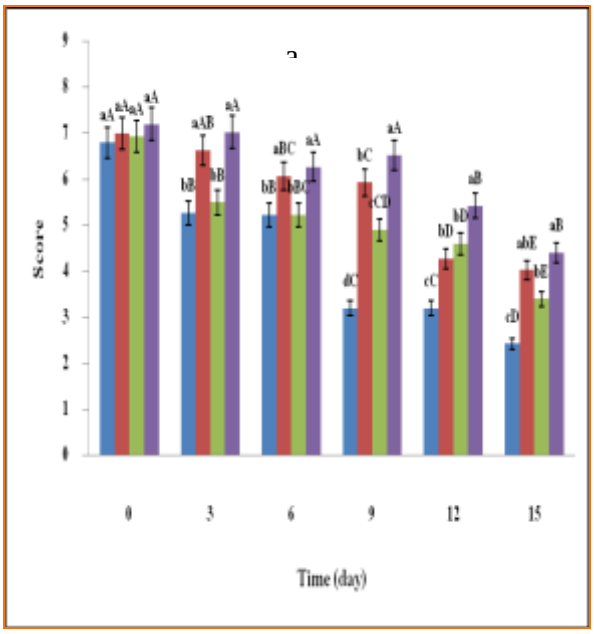

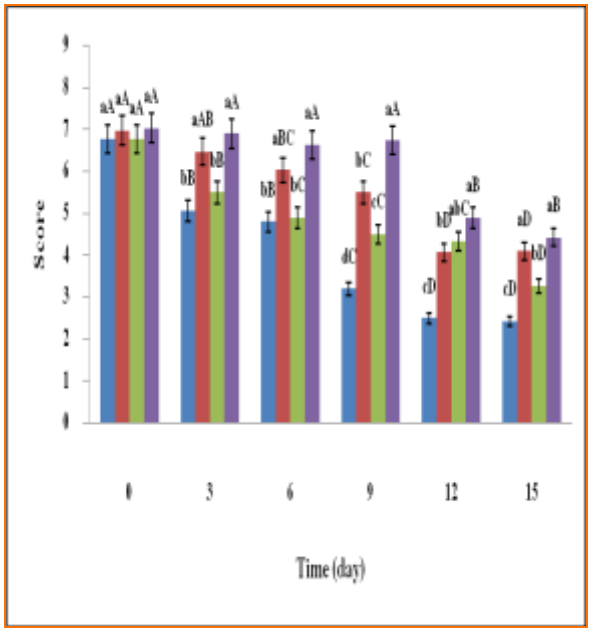

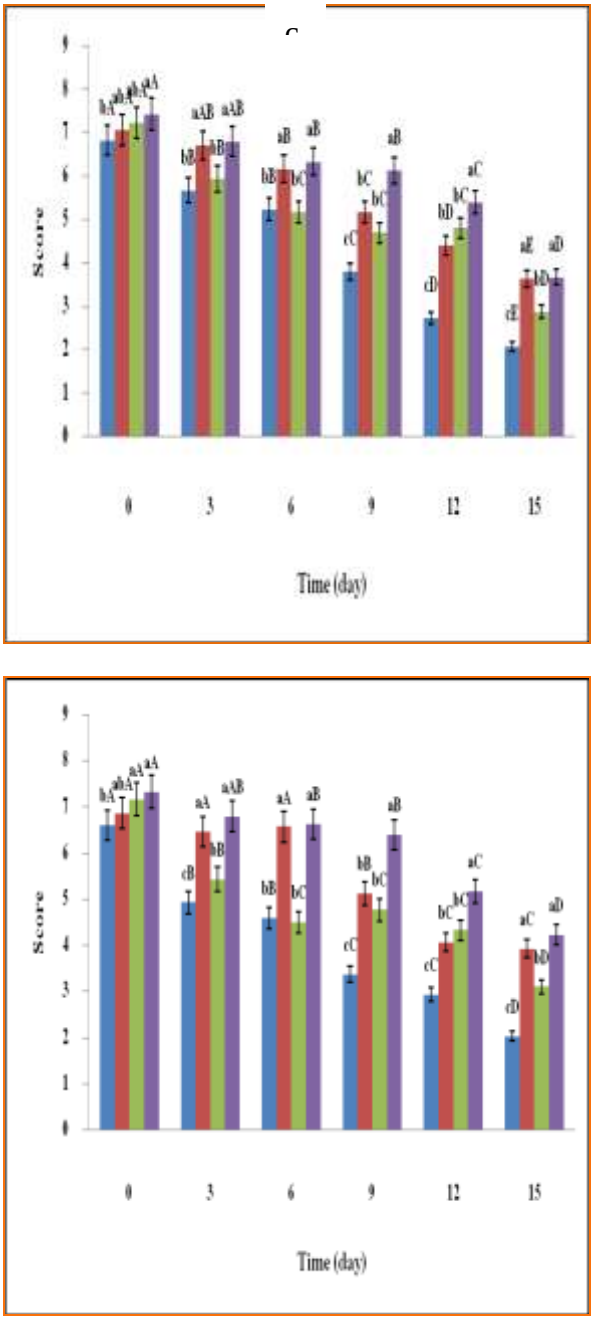

Figure 4 Color (a), texture (b), odor (c) and overall liking (d) from sensory evaluation of Giant Perch meat during storage at 4°C for 15 days; control (◆), modified atmosphere packaging (■), added with chitosan (▲) and added with chitosan and modified atmosphere packaging (✿). Bars represent the standard deviation from triplicate determinations. Different capital letters on the bars within the same treatment indicate the significant differences ($P<0.05$). The different letters on the bars within the same storage time indicate significant differences ($P < 0.05$).

4. Conclusion

Natural and safe chitosan could be used together with modified atmosphere packaging to extend the shelf life of Giant Perch meat during cold storage.

LSBE 405

Biosynthesis of value-added green material from renewable resources using a marine *Bacillus megaterium* isolate KB-1

Kesaven Bhubalan
Faculty of Maritime Studies and Marine Science, Universiti Malaysia Terengganu
21030 Kuala Terengganu, Terengganu, Malaysia

Maizatul Nuzi Othman
Faculty of Maritime Studies and Marine Science, Universiti Malaysia Terengganu
21030 Kuala Terengganu, Terengganu, Malaysia

Ishak Muhammad Syafiq
Faculty of Maritime Studies and Marine Science, Universiti Malaysia Terengganu
21030 Kuala Terengganu, Terengganu, Malaysia

Mohd Effendy Abdul Wahid
Institute of Marine Biotechnology (IMB), Universiti Malaysia Terengganu
21030 Kuala Terengganu, Terengganu, Malaysia

Al-Ashraf Abdullah Amirul
School of Biological Sciences, Universiti Sains Malaysia
11800 USM, Pulau Pinang, Malaysia

The corresponding author: Kesaven Bhubalan

Abstract

Polyhydroxyalkanoate (PHA) is a microbial derived polymer produced under imbalanced growth conditions. It serves as an intracellular carbon and energy reserve. PHA is considered to be a potential alternative for some petrochemical-derived plastics because of its thermoplastic characteristics and yet it is completely biodegradable. In this study, efforts were taken to identify PHA producing bacteria from marine sponge samples collected from the waters surrounding Langkawi Island, Malaysia. Marine sponges are known as ecologically diverse hotspots of unexplored microbial communities. Here, a bacterium (KB-1) with the ability to produce PHA was identified from tissue samples of marine sponge *Callyspongia* sp. The strain was later identified to the genus *Bacillus* with 99% similarity to *Bacillus megaterium*. Wild-type *B. megaterium* isolate KB-1 was found to utilize glucose as well as glycerol, a common by-product of biodiesel production as carbon source for PHA

accumulation. The marine isolate KB-1 is also capable of producing PHA using sea water as growth medium and in the presence of carbon source. This eliminates the use of conventional PHA biosynthesis medium. PHA is known for its biocompatibility and uses in pharmaceutical and medical field. However, most types of PHA is produced by Gram-negative bacteria and upon extraction of this biopolymer, a layer of endotoxin is usually present. PHA produced from the Gram-positive *B. megaterium* isolate KB-1 is endotoxin free, thus, eliminating additional endotoxin removal process and suitable to be used for selected medical applications.
Keywords: polyhydroxyalkanoate, biopolymer, biodegradable, *Bacillus megaterium*, glycerol

1. Introduction

PHA is a group of naturally occurring polymers synthesized by microorganisms. It has been recognized to be thermoplastic, biodegradable, biocompatible and possessing similar properties to synthetic petrochemical plastics [1, 2]. PHA is identified as a carbon and energy source of bacteria which is produced in the presence of excess carbon source under conditions with limiting nutrient elements (e.g., nitrogen, phosphorus, magnesium) [3,4]. PHA is comprised of various types of hydroxycarboxylic acids and can be classified as homopolymers or copolymers of two or more monomers. The monomer composition of PHA can be manipulated and predicted by means of the carbon sources used and by changing the growth conditions. Nevertheless, PHA synthesis mainly depends on the type of bacterial strain employed and the substrate specificity of the PHA synthase gene (*phaC*) present [2]. To date approximately 150 monomers with different structures have currently been reported with regards to the number of carbon atoms in monomer structure [2, 4]. Among the commonly studied PHA producing bacteria isolated from both terrestrial and marine environment belongs to the genus *Acinetobacter, Aeromonas, Burkholderia, Bacillus, Cupravidus, Delftia, Desulfococcus, Desulfosarcina, Pseudoaltermonas, Pseudomonas* and several microalgae [5, 6, 7].

The most common type of PHA found in the natural environment is poly(3-hydroxybutyrate) [P(3HB)] [8]. The properties of P(3HB) such as melting temperature, flexibility, elasticity and higher elongation at breaking point was improved by incorporating secondary monomer such as 3-hydroxyvalerate (3HV) or 4-hydroxybutyrate (4HB) [2,4]. PHA such as P(3HB) and its copolymers containing 3HV or 4HB had become attractive material in biomedical research and applications due to its biocompatibility [1,9]. Several established PHA products such as sutures, pins, films and screws are now being commercialised by some established companies namely P&G (U.S.A) and Metabolix [1,4]. PHAs applications are also expanded in wound healing management, orthopaedics and drug delivery [1,4].

The high production cost of PHA is the major setback for commercialization

[9]. The high cost includes set-up of fermentation systems, carbon feed stocks and downstream processes which requires the usage of various chemicals and enzymes [9,10]. Research is now geared towards minimizing the production costs of PHA by isolating suitable PHA producers capable of generating high yields of PHA, screening for strains capable of utilizing cheaper and renewable carbon sources as well as growing in simple growth medium, and genetically engineering strains to improve its PHA producing ability [4,9,10]. Here we report the efforts taken to identify PHA producing bacteria from marine sponge samples collected from the waters surrounding Langkawi Island, Malaysia. Marine sponges are known as ecologically diverse hotspots of unexplored microbial communities. The high level of biological activity in the sponges is believed to reveal PHA producing bacteria with varying potentials.

2. Results and Discussion

A bacterium (KB-1) with the ability to produce PHA was identified from tissue samples of marine sponge *Callyspongia* sp. The strain was later identified to the genus *Bacillus* with 99% similarity to *B. megaterium*. *B. megaterium* isolate KB-1 was able to use glucose and glycerol as carbon source for the production of P(3HB). From previous studies, *Bacillus* is known to produce P(3HB) from carbon sources such as glucose, fructose, 1,4-butanediol and plant oils [9,11]. PHA accumulation in bacterial cells can be controlled by varying the ratio of carbon to nitrogen (C/N). The C/N ratios of 20 – 50 are widely used for PHA biosynthesis [12]. The production of P(3HB) by *B. megaterium* isolate KB-1 was investigated by varying the ratio of (C/N). It was found that the P(3HB) content increased with C/N ratio of 15 □□30 when glucose was used (Table 1a). The P(3HB) was found to decrease at C/N ratio above 35. On the other hand, when glycerol was supplemented as the carbon source, highest P(3HB) content was detected with C/N ratio of 45 and it decreased with C/N ratio above 50 (Table 1b). The results show that this strain has different preference of C/N ratio based on the type of carbon source used.

Table 1a: Production of P(3HB) using glucose at different C/N ratio[a].

Carbon source	C/N	P(3HB) content (wt%)[b]
Glucose	15	16 ± 3
	20	24 ± 3
	25	30 ± 3

Table 1b: Production of P(3HB) using glycerol at different C/N ratio[a].

Carbon source	C/N	P(3HB) content (wt%)[b]
Glucose	35	12 ± 1

40	14 ± 1
45	20 ± 1

a. The cells were harvested after 72 hours cultivation at 200 rpm at RT. NH_4Cl was used as the nitrogen source. Data shown are means of triplicates.

b. The P(3HB) content was determined via GC analysis.

B. megaterium isolate KB-1 was grown is sea water as the growth medium and supplemented with glucose as carbon source. The findings show the possibility of this strain to accumulate P(3HB) in its natural environment in the presence of excess carbon source. *B. megaterium* isolate KB-1 was able to produce 15 ± 1 wt % of P(3HB) in sea water using glucose as the carbon source and up to 21 ± 3 wt% when sea water was added with mineral salts used to prepare the common PHA biosynthesis medium (Na_2HPO_4, KH_2PO_4 and NH_4Cl) [Table 2]. In a previous study, marine *Vibrio spp*. cultured in sea water as the PHA production media showed similar results of P(3HB) content and cell biomass [13]. The ability These results of P(3HB) production and cell growth was suggested to be improved by optimizing the salinity of the culture media at the optimal range in order to reduce high osmotic stress and its effect on P(3HB) production [13]. Such attempts could be made in the future with isolate KB-1 in order to improve its PHA producing ability.

Table 2: Production of P(3HB) by *B. megaterium isolate* KB-1 using sea water[a].

Production media	P(3HB) content (wt %)[b]
Sea water	15 ± 1
Sea water and mineral salts	21 ± 3

a. The cells were harvested after 72 hours cultivation at 200 rpm at RT. NH_4Cl was used as the nitrogen source. Data shown are means of triplicates.

b. The P(3HB) content was determined via GC analysis.

3. Conclusion

B. megaterium isolate KB-1 was able to grow and produce P(3HB) using simple sugar such as glucose and glycerol, a common by-product of biodiesel production. It was interesting to note that this strain could produce P(3HB) without any growth limitation in sea water. Most strains require limitation of certain essential nutrients such as nitrogen or phosphorus. The P(3HB) content was in the range of 17–21 wt%. The ability to use sea water as the culture medium and glycerol as carbon source might help to reduce the overall P(3HB) production cost. In future, a

transformant *B. megaterium* isolate KB-1 will be constructed to further analyze its ability to synthesize different PHA monomer using various renewable carbon sources.

4. Acknowledgments

This study was supported by Young Researchers' Fund (Tabung Penyelidik Muda), Universiti Malaysia Terengganu.

5. References

[1] Reddy C S K, Ghai R, Rashmi, Kalia V C. Polyhydroxyalkanoates: an overview. *Bioresource Technology*, 2003, 87: 137□146.

[2] Sudesh K, Abe H. *Practical guide to microbial polyhydroxyalkanoates*. Smithers Rapra, United Kingdom, 2010, pp 1□143.

[3] Chien C C. Production of poly-β-hydroxybutyrate (PHB) by *Vibrio* spp. isolated from marine environment. *Journal of Biotechnology*. 2007, 132: 259□263.

[4] Bhubalan K, Lee W H, Sudesh K. *Polyhydroxyalkanoate*. In A. Domb, N. Kumar and A. Ezra, (eds). *Biodegradable polymers in clinical use and clinical development*. New Jersey: John Wiley & Sons, 2011, pp 249□315.

[5] López- Cortés A, Rodríguez-Fernández O, Latisnere-Barragán H, Mejía-Ruíz H C, González-Gutiérrez G. Characterization of polyhydroalkanoate and the *phaC* gene of *Paracoccus seriniphilus* E71 strain isolated from a polluted marine microbial mat. *World Journal of Microbiology and Biotechnology*, 2012, 26: 109□118.

[6] Shrivastav A, Mishra S K, Mishra S. Polyhydroxyalkanoate (PHA) snythesis by *Spirulina subsalsa* from Gujarat coast of India. *International Journal of Biological Macromolecules*, 2010, 46:255□260.

[7] Wang Q, Zhang H, Chen Q, Chen X, Zhang Y, Qi Q. A marine bacterium bacterium accumulates polyhydroxyalkanoate consisting of mainly 3-hydroxydodecanoate and 3-hydroxydecanoate. *World Journal of Microbiology and Biotechnology*, 2010, 26: 1149-1153.

[8] Doi, Y. *Microbial polyesters*. New York, VCH, 1990.

[9] Shrivastav A, Mishra S K, Shethia B, Pancha I, Jain D, Mishra S. Isolation of promising bacterial strains from soil and marine environment for polyhydroalkanoates (PHAs) production utilizing Jatropha biodiesel byproduct. *International Journal of Biological Macromolecules*, 2010, 47(2):283-287.

[10] Tsuge T. Metabolic improvements and use of inexpensive carbon sources in microbial production of polyhydroxyalkanoates. Journal of Bioscience and Bioengineering, 2002, 94 (6): 579□584.

[11] Tay B Y, Lokesh B E, Lee C Y, Sudesh K. Polyhydroxyalkanoate (PHA) accumulating bacteria from the gut of higher termite *Macrotermes carbonarius*

(Blattodea:Termitidae). *World Journal of Microbiology and Biotechnology*, 2010, 26: 1015□1024.

[12] Amirul A A., Yahya A R M, Sudesh K, Azizan M N M, Majid M I A. Biosynthesis of poly(3-hydroxybutyrate-*co*-4-hydroxybutyrate) copolymer by *Cupriavidus* sp. USMAA1020 isolated from Lake Kulim, Malaysia. *Bioresource Technology*, 2008, 99(11), 4903□4909.

[13] Wei Y H, Chen W C, Wu H S, Janarthanan O M. Biodegradable and biocompatible biomaterial, polyhydroxybutyrate, produced by an indigenous *Vibrio* sp. BM-1 isolated from marine environment. *Marine Drugs*, 2011, 9: 615□624.

LSBE 416
Characterization of allergenic compounds from *Pleurotusostreatus* and *Pleurotussajorcaju*

Elbatrawy Nasr Eman[1,2]
Department of biology, Virginia Commonwealth Univ, USA
enelbatrawy@vcu.edu and osho_sasa2000@yahoo.com

GhonimyAbdouallah Eglal[2]
faculty of sience, department of biology, Al Azhar Uni. cairo
eglalghoneimy@hotmail.com

Wu Fang sheng [3]
Department of biology, Virginia Commonwealth Univ, USA
fwu@vcu.edu

The corresponding author: Elbatrawy Nasr Eman[1,2]
Tel:01 804 937 7660
Presenting author:Wu Fang sheng [3]
Tel:01 804 747 6540

Abstract

Our study aims to isolate and purify allergenic compounds from two investigated mushroom strains, *Pleurotusostreatus* and *Pleurotussajorcaju*. Furthermore, the purified allergens were subjected to biochemical investigations in an attempt to determine its nature and characterization. Crude extracts of *P. ostreatus* and *P. sajorcaju* (spores, mycelia, broth, fresh and cooked fruit bodies) were tested by skin prick test onto three groups; A, B and C (patients suffered from allergy, mushroom workers and normal cases respectively). Positive response toward the extracts was detected in numbers of patients and mushroom workers, while negative response was detected for the normal cases and the extract of cooked mushrooms for all cases. The crude extracts were fractionated; all fractions were subjected to antigen-antibody reaction using ELISA. The effective allergens appeared in fraction no. 6 in spores and broth extracts of the investigated strain, while appeared in fraction no. 8 in the case of mycelia and fruit bodies extracts. Characterization of the active fractions was performed using spectrophotometer, capillary electrophoresis, and amino acid analysis, as well as mass, IR and NMR spectroscopy. Our results indicate that this strain possessed four different allergens which were proteinic in nature. Keywords: *Pleurotusostreatus*, *Pleurotussajorcaju* allergy, ELISA, protein.

Keyword:*Pleurotusostreatus*, *Pleurotussajorcaju*, allergy, ELISA, protein.

1. Introduction

Human health represents a real and hard challenge, the protecting of human health is an integral part of our life. Allergens are widely found in several food and feed, and also widely distributed in the air where unavoidable contaminants are present. There is a positive Relationship between concentration of Immunoglobulin E (IgE) antibodies and the concentration of allergenic compounds where IgE produced due to stimulation of the immune system by antigen (allergens) resulted in production of IgE mediated reaction[1]. The immediate positive skin test reactions in the prick-to-prick tests, and the demonstration of a significant amount of IgE to shiitake and oyster extracts supported the allergic, IgE-dependent pathogenesis of this occupational asthma [2]. Horner [3] reported that more than 80 genera of fungi have been associated with symptoms of respiratory tract allergy. The famous five genera producing allergens (belonging to basidiomycetes) are Calvatia spp., Coprinus spp., *Ganoderma spp*., *Psilocybecubensis* and *Pleurotus spp*. Oyster mushrooms (*Pleurotusostreatus*) are cultivated for human consumption in various subspecies. Their spores are highly potent allergens which can cause exogenous allergic alveolitis, hypersensitivity pneumonitis (HP) and occupational asthma by mushroom spore proteins [2]. About 30-40% of mushroom worker infected by respiratory allergic reaction due to inhalation of oyster mushroom spore which released vigorously into the atmosphere of growing rooms [4]. Spores allergy is one of the most important limiting factors for the large scale cultivation of *Pleurotussajorcaju.* Different approaches are being adopted for the production of commercial sporeless/low-sporing strains of *Pleurotus* through ultraviolet (UV) mutation to alleviate the spores allergy problem [6, 5].

2. MATERIALS AND METHODS

Fungal strain, Spores print, and Preparation of crude extracts

Pleurotus sp. was used in the present study obtained from the Fujian Edible Mushroom Association, Fuzhon, China and Fujian Jun-Cao Develop Project Association, China (*P. ostreatus* NO. 239 and *P. sajorcaju* NO. 292).Ou r invistegated mushrooms were inoculated and cultivated according to [7, 8, 9, 10]. Spores print was determined according to Thomas [11]. All spores collection processes yielded >95 % of pure spores as determined by Image analysis system (system soft imaging system GmbH software (analysis pro ver.3.0). Crude extracts were extracted from spores according to Horner [7].

Population study, clinical profile, blood investigation of (the patients, mushroom workers and normal cases) and skin prick test

The five crude extracts from spores, mycelia, broth, fruit bodies and cooked fruit bodies were injected into three groups of 37 volunteers, 17 of them (group A) with personal history of respiratory allergy attending the charity hospital of Tanta allergy clinics at university of Tanta, Cairo. The second group (group B) consisted of 15 persons worked in the field of mushrooms cultivation. Group (c) 5 normal adult cases. Blood investigation of volunteers, 10 ml of venous blood was withdrawn from each patient to perform complete blood picture (CBC) and Immunoglobulin E (IgE).Only one case of each group (which has the highest concentration of IgE) was selected for performance of antigen-antibody reaction between all fractions and the sera of selected cases, to determine the active fractions. The absorbance was measured at 450 nm using ELISA Reader (Sunrise TecanAustria 5082 Ref. F039300; Incubator Awareness Technology Inc. model stat fox-2200 Washer Tecan M8/2R Colunmbus plus A-5082 Austria F109201) [12]. Skin prick test was performed by 5 mg of lyophilized crude extracts were dissolved in 1 ml glycerol (50%) by phosphate buffer pH 7.2 (v/v) [7].

Purification of antigenic proteins and Biochemical analyses:

The Pharmacia column (40×2 cm) was packed by sephadex G l00 after its soaking with phosphate buffer (pH 7.2) overnight and the samples were mixed with blue dextran and bromophenol blue dyes, and loaded on the top of the column and fractionated using LPLC system (pumb model MINI Puls3, detector UV/VIS-151 FC 203B, Gilson). The total protein of the active fractions was determined by Lowry method [13] and as modified by Waterborg and Mathews [14]. Followed by determination of total soluble carbohydrates of the active fractions were determined by the anthrone reagent method as described by Umbriet [15]. The active fractions of the investigated strain were applied to capillary electrophoresis (Biofocus 3000, Bio-RAD, USA), using SDS-protein Kit for the determination of the molecular weights [16]. Proteinic amino acid profile of the active fractions was determined using amino acid analyzer system (Model eppendorf, Biotronik, LC 3000, the hydrolysis cation-exchange column was used and the resin particle size was 4 µm and the column size was 125×4mm) [17]. The active fractions were subjected to Mass spectroscopy using DI- 50 unit of Shimadzu GCMS-QP5050A [18]. The infrared absorption spectrum of the purified active fractions was estimated using BRUKER, Vector 22, Germany [19]. The active fractions were subjected to the proton (1H) NMR spectra and were recorded in deutrated dimethyl sulphoxide (DMSO-d6) on a Varian a Mercury-VX-300 NMR spectrometer [20].

3. RESULTS and Discussion

Clinical profile and blood investigation of the investigated cases

Crude extracts of spores, mycelia, fruit bodies and fungal broth of the investigated mushrooms *P. ostreatus* and *P. sajorcaju* were applied onto 37 volunteers who

divided into two groups.The first group (group A) consisted of 17 patients who suffered from allergy ranged from 3 cases suffered from asthma (17.6 %), 2 cases suffered from rhinitis (11.76 %) and 12 cases suffered from asthma and rhinitis (70.5 %). The second group (group B) consisted of 15 mushroom workers, eight of them suffered from asthma and rhinitis(53.4 %) during working in green house, (46.6%) were suffering from rashes during their work in green house. The values of total immunoglobulin E of group A were higher than of group B.IgE ranged from 18 to 965 IU/ml, meaning that not all of the investigated cases have a high level of IgE and this result agreed with Allansmith [21] who reported that there is a positive relationship between both the scope and the number of different allergens and the concentration of IgE. Eosinophils count of volunteers possessed a high reading especially in the cases of high reading in IgE count and these results are consistent with Butterfield [22] who reported that when IgE reach and reacted with mast cells and basophils cells promote the production of inflammatory mediators.

Toxicity test.

No toxic effect was observed on female Swiss Webster mice that were injected by spores, mycelia, fruit bodies(fresh and cooked) extracts of *P. ostreatus* and *P. sajurcaju*and fungal filtrate at all investigated time intervals and after 72 hours.

Skin prick test of group A and B toward the investigated mushroom extracts: Spores extract of each strain showed the highest allergenic effect toward all cases. Mean wheel and flare diameters stimulated by spores extracts were higher than that exerted by mycelial, broth and fruit bodies extracts. While, cooked fruit bodies of both organism reveal negative result. the mean wheel and flare diameters of *P. ostreatus* spores, mycelia, broth and fruit bodies extracts were slightly increased than that stimulated by *P. sajorcaju* extracts in most cases. Also, the highest mean wheel and flare diameters were observed with spores extract of both *P. ostreatus* and *P. sajorcaju*, while the lowest mean wheel and flare diameters were produced by fruit bodies extract. These results may be attributed to the age of cases, duration of illness, type of antigen and also due to the differences of immune system expression. Brian [23] stated that prevalence of basidiospores specific positive skin prick test for each spores extract varied from a low of 28.6 for *Pisolithustinctorius* to a high of 55.6% for *Geastrumsaccatum*, 54.8 % for *Coprinusquadrifadus* and 42.9% for *Pleurotusostreatus*. Concerning the allergenic potency of fungal crude extracts, the foregoing results show slight increase in the potency of spores, mycelia, broth and fruit bodies of *Pleurotusostreatus* respectively. Similar findings were observed by Samuel [8]. Spore extract of *Cladosporiumcladosporides* is more potent than the mycelial extract of the same organism. Additionally it was clear that both mycelium and spore extract have totally different allergenic compound however, in certain cases mycelial extract of *Alternariaalternata*have greater potency than of spores due

probably to higher concentration of the allergens [24]. The mean wheel diameter of skin prick test of crude extracted of the investigated mushroom varied from 4-7.9 mm, with the greatest reaction value observed with spores followed by mycelia, broth and fruit bodies extracts these results agreed with that reported by [8,24].

Determination of antigen-antibody (Ag-Ab) reaction of crude extracts of *P. ostreatus* and their fractions with serum of selected patient, mushroom worker and normal case using ELISA.

purified fractions of *P. ostreatus* spores, mycelia, broth and fruit bodies contained high antigenic concentrations compared to the values of respective forms of crude extracts appeared in fractions no 6,8,6 and 8 respectively with values of 163, 76, 70 and 64 IU/ml in case of patient serum.While in case of mushroom cultivator serum appeared to be (150, 72, 66, and 60 IU/ml) lower than that of patient one. While, the highest concentration of purified antigen of *P.sajorcaju* compared to that of crude extract without purification (72, 65 ,62, 61 IU/ml) while the antigen concentration of crude extracts of spores, mycelia, broth and fruit bodies were 151, 72, 70 and 63 IU /ml respectively with mushroom serum. In conclusion our results revealed that, *P. ostreatus*extracts are rich in allergenic compounds more than *P. sajorcaju*. And spore of each strain possesses higher allergenic activity than mycelium extract followed by broth extract. However the lowest activity were viewed with fruit bodies extracts in both of them. But, antigen antibody reaction with selected mushroom cultivator case was lower than that observed in patient case. Our results agree with that demonstrated by Asturias [27] who reported that nowadays diagnosis of allergic disease and therapy based on the crude allergen extracts, and we have to consider that the composition and potency of allergenic compounds may differ from extract to extract according to nutrition, atmosphere and different measurements. Gel filtration enhanced the radioallergosorbent test (RAST) activity of the active pool relative to crude extract [7]. This result attributed to a greater concentration of allergen(s) in the sephadex G 75 fraction, by removal of inert material or the removal of substances inhibitory to the coupling reaction between allergens and antibodies.

Characterization of the purified allergens.

Protein concentrations of the antigenic fraction *P. ostreatus* spores, broth, mycelia and fruit bodies were 0.031, 0.021, 0.024, and 0.020 mg/ 100 ml respectively. While, it was 0.030, 0.027, 0.019 and 0.21 in case of *P. sajorcaju* respectively. However, the results revealed that, active fractions were free from soluble carbohydrates. There are three different molecular weights ranged from 31 KDa to 90 KDa were determined using capillary electrophoresis. Our result disagree with Horner[10] who reported that, allergen extract of *P.ostratus* spore are low molecular weight less than 10 KD.

Amino acid composition of the antigenic fractions (*P. ostreatus* and *P. sajorcaju)*

Histidine was detected only in the fruit bodies. Regarding to amino acid contents of *P. sajorcaju*, proline was detected only in mycelia and broth. While, methionine, phenyl alanine and lysine were found in mycelia, broth and fruit bodies. The characteristic amino acids composition of spores, mycelia and broth allergens of *P. ostreatus* and P. *sajorcaju*revealed the presence of arginine in high concentration, Nevertheless, allergens recorded relatively moderate to high quantities of amino acids as aspartic acid in broth and fruit bodies, glycine in mycelia, broth and fruit bodies allergens, alanine in mycelia and broth, leucine and tyrosine in fruit bodies allergen, proline in mycelia and broth allergen, and lysine in broth allergen. Allergens from mycelia and broth possessed the same amino acids but different in concentrations. Obviously, these allergens were rich mainly in aspartic acid, glycine, arginine, and proline, also contain moderate concentration of glutamic acid. These results are somewhat similar to that reported by Heimo and Christof [28] who found that the Berthoolletia excels contains allergenic protein known as 2S albumins this protein is rich in arginine, glutamine, asparagine, and often cysteine.

Identification of pure antigen compounds.

The mass spectrum of active fractions *P. sajorcaju* spores, mycelium, broth and fruit bodies reveals that the fraction was pure and the molecular ion peak (M+) was 256,165,273and 319 respectively. Regarding *P.ostreatus* active fractions it was 407,303,275 and 279 respectively. The IR spectrum of the pure fractions shared absorption bands ranged from 3315-3494 cm-1 due to the presence of –NH2 group, shared absorption bands ranged rom1080-1310 cm-1 for –C– N group (amine), For –C=C– alkene group (1599-1652).While amide group represented only in active fractions of *P.ostreatus* spore and mycelium of *P. sajorcaju*. And 1403-1451 cm-1 for –C=C– group (alkene) only in case of mycelium and fruit bodies of *P. ostreatus*. The results of Nuclear Magnetic Resonance spectroscopy reveals different signals as follows 3.617 δ for –C– N group (amine), 2.495 and 2.231δ for CH2 group (alkane), 1.885 δ for C–CH3 and 0.861δ for R–CH3. And explain the presence of aromatic group in active allergenic compounds of spores and broth of *P.sajorcaju* also, active fraction of *P.ostreatus*. Allergens extracted from *P. ostreatus* were proteinic in nature, possessing special features that influence allergenicity potentiality. The size, physicochemical properties of the protein and the way in which the protein is processed and presented to the immune system affected the potential allergenicity. Also, specific amino acids might play a role in allergenic potency and determine its activity.

4. Conclusion

Antigens were detected in patients and mushroom workers and this might be due to its presence in high concentrations in air. Allergens extracted were proteinic in

nature,possessing special features that influence allergenicitypotentialitywhich may disappear by heating. The size, physicochemical properties of the protein and the way in which the protein is processed and presented to the immune system affected the potential allergenicity. Also, specific amino acid might play a role in allergenic potency and determine its activity.

5. REFERENCES

[1] Horner W E, Helbling A, Salvaggio J E, Lehrer S B. Fungal allergens. ClinMicrobiol, 1995, 8(2):161-79.

[2] Senti G, Leser C, Lundberg M, Wuthrich B. Allergic asthma to shitake and oyster mushroom. Allergy, 2000, 55(10):975-978.

[3] Horner W E, Ibanez M D, Lehrer S B. Immunoprint analysis of Calvatiacyathiformis allergens. I. Reactivity with individual sera. J. Allergy Clin. Immunol, 1989, 83(4):784–792.

[4] Martinez C D. Past and future of edible mushroom cultivation in tropical America. Mushroom Science, 1989, 12(1):795-805.

[5] Butcher B T, O'Neil C E, Reed, M A, Altman L C, Lopez M, Lehrer S B. Basidiomycetes allergy: measurement of spore-specific IgE antibodies. J. Allergy Clin. Immunol, 1987, 80(6):803–809.

[6] Ravishankar S, Pandey M, Tewari R P, Krishna V. Development of sporeless/low sporing strains of Pleurotus through mutation. World Journal of Microbiology and Biotechnology, 2006, 22(10):1021-1025.

[7] Horner W E, Ibanez M D. Liengswangwong B, Salvaggio J E, Lehrer, S B. Characterization of allergens from spores of the oyster mushroom, Pleurotusostreatus. J. Allergy Clin. Immunol, 1988, 82 (6):978–986.

[8] Samuel B,.; Lehrer S B, Manuel M D, Brian B T, Jonolsos M S, Margret R M S, John E, Salvaggio M D. Basidiomycetes mycelia and spore- allergen extract: skin test reactivity in adult with symptoms of respiratory allergy. J. Allergy Clin Immunology, 1986, 78(3):478-485.

[9] Zhanxi L, Zhanhua L. Design of mushroom cultivation. Martinez-Carrera Journal, 1991, 137(3): 355-366.

[10] Zhanxi L, and Zhanhua L. Training Manual of APEMT China- Chapter 11, Volvariellavolvacea cultivation 2000, p. 100-109

[11] Thomas D A, Malcolm M J, Drichardson M D, David S S. Fungal infection: Diagnostic and management. London Press, 3 ed, 1996, P. 3.

[12] Zetterstrom, O, Johansson S G. IgE concentrations measured by PRIST in serum of healthy adults and in patients with respiratory allergy. A diagnostic approach. Allergy, 1981, 36(8):537-547.

[13] Lowry O H, Rosebrough N J, Farr A L, Randall R J. Protein measurement with the folin phenol reagent. J. Biol. Chem, 1951, 193(53): 265-275.

[14] Waterborg, J. H. and Matthews, H. R. (1998): The lowry method for protein quantitation In: The protein protocols Handbook (walker, J. M. ed.) Humana press Inc.

[15] Umbriet W W, Burris R H, Stauffer, J F, Cohen P P, Johnse W L, Leepage G A, Patter V R, Schneider W C. Manometric techniques a manual describing methods applicable to the study of tissue metabolism. Burgess publishing company, 1959, P. 239.

[16] Patrick C. Separation of peptide and protein In: Capillary electrophoresis theory and practice. (Second edition CRC press), 1997, p.363.

[17] John A A. High performance liquid chromatography In: Chromatographic analysis of pharmaceuticals. (Second edition New York press), 1997, pp. 157.

[18] Wilson K, Walker J. Mass spectrometric techniques. In: Practical biochemistry principles and techniques (Fourth edition. Cambridge University Press), 1994, pp. 382.

[19] Silverstein R M, Passler G C, Morrill T C. Spectrometric identification of organic compounds. 4th ed (John yiley and sons) New York press. 1981, pp. 215

[20] Daniel C, Thomas B J, Corren M D. Introduction to immune system. In: Manual of allergy and immunology (Fourth edition), 2002, pp. 2.

[21] Allansmith M R. Immunology of the external ocular tissue. Journal American optometric association; 1990, 61(6): 16-22.

[22] Butterfield J, Weiler D, Dewald G, Gleich G J. Establishment of an immature mast cell line from a patient with mast cell leukemia. Leuk. Res. 1988, 12 (4):345–355.

[23] Brian T C, Carol E, O'Neil C E, Margret A, Reed M S, Leonard C A, Ltman M D, Manuel M D, Lehrer S B. New orlean, Basidiomycetes allergy: Measurement of spores specific IgE antibodies. J. Allergy Clin. Immunology, 1987,80 (6):803-809.

[24] Bouziane H, Platage J, Fitting C, Mecheri S, Lelong M, David B. Comparison of the allergenic potency of spores and mycelium of Cladosporium. AllergolImmunopathol, 2005, 33(3):125-130.

[25] Asturias J A, Arilla M C, Aguirre M, Gomez B N, Martinez A, Palacios R, Sanchez G F, Martinez J. Quantification of profilins by monoclonal antibody-based sandwich ELISA .Journal of immunological methods, 1999, 292(2):61-71.

[26] Heimo B, and Christof E. Molecular and biochemical classification of plant derived food allergens. J. Allergy Clin. Immunol, 2000, 106 (1):27-36.

LSBE 137
Functional Physicochemical Properties and Their Application in Food Processing of Thai Indigenous Red Rice Varieties

Rutrada Sompong
Thaksin University, Department of Food Science and Technology,
Faculty of Technology and Community Development,Thailand
E-mail address: dongrutrada@hotmail.com

The corresponding author: Rutrada Sompong

Abstract

Red rice is pigmented rice, which has good nutritive properties, high content of polyphenolic compounds and high antioxidative capacities. Thus, it offers a high potential for production of functional food. The aims of this study were to characterise the chemical functional and physical properties of various indigenous red rice varieties and to investigate the influence of food processing (drum drying, heat moisture treatment, yellow alkaline noodles production and rice beverages production) on their properties. Six red rice varieties from Thailand were determined for proximate composition, total phenolic content (TPC) and their antioxidant activities. The proximate composition (g/100g) of all red rice tested was 9.28 - 13.12 moisture, 2.37 - 3.19 fat, 7.16 - 10.36 protein, 1.26 - 1.50 ash, 3.17 - 4.51 total dietary fibre and 73.73 – 77.53 total carbohydrate. Highest antioxidant activity and TPC was found in Bahng Gawk varieties. Varieties with the highest amylose showed the highest peak viscosity and final viscosity ($p<0.05$) while contrast resulted with low amylose rice varieties. All applied food processes affected the functional and physicochemical properties of the final products. However, all products had remaining levels of functional properties which still allows to recommend their use for functional food production.

Keywords: Red rice; Drum drying; Heat moisture treatment; Yellow alkaline noodles; Rice beverages

LSBE 322
Nutrient reduction and the marine plankton in ToloHarbour, Hong Kong

C. Kim Wong[1], Alle A.Y. Lie[1, *], Guangtao Zhang[2], Y. Kit Yung[3]&Qingchao Chen[4]

[1] Department of Biology, The Chinese University of Hong Kong, Shatin,Hong Kong

[2] Key Lab of Marine Ecology & Environmental Science, Institute of Oceanology, Chinese Academy of Sciences, Qingdao, China

[3] Water Policy and Science Group, Hong Kong Environmental Protection Department, Hong Kong

[4] The South China Sea Institute of Oceanology, Chinese Academy of Sciences, Guangzhou, China

[*] Current address: Department of Biological Sciences, University of Southern California, 3616 Los Angeles, 90089-0371, CA, USA

Abstract

ToloHarbour is a semi-enclosed bay in the northeastern corner of Hong Kong. During the 1980s, excessive nutrient loading led to a dramatic increase in nutrient concentrations, which in turn caused noticeable increases in algal biomass and algal bloom occurrences. An action plan to reduce nutrient loading was launched in 1987 and became fully operational in 1998. Comparison between data collected before (1986–1997) and after (1998–2008) the full implementation of the nutrient reduction measures revealed significant decreases in the concentrations of total nitrogen, total phosphorus and silica. Decrease in nutrient levels was accompanied by significant decreases in chlorophyll-*a* biomass and the number of algal blooms.The density of dinoflagellates did not change significantly, but increases in the densities of diatoms andsmall flagellates led to a significant increase in the abundance of total phytoplankton. The zooplankton in ToloHarbour was dominated by copepods, and a comparison of the copepod communities in 1987–1991 and 2003–2004 revealed that copepod densities were much lower in 2003–2004(4,810 ind.m^{-3})compared to 1987–1991 (6,392 ind.m^{-3}). Increase in the abundance of diatoms and small flagellates suggests that the observed decrease in copepod densities was not caused by food limitation. Small copepods, notably species of *Paracalanus*and *Oithona*, dominated the copepod communities both before and after nutrient reduction, but an increase in species evenness, caused mainly by an increase in the number of

speciesfrom 48 in 1987–1991 to 52 in 2003–2004, was recorded after nutrient reduction. Nutrient reduction had therefore led to considerable changes in the plankton community and the dynamics of the planktonic food web in ToloHarbour.
Keywords: nutrient, phytoplankton, zooplankton, ecology

LSBE 309
Methamphetamine Administration on Alterations of Sperm Quality and Hormone receptors in Rat testis

SutisaNudmamud-Thanoi
Department of Anatomy and Centre of excellence in medical biotechnology,
Faculty of Medical Science, Naresuan University, Phitsanulok, Thailand
E-mail: sutisat@nu.ac.th

WanvipaSueudom
Department of Anatomy and Centre of excellence in medical biotechnology,
Faculty of Medical Science, Naresuan University, Phitsanulok, Thailand
E-mail: nujip_anatomy@hotmail.co.th

Nareelak Tangsrisakda
Department of Anatomy and Centre of excellence in medical biotechnology,
Faculty of Medical Science, Naresuan University, Phitsanulok, Thailand
E-mail: nareelakt@hotmail.com

Samur Thanoi
Department of Anatomy and Centre of excellence in medical biotechnology,
Faculty of Medical Science, Naresuan University, Phitsanulok, Thailand
E-mail samurt@nu.ac.th Tel: +668-1886-7445

The corresponding author: Samur Thanoi

Abstract

Methamphetamine (METH) is a psychostimulantwhich can degenerate neurons and induce psychosis. METH can cause apoptosis in seminiferous tubule and changes of plasma testosterone concentration. Therefore, the present study was carried out to investigate the effect of METH dependence on rat sperm quality and expressions of progesterone receptor (PR) and estrogen receptors (ER) in seminiferous tubules of rat testis. Sperm quality parameters including sperm motility, sperm morphology and sperm concentration were examined. Immunohistochemistry was used to demonstrate PR andERβ expressed cells. The percentages of normal sperm motility and normal sperm morphology were significantly decreased in animals treated with METH when compared with controls, especially in escalating dose (ED METH) and escalating dose-binge (ED-binge METH) groups. In addition, sperm concentrations in ED METH and ED-binge METH groups were numerically decreased when

compared with the control group but it just failed to reach significant. Furthermore, the expressions of PR andERβ were significantly decreased in spermatogenic cells and sertoli cells per total cells in each cell type in all METH treated animals.These results indicate that METH can induce abnormal sperm quality. These changes of sperm quality may relate to fertilizing abilities of sperm.A decrease of PR and ERβ expressionsin spermatogenicand sertolicells may lead to impairments of spermatogenesis and fertilizing ability of sperm.
Keywords: rat testis, methamphetamine, sperm quality, estrogen receptor, progesterone receptor

1. Introduction

Methamphetamine (METH) is an illicit drug which has a primary action in the brain. METH has been reported as a neurotoxicant (1) which can induce euphoria, alertness, anxiety, hallucination and psychosis (2,3).METH also has effects in reproductive system. It can induce apoptosis in seminiferous tubules and changesof serum testosterone concentration in male mice (4,5,6). Recently, METH has been reported to decrease normal sperm morphology and sperm count and increase apoptotic cells in seminiferous tubule (6). Moreover, METH can decrease proliferation of spermatogonia and the ratio of proliferation/apoptosis in seminiferous tubule of rat testis (7). Progesterone and estrogen are hormones that play a role in spermatogenesis (8). The functions of progesterone are associated with sertoli cell function, spermiogenesis, sperm capacitation, and synthesis of testosterone as well as induction of hyperactive sperm motility and acrosome reaction of mammalian spermatozoa (9,10). Estrogen is an important hormonefor proliferation and differentiation of germ cells during development and inhibiting apoptosis in testis (11).

However, study of METH addiction with doses that imitate METH addiction in human has not been reported its effects in reproductive system. Therefore, the objective of this study was to investigate the effect of METH addiction that imitates METH addiction in human on the alterations of sperm quality andexpressions of ER and PR in seminiferous tubule of male rat

2. Main Body

2.1 Materials and Methods

Animals and drug administration

D-methamphetamine hydrochloride (Lipomed AG, Arlesheim, Switzerland) with the consent from the Ministry of Public health was used in this experiment.24 male Sprague-dawley rats (National Animal Center, Salaya, NakornPathom). The protocol for this study was approved by the Animal Research Committee of Naresuan University, Thailand. Animals were divided into 4 groups with 6 animals each. In

control group, rats were treated with 0.9% saline 3 times per day for 14 days and 4 times at 2 hours intervals on day 15. In acute binge (AB METH) group, rats were treated with 0.9% saline 3 times per day for 14 days and treated with 6mg/kg METH 4 times at 2 hours intervals on day 15. In escalating dose (ED METH) group, rats were gradually increase treated with METH3 times per day for 13 days and treated with 4.0 mg/kg METH 3 times on day 14 and treated with 0.9% saline 4 times at 2 hours intervals on day 15. In escalating dose-binge (ED-binge METH) group, rats were gradually increase treated with METH3 times per day for 13 days and treated with 4.0 mg/kg METH 3 times on day 14 and treated with 6 mg/kg METH 4 times at 2 hours intervals on day 15. After treatments, rats were sacrificed by cervical dislocation and cauda epididymis was removed to release spermatozoa in phosphate buffer saline.

Sperm quality

Sperm motility was immediately evaluated after release from cauda epididymis. Motile and non-motile sperm were counted and expressed in percentage of normal sperm motility. After that, semen samples were fixed and stained with eosin solution to evaluate sperm morphology. 200 spermatozoa per animal were evaluated and sperm morphology was expressed in percentage of normal sperm morphology. To evaluate sperm concentration, spermatozoa were counted and expressed in millions per milliliter (10^6/ml).

Immunohistochemistry

Testicular tissues were fixed and histologically performed by auto-tissue processor. Testicular sections were processed for antigen retrieval and incubated with 5% normal goat serum. Testicular sections were then incubated with primary antibody comprised of progesterone receptor (PR) (Santa Cruz, Biotechnology, Santa Cruz, California), estrogen receptor beta (ERβ) (Santa Cruz, Biotechnology, Santa Cruz, California). Testicular sections were incubated with biotinylated secondary antibody, avidinbiotinylated horseradish peroxidase complexes (ABC kit) (Vector Laboratories, Burlingame, California), respectively. The specific proteins were visualized by chromogen 3, 3-diaminobenzidine (DAB)substrate(Vector Laboratories, Burlingame, California). The immunoreactive cells were quantified with Image J Program (Version 1.45).

Statistical analysis

One way ANOVA following by post hoc Dunnett test were used for statistical analysis.

2.2Results

The percentages of normal sperm motility and normal sperm morphology were significantly decreased in all groups of METH treated animals. However, the sperm

concentrationswere not reached significance when compared with control.Percentage of normal sperm motility was significantly decreased in AB METH group (32.79±5.35%), in ED METH group (45.50±2.83%), and in ED-binge METH group (42.66±4.71%) when compared with control group (66.50±2.79%) (Figure 1). Percentage of normal sperm morphology was significantly decreased in ED METH group (49.20±1.39%), and in ED-binge METH group (44.08±4.53%) when compared with control group. (68.33±7.41%) (Figure 2). The sperm concentrations were numerically decreased in ED METH group and ED-binge METH group when compared with control group, but it just failed to reach significant (Figure 3).

The immunohistochemistry demonstrated that PR and ERβ were expressed in all types of spermatogenic cells as well as sertoli cells in seminiferous tubule. Quantitative results demonstrated that the percentage of PR expression was significantly decreased in all METH treated animals in every cell types especially sertoli cells when compared with the control (Figure4). Similarly, ERβ expressions were significantly decreased in all METH treated groups (Figure 5).

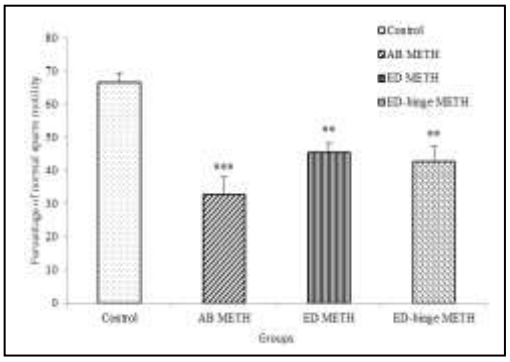

Figure 1. Percentage of normal sperm motility of male rats after treated with METH compared with control group. Data are presented as mean±SEM, n = 6, ** *P*<0.01 vs control group and *** *P*<0.001 vs control group.

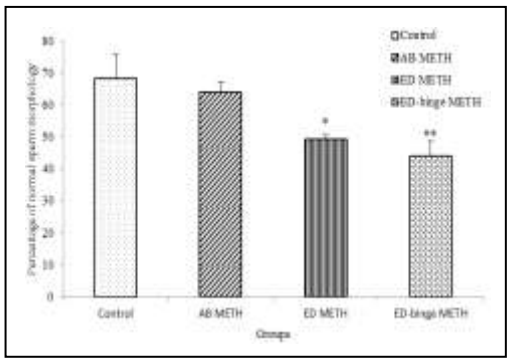

Figure 2. Percentage of normal sperm morphology of malerats after treated with METH compared with control group. Data are presented as mean±SEM, n = 6, * *P*<0.05 vs control group and** *P*<0.01 vs control group.

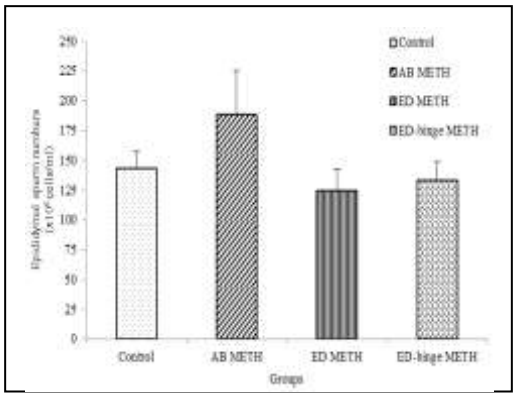

Figure 3. Sperm number of cauda epididymis (x10^6/ml) of male rats after treated with METH compared with control group. Data are presented as mean±SEM, n = 6

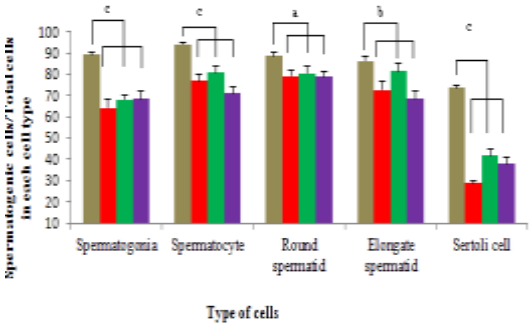

Figure4. The percentage of PR expression in each all type cells/total cells in seminiferous tubulesof control (brown), ED-binge METH (red), ED METH (green)andAB (violet)[a] $p<0.05$, [b] $p<0.01$ and [c]$p<0.001$ one-way analysis (ANOVA post – hoc Dunnett test).

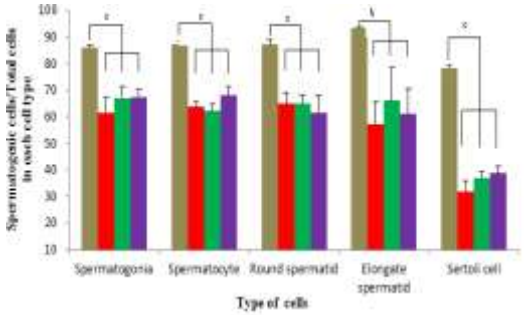

Figure5. The percentage of ERβ expression in each all type cells/total cells in seminiferous tubulesof control (brown), ED-binge METH (red), ED METH (green)andAB (violet)[b] $p<0.01$ and [c] $p<0.001$ one-way analysis (ANOVA post – hocDunnett test).

3. Discussions

The results demonstrated that animals treated with METH that imitates human addiction show abnormal parameters of sperm quality, especially sperm motility and sperm morphology. These results are in agreement with a previous study which reported a decrease of normal sperm morphology in seminiferous tubulesafter chronic exposure of METH (6). A reduction of sperm motility of male mice has also been reported in animals treated with 15 mg/kg METH at 24 and 48 hours after administration (12). However, 15 mg/kg METH used in that study seemed to be higher than daily consumption of METH dependence.

The present study also demonstrated the effects of METH on the alteration of PR, ERβ and ERα expressions in spermatogonic cells and sertoli cells in seminiferous tubule of rat testis. The deceases of PR and ERβexpressions in spermatogonic cells and sertoli cells, in particular, may affect the process of sperm production as progesterone and estrogen have been reported to be essential hormones for spermatogenesis (8).

In conclusion, METH administration that imitates human addiction can induce abnormalities in sperm quality. Decreases of sperm motility and sperm morphology caused by METH may be involved their fertilizing abilities of sperm leading to reproductive problems in males.A decrease of PR and ERβ expressionsin spermatogenicand sertolicells may lead to impairments of spermatogenesis and fertilizing ability of sperm.This present study, therefore, can reflect toxicity of methamphetamine in male reproduction.

4. Acknowledgements

This research was supported by Naresuan University Research Fund and TRF-Master Research Grant(MAG Window II 53).

5. References

[1] Barr AM, Panenka WJ, William MacEwan G, Thornton AE, Lang DJ, Honer WG, Lecomte T. The need for speed: an update on methamphetamine addiction. *Journal of Psychiatry Neuroscience* 2006; 31: 301-313.

[2] Derlet RW, Heischober B. Methamphetamine Stimulant of the 1990s?*The Western Journal of Medicine* 1990; 153: 625-628

[3] Albertson TE, Derlet RW, Van Hoozen BE. Methamphetamine and the expanding complications of amphetamines.*The western journal of medicine* 1999; 170: 214-219

[4] Yamamoto Y, Yamamoto K, Hayase T, Abiru H, Shiota K, Mori C. Methamphetamine induces apoptosis in seminiferous tubules in male mice testis. *Toxicology and Applied Phamacology* 2002; 178: 155-160Report, 1999

[5] Alavi SH, Taghavi MM, Moallem SA. Evaluation of effects of methamphetamine repeated dosing on proliferation and apoptosis of rat germ cells. *Systems Biology in Reproductive Medicine* 2008; 54: 85–91.

[6] Nudmamd-Thanoi S, Thanoi S**.** Methamphetamine induces abnormal sperm morphology, low sperm concentration apoptosis in the testis of male rats. *Andrologia* 2011; 43: 278-282

[7] Alavi SH, Taghavi MM, Moallem SA. Evaluation of Effects of Methamphetamine Repeated Dosing on Proliferation and Apoptosis of Rat Germ Cells. *Systems Biology in Reproductive Medicine* 2008; 54: 85 – 91

[8] Shah C, Modi D, Sachdeva G, Gadkar S, Puri C. Coexistence of Intracellular and Membrane-Bound Progesterone Receptors in Human Testis. *Clinical Endocrinology & Metabolism* 2009; 90(1): 474-483.

[9] Schwarzenbach H, Manna R, Stocco D, Chakrabarti G, Mukhopadhyay K. Stimulatory Effect of Progesterone on the Expression of Steroidogenic Acute Regulatory Protein in MA-10 Leydig Cells. *Biology of Reproduction* 2003; 68: 1054–1063.

[10] Losel R, Breiter S, Seyfert M, Wehling M, Falkenstein E. Classic and non-classic progesterone receptors are both expressed in human spermatozoa. *Hormone Metabolism Research* 2005; 37: 10–14.

[11] Hess RA, Carnes K. The role of estrogen in testis and the male reproductive tract: a review and species comparion. *Animal Reproduction* 2004; 1: 5-30.

[12] Yamamoto Y, Yamamoto K, Hayase T**.** Effect of methamphetamine on male mice fertility. *ObstetGynaecol* 1999; 25: 353-358

LSBE 300
Rubber Stand Predictive Model Applications using Pixel-Based Classification and Image Segmentation on Landsat TM in Selangor, Malaysia

Mohd Nazip Suratman
Faculty of Applied Sciences and Centre for Biodiversity and Sustainable Development
Universiti Teknologi MARA, 40450 Shah Alam Malaysia
nazip@salam.uitm.edu.my

Abstract

Rubber tree (*Hevea brasiliensis*) plantations in Malaysia are important sources of natural rubber and wood products. Effective management and appropriate policy for these resources require reliable information on resource dynamics and forecasts of resource availability. The need for inventories and monitoring systems prompted this research into utilising ground information and satellite imagery for developing methods for plantation inventory. The objectives of this study are to demonstrate the application of volume estimation procedure, based on prediction models developed by Suratman *et al*. (2004), across an extended sample of rubber plantations south of Kuala Lumpur, Malaysia and to perform image segmentation and pixel-based techniques for application of rubber stand predictive models on Landat TM imagery. For image segmentation, the mean of spectral radiance of rubber stands were extracted by segments, and then the equation was applied to each segment. The image segmentation technique resulted in 812 rubber segments, with segment areas ranging from 1.5 – 14 ha. The mean area of the segments was 3.3 ha, and the estimated mean of rubber volume derived from the model was 237 m^3/ha. For pixel-based classification, a reasonable signature separation between the five rubber volume classes and the four land use/cover types (i.e., water bodies, forests, cleared areas, and urban) was achieved. In conclusion, both techniques can be a useful tool for estimating average volume within localised areas. In the context of rubber plantation management and planning, segmentation technique is preferred as it partitions rubber pixels into spatial units that could be referred to as rubber estates or rubber small landholding units.

1. Introduction

The total natural forest area in Malaysia is 18.9 million ha, or 57.5% of the total land base. Of this total, 14.3 million ha has been set aside for a permanent forest reserve to be managed sustainably. From this area, about 10.9 million ha are production forests and 3.4 million ha are protection forests [1]. An additional 2.4 million ha of forest area is known as conversion forest, which in due time, will be converted to other uses to meet the needs of population growth and balanced economic development. In

addition to natural forests, the country has established about 0.19 million ha of forest plantations consisting of fast growing tree species such as acacia (*Acacia mangium* Willd.), batai (*Albizia falcataria* (L.) Fosb.), and yamane (*Gmelina arborea* Roxb.). Additionally, Malaysia has approximately 4.82 million ha of agricultural tree crops which are mainly rubber, oil palm, coconut, and cocoa [2].

Rubber tree crops play pivotal roles in providing natural rubber, sources of wood products, and other benefits that support basic human needs and economic development [1][3]. Despite their importance, little attention has been given to inventory, mapping, and monitoring the crops. This could be because government agencies are often under-funded, thus data on tree crop resource monitoring tend to be sporadic. In spite of the country's awareness of the socio-economic roles of rubber plantations, a decline in the total area of rubber plantations in Malaysia occurred throughout the 1990s. In 2000, Malaysia had about 1.43 million ha of rubber plantations compared to 1.02 million ha in 2011, representing about a 29% reduction [4]. The objectives of this study are to demonstrate the application of the rubber area and stand volume prediction models developed by Suratman *et al*., [5] across an extended sample of rubber plantations south of Kuala Lumpur, Malaysia and to compare pixel-based and segmentation techniques for the application of rubber stand predictive models on Landat TM imagery.

2. Materials and Methods

2.1 Study Area

The area chosen was located about 20 km south of Kuala Lumpur, in the State of Selangor, Malaysia, between 101^{o} 25'and 101^{o} 45' E latitudes and 2^{o} 50' and 3^{o} 05' N longitudes, covering about 250 km^2. The region has a tropical climate characterised by a dry season (March to May) and a wet season (November to January), with a mean annual precipitation of 2,178 mm. Daytime mean temperature ranges from 22.9^{o}C to 27.7^{o}C (Meteorological Service 2002). The selected area consists of three districts namely Petaling, Sepang, and Kuala Langat. The topography in the area is predominantly flat, with altitudes ranging from 5 – 80 m above sea level. The forest type is Lowland Dipterocarp Forests, which contains a high percentage of commercial tropical hardwood species. Crop types are primarily rubber and oil palm plantations, as well as varying sizes of mixed crops. The mixed crops are characterised by diverse intercropping of traditional homegarden systems, with a mixture of coffee, cocoa, coconut, banana, shrubs, and herbaceous plants [6].

2.2 Satellite Image Acquisition

The remote sensing data consisted of a full scene image of the State of Selangor (*path* 127/*row* 58), Malaysia from the TM sensor on Landsat-5. Available reference data to

support this work consisted of a 1999 State of Selangor map at a scale of 1:125,000 (series 9101), and 1990 topographic maps at a scale of 1:50,000 (sheet numbers 3756 and 3757), both produced by the Department of Survey and Mapping, Malaysia. The land use and land cover and soil maps were obtained from the Department of Agriculture, Malaysia.

2.3 Image Pre-Processing

A PCI Geomatica (Version 7.0) software was used to perform all image-processing functions required to complete the land use/cover classification and change analyses [7]. ArcView GIS (Version 3.2) was used to carry out data management and a spatial analysis [8]. Geometric correction was performed for producing spatially corrected maps of land use/cover.

2.4 Application of the Rubber Area Model

The rubber area model based on logistic regression developed by Suratman *et al*. [5] was applied to the 1999 Landsat TM imagery using the MODEL command in 'Xpace' utilities of PCI Geomatics software [7]. Output bitmaps of predicted rubber pixels were produced where the probability of rubber was $\geq$ 0.5 and displayed on the imagery.

2. 5 Application of the Rubber Stand Volume Model

Two methods of applications of rubber stand volume models developed by Suratman *et al.* [5] were conducted *viz.* image segmentation and pixel-based classification methods. For image segmentation technique, an *eCognition*'s Version 2.1 software [9] was used to automatically segment the pixels of the 1999 Landsat TM image. The volume model was applied to the mean values of all pixels classified as rubber through a supervised classification process. This produced the predicted rubber volume for the segment. Rubber pixels within the segment area were then exported into a shape file (.shp) in ArcView GIS.

2.6 Supervised Image Classification

A supervised classification of the 1999 Landsat TM image was used to produce general land use/cover types and rubber volume classes. This operation produced a thematic map with 12 class categories. Pixel-based rubber volume classification was performed to evaluate the capability of the classifier to categorize rubber stand volume measured from the field in combination with other land use/cover classes. Training and testing areas for rubber volume classes were delineated in the image. A final 12-class map was created from the combination of seven non-rubber classes and five rubber volume classes: (1) water; (2) forest; (3) oil palm; (4) mixed crops; (5) grasslands; (6) cleared areas; (7) urban; (8) rubber volume class 1; (9) rubber volume class 2; (10) rubber volume class 3; (11) rubber volume class 4; and (12) rubber volume class 5.

2.7 Accuracy Assessment Rubber Models and Land Use/Cover Classification

The accuracy of the classified products was assessed by comparison with independent test areas using the standard procedures [10]. This created error matrices, which encompassed reference pixels with classified pixels. Four criteria were used to assess the accuracy of the classifications: (1) overall accuracy; (2) user's accuracy or commission error; (3) producer's accuracy or omission error; and (4) Kappa coefficient = ((overall accuracy-expected accuracy)/(1-expected accuracy)).

3. Results and Discussion

3.1 Rubber Area Model Application

Prior to volume model application, consideration was made to decide whether to use the area model developed from logistic regression or supervised classification for producing rubber area masks. For this purpose, the output rubber bitmaps and classification accuracies produced from both techniques were evaluated (Figure 1). Comparison of rubber area bitmaps produced from these techniques indicated some spatial agreements. In terms of accuracy, it was found that the supervised classification using the maximum likelihood algorithm was superior to the area model. When refitted with the entire data set, overall, the area model correctly assigned 94.5% of the pixels. However, the model did a better job in predicting non-rubber (96.3%) than that of rubber (87%). Using the same image (Landsat TM 1999), the supervised classification produced a higher accuracy of classifying rubber at 96.9%. Therefore, it was decided that the rubber area map produced from supervised classification would be used for the volume model application.

3.2 Rubber Volume Model Application

With an image segment-based approach, the application of the rubber stand volume model in classified rubber pixels was demonstrated. The mean of spectral radiance of rubber stands were extracted by segments, and then the equation was applied to each segment. The image segmentation technique resulted in 812 rubber segments, with segment area ranging from 1.5 – 14 ha. The mean area of the segments was 3.3 ha, and the estimated mean of rubber volume derived from the model was 237 m^3/ha.

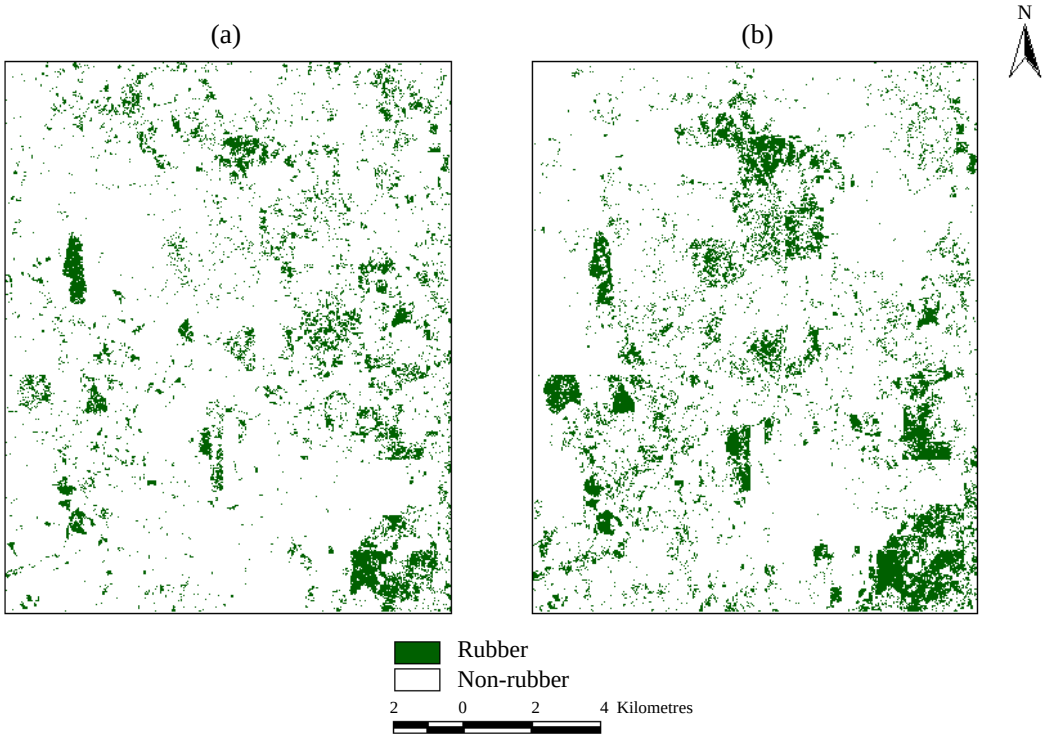

Figure 1. Rubber area maps from the 1999 Landsat TM image of the demonstration area: (a) output bitmaps of rubber area predicted by area model using a logistic regression, and (b) thematic map of rubber area produced by a supervised classification.

Applying the model at the stand level allowed for the extraction of spectral features to be carried out by segments, which are homogenous in the sense of their spectral and stand characteristics. In the context of rubber management planning, the segments could be referred to as rubber estates or rubber small landholding units. The resulting rubber assessment polygons with six volume classes (m^3/ha) estimated from the model are shown in Figure 2 the analysis demonstrated that the stand attribute model derived from satellite data could be applied using the image segmentation technique. This provides a useful tool for estimating average volume within localised areas, plantations, or segments.

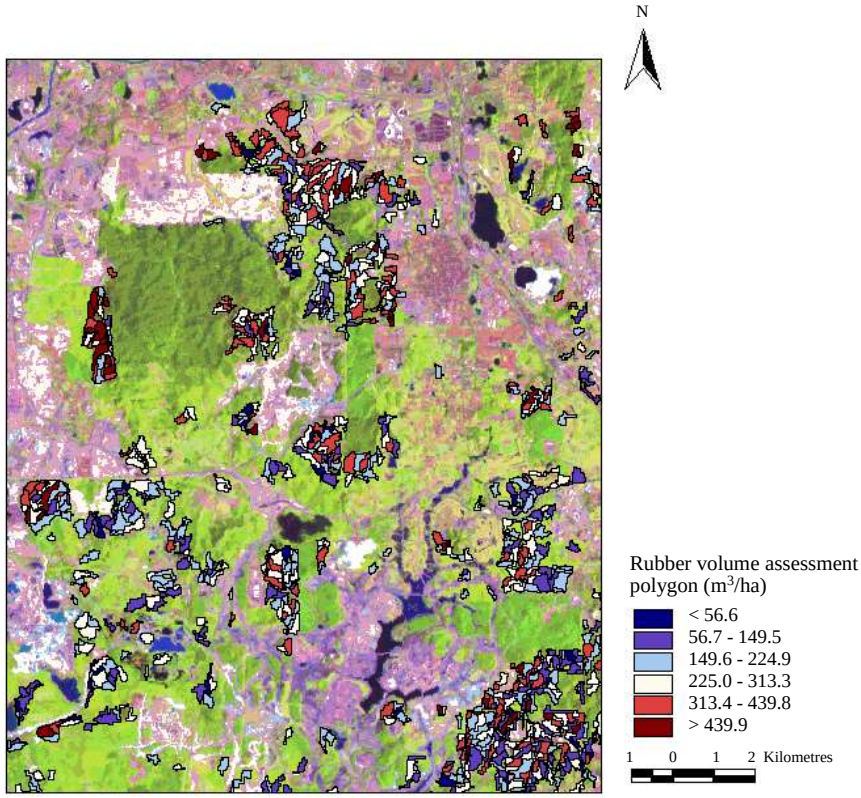

Figure 2. Rubber volume assessment polygon produced from an application of volume model and an image segmentation technique superimposed on the 1999 Landsat TM pseudocolour composite (RGB = bands 5, 4, 3) image of the demonstration area.

3.3 Rubber Volume Classification Accuracy

Supervised classification resulted in a thematic map (Figure 3) and error matrix (Table 1) consisting of seven land use/cover-class categories combined with five rubber stand volume classes. The overall accuracy and Kappa coefficient values were 67.7% and 0.64, respectively. While water bodies, forests, cleared areas, and urban areas were displayed without much confusion, however mixed crops, grasslands, and all rubber volume classes showed high amounts of misclassification. Also, the low accuracy was attributed to the difficulty in separating grasslands from rubber volume class 1. In particular, 72% (430) pixels belonging to grasslands were misclassified as volume class 1. Only 18.2% of the pixels (user's accuracy) were correctly classified. Major confusion was also observed between mixed crops and volume class 1. About 58% (417) of pixels belonging to mixed crops were confused with volume class 1, which resulted in a user's accuracy of 27.1% (Table 1). These confusions where the majority of the area of grasslands and mixed

crops were occupied by rubber volume class 1 (0 – 75 m^3/ha). Again, this result can be attributed to the existence of ground vegetation and low rubber crown closure in young rubber plantations (3 – 8 years of age for volume class 1), resulting in similar signatures to grasslands and the undergrowth components of mixed crops. As expected, due to poor separability, each of the volume classes recorded only poor to moderately good classification accuracies. The user's accuracy ranged from 18.2% (volume class 3) to 71.0% (volume class 1) (Table 1).

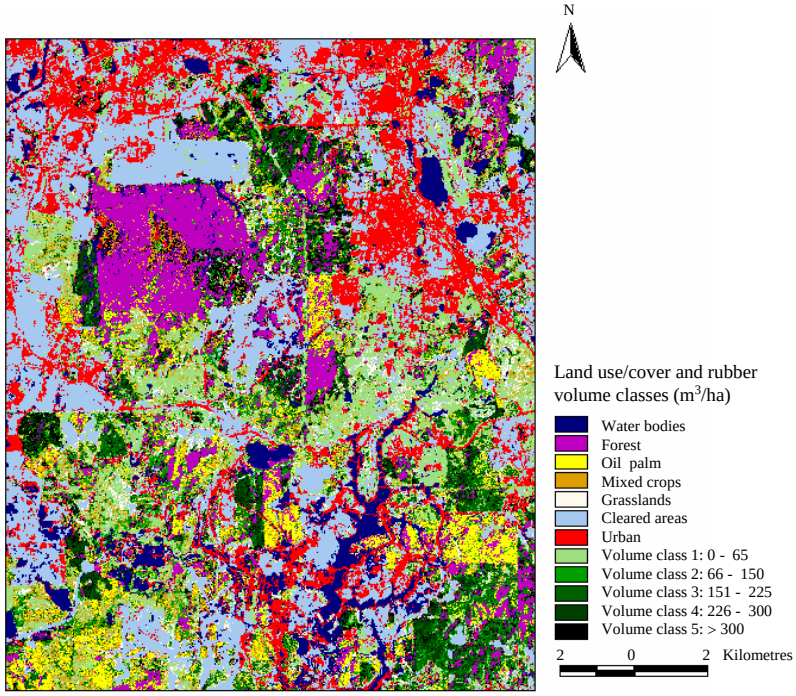

Figure 3.
Land use/cover thematic map combined with rubber volume class map produced by a supervised classification of the 1999 Landsat TM image

Table 1. Confusion matrix of land use/cover and rubber volume classification accuracy by the number of pixels classified correctly in the thematic map of the 1999 Landsat TM.

Land use/cover and rubber voume classes	Pixels classified by class													User's accuracy
	Water	Forest	Oil palm	Mixed crops	Grasslands	Cleared areas	Urban	Vol. class 1	Vol. class 2	Vol. class 3	Vol. class 4	Vol. class 5	Total	
Water	**664**												664	100.0
Forest	10	**1,058**	24	11			1		46	9	15	48	1,222	86.6
Oil palm		26	**685**	69	4		4	9	60	1		2	860	79.7
Mixed crops		1	52	**195**	26			417	10	18			718	27.1
Grasslands	2		8	34	**109**	10		430	3	3			599	18.2
Cleared areas						**637**							637	100.0
Urban						15	**368**						383	96.1
Vol. class 1			5	9	4	1		**96**	9	9		2	135	71.0
Vol. class 2		10	1	7	1	1		13	**38**	10	32	54	167	22.8
Vol. class 3		1	23	6				7	20	**16**	3	12	88	18.2
Vol. class 4	1	1	1	11	1	2		4	54	62	**232**	53	422	55.1
Vol. class 5		3	4	2		1		1	23	37	124	**69**	264	26.1
Total	676	1,100	803	344	145	667	374	977	264	164	406	240	6,159	
Producer's accuracy	98.2	96.2	85.3	56.7	75.1	95.5	98.5	9.8	14.4	9.7	57.2	28.8		

Notes: The bold values show the correctly classified pixels in each category. Numbers of pixel in the grey boxes were used to highlight accuracy

comparison between general land use/cover and rubber volume classes.

$$\text{Overall accuracy} = \left(\frac{664 + 1{,}058 + 685 + 195 + 109 + 637 + 368 + 96 + 38 + 16 + 232 + 69}{6{,}159} \right) \times 100 = 67.7\%$$

Overall Kappa coefficient = 0.64

Rubber volume class 1 was clearly associated with grasslands and mixed crops, and there was confusion among the five rubber volume classes. However, it is also interesting to explore how well the classification with multiple volume classes performed for just separating rubber from non-rubber classes and broader volume class of rubber. Three approaches were used to investigate these questions.

The first approach was to reclassify the image by omitting volume class 1 from the classification, reducing the number of classes to 11 classes. While this resulted in improvements in the overall classification accuracy (67.7% to 76.7%), the user's accuracies of mixed crops (27.1% to 69.3%), and grasslands (18.2% to 57.8%), it did not result in an appreciable increase in all rubber volume class accuracies (table not shown).

The second approach involved comparing overall rubber volume classification accuracy to general land use/cover classification (see grey boxes in Table 1). Results from these analyses indicated that combining all rubber volume classes together produced an overall user's accuracy of 91.0% ((980/1078) × 100) and producer's accuracy of 47.8% ((980/2051) ×100). The poor overall producer's accuracy was attributed to the association of mixed crops and grasslands with rubber volume class 1 as described in Section 5.3.4.3. Combining all classes together except volume class 1 produced 89.2% user's accuracy ((839/941) × 100) and 78.1% producer's accuracy ((839/1074) ×100) overall. The main source of error was in separating oil palm and rubber volume class 2. Subsequently, combining all classes together except volume classes 1 and 2 produced an overall user's accuracy of 78.6% ((608/774) × 100) and producer's accuracy of 75.1% ((608/810) ×100).

Generally, errors from rubber volume classification were resulted from high natural variability within volume classes. Also, the high error was likely due to the volume classes used for the classification being too fine. This caused an overlap of spectral signatures because the spectral characteristics of the volume classes were not distinctive enough to be used for the identification and separation of individual rubber volume classes. As well, the volume classes are a continuum with transition zones between them. A combination of these factors, in part, may have contributed to the confusion in determining the volume classes using the maximum-likelihood classifier.

4. Conclusions

This paper shows a comparison of two approaches for applying rubber stand volume model in an extended area of rubber plantations. They are: (1) the use of a supervised classification to delineate a rubber bitmap for an application of rubber volume model based on image segmentation technique, and (2) the use of ground information to provide training areas for a combined supervised classification of land use/cover and volume classes. The first approach resulted in 11.7% overall classification error with

eight land use/cover as compared to an overall classification error of 32.3% for the twelve classes in the second approach. The classification error using the first approach was 3.6% as compared to a classification error of 29.0 – 81.8% for the five rubber volume classes in the second approach. Therefore, for the purpose of predicting rubber volume classes within a spatial unit, the first approach was preferred.

5. References

[1] Forestry Department Peninsular Malaysia. Country report – Malaysia. Forestry Department Headquarters, Peninsular Malaysia. Asia Pacific For. Sector Outlook Study Working Pap. Series. No. APFSOS/WP/07. FAO, Rome. 1997. 24 pp.

[2] Department of Agriculture. Industrial tree crop statistics. 2002. (Web page). Available at: http://agrolink.moa.my/doa. 25 Sep. 2002.

[3] MRB. Malaysian rubber boards rubber statistic (Web page). Available at: http://www.lgm.gov.my. 16 Sep. 2002.

[4] MRB. Natural Rubber Statistics. 2013. Available at: http://www.mrb.gov.my. 7 January 2013.

[5] Suratman M N, Bull G Q, LeMay V M, Leckie D G, Marshall P L, Mispan M R. Prediction models for estimating volume, age and predicting area of rubber plantations in Malaysia using Landsat TM Data. *International Forestry Review*. 6 (1): 2004, 1–13.

[6] Suratman M.N, Muhammed M, Rahman N, Jiwan D. A preliminary survey of agroforestry systems in Malaysia. *In Proc. of the Fourth Conference on Forestry and Forest Products Research*. FRIM, Malaysia. 2000. pp. 497−507.

[7] PCI. ImageWorks. Version 7.0. Richmond Hill, Ontario, Canada. 1997. 203 pp.

[8] ESRI. ArcView GIS. Version 3.2. Redlands, CA. 1996. 340 pp.

[9] Defisiens Imaging. *eCognition* - Object oriented image analysis. White Paper. 2002. 4 pp.

Congalton R G. 1991. Review of assessing the accuracy of classifications of remotely sensed data. *Remote Sensing Environ*. 1991. 37:35−46.

Civil Engineering II

2013/3/16 Saturday 10:45-12:15 Room 604

Session Chair: ***Prof. Mehmet Sahin***

ACCMES 158

Modal Analysis of Regular Shear Buildings; an Analytical Approach

Mehmet Sahin | *Turksat A.S.*

ACCMES 159

Critical Direction of Horizontal Load for Maximum Forces in Columns and Braces for Elevated Water Tanks

Abhay Genu Khandeshe | *Visvesvaraya National Institute of Technology*
Ramakant K Ingle | *Visvesvaraya National Institute of Technology*

ACCMES 161

Feasibility of Applying Chimney Effect Theory to Cool Reinforced Concrete Exterior Walls

Chih Yuan Chang | *Feng Chia University*
Kuei Sheng Ko | *Feng Chia University*
San Shan Hung | *Feng Chia University*
Chung Yu Yang | *Feng Chia University*

ACCMES 164

Live Loads Dependent Structural Behavior of Large-Sized Concrete Floating Container Terminals

Youn Ju Jeong | *Korea Institute of Construction Technology*
Du Ho Lee | *Korea Institute of Construction Technology*
Min Su Park | *Korea Institute of Construction Technology*
Young Jun You | *Korea Institute of Construction Technology*

ACCMES 168

Replacement of Ordinary Portland Cement by Rice Husk Ash (RHA) to Produce Concrete of Grade M20, M25 & M30

Kalyan Kumar Moulick｜*Bengal Engineering and Science University*

ACCMES 186

Analysis of Factors for Growth of Local Industries and Changes in the Clustering of Manufacturing in Japan

Katsutoshi Kato｜*Osaka Institute of Technology*
Yukikazu Yamaguchi｜*Osaka Institute of Technology*
Katsutoshi Kato｜*Osaka Institute of Technology*
Yoshikazu Iwasaki｜*Osaka Institute of Technology*

ACCMES 158

Modal Analysis of Regular Shear Buildings; an Analytical Approach

Mehmet Sahin
TURKSAT AS Arge Dir. Gazi Teknopark B Blok Golbasi Ankara TURKEY
msahin@turksat.com.tr

Abstract

The governing dynamic equilibrium equation of *N*-story regular shear building witharbitrary top story mass, arbitrary base story stiffness and subjected to base excitation is given in theform of constant coefficient second order finite-difference equation. The z-transform method isapplied to the equation to obtain the general solution for displacement mode shapes. Applying thesecond boundary condition the result in a nonlinear characteristic equation in which the frequenciesare obtained by solving it. The general form of the characteristic equation for eigen-frequencies ispresented and displacement and drift modeshape functions are obtained. All the modal parameters including modal mass, excitation factor,participation factor, and the effective modal mass are presented as sum and sum of square of modaldisplacements.Some special top mass cases is discussed in detail and their modal parameters are given in the exact analytical form.The method discussed in this study can also be extended for the other 1-D engineering systems which may have the same equation of motion, such as repetitive spring-mass vibration system.

Keyword:eigen-analysis, modal analysis, z-transform, shear buildings, repetitive structures

5. Introduction

The some systems, such as structures, electrical/electronic systems etc., with manyidentical parts, substructures or subsystems joined together in various forms are frequently encountered in engineering practice. Examples ofsuch engineering systems are rotors, monorail tracks, aircraft fuselages with segments, buildings,towers, etc. These kinds of structures are sometimes named as, periodic, repetitive, identical, regular,or uniform structures. The periodicity of the substructures makes the structures easy to analysis in asimplified manner. There are mainly four approaches to analyses of the periodic structures asmentioned in the Stephen's study[HYPERLINK \l "Stephen1999" 1]. These are direct, direct field, periodic structure and substitutecontinuum methods. The direct method is direct solution of the governing mathematical equations bynumerical methods, such as the matrix methods. The matrix methods are readily available and widelyused in engineering practice, but, they can be computationally least efficient and time consuming forperiodic structures. The direct field method uses finite-differences to relate the displacements oneither side of

the cell elements. The periodic structure method typically uses a transfer matrix to relatethe state vector of displacement and force components of on either side of the generic cell. Lastly, thesubstitute continuum approach can be suitable if the number of periodic substructures is sufficientlylarge to approximate the structure as a continuum.

Buildings with identical stories at each floor level are well-known examples of periodicstructures. The shear building model is actually an idealized model where it assumed that floors arerigid and columns are inextensible so that no joint rotation occurs at the floor and column connections2][HYPERLINK \l "CloughPenzien2003" 3]4][HYPERLINK \l "Sahin2008" 5]6][HYPERLINK \l "WilsonEERIHabibullah1987" 7]8][HYPERLINK \l "Timoshenko1971" 9]. This idealization reduces the number of degrees of freedom since only thelateral translational degrees of freedoms are taken into account. The eigen-solution of uniform shearbuildings using direct field method is available in the literature4][HYPERLINK \l "Thompson1993" 10]5][HYPERLINK \l "sah1" 6]. This study is an application ofdirect field approach using z-transform method to solve eigen-analysis of the discrete uniform shearbuilding and is to obtain the modal parameters. However, the formulation can be valid for any one-dimensional periodic structures havingthe same equation of motion as discussed in this study. Twoboundary conditions are the top story equilibrium equation and base story zero displacement. The topstory mass for the boundary condition and base stiffness are selected arbitrarily to obtain more generalform of the system model including buildings with soft-story or base isolation systems. Thecharacteristic equation is obtained by applying these boundary conditions and can be solvedanalytically for certain boundary conditions otherwise it requires numerical solution method.

Generally, a dynamical system consisting of *N*-degree of freedom system may require thesolution of a *N*th order polynomial characteristic equation or the eigen-solution of *N*x*N* matrix.The z-transform method is widely used in digital signal processing, digital control,communication field of electronic engineering. The transformation is discrete form of Laplacetransformation and makes it suitable solution method for discrete systems as compared to Laplacemethod for continuous systems11]. There are numerous studies, which are toomany to mention all them here, related to structures with identical subsystems[HYPERLINK \l "Jennings1997" 2]4][HYPERLINK \l "Sahin2008" 5]12][HYPERLINK \l "MeirovitchEngels1977" 13]. Meads12] summarizes and reviews all the studies regarding wave propagation and response analysis of periodic structures until 1995. Stephen[HYPERLINK \l "Stephen1999" 1] uses periodic structure and substitute continuum approach to study frequency analysis of pin-jointed one-dimensional framework and compare various continuum models with actual FEM model frequencies. Karpov et al.14] use

discrete Fourier transform method for thestatic analysis of repetitive lattice structures. Meirovitch[HYPERLINK \l "MeirovitchEngels1977" 13] applied the z-transform method to the matrix difference equation to obtain the general form of response for the periodic structures. This study is an application of the z-transform method to the repetitive shear building with arbitrary top story mass and base stiffness.

6. Formulation and Solution

Consider *N*-story uniform shear building with equal story masses, lateral stiffnesses, and heights are shown by *m*, *k*, and *h* respectively (Fig.). However, the top story mass and base story stiffness are assumed to be arbitrary to consider more general case for the various boundary conditions. The origin of the index variable *n* starts from the top of the building and ends at the base. The base story stiffnes is multiple of regular mass, i.e. $k_{N-1} = bk$ and relation between top story mass and regular mass is given as $m_0 = m(1+\alpha)$. The building is assumed to be standing on rigid foundation and subjected to a ground excitation $\ddot{u}_g(t)$. The governing equilibrium equation for *n*-th floor level at time *t* can be written in constant coefficient second-order finite-difference form as

$$k\nabla\Delta u_{n.t} = k\delta^2 u_{n.t} = -m\left(\ddot{u}_{n.t} + \ddot{u}_g\right), \qquad 0 < n < N \tag{1}$$

$$BC's = \begin{cases} k\Delta u_{0.t} = -m_0\left(\ddot{u}_{0.t} + \ddot{u}_g\right) = m(1+\alpha)\left(\ddot{u}_{0.t} + \ddot{u}_g\right) \\ u_{N,t} = 0 \end{cases}$$

where ∇, Δ, and δ are backward, forward and central difference operators respectively.The first boundary condition is the force equilibrium at the top of building. The second boundary condition is base displacement which is assumed to have zero displacement, i.e. $u_{N,t} = 0$.

For free-vibration analysis, the displacement $u_{n,t}$ can be separated into the displacement mode shape functionU_n and time dependent function $Y(t)$ by using the separation of variables method.

$$u_{n,t} = U_n \sin(\omega t + \varphi) \tag{2}$$

In the Eq. 2, ω is the vibration frequency and φ is the phase angle. Then, the governing equation of free-vibration for modal displacement shape function becomes.

$$\nabla(\Delta U_n) = U_{n+1} - 2U_n + U_{n-1} = -\Omega^2 U_n, \qquad 0 < n < N$$

$$BC's = \begin{cases} \Delta U_0 = \Omega^2(1+\alpha)U_0 \\ U_N = 0 \end{cases} \tag{3}$$

where$\Omega = \omega/\sqrt{k/m}$ is normalized frequency of the shear building. The boundary condition at the top story level includes the top story mass which can be taken arbitrarily for more general case analysis. Two common different cases for the top story mass will be considered in detail, the first case is all masses including top

masses are the same i.e. $m_0 = m$, the second case is the top story mass is half of the other story masses, i.e. $m_0 = m/2$. The latter case is just for simplification in the formulation and may be suitable for discretization of some real continuous bars[HYPERLINK \l "Thompson1993" 2].

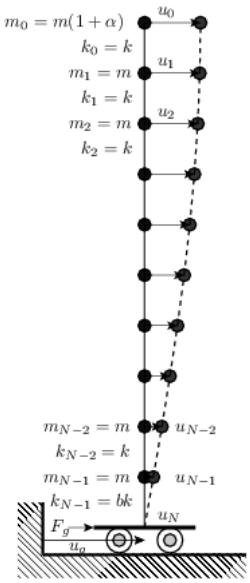

Fig. 1